Tuning the thermal conductivity of polycrystalline films via multiscale structural defects and strain

Juliana Jaramillo Fernandez

École Centrale Paris

THÈSE

présentée par

Juliana JARAMILLO FERNANDEZ

pour l'obtention du

GRADE de DOCTEUR

Formation doctorale : Physique - Énergétique

Laboratoire d'accueil : Laboratoire de Récupération des Micro-énergies
LITEN, CEA Grenoble

Tuning the thermal conductivity of polycrystalline films via multiscale structural defects and strain

Soutenue le 13 mai 2015

Jury :	Mme	SOTOMAYOR	C. M.	Examinateur
	MM	BOURGEOIS	O.	Rapporteur
		TABBAL	M.	Rapporteur
		PERRAUD	S	Examinateur
		OLLIER	E.	Co-encadrant
		VOLZ	S.	Directeur de thèse

École Centrale des Arts et Manufactures
Grand Établissement sous tutelle
du Ministère de l'Éducation Nationale
Grande Voie des Vignes
92295 Châtenay Malabry Cedex
Tél 33 (1) 41 13 10 00
Télex 634 991 F EC PARIS

Laboratoire d'Énergétique Moléculaire et Macroscopique, Combustion (E.M2.C.)
UPR 288, CNRS et École Centrale Paris
Tél : 33 (1) 41 13 10 31
Fax : 33 (1) 47 02 80 35

2015

It has been a beautiful fight.

Still is.

Charles Bukowski

Dedicated to the strongest woman
I have ever known: my mother.

Acknowledgments

When I decided to pursue my doctoral studies, it was impossible to imagine to what extent this experience could be enriching. Evidently, from the academic point of view, the last three years represented an exciting intellectual challenge and a beautiful journey through knowledge. Still, the most striking revelation was to realize how much you can learn from others. I marveled at discovering that people around you have the power to transform hard times into precious memories and life experiences. These last three years taught me to deeply understand what Aristotle successfully put into words a long time ago: *Man is by nature a social animal.*

I have been extremely lucky, because through this journey, I have had the honor and the privilege to meet and work with extraordinary people. In no particular order, I would like to express my profound gratitude to them.

I wish to express my thoughtful appreciation to my thesis committee members, namely Prof. Dr. Clivia M. Sotomayor Torres, Dr. Olivier Bourgeois, Prof. Dr. Malek Tabbal, Dr. Simon Perraud, Dr. Emmanuel Ollier and Dr. Sebastian Volz, for their valuable time and for the depth to which they inspired me to think. I am greatly indebted to my reviewers, Prof. Dr. Malek Tabbal and Dr. Olivier Bourgeois, who kindly agreed to read this manuscript in record time, allowing me to meet a very tight time schedule, and provided me with strong critical feedback and rich discussions about my work.

I owe very much to my colleagues and friends at CEA-Liten, LRME laboratory. Firstly, I want to address my heartfelt thanks to Helga, Christelle, Geraldine, Francoise and Viviane. They have not only helped me with many technical details but they have always found the appropriated words to keep me motivated. Our discussions have been crucial to keep me sane! I express my vivid appreciation to Helene, Delphine, Jacqueline, Michel, Henri, Titi, Fabrice, Pascal, Seb, Cedric and Nico, who have contributed intellectual and personal ingredients to the success of this thesis. I am also grateful to Estef, Christophe and Mathew for giving me priceless excuses to take my mind out of work and change my ideas. I take this opportunity to wish all the best to the brave PhD candidates that are approaching the finish line: Carine and Duy.

I owe special recognition to my extraordinary friend, Toso. Thank you Toozzz for the Mediterranean food and the humus, for the most delicious orangettes, for your music, for the crazy laughs and for showing me that it was possible. I am also indebted to Jeremy Tillier. His invaluable advice on crystallography, material fabrication and characterization as well as our interesting discussions were key elements to successfully obtain highly textured AlN films.

I want to thank Ulrich Soupremanien as well as my co-advisor, Emmanuel Ollier, who both kindly read this manuscript and provided critical comments. Throughout my PhD studies, Ulrich always gave me useful suggestions and Emmanuel provided me with the autonomy necessary to conduct and develop my research ideas.

Words cannot express my deep and lastly gratitude to my brightest collaborator and friend: Vincent Remondier, Grand-Père. He has been an inexhaustible source of motivation, encouragement and intellectual stimulation throughout the last years. He is, furthermore, the only person that has the ability to transform a tough situation into an explosion of laughter. Vincent is also the author of several graphical "chefs-d'oeuvre" included in this manuscript and, without his support, the realization of the strain-mediated experimental set-up would not have been possible. I also truly appreciate help provided by Helene, Jean, Tristan, and Sylvain and I enjoyed fruitful conversations with Natalio Mingo.

I deeply thank Nathalie Pelissier from CEA-Liten, for her helpful assistance in preparing the TEM samples and her collaboration for the transmission electron microscopy characterization. I express my vivid acknowledgments to Jacques Cluzel and Denis Blachier from CEA-Leti for their willingness to share their knowledge as well as the electrical characterization facilities for the 3ω measurements. I feel also very grateful towards Jean-Sebastien Micha, Odile Robach and their group from ESRF, for their kindness and for letting me play with their big monster, the synchrotron, to look for AlN's Laue micro-diffraction signal.

I wish to express my sincere thanks to all the members of the Thermal Nanoscience Group at EM2C, namely, Yann Chalopin, Thomas Antoni, Pr. Michel Kazan and, of course, all the Ph.D. candidates and doctors: Sergei Gluchko, Haoxue Han, Jordane Soussi, Benoît Latour, Wassim Kassem, Laurent Tranchant, Shiyun Xiong and Aymeric Ramiere. I truly enjoyed the conferences, our enriching debates and the constant support that I received from all the group members. I feel particularly thankful towards Dr. José Ordoñez-Miranda, to whom I owe not only the formulation of the thermal conductivity model presented in Chapter 4, but also many inspiring conversations, fruitful collaboration and useful advice on preparing manuscripts for publication.

I have had the privilege to conduct my research under the direction of Dr. Sebastian Volz, an outstanding scientist and a brilliant mentor. I would like to express my deepest gratitude to him for his continued support during my research studies. Sebastian somehow managed to meet with me at least once a month to impart his expertise, despite a large research and administrative load. Every suggestion from Sebastian was always full of meaning and relevance. Also, he has provided me with professional opportunities that I did not dream possible. My experience working with Sebastian has been personally and academically enriching, he has taught me more than I could ever recount here. He is an exceptional role model of research excellence and integrity. His character and his important contributions to the scientific community will continue inspiring me throughout my future academic carrier.

Now, I have the privilege to start a new exiting adventure working with Prof. Dr. Clivia M. Sotomayor Torres, an outstanding scientist and exceptional woman with a remarkable energy. I am deeply grateful to her, because she has already taught me so much.

My final acknowledgments, to my family and friends, must be of a rather different sort. After nearly five years of living in France, I have had the good fortune of knowing extraordinary people and keeping close to me those that consciously erased the notion of distance and time. It is hard to imagine having made it to this point without them. I wish to express my heartfelt thanks to Aurorita, Hugo, Alizée, Fab, Charlotte, who allowed me to find my place here and make me feel at home. I extend my profound gratitude to Toño, Lili, Pipe, Laura, Adri, Andre, Cecile and Caro for their magic and enchanting madness. My deepest appreciation also goes to my French family: Edith, Arnaud, Pierre and Matthieu Catelain for their love and constant support. I am enormously grateful to Hubert, who is not only an extraordinary friend but also a constant source of intellectual stimulation that expanded my horizon of knowledge beyond science. I will always be grateful to my untouchable group: Dani, Juandu y Fede, who have always found the way to make my journey more enjoyable. Words seem so inadequate to express the depth of my gratitude to Sara, the only person with whom I have ever been able to communicate without words. Most of my dreams have taken shape during our "rêveries philosophiques" and her existence has proven to be vital to make them come true. I am largely indebted to Thibault, who always stood by me and knew how to give me back the smile that I let disappear in the hardest moments.

I owe too much to my parents, from whom I have learned to dream big and dare to fail, and thanks to them, I have understood that when one follows their passion, hard work becomes a labor of love. They always have taught me to live, work and follow my dreams with passion, and it was both of them that spread the love of science to me. I do not know how to give them thanks.

Of course, squirrels and cochon deserve a big thank you too.

Abstract

The understanding and control of the thermal conductivity of nano and microscale polycrystalline thin films is of fundamental importance for enhancing the performance and reliability of micro- and optoelectronic devices. However, the accurate description and control of the thermal performance of these bidimensional materials remain a difficult task due to their anisotropic and heterogeneous structure. Indeed, thin films obtained with a large number of deposition techniques and parameters, are composed of small crystallites at the interface with the substrate, which coalesce and evolve towards a columnar structure near the outer surface. These grains along with various crystallographic defects, such as oxygen impurities, increase the scattering processes of the energy carriers inside the materials, which in turn, reduce significantly their thermal conductivity. Experimental thermal characterization, accurate theoretical description and controlled modulation of the thermal properties of these materials are therefore desirable.

This work is devoted to the investigation of the thermal conductivity of nanoscale polycrystalline films and explores the possibility to modulate heat transfer across these low dimensional structures. Because of its great interest in new technological applications, and its outstanding thermal and piezoelectric properties, aluminum nitride (AlN) served as a test material in this study. Highly-textured AlN mono- and multilayers were obtained by reactive radio-frequency magnetron sputtering on single-crystal silicon substrates. The microstructure and distribution of crystallographic orientations along the cross plane were characterized by transmission electron microscopy to accurately determine the grain structure and size evolution. The impact of local oxidation and structural inhomogeneity along the cross plane on the thermal conductivity was investigated by thickness-dependent measurements performed by the differential 3ω technique. The diffusive scattering caused by oxygen-related defects, localized at the interface between two AlN layers, was studied by thermal measurements on the multilayered configuration. Structural features of the polycrystalline films were correlated with their thermal properties using a theoretical model, which takes into account the distribution of the grain geometry and considers the films as a serial assembly of three layers, composed of parallelepiped grains.

The experimental values of the thermal conductivity of the mono- and multilayer AlN polycrystalline films are well predicted by the developed model, with a deviation of less than 10%. Physical description of scattering phenomena at the interface, grain boundaries, and oxygen related defects, as a function of the characteristic structural heterogeneity, was achieved by comparing the experimental results to the theoretical predictions. It was found that grain mean sizes that evolve along the cross-plane direction, and structural features at the interface and transition domains, are key elements to understand and tailor thermal properties of nanocrystalline films with inhomogeneous structures. The results demonstrate that the structural inhomogeneity and oxygen-related defects in polycrystalline AlN films can be efficiently used to statically tune their cross-plane thermal conductivity. Finally, dynamic modulation of heat transfer by means of externally induced elastic strain on mono- and multilayer AlN films was investigated using a novel experimental approach consisting of a 4-points bending system coupled to the 3ω method.

Résumé

La compréhension et le contrôle de la conductivité thermique des couches minces polycristallines est fondamentale pour améliorer la performance et la fiabilité des dispositifs micro- et optoélectroniques. Toutefois, une description et un contrôle précis de la performance thermique de ces matériaux bidimensionnels restent une tâche difficile en raison de leur anisotropie et structure hétérogène. En effet, les couches minces obtenues par diverses techniques et avec une large gamme de paramètres de dépôt, sont composées de petites cristallites à l'interface avec le substrat, qui coalescent et évoluent vers une structure colonnaire à proximité de la surface extérieure du film. Ces grains, ainsi que d'autres défauts cristallographiques, tels que les impuretés d'oxygène, augmentent les processus de dispersion diffuse des porteurs d'énergie dans les matériaux, ce qui en conséquence, réduit considérablement leur conductivité thermique. La caractérisation thermique expérimentale, la description théorique et la modulation contrôlée des propriétés thermiques de ces matériaux sont, par conséquent, indispensables.

Cette thèse est consacrée à l'étude de la conductivité thermique des couches polycristallines présentant une non-homogénéité structurelle et elle a pour but d'explorer la possibilité de moduler le transfert de chaleur à travers ces structures bidimensionnelles. Le nitrure d'aluminium a été sélectionné pour cette étude du fait de ses propriétés thermiques et piézoélectriques, particulièrement intéressantes pour des nouvelles applications technologiques. Réalisées par pulvérisation cathodique magnétron, des monocouches et multicouches d'AlN hautement texturées sur des substrats de silicium monocristallin ont été obtenues. Leur microstructure et distribution d'orientations cristallographiques le long de la normale à la surface, ont été caractérisées expérimentalement pour déterminer, avec précision, l'évolution de la structure et de la taille des grains. L'impact de l'oxydation locale et l'évolution de la morphologie de grains sur la conductivité thermique transversale a été étudiée par la méthode 3ω différentielle. La dispersion diffuse des phonons due aux défauts liés à la présence d'atomes d'oxygène, localisés à l'interface entre deux couches d'AlN, a été étudiée par des mesures thermiques sur la configuration multicouche.

Les caractéristiques structurelles des couches polycristallines ont été corrélées avec les propriétés thermiques à partir d'un modèle théorique, qui tient compte

de la répartition et de la géométrie des grains, et considère les films comme un ensemble en série de trois zones, composées de grains parallélépipédiques. Les résultats de conductivité thermique obtenus par la mesure des monocouches et multicouches polycristallines d'AlN sont bien prédits par le modèle développé, avec une différence inférieure à 10%. Une description physique détaillée des phénomènes de dispersion diffuse à l'interface avec le substrat, aux joints de grains, et aux défauts liés à l'oxygène, en fonction de l'hétérogénéité structurelle caractéristique, a été réalisée en comparant les résultats expérimentaux aux prédictions théoriques. Enfin, pour explorer la modulation dynamique du transfert de chaleur, l'influence de la déformation du réseau cristallin, causée par des contraintes mécaniques, sur la conductivité thermique des monocouches et multicouches d'AlN, a été étudiée en utilisant une nouvelle approche expérimentale qui couple un système de flexion 4-points avec la méthode 3ω.

Contents

Acknowledgments vii

Abstract xi

Résumé xiii

Nomenclature xxviii

I Context & Literature review 1

Introduction 3
Phonon engineering . . . 5
Thermal conduction in polycrystalline films . . . 6
Tailoring thermal properties of polycrystalline thin films . . . 7
Outline of the thesis . . . 9

1 State of the art: Heat transfer in nanoscale 2D structures 11
1.1 Thermal conduction in nanocrystalline materials . . . 12
1.2 Thermal conductivity of thin films of polycrystalline Aluminum Nitride . . . 14
1.3 Tuning the thermal properties of low-dimensional structures . . . 17
1.4 Aim of the thesis . . . 21

II Methodology 23

2 Deposition of AlN films and material characterization methods 25
2.1 Aluminum Nitride . . . 25
2.2 Deposition of films by magnetron sputtering . . . 28
2.3 Structural analysis . . . 38
2.4 Summary . . . 43

3 Thin film thermal conductivity measurements 45
3.1 Challenges and practical considerations . . . 45

3.2 Fundamentals of the 3ω method . . . 47
3.3 Experimental uncertainty analysis . . . 58
3.4 3ω experimental setup . . . 64
3.5 Sample preparation . . . 67
3.6 Thickness dependent thermal conductivity measurements on AlN films . . . 69
3.7 Strain dependent thermal conductivity measurements . . . 71
3.8 Summary . . . 83

4 Thermal conductivity model for polycrystalline materials with a non-homogeneous microstructure 85

III Results and discussion 93

5 Microstructure and crystallographic analysis of Aluminum Nitride films 95
5.1 Texture evolution and out-of-plane accommodation through film thickness . . . 95
5.2 Microstructure and crystallite orientation : TEM . . . 104
5.3 Evolution of the grains size distributions . . . 112
5.4 Competitive growth in AlN films . . . 118
5.5 Chemical characterization by energy-dispersive X-ray spectroscopy 120
5.6 Summary . . . 123

6 Tuning the thermal conductivity of polycrystalline films via multiscale structural defects and strain 125
6.1 Thickness-dependent thermal conductivity measurements on monolayers and multilayers . . . 126
6.2 Strain-dependent thermal conductivity measurements . . . 152
6.3 Summary . . . 161

Conclusion 163
Future directions . . . 166

A Uncertainty propagation in the differential 3ω method 169

B Experimental variables of 3ω measurements 171

C Cross-sectional brigth field TEM micrographs 173

D Fast Fourier transform pattern of (100) single crystal silicon 175

E EDX spectroscopy on a 850 nm monolayer 177

References 191

List of Tables

2.1 Fixed deposition parameters of AlN thin films 36

3.1 Fundamental approximations and assumptions used in the 3ω method, experimental design criteria, and measurement ranges used in this work. 59
3.2 Uncertainty analysis in an 640 nm thick AlN monolayer system. 64
3.3 Geometrical parameters and physical properties of the materials used for the numerical simulation. 77

6.1 Thermal conductivity data for 3ω experiments performed on SiO_2 layer. 127
6.2 Thermal properties measured experimentally for the monolayer and multilayer AlN films. 133
6.3 Strain-dependent thermal measurements: Physical properties of the samples analyzed under strain. 154
6.4 Comparison between κ_{eff} measurements of unstrained samples performed onto a chuck at room temperature (classical 3ω method) and on the four points bending set-up. 156
6.5 Average temperature rise due to a multilayer film as a function of strain. 159

A.1 Uncertainty propagation in the differential 3ω method 169

B.1 Experimental variables of 3ω measurements on monolayer . . . 171
B.2 Experimental variables of 3ω measurements on multilayer samples, and the reference specimen. 172

List of Figures

1 Electromagnetic spectrum 4
2 Phononic spectrum 5

2.1 Crystal structure of AlN in its wurtzite phase. 26
2.2 Stacking of layers Al and N in a hexagonal close packed crystal 26
2.3 Fundamental lattice vectors of the hexagonal (0001) plane. . . . 27
2.4 Common crystal planes of AlN. 28
2.5 Schematic representation of sputtering process and chamber geometry. 29
2.6 Thornton structure zone model. 31
2.7 Voltage dependence on the nitrogen flow 34
2.8 Voltage dependence on the nitrogen flow 35
2.9 Schematic representation of the samples studied in this work. . 37
2.10 Bragg's diffraction 39
2.11 Schematic representation of a symmetric $\theta - 2\theta$ scan using the Bragg-Bretano geometry. 39
2.12 Schematic representation of an ω scan or rocking curve measurement. 40
2.13 Optical micrograph of TEM thin slice specimen 43

3.1 Typical experimental set for thermal measurement on thin films and associated challenges 46
3.2 Typical geometry of the heater 49
3.3 Cylindrical heat pattern generated by an infinitely narrow heater 51
3.4 Time evolution of the thermal wave amplitude 52
3.5 Cylindrical heat pattern from a metallic strip of finite width $2b$ 53
3.6 Heat patterns produced by (a) a heater larger than the film thickness and (b) a heater of width comparable to the film thickness. 56
3.7 Scheme of the experimental setup used for the 3ω measurements. 65
3.8 Microfabrication process flow for 3ω patterns. 67
3.9 (a) SEM micrograph of 20 nm and 230 nm thick Ti and Au layers deposited onto an AlN film. (b) SEM top view of a microfrabricated 3ω strip of $10\mu m$ width. 68

3.10 Four-points bending principle. 72
3.11 CAD layout of the four-points bending setup. 74
3.12 Four-points bending setup. 75
3.13 Scheme of load cell components. 76
3.14 Load cell calibration curve. 76
3.15 Geometry of the sample used in the numerical simulations . . . 77
3.16 First principal stress distribution of the bending sample under an applied load of 10 N 78
3.17 First principal strain distribution of the bending sample under an applied load of 10 N 79
3.18 Geometry of the rectangular beam. 79
3.19 Four points bending setup, mounted to perform strain-mediated V(I) measurements. 82
3.20 Typical raw data of a V(I) measurement 83

4.1 (a) Scheme of the grain structure of AlN films along the cross-plane. Modeled grain structure in 2d (b) and in 3d (c). 86
4.2 Phonon-phonon and phonon-boundary scattering processes inside a parallelepiped grain. 88
4.3 Mean free path of phonons due to their collisions with the inner surface of a parallelepiped grain. 91

5.1 XRD $\theta - 2\theta$ scan patterns of the AlN a) monolayer and b) multilayer films of different thicknesses. 96
5.2 XRD $\theta - 2\theta$ scan patterns of the AlN a) monolayer and b) multilayer films of different thicknesses. 98
5.3 Effect of lattice strain on diffraction peak position 99
5.4 XRD rocking curves of the (0002) reflection of monolayer films 101
5.5 Comparison between (0002) rocking curve measurements for a monolayer and a multilayer of equivalent thickness. 102
5.6 FWHM values of the (0002) XRD rocking curves of monolayer and multilayer films as a function of the film thickness. 102
5.7 Cross sectional bright field TEM image of a highly c-axis oriented 640nm thick AlN monolayer film. 104
5.8 a) HRTEM close-up view of the near-interface region (domain I), and b) its corresponding indexed FFT pattern. 106
5.9 HRTEM close-up view of the beginning of the transition region (domain II) 107
5.10 a) HRTEM close-up view of the transition region (domain II) at the limit with the columnar domain, and b) its corresponding indexed FFT pattern. 108
5.11 a) HRTEM micrograph of two adjacent columnar grains in the columnar region (domain III), and b) its corresponding indexed FFT pattern. 109

5.12 a) HRTEM close-up view of the near-interface region (domain I), and b) its corresponding indexed FFT pattern for a 935 nm mumtilayer 110
5.13 Bright field TEM images of the oxidized interface between two successive AlN layers of a$L = 3 \times (\approx 270$ nm) multilayer, captured in the columnar region (Domain III) 111
5.14 a) HRTEM micrograph of columnar grains from a $L = 3 \times (\approx 270$ nm) multilayer (domain III), and b) its corresponding indexed FFT pattern. 112
5.15 Evolution of the grained structure through the c-axis from small grains at the near-interface region to aligned grains in the columnar region. 113
5.16 a), d) Crystallite edge detection by a spiral phase digital filter for a monolayer and a multilayer, respectively. b), f) Original micrographs with overlayed 8-bit binary images containing outlines of the filter output for identified grains. c), g) Original micrographs with overlayed 8-bit binary images containing outlines of the measured grains. 114
5.17 Grain size distribution associated to the a), b) near interface and c), d) transition regions for 640 nm and 850 nm thick samples, respectively. 116
5.18 a) Original SEM micrograph of a 380 nm thick monolayer, b) overlayed 8-bit binary image containing outlines of the threshold filter output for edge detection of columnar grains. 117
5.19 Profile plot of the edge detection output for columnar grains (380 nm thick monolayer) 117
5.20 Evolution of column diameter through the cross-plane of AlN a) monolayer and b) multilayer samples as a function of film thickness. 118
5.21 Structure evolution AlN films grown by normal incidence deposition. 119
5.22 a) HAADF-STEM image of a $L = 3 \times (\approx 270$ nm) nm multilayer and its corresponding element distribution maps performed by energy-dispersive X-ray spectroscopy (EDX). 121
5.23 Composite element distribution map performed by energy-dispersive X-ray spectroscopy (EDX) on a $L = 3 \times (\approx 270$ nm) multilayer sample. T 122
5.24 a) Cu and b) Cu/O element distribution maps performed by energy-dispersive X-ray spectroscopy (EDX). 122

6.1 Amplitude of the temperature fluctuation ($\Delta T_{2\omega}$), as a function of the logarithmic modulation frequency (ω) for the SiO_2/Si reference sample 128
6.2 Process and thickness dependence of thermal conductivity of silicon dioxide. 129

6.3 Thickness dependence of the thermal wave amplitude generated by AlN monolayers of different thicknesses. 131
6.4 Thickness dependence of the thermal wave amplitude generated by AlN multilayers of different thicknesses. 132
6.5 Comparison between the experimental and theoretical values of the effective thermal conductivity of grained monolayers and multilayers, as a function of the film thickness. 134
6.6 Effective thermal resistance as a function of the film thickness, for the monolayer and multilayer configurations. 137
6.7 Size evolution of grains as a function of film thickness 140
6.8 (a) Mean free paths of phonons due to their collisions with the inner surface of grains and (b) Effective mean free path inside grains, l_n. 141
6.9 Relative effect of phonon-phonon and phonon boundary interactions on the thermal conductivity of polycrystalline AlN layers, as a function of the film thickness. 142
6.10 Bulk effective thermal resistance as a function of the film thickness, for the monolayer and multilayer configurations. 144
6.11 Effects of grain boundaries and finite size on bulk thermal resistance ($R_{n0} = d_n/k_{n0}$), as a function of the film thickness. . . . 144
6.12 AlN effective thermal resistance (L/k_{AlN}) as a function of the film thickness for the monolayer and multilayer configurations. . 146
6.13 Relative influence of the three different structural domains ($R_n = L_n/k_n$) on the AlN effective thermal resistance, as a function of the film thickness. 146
6.14 Relative influence of the intrinsic AlN and interfacial thermal resistances on the effective thermal resistance of monolayered films. 148
6.15 Relative effect of the intrinsic AlN resistance, as well as AlN-Si and AlN/AlN interfacial thermal resistances on the effective resistance of multilayered films. 149
6.16 Variation of electrical resistance as a function of strain for a Au/Ti heater 155
6.17 Effective thermal conductivities (κ_{eff}) as a function of strain . 158

C.1 Cross sectional bright field TEM images for a) highly c-axis oriented 640 nm thick AlN monolayer, b) highly c-axis oriented 935 nm thick AlN multilayer, and c) poorly textured 850 nm thick monolayer. 174

D.1 Fast Fourier transform pattern of (100) single crystal silicon obtained from a cross sectional HRTEM micrograph of the Si/AlN interface 175

E.1 a) HAADF-STEM image of a 850 nm monolayer and its corresponding element distribution maps performed by energy-dispersive X-ray spectroscopy. 177

Nomenclature

Abbreviations

CAS	Computer algebra system
DAQ	Data Acquisition
DC	Direct electrical current
EDX	Energy-dispersive X-ray spectroscopy
FWHM	Full width half maximum
HRTEM	High resolution transmission electron microscopy
MFP	Mean free path
Op-amp	Operational amplifiers
RIE	Reactive ion etching
RMS	Root mean square
SEM	Scanning electron microscopy
TEM	Transmission electron microscopy
XRD	X-ray diffraction

Chemical elements & compounds

O_2	Dioxygen
AlN	Aluminum Nitride
Cu	Copper
SF_6	Sulfur hexafluoride
Si_3N_4	Silicon Nitride
SiO_x	Silicon oxide
SiO_2	Silicon dioxide
Si	Silicon

Ti	Titanium	

Greek Symbols

α	Temperature coefficient of electrical resistivity	1/K
β	Coefficient of thermal expansion	1/K
κ_0	Reference effective thermal conductivity at zero strain	W/m·K
κ_{eff}	Effective thermal conductivity of the AlN/SiO_2 specimens	W/m·K
ν_n	Phonon group velocity in bulk aluminum nitride	m/s
ω	Angular modulation frequency	rad/s
ρ	Density	kg/m^3
σ	Mechanical stress	Pa
ε	Strain. In a crystalline solid it is defined as the percentage change of the material lattice constant relative to its equilibrium value	m/m
φ	Phase angle of a signal	rad
T	Period of a signal	s

Roman Symbols

$2b$	Width of the resistive heater	m
ΔT_{2w}	Amplitude of the temperature fluctuation at a frequency 2ω	K
Λ	Exponent ranging from 1/2 to 3/4 which serves to express the intragranular grain thermal conductivity as an exponential function of the grain size d_n (Dong et al. (2014))	m
A	Arbitrary point of spatial coordinates x, y and 0 on the plane $z = 0$ of a parallelepiped grain	
a	Average length of the base side of the parallelepiped grains considered to model the columnar region	m
a_j	Coefficient of the Fourier series	
a_{Kg}	Kapitza radius of grains.	m
a_{Ks}	Kapitza radius of the Si-substrate/AlN-film	m
a_K	Kapitza radius of the AlN-layer/AlN-layer	m
B	Arbitrary point of spatial coordinates ζ, 0 and z on the plane $y = 0$ of a parallelepiped grain	
b	Average side length of the cubic grains considered to model the transition region	m
b_j	Coefficient of the Fourier series	

c	Average side length of the cubic grains considered to model the near-interface region	m
c_{p_h}	Heater specific heat capacity	J/kg · K
c_{p_n}	Specific heat capacity of region n	J/kg · K
c_p	Specific heat capacity	J/kg · K
D	Thermal diffusivity	m^2/s
D	Arbitrary point of spatial coordinates ξ, s and b on a plane parallel to $z = 0$ of a parallelepiped grain	
d	Average side length of the cubic grains considered to model the transition region	m
D_n	Mean free path of phonons due to carrier-boundary scattering processes	m
d_n	Mean size of the grain distribution in the interface ($n = I$), transition ($n = T$), and columnar ($n = C$) regions	m
E_s	Young's modulus of the substrate	Pa
F	coefficient of strain sensitivity of resistance, (or gauge factor)	
h	Thickness of the rectangular beam used in four-point bending experiments	m
I	Electrical current	A
I_0	Amplitude of the current signal	A
I_{xy}	Geometrical moment of inertia	m^4
j	Integer	
K_α	X-ray emission occurring when Cu electrons make transitions between the lower atomic energy levels. i.e. from $n = 2$ to $n = 1$.	eV
k_n	Thermal conductivity of the interface ($n = I$), transition ($n = T$), and columnar ($n = C$) regions	W/m · K
k_{0n}	Bulk thermal conductivity when $L_n \to \infty$	W/m · K
K_0	Zeroth order modified Bessel function of the second kind	
k_{gn}	Thermal conductivity of a single grain with average size d_n in the direction of heat conduction in the region n	W/m · K
L	Film thickness	m
l	Length of the electrical conductive strip, defined by the distance between the outer pads	m
l_0	Intrinsic mean free path of phonons, due to phonon-phonon scattering processes	m

L_1	Distance between the two outer supports in a four-point bending setup	m
L_2	Distance between the two inner supports in a four-point bending setup	m
L_n	Thickness of the region n	m
l_n	Mean free path (MFP) of phonons in the region n	m
L_s	Nominal length of the rectangular beam used in four-points bending experiments	m
M	Bending moment	$\mathrm{N \cdot m}$
N	Integer representing the number of AlN layers in a multi-layer system	m
P	Dissipated power in the wire	W
$P_{2\omega}$	Heat generated at a frequency 2ω	W
P_{DC}	DC component of the dissipated power	W
P_l	Power per unit of length	W/m
R	Thermal boundary resistance at interfaces between two AlN layers in multilayer structures	$\mathrm{m^2 \cdot K/W}$
r	Radial distance from the heat line source at any point (x, y)	m
R_g	Average interface thermal resistance among grains	$\mathrm{m^2 \cdot K/W}$
R_s	Thermal boundary resistance between the AlN layer and the substrate	$\mathrm{m^2 \cdot K/W}$
R_{AlN}	intrinsic thermal resistance of each AlN layer	$\mathrm{m^2 \cdot K/W}$
R_{e_0}	Value of the electrical resistance at a reference temperature T_0	Ω
R_e	Electrical resistance	Ω
R_K	Kapitza resistance	m
T	Temperature	K
T_0	Reference temperature	K
V	Voltage amplitude measured between the inner pads of the 3ω pattern	V
V_ω	Voltage reference signal in the 3ω closed circuit	V
V_{out}	Voltage signal obtained from the output of the operational-amplifier A_4	V
w	Width of the rectangular beam used in four-point bending experiments	m

Part I

Context & Literature review

Introduction

The progressive evolution of 1900's intellectual framework gave birth to modern physics with the discovery of the new radiation law, which explained that the energy scale of the blackbody oscillators is divided into intervals composed of "energy elements" ($E = hf$, where h is the Planck's constant and f is the frequency of the oscillators, Planck (1901), Kragh (2000)). A few years later, this breakthrough yielded to a technological upheaval. As modern physics revealed the very different properties of matter when its characteristic length decreases to small time and dimension scales, it left open the possibility of engineering matter at the atomic or molecular scale to obtain materials with suitable properties to perform a determined function. This way of thinking further evolved and our society witnessed remarkable scientific advances which rapidly led to the emergence of new technologies. For example, advances in nanotechnology had enabled the fabrication of materials and devices with characteristic lengths that can now approach a few nanometers. These new nanoscale structured materials are becoming increasingly important in our daily-life, because of the unusual properties that they exhibit when their length scale is scaled down to the nano-realm. Examples of these novel structures include quantum dots, nanotubes, nanowires, thin films, superlattices and nanocomposites. They encompass a great number of applications in diverse fields. Well known examples include photovoltaics, which aims at converting sunlight into direct current electricity, or thermoelectrics which transforms thermal energy from a temperature gradient into electrical energy. These novel technologies seem to be an interesting alternative to the increasing environmental issues and limitations of energy resources.

Our progressive understanding of matter behavior at the nanoscale has enabled the successful management of photon and electron based technologies. In particular, the control of electrons in semiconductor materials resulted in the solid-state transistor breakthrough, giving rise to all modern electronic devices. Analogously, photonic engineering has led to fundamental changes in society, with the development of optical networks in telecommunications and the use of optical fibers and microwaves, now products that represent the infrastructure on which the modern information society is built. The ability to effectively engineer the electromagnetic (EM) spectrum is evidenced by the large number

of EM based technologies now available (Fig.1). These applications have been developed throughout a wide range of frequencies, which extends over 16 orders of magnitude. For example, at frequencies smaller than 10^6 Hz, daily-life applications such as amplitude and frequency modulated radios, and at frequencies higher than 10^{22} Hz, technologies such as gamma radiation imaging in nuclear medicine have been developed (Maldovan (2013)).

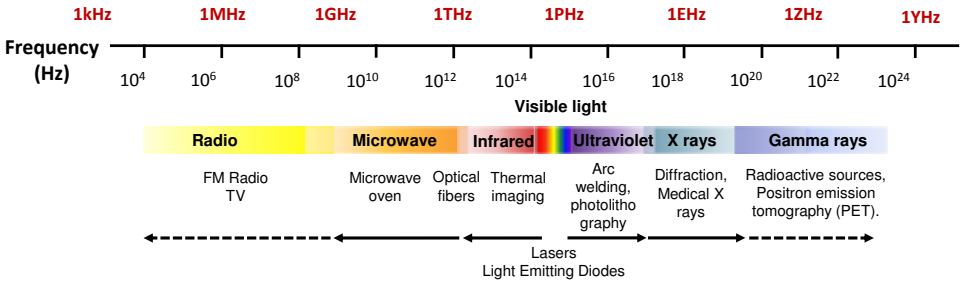

Figure 1: *Electromagnetic spectrum and its applications. Adapted from Maldovan (2013)*

As in the case of electromagnetic radiation, quantum mechanics dictates that the vibrational energy must also be an integer multiple of the universal quantum, which is proportional to the frequency. The quanta of crystal lattice vibrations are called phonons. Although the scientific and engineer communities have found creative methods to efficiently manipulate photons and electrons (the quanta of electromagnetic radiation), satisfactory understanding and similar degree of control of phonons have not been accomplished so far. The main reason is that, unlike photons and electrons, interactions involving phonons of different frequencies can occur among them, i.e producing a different wavelength (Li et al. (2012)). This mechanism turns the prediction and control of phonon behavior into a much more difficult task.

Phonons are responsible for conduction of sound and heat in solids. Low frequency vibrations, smaller than 10^{11} Hz correspond to sound, while higher frequency ones manifest themselves as heat. Phonons are involved practically in all kind of mechanical, optical, electrical and thermal phenomena. They play a dominant role in heat transfer and are intricately related to a variety of fascinating mechanism, including phase transitions, ferroelectricity, superconductivity and catalysis. Advances in nanotechnology and the emergence of nano-structured materials have provided new possibilities of conquering numerous degrees of control of the phononic spectrum (Fig.2). Thus, the analysis and modulation of the rich and diverse physical phenomena involving phonon transport may draw a new technological frontier with a potential impact comparable to the one achieved by controlling charge and light transport.

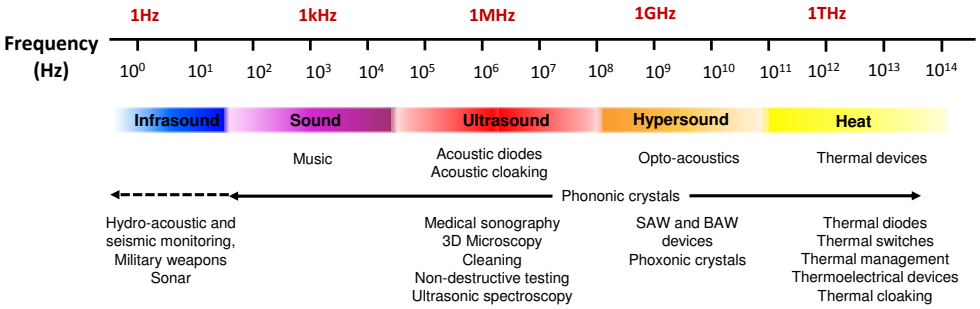

Figure 2: *Phononic spectrum and its applications. Adapted from Maldovan (2013)*

Phonon engineering

Detailed understanding of thermal transport in low dimensional structures is crucial mainly because of two technological challenges: one is the need of efficiently removing the heat generated in nanodevices and, contrarily, the second one is associated with inhibiting heat flow. The continued trend of electronic industry towards miniaturization causes significant thermal issues, making heat one of the most important limiting factors in electronic system design. As volume density of components in integrated circuits is increased and the characteristic dimensions are scaled down to a few nanometers, higher temperatures in localized volumes are reached by means of the Joule effect and the thermal resistances at the interface between elements. The inefficient removal of heat is detrimental to the functionality, reliability and lifetime of the device. Conventional and high power microelectronic devices, light emitting diodes (LED's) and semiconductor lasers are examples of applications that undergo important thermal issues. Optimizing physical properties of their elemental components is therefore desirable to enhance thermal conduction processes and overcome heating issues.

While materials with high thermal conductivities are required for thermal management applications, the opposite is true for thermoelectric devices and thermal barrier coatings. The performance of thermoelectric devices depends on the dimensionless figure of merit, defined as $ZT = \rho S^2 T/k$, with ρ being the electrical conductivity, S the Seebeck coefficient, T the temperature and k the thermal conductivity. Therefore, thermoelectric applications seek to impede heat transfer to ensure significant temperature gradients. However materials that conduct efficiently electricity and minimize thermal transport do not occur spontaneously in nature. To achieve high thermoelectrical performance, engineering materials properties is therefore required. Similarly, thermal barrier coatings require control of their structural features to enhance thermal insulation of components from large and prolonged heat loads.

Phonon engineering is a research field that recently emerged as a consequence of these needs. It aims at applying the understanding of phonon transfer to effectively manipulate the phonon spectrum and adapt the thermal, electrical or optical properties of a material for a suitable functionality. It investigates materials ranging from low-dimensional structures to macroscopic systems. This work focuses on the thermal properties of thin films because of their high technological impact.

Thermal conduction in polycrystalline films

The performance and reliability of the above-mentioned devices strongly depend on the thermal properties of their constitutive materials. In particular, the thermal conductivity of thin films, the building block of solid-state systems, is of critical importance because of its direct impact on thermal performance. Bidimensional structures, such as thin films, are generally obtained by physical or chemical vapor deposition processes, which generally result in polycrystalline structures that are anisotropic and heterogeneous. The size and morphology of grains in thin films deposited at room temperature typically evolve along the film thickness, yielding to a structural inhomogeneity. Thus, in nanocrystalline films, grain boundaries along with various and common crystallographic defects, such as oxygen impurities, increase the scattering processes of the energy carriers, which in turn, reduce significantly the thermal conductivity. These changes in the transport properties are particularly important when the size of the grains is comparable to the mean free path of the heat carriers.

Due to its importance in new technological applications, many efforts have been devoted to the study of thermal conductivity of nanocrystalline thin films. The effect of phonon scattering at grain boundaries, as well as grain size effects have been identified as the dominant mechanisms for thermal conductivity reduction (Wang et al. (2011), Dong et al. (2014)). Yet, an accurate description of the thermal properties of polycrystalline thin films has been achieved to a limited extent, and it remains a challenging task, because of the complexity of the structure of these materials and the large number of scattering mechanisms involved. In the reported literature, the role of the structural inhomogeneity along the film thickness in thermal properties has neither been experimentally studied nor explained theoretically. To describe thermal properties of polycrystals, previous studies have considered either a distribution function of grains of a given size (Nan (1993)) or an effective grain size (Hao (2012)). The main reason is that experimental characterization of the evolution of the thin film structure is quite difficult. Therefore, structural and thermal characterization, as well as accurate theoretical description considering the size and morphology evolution of grains in polycrystalline films, is desired to further understand heat transport in these materials.

Tailoring thermal properties of polycrystalline thin films

Certainly one of the most interesting consequences of developing accurate knowledge of thermal transport at the nano and microscale in polycrystalline thin films, is that it opens up the possibility of engineering their thermal properties. Given the wide number of technological applications in which polycrystalline thin films are involved, controlled modulation of their thermal response promises major new technological developments. Tunability of heat transport can be achieved either statically or dynamically. It has been shown that thermal transport is strongly influenced and can be statically controlled by the introduction or removal of crystalline defects such as grain boundaries, dislocations, vacancies, interstitial voids, mass differences, and substitutional impurities (Murphy et al. (2014), Hopkins (2013), Slack et al. (2002)). These means of altering the crystal lattice symmetry strongly affect phonon scattering rates due to localized changes in the vicinity of the defects. If the interactions of the heat carriers with these structural modifications are well understood and well controlled, it is therefore possible to adapt the material thermal properties for a suitable application.

Although statically tailoring thermal conduction processes is relevant for many applications, on-demand tunable transport is useful for systems where a dynamic thermal response is required. Dynamically regulated phonon transport could be of great interest for applications such as heat-mediated data storage, thermal transistors and phonon logic computation (Yang et al. (2012), Li et al. (2012), Wang and Li (2007)). Other examples include thermoelectric devices that adapt to their environmental temperature to maximize efficiency, and switchable thermal conductors for heat management (Murphy et al. (2014)). However, dynamically tunable thermal conductivity of solid-state structures has remained inaccessible for the scientific community. Although thermal rectification has been achieved in the past (Tian et al. (2012), Kobayashi et al. (2010) Chang et al. (2006)), gating, switching and dynamic modulation are yet to be demonstrated. As crystallographic defects, strain is an effective way to disturb the crystal symmetry, and therefore potentially provides a means of reversibly regulating thermal conductivity. Indeed, the effect of strain on transport properties has been successfully exploited in the electronic industry to improve the carrier mobility and enhance transistor performances (Maiti et al. (1999)). As a consequence, interest in the effect of strain on the thermal properties of low dimensional structures has surged recently. A reasonable number of theoretical studies had dealt with the influence of elastic strain on the thermal conductivity of thin films in the literature (Wang and Shen (2014), Li et al. (2010), Xu and Li (2009), Samvedi and Tomar (2010), Zhu and Zheng (2009), Picu et al. (2003)). However, experimental results showing stress/strain effects on the thermal conductivity of thin films are very limited (Takashiri et al. (2014), Kumar et al. (2013), Alam and Manoharan (2012), Lee et al. (2010)). The

evident lack of experimental studies on strain-mediated thermal conductivity is due to the complexity associated with simultaneously inducing and measuring strain in a low-dimensional structure, while performing thermal conductivity measurements.

Three important research axes on the thermal conduction processes involved in nanocrystalline films can be identified from the discussion above:

- The role of the structural inhomogeneity along the film thickness on thermal properties should be clarified by making use of both experimental and analytical tools.
- New strategies to statically tune thermal conductivity of nanocrystalline films should be identified.
- Novel experimental approaches should be implemented to study the dynamic regulation of phonon transport in low-dimensional structures.

Motivated by the need of making progress towards the resolution of these issues, this work was devoted to the investigation of the thermal conductivity of nanoscale polycrystalline films and explored the possibility to modulate heat transfer across these low dimensional structures.

Because of its great interest in new technological applications, aluminum nitride (AlN) served as a test material in this study. Owing to its outstanding performance as a thermal conductor and electric insulating ceramic, AlN has been widely integrated in advanced micro- and optoelectronic devices, where it is typically exploited as a thermal management material. With a thermal conductivity of ≈ 320 W/m$\cdot$K at room temperature in its bulk form, AlN stands as a promising solution to overcome undesirable heating effects that appear in solid-state systems. Thermal properties of polycrystalline AlN thin films are crucial for many engineering applications, including surface acoustic wave (SAW) devices, light emitting diodes (LEDs), high electron mobility transistors (HEMTs), heat sinks in micro-electronic packaging, and dielectrics films in thermal management. Additionally, AlN thin films exhibit the aforementioned characteristic structural non-homogeneity, like other materials of great technological interest, such as GaN, diamond or ZnO. It also exhibits a piezoelectric response providing the possibility to electrically induce strain, and therefore to potentially yield to dynamic thermal conductivity modulation. Thus, AlN is a particularly suitable candidate for this study.

Outline of the thesis

This work is divided in three parts: Part I reviews the advances on the description of thermal conduction in nanocrystalline films and analyses the state-of the art measurements. In Part II, the experimental procedures used to synthetize and characterize the physical properties of AlN films are thoroughly described. Then, an analytical model for films with inhomogeneous microstructures is formulated. Finally, in Part III, the effect of microstructure, localized oxidation, and lattice deformation caused by externally induced strain on thermal conduction processes are investigated. The analysis is extended by presenting the obtained results and discussing the possibility to effectively modulate thermal transport in the films via multiscale defects and strain.

The manuscript is therefore composed of 6 chapters, devoted to the study of heat transfer and thermal conductivity modulation in AlN thin films.

- In Chapter 1, a review of the literature is given. First, the theoretical description of thermal conduction in thin films is presented briefly, and the state-of-the-art thermal conductivity measurements of polycrystalline AlN films are analyzed. Then, the most relevant theoretical and experimental studies concerning the dynamic modulation of thermal properties of nanostructures are discussed, focusing on the effect of strain in the thermal conductivity of thin films.

- Chapter 2 provides a description of the experimental procedures used to synthesize AlN films and characterize their structural and chemical properties. The chapter covers the deposition of thin films by radio-frequency (RF) reactive magnetron sputtering, and the crystallographic, structural and chemical analysis methods.

- Chapter 3 is dedicated to thoroughly describe the 3ω methodology, covering the data reduction and the analysis of the experimental uncertainty. Both, contributions arising from the assumptions involved in the heat conduction model and from the accuracy level of the measurement apparatus are detailed. Additionally, the procedure to perform thickness-dependent thermal conductivity measurements is discussed, and a novel experimental setup implemented to carry out strain-mediated thermal measurements is presented.

- In Chapter 4, a thermal conductivity model for polycrystalline materials is developed by considering the films as a serial assembly of grains which evolve along the cross plane.

- Experimental evidence of grain morphology and texture evolution along the cross plane of the films as a function of thickness is presented in Chapter 5.

- Thickness- and strain-dependent thermal conductivity measurements on AlN films are studied in Chapter 6. The impact of the structural inhomogeneity and oxygen defects on the thermal conductivity of polycrystalline AlN thin films is discussed. In addition, the experimental results are explained through the thermal conductivity model developed in Chapter 4. Furthermore, the effect of elastic strain on the thermal conductivity of AlN films is studied experimentally by a novel approach coupling a four points bending system to the 3ω method. The results of the strain-dependent thermal conductivity measurements are presented.

Finally, the Conclusion contains a summary of the results, and an outlook of the perspectives for future works is given.

Chapter 1

State of the art: Heat transfer in nanoscale 2D structures

According to their physical and chemical properties, solids can be broadly divided into metals (i.e. electrical conductors), insulators (i.e. dielectrics), semiconductors and semimetals, with the latter standing at the metal-nonmetal frontier. In the solid-state, heat conduction is mediated by free electrons and lattice vibrations, which are the concerted harmonic motion of the atoms that form the crystalline lattice. As electromagnetic waves, the elastic fluctuations in a crystalline solid carry an amount of thermal energy that is quantized. These energy elements are the so-called phonons ($E_p = hf$, where f is the frequency). The thermal conductivity of a solid is therefore determined by the ability of phonons and electrons to transport thermal energy as they propagate through the crystal, such that $k = k_e + k_p$, where the subscripts p and e refer to phonons and electrons, respectively (Kaviany (2011)).

The classic kinetic theory of gases has been widely used to describe the thermal conductivity of metals, nonmetals and semimetals, by relating it to the physical properties of their energy-carriers (Ziman (1960)):

$$k = \frac{1}{3} C_n \nu_n l_n \tag{1.1}$$

being C_n the specific heat capacity per unit volume, ν_n the mean velocity (also called group velocity), and l_n the mean free path of the carrier being analyzed. In the kinetic theory, the values of C_n, ν_n and l_n are considered identical for all the frequency interval of the energy carriers. This is the so-called "gray approximation", in which the carriers are considered frequency-independent and therefore contribute to heat conduction equally, being indistinguishable or "gray". The product of $C_n \nu_n l_n$ is normalized over three degrees of freedom to obtain the average value in a given direction. The mean free path is defined as the average distance traveled by an energy carrier before experiencing a collision.

While the specific heat and group velocity are not sensitive to crystallographic defects, the mean free path is affected by the distortion of the crystal symmetry, and it governs the variability of the thermal conductivity due to size effects (Klemens (2001)). Since polycrystalline films exhibit a large volume fraction of grain boundaries, as well as other common crystallographic imperfections, their thermal conductivity can differ from that of their bulk counterparts by several orders of magnitude.

In this Chapter, the theoretical advances describing the thermal conductivity of polycrystalline films will be briefly reviewed. Then, the state-of-the-art thermal conductivity measurements on polycrystalline AlN films will be examined. Finally, relevant theoretical and experimental studies concerning the dynamic modulation of thermal properties of nanostructures will be discussed, focusing on the effect of strain in the thermal conductivity of thin films.

1.1 Thermal conduction in nanocrystalline materials

This work addresses thermal conduction in polycrystalline films of aluminum nitride, a wide bandgap semiconductor, that simultaneously exhibits high thermal conductivity and electrically insulating properties. In a semimetal, such as AlN (and in nonmetals as well), transfer of heat is predominated by phonons. Thus, the discussion that follows neglects the conduction by electrons ($k_e \to 0$), and focuses on the mechanisms by which phonon transport is affected i.e crystal structure and the length-scales involved in the studied samples.

Before describing phonon transport in polycrystals, it might be relevant to evoke the scattering processes involved in a perfect monocrystalline film. Because of the defectfree nature of an ideal single-crystal, the mean free distance traveled by the quanta of lattice vibrations is limited by the interactions among energy carriers and with the boundaries of the structure. If the length scale of the system, i.e the film thickness, is comparable to the phonon mean free path, boundary effects (collisions with the walls or boundaries of the film) due to small size appear.

On the other hand, nanocrystalline materials generally exhibit an anisotropic and heterogeneous structure which is composed of grains with irregular shapes and sizes (Adamik et al. (1998), Barna and Adamik (1998)). In addition to the complex grained structure, various crystallographic defects, such as dislocations, vacancies, interstitial voids, mass differences, and substitutional impurities are usually present (Júnior and Shanafield (2004)). Interactions of the heat carriers with these point-like and planar defects increase the scattering events, which in turn, significantly reduce the thermal conductivity of polycrystalline materials compared to that of their corresponding single-crystal counterparts (Mayadas and Shatzkes (1970)). Thus, in a grained structure, besides phonon-phonon and phonon-boundary interactions, two main additional

scattering processes affect thermal conduction. In this case, lattice vibrations mean free paths are reduced namely due to increased grain boundary scattering (intergranular transport) and scattering within the grains, owing to the reduced grain size (intragranular transport). These changes in the transport properties are particularly important when the size of the grains in nanoscale structured materials is comparable to the mean free path of the heat carriers (Majumdar (1969)).

Conduction of heat in perfect single-crystalline thin films has been widely studied in the literature, both theoretically (Ordonez-Miranda et al. (2014), Kazan et al. (2010), Turney et al. (2010), Chen (1998), Fuchs (1938)) and experimentally (Chávez-Ángel et al. (2014), Liu and Asheghi (2004), Yu et al. (1992), Crommie and Zettl (1990), Glassbrenner and Slack (1964)) Nevertheless, in spite of its importance in new technological applications, the accurate description of the thermal properties of polycrystalline thin films has been much less explored, and remains a challenging task because of the complexity of the structure of these materials and the large number of scattering mechanisms implied. Braginsky et al. (2002) proposed a phonon-hopping formalism, based on the assumption of scattering at the grain boundaries as the main mechanism limiting thermal conductivity of granular materials. Yang et al. (2002) observed experimentally a strong grain size effect on the thermal conductivity of nanocrystalline yttria-stabilized cubic zirconia films, over a range of 10 to 100 nm. In order to provide more accurate predictions for nanograined materials, Monte Carlo (MC) simulations (Hao et al. (2010)) and numerical solutions of the Boltzmann transport equation (BTE) (Kazan and Volz (2014), Miyazaki et al. (2006), Yang et al. (2005)) were implemented, considering the structure geometry and interface thermal resistance (Kapitza resistance, R_K). Hao (2014) developed a modified effective medium formulation considering the frequency dependence of phonon properties to obtain the lattice thermal conductivity of general nanograined polycrystals. A comparison of the results obtained in these two latter studies agreed well with MC simulations for silicon (Hao et al. (2009)) and lead telluride polycrystals at 300 K (Chen and Dames (2005)), both in the frequency-dependent and the frequency independent (Jeng et al. (2008)) cases. Yet, these theoretical formalisms are intrinsically computer time-consuming and complicated to implement. Recently, a simple analytical model was proposed by Dong et al. (2014). By considering equisized spherical crystallites of mean grain size d_n, and including size effects, as well as diffusive scattering at grain boundaries, their analysis yields the effective thermal conductivity, k_{eff}, of a nanocrystalline material:

$$k_{eff} = \frac{k_0(1 + l_0/d_n^{\Lambda})^{-1}}{1 + R_K \left[k_0/(1 + l_0/d_n^{\Lambda})\right]/d_n} \tag{1.2}$$

where k_0 is the corresponding single-crystal thermal conductivity, and l_0 is the single-crystal phonon mean free path. To derive this expression, Dong

et al. (2014) have considered that the intragranular grain thermal conductivity, $k_{intra} = k_0/(1 + l_0/d_n^{\Lambda})$, can be expressed as an exponential function of the grain size d_n. Thereby, Λ is an exponent ranging from 1/2 to 3/4, according to the phenomenological theory (Gurevich (1986)). This analytical formulation proves to be very useful because the effective thermal conductivity of the material can be easily obtained by knowing its mean grain size, the single-crystal thermal conductivity, the single-crystal phonon mean free path and the Kapitza thermal resistance. However, this formalism does not account for the distribution of the grain shape and size along the growth direction of the film. Furthermore, the model focuses on thermal properties of bulk or freestanding nanocrystalline materials, rather than film-on substrate systems, and therefore does not consider the interfacial thermal resistance between a film and its substrate.

From the reviewed advances related to the understanding of phonon transport inside nanograined polycrystals, it appears that early works have focused on materials composed of equisized grains. Yet, films deposited at room temperature by physical and chemical vapor techniques generally exhibit a grained structure that increases in size and evolves in shape from the bottom to the top of the film, along the cross-plane direction (Barna and Adamik (1998), Jaramillo-Fernandez et al. (2015)). In addition, MC and BTE simulations, have proven to be tedious in their implementations because the quantities that determine the lattice thermal conductivity are frequency dependent and therefore difficult to obtain, requiring high computation times (Tian et al. (2014)). The need to describe in a simple yet accurate fashion, the thermal conductivity of polycrystalline films with complex structures, is therefore evident. To obtain an overall picture of the advances in the understanding of thermal response of polycrystalline AlN films as a function of their structural features, a brief review of the state-of-the-art thermal measurements on nanoscale polycrystalline AlN films is presented in the section immediately to follow.

1.2 Thermal conductivity of thin films of polycrystalline Aluminum Nitride

Aluminum nitride is a ternary wurtzite semiconductor that exhibits several outstanding physical properties. Being highly chemically stable, it is an excellent thermal conductor that resists to high temperatures, and presents a relatively small thermal expansion mismatch compared to that of silicon and gallium arsenide, materials that are often combined with AlN in semiconductor devices. These properties are typically exploited in microelectronic packaging applications, where AlN is used as a heat sink for thermal management. With a thermal conductivity of about 320 $\mathrm{W/m \cdot K}$ at room temperature in its bulk

form (Slack (1973)), AlN also stands as a promising solution to eliminate undesirable heating effects that appear in solid-state systems. In addition, its relatively wide bandgap of 6.28 eV, which is the underlying reason for AlN to be widely touted as an excellent electric insulating ceramic, makes it an ideal candidate for semiconductor device applications. Its success as a micromechanical transducer relies on its piezoelectric properties and high acoustic velocity, making AlN a particularly suitable material for surface (SAW) and bulk (BAW) acoustic wave applications. Epitaxially grown AlN interlayers are commonly found in gallium nitride-based light emitting diodes (LEDs) and high electron mobility transistors (HEMTs). This is mainly due to its ability to form alloys with GaN, producing AlGaN and allowing the fabrication of AlGaN/GaN, AlGaN/InGaN and AlInGaN-based electronic and optical devices (Morkoc (2009)).

The thermal conductivity of deposited AlN thin films generally differs from that of the corresponding bulk form, because of extrinsic phonon scattering mechanisms, which represent a major source of thermal resistance. In single-crystal AlN, phonon scattering occurs mainly due to interactions among phonons, as well as scattering at the sample boundaries and with impurities and vacancies. Conversely, in thin films, additional contributions arise from grain boundaries, dislocations and extended defects. In addition, the interfacial thermal resistance between the film and the substrate has been identified as a major parameter influencing thermal conductivity (Su et al. (2013)). Thus, thermal conduction processes in these bidimensional structures, are directly affected by grain sizes, crystallographic defects and structural features near the interface with the substrate. The microstructure resulting from the fabrication processes is therefore a key issue in assessing and controlling thermal properties of polycrystalline AlN films, which as explained above, are of major importance for a broad range of applications. However, limited studies focused on their thermal conductivity. The reasons are namely: a) the recent development of new thermal characterization techniques for low dimensional structures, and b) the high reactivity of aluminum with oxygen, which greatly affects AlN physical properties, and makes its fabrication in a highly pure form difficult. Indeed, the properties of AlN strongly depend on its variable chemical purity, and therefore is a challenging material to investigate (Morkoc (2009)).

Very few studies have reported effective thermal conductivities at room temperature of polycrystalline AlN films deposited on Si substrates by RF magnetron sputtering, and most of the reported values vary from 0.5 to 50 $W/m \cdot K$ (Zhao et al. (2004), Choi et al. (2006), Pan et al. (2012)). The considerable variability of the published effective thermal conductivities arises from a strong dependence on deposition conditions and techniques, and chemical purity of the samples, which is often related to the presence of oxygen atoms. Although a comparison is difficult because of this variability, it appears as a common evidence for all studies that the thermal conductivity has a thickness dependent

behavior. Zhao et al. (2004) analyzed their results based on the microstructure and oxygen impurities. They attributed the observed thickness-dependence to the increase of grain size and the decrease of oxygen impurities as the films become thicker. Choi et al. (2006) suggested that the microstructure developed at the interfacial region near the substrate could be poor due to the lattice mismatch between AlN and Si. Thus, they attributed the observed trend to the low thermal conductivity in the interfacial region. A similar result was obtained by Pan et al. (2012), who found that the thermal conductivity of polycrystalline aluminum nitride thin films can be enhanced by optimizing the interface structure.

More recently, a similar trend for the thickness dependence of the effective thermal conductivity has been observed by Belkerk et al. (2012) and Duquenne et al. (2012), who studied thermal transport properties of AlN films deposited by direct-current (DC) balanced and unbalanced magnetron sputtering. The terms "balanced" and "unbalanced" refer to the magnetron classification. The former is the classic configuration, while the latter is a technology that uses additional magnetic coils to enhance and intensify the plasma containing the ionic species. Because of the "unbalanced" magnetic field, this magnetron configuration results in higher energies and therefore higher temperatures involved during the deposition process. Both studies found that the balanced magnetron process yielded to effective thermal conductivities of $\approx 2.5-50$ W/m$\cdot$K for 800 - 3500 nm thick AlN films. On the other hand, unbalanced magnetron sputtering led to $k_{eff} \approx 20-130$ W/m$\cdot$K for film thicknesses varying from 150 to 3500 nm. Because of the high measured values, these investigations lead to progress towards highly thermally conductive sputtered AlN thin films. Moreover, both studies observed that "crystalline quality" of AlN films changed with thickness to a large extent. As Choi et al. (2006), these investigations identified striking differences in the microstructure near the interfacial region, which appeared to be highly disordered within a limited thickness. Beyond this amorphous-like interlayer, they identified a structural zone, where the grain size was large with a preferential crystalline orientation, or what they called the "bulk region" of the film. These works addressed the thickness-dependence problem by attributing the increase of k_{eff} with film thickness to synthesis conditions, microstructure and average grain size (obtained using the Scherrer equation). Crystalline quality, structural features and thickness of the different regions of the films were identified as major factors influencing thermal properties of AlN films. Also, they interpreted as a thermal resistance, the disordered atomic structure observed at the interface with the silicon substrate. Finally, Belkerk et al. (2012) suggested that grains of different shapes and sizes present at the transition region (between the bulk and amorphous zones) play a dominant role on the boundary thermal resistance.

Although the above mentioned studies somehow made progress by indicating qualitatively that structural features may be responsible for the changes in thermal conduction, a physical description in terms of both morphology and grain

structure evolution, along the cross plane direction, has not been achieved so far, and is highly desirable. In an attempt to gain understanding on the effects of the structural inhomogeneity and oxygen impurities on thermal conduction processes, this work was devoted to characterize experimentally AlN structural features and thermal conductivity of monolayer and multilayer samples, to then correlate them through an analytical model. This analysis yielded a physical interpretation describing quantitatively the effects of multiscale structural defects.

Developing in-depth understanding of the processes governing thermal transport opens up the possibility of controlled modulation of the thermal properties of polycrystalline films. The discussion that follows focuses on the efforts that have been dedicated to statically and dynamically tune the thermal conductivity of low-dimensional structures in the scientific community.

1.3 Tuning the thermal properties of low-dimensional structures

Controlled modulation of phonon transport in solid-state systems promises major new technological developments. Thermal conductivity regulation and heat flow control at small scales are of great interest for a wide range of applications such as phononics, thermoelectrics, heat sensors, energy devices and thermal management in micro and nano-electronics. In a conceptual basis, tailoring thermal conductivity can be achieved either statically or dynamically. In other words, the thermal output can or cannot depend explicitly on time or other independent variables.

The static approach has proven to be very interesting for thermoelectric and thermal barriers applications. Both research domains seek to engineer the structure of advanced technical materials to adapt their thermal response in order to be as low as possible. One strategy consists in introducing or removing crystallographic defects, which has been confirmed to be an effective means of tailoring thermal conduction. The field of thermoelectrics has experienced remarkable advances in last decades, overcoming the impossibility to find values of the figure of merit, ZT, significantly greater than unity. Surprising values of ZT have been achieved by nanostructuring thermoelectric materials. Grain boundaries are known to greatly increase phonon scattering and are the object of active research, in which grain sizes of nanocrystalline materials are engineered to dramatically reduce the lattice thermal conductivity and therefore increase ZT values (Suriano et al. (2015), Gunes and Ozenbas (2015), Wu et al. (2014), Carrete et al. (2014)). The same is true for thermal barrier coatings, where microstructure plays a dominant role in decreasing thermal conduction (Pourbafrani and Razavi (2015), Schlegel et al. (2015), Li et al.

(2015)). Substitutional impurities and other means of disturbing the crystal symmetry, such as vacancies and dislocations, are currently used (and have been widely used in the past) to adapt the thermal response of low-dimensional structures (Iskandar et al. (2015), Zhao et al. (2015), Murphy et al. (2014), Xingli and Zhaowei (2011), Hopkins (2013), Slack et al. (2002)).

Although statically tailoring thermal transport is of great interest, dynamic controlled modulation may be suited for systems requiring thermal outputs that change and adapt to the environment, as a function of an independent variable. The ability to control phonon transport is crucial for applications such as heat-mediated data storage, thermal transistors and phonon logic computation (Yang et al. (2012), Li et al. (2012), Wang and Li (2007)). Furthermore, on-demand variations of material transport properties may result in a vast range of exotic and unforeseen technological applications. Among a considerable range of possibilities, one example is an advanced thermoelectric device that adapts to its surrounding environmental temperature in order to maximize efficiency, exhibiting high values of the thermoelectric figure of merit over a broad temperature range. Other examples involve devices that can increase their performance by adapting the thermal response as a function of a variable heat load, such as switchable thermal conductors for onchip heat management and solid-state thermal diodes (or switches) for cooling system applications. Clearly, tunable thermal devices should play an important role in our near future, but to date dynamic heat modulation in solid-state structures has remained elusive.

In spite of the important scientific and engineering challenge that modulation and control of heat flow represents, efforts to dynamically tune heat transfer at nanoscale have been made in the past. For example, thermal rectification has been observed experimentally (Tian et al. (2012), Kobayashi et al. (2010) Chang et al. (2006)), but the rectification coefficients, k_{high}/k_{low}, remain very small for potential integration in applications. Other interesting investigations have been performed by van Zwol et al. (2011), who showed electrically controlled fast nanoscale heat-flux modulation with phase-change materials. They obtained a significant contrast of heat flux due to the interplay between radiative heat transfer at the nanoscale and phase-change materials. Additionally in later work, van Zwol et al. (2012) showed experimentally that the metal-insulator transition of VO_2 entails a change of surface polariton states that significantly affects radiative heat transfer in near field. Zhang and Luo (2013) demonstrated theoretically that high-contrast and fully reversible thermal conductivity regulation can be achieved using the phase transition of polyethylene nanofibers. This method changes thermal conductivity by a factor ranging from 5 to 12. Very recently, Li et al. (2014) showed theoretically that large reversible changes of thermal conductivity, induced by mechanical stress, can be achieved with multiferroic-twinned films. By controlling the magnitude and direction of the applied shear strain field, which varies from 0 to 2 %, the density of twin boundaries perpendicular to the direction of heat flow increases and therefore

the thermal conductivity decreases by a factor of about 3.75. Perhaps even more interestingly, Ihlefeld et al. (2015) have experimentally demonstrated, for the first time, active and fully reversible control of thermal transport in a solid-state device, using ferroelectric thin films. The reversibly tunable phonon transport at room temperature was achieved by reconfiguration of the domain wall density of a lead zirconate titanate (PZT) bilayer, induced by the application of an electric field. Time domain thermo-reflectance measurements displayed a thermal conductivity variation from 1.06 to 1.15 $W/m \cdot K$ for an applied electric field that switched between 0 and 475 kV/cm. Although the thermal conductivity variation remains very low, this result gives insight into potential solutions for the successful development of technological approaches leading to controlled modulation of phonon transport.

Although important advances have been achieved recently, performance- and cost-effective, as well as engineeringly feasible methods for gating, switching and dynamically modulating heat transport have been barely demonstrated so far. As crystallographic defects, strain is an effective way to alter the crystal symmetry. In a crystalline solid, strain is defined as the percentage change of the lattice constant relative to its equilibrium value (Ueda and Pearton (2013)). Changing the lattice spacing in a solid could potentially provide an approach to reversibly and adaptively regulate thermal conductivity. Indeed, the effect of strain on transport properties has been successfully exploited in the electronic industry to improve the carrier mobility and enhance transistor performances (Maiti et al. (1999)). As a consequence, an increased interest on the effect of strain on the thermal properties of low dimensional structures has emerged recently. A reasonable number of theoretical studies had dealt with the influence of elastic strain on the thermal conductivity of thin films in the literature (Ding et al. (2015), Wang and Shen (2014), Li et al. (2010), Xu and Li (2009), Samvedi and Tomar (2010), Zhu and Zheng (2009), Picu et al. (2003)). While most of them agreed that thermal conductivity should decrease as tensile strain increase, recent first-principle calculations have shown that materials, such as graphene, are relatively insensitive to uniaxial strain for values smaller than 1%. All theoretical studies have addressed thermal conduction on single-crystalline films and the results strongly depend on the studied material. Most of them predicts significant variations on thermal transport only at very high values of applied strain (of about 5-15%), which are barely engineeringly achievable for ceramic and semiconductors, due to the fact that fracture would occur at strain values that are well below.

On the other hand, experimental results showing stress/strain effects on the thermal conductivity of thin films are mainly limited to studies performed by Gan et al. (2014) Takashiri et al. (2014), Lee et al. (2010), Kumar et al. (2013), and Alam and Manoharan (2012). It is worth noting that the 3 latter authors belong to a common research team at the Pennsylvania State University. Therefore, the sources of experimental evidence are quite reduced.

The aforementioned studies (except for the one carried out by Takashiri et al. (2014)), suggest that the thermal conductivity of thin films can drastically change by inducing strain. Gan et al. (2014) studied thermal conductivity of silicon cantilevers by Raman thermometry, and found that the thermal conductivity at room temperature increased by 18% with increasing uniaxial compressive strain from 0 to 0.25 %. They attributed the observed effect to the influence of mechanical stress on the group velocities of mode-specific phonons and on the specific heat. Takashiri et al. (2014) studied the combined effects of residual strain and grain size on the thermal conductivity of nanocrystalline bismuth antimony telluride thin films by the 3ω method. They observed a slight decrease of the lattice thermal conductivity which was attributed to the nano-size effect rather than the strain effect. Lee et al. (2010) investigated the thermal conductivity of polycrystalline aluminum films as a function of tensile thermo-mechanical strain, using a modified version of the 3ω technique. They observed a pronounced strain-thermal conductivity coupling, with 50% reduction in thermal conductivity at 0.25% strain. The observed effect was attributed to a decreases of the mean free path of the thermal conduction electrons through enhanced scattering at the moving grain boundaries, due to mechanical strain.

Kumar et al. (2013) and Alam and Manoharan (2012) analyzed freestanding amorphous Si_3N_4 thin film, using a self-actuation system based on the film residual stress, to investigate the coupling between mechanical strain and thermal conductivity. In the former work, they obtained a decrease of about 87.4% at about 2.4% tensile strain. In the latter study, it was observed that the thermal conductivity decreased by 44.5% for tensile strain varying from 0 to 1.5%. They have explained their observations through highly localized high frequency oscillators present in amorphous materials, which transport heat by a hopping mechanism. They suggested that with increasing tensile strain, heat energy hopping between two oscillators is degraded, yielding to a further reduction of the thermal conductivity. The trend reported in these studies differ markedly from experimental measurements performed by Ftouni (2013), who studied thermal transport in SiN_x membranes by coupling the 3ω method to the Völklein geometry and observed that residual stress has no effect neither on the specific heat nor on thermal conductivity. In addition to this controversy, Alam and Pulavarthy (2015) recently reported that 2.5% tensile strain can increase thermal conductivity of 200 nm thick freestanding amorphous silicon thin films from 1 to 2.4 $W/m \cdot K$, which represents a percentage change of 140%. They proposed that such increase in thermal conductivity might be due to strain-induced changes in microstructure and/or carrier density. This result strikingly contrasts with the expectation that strain should decrease the relative thermal conductivity below its unstrained value.

It can be seen that the theoretical and experimental information addressing the effect of strain on thermal conduction of thin films is available to a limited extent, exhibits significant variability, and even in some cases shows opposite

trends. A comparison to mutually validate experimental observation and theoretical predictions is complicated because the studied materials have different crystallographic nature i.e amorphous, nanocrystalline and monocrystalline, and the mechanisms that drive thermal transport largely differ from one case to another. Also, various experimental techniques are used, and often involve complex microfabrication processes that are difficult to reproduce. The important variability among the available experimental data, which is, in some cases, contradictory (large *versus* non significant effects, and even opposite trends) can be partly attributed to the experimental uncertainty involved in the currently available thermal measurements, which are often large. In addition, the evident lack of experimental studies on strain-mediated thermal conductivity is certainly due to the intrinsic complexity associated with simultaneously inducing and measuring strain in a low-dimensional structure, while performing thermal conductivity measurements. To overcome these issues, improved understanding of the effect of strain on thermal conduction processes in monocrystalline, polycrystalline and amorphous thin films is required. Additionally, development of reproducible and easy-to-implement experimental methods is highly desirable.

1.4 Aim of the thesis

Although polycrystalline films used in technological applications often exhibit a structural heterogeneity, the influence of the latter on thermal transport has not been considered so far. Understanding the effect of these structural features and other multi-scale crystallographic defects, is a key element to investigate new means of controlling phonon transport in solid-state systems. This work aims at providing fundamental knowledge about thermal properties of polycrystalline films by investigating the effects of the evolution of the crystal structure and the presence of oxygen-related defects on thermal conduction processes. Then, microstructure and localized oxidation are exploited to effectively tune thermal properties of AlN films deposited onto silicon substrates, and the obtained results are explained through an analytical model.

Furthermore, to address the controversy about the possibility of tuning the thermal conductivity by means of strain, a simple and reproducible experimental technique is developed to perform strain-mediated thermal measurements on thin films-on-substrate specimens.

Part II

Methodology

Chapter 2

Deposition of AlN films and material characterization methods

The thermal properties of a thin film are intricately related to its microstructure, and therefore its accurate characterization is crucial to understand thermal transport. This chapter provides the description of aluminum nitride and the experimental methodology used to synthesize AlN thin films. The experimental techniques used to characterize the film crystalline structure and morphology are discussed in details. The methodology used to determine crystallite sizes distributions along various regions of the films is also given.

2.1 Aluminum Nitride

Aluminum nitride is an ionic binary compound that belongs to the III-V group. In its wurtzite phase (Fig.2.1), it is the largest-bandgap nitride semiconductor (6.28 eV). Wurtzite AlN crystallizes in a hexagonal structure with lattice parameters a and c of 3.11 Å and 4.98 Å, respectively. The ordered structure is described by the space grouping $P6_3mc$ (in the Hermann-Mauguin notation) and consists of two interpenetrating hexagonal close-packed sublattices, each one containing either aluminum or nitride atoms (Fig.2.2). There are four Al atoms per unit cell, located at $(0,0,0)$, $(\frac{1}{3},\frac{2}{3},\frac{1}{2})$, $(0,0,\frac{3}{8})$ and $(\frac{1}{3},\frac{2}{3},\frac{7}{8})$. The N lattice is separated from the Al arrangement along the $c-$axis direction by an offset 3/8 of the cell height ($3c/8$), or $(0,0,\frac{3}{8})$ (Quinn and Yi (2009)). In such structure, each Al atom is coordinated tetrahedrally to form four equivalent bonds with N atoms. Conversely, each N atom is coordinated by four Al atoms.

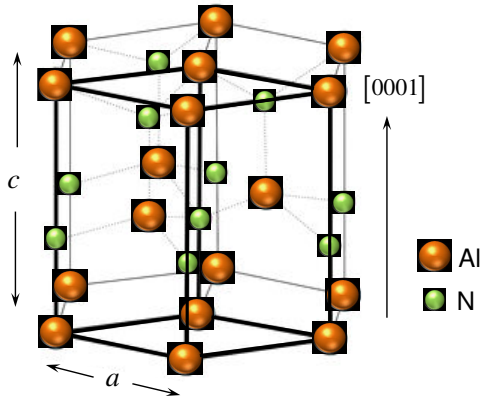

Figure 2.1: *Crystal structure of AlN in its wurtzite phase. The bold solid lines refer to the hexagonal unit cell but adjacent atoms are included to show the overall hexagonal nature of the structure. Al-N bonds are depicted by the dashed lines. Adapted from Zhu and Oliver (2012).*

Because of the intrinsic asymmetry of the ionic bonding along the [0001] direction in the equilibrium wurtzite structure, the c/a ratio of "real" AlN can deviate from the that of an ideal wurtzite crystal ($c/a = 1.633$). This happens for all group IIIA nitrides, and is the reason these materials experience spontaneous polarization. Furthermore, mechanical stress also results in polarization, which is called in that case piezoelectric polarization. This has been found to increase from GaN over InN to AlN, the latter having the highest piezoelectric coefficient ($5.1 - 6.72$ pm/V) among group IIIA nitrides (Moram and Vickers (2009)).

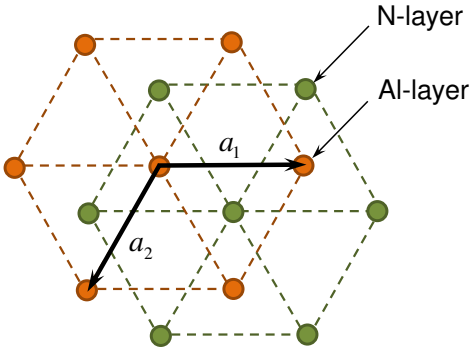

Figure 2.2: *Stacking of layers Al and N in a hexagonal close packed crystal of lattice constants $a = a_1 = a_2$, and c. Adapted from Quinn and Yi (2009).*

The piezoelectric and thermal properties of AlN make it a particularly suited material for this study. The reason is that an electric field can be used to

induce lattice deformation and therefore potentially provides a means to electrically tune its thermal properties. This will be further discussed in section 3.7 of Chapter 3, where the experimental approach proposed to perform strain-mediated thermal measurements is presented.
It is noteworthy that although three miller indices are sufficient for accurately identifying different crystal planes and directions, in hexagonal systems, the four Miller-Bravais notation is conventionally used. Such notation makes use of four indices u, v, s, w, where $u + v + s = 0$. To illustrate this briefly, the fundamental lattice vectors of the hexagonal (0001) plane are depicted in Fig.2.3.

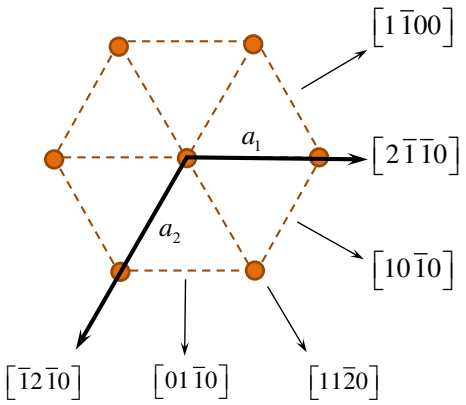

Figure 2.3: *Fundamental lattice vectors of the hexagonal (0001) plane in the Miller-Bravais notation. Adapted from Hanada (2009).*

Some common growth planes of wurtzite AlN crystals, particularly relevant for studying the films fabricated and characterized in the course of this work, are shown in Fig.2.4, along with their corresponding Miller-Bravais crystal indexation.
Under special conditions, AlN can exist in the zincblende and rocksalt structures (cubic), though the wurtzite phase is the thermodynamically stable structure under ambient conditions. The metastable zincblende polytype has been observed in epitaxially grown AlN/W superlattices on MgO substrates (Kim et al. (2001)), and the rocksalt phase has been stabilized in epitaxial AlN/TiN superlattices, under high temperature and pressure conditions (Madan et al. (1997)). In the past years, several techniques have been used to prepare AlN thin films. Some examples are molecular beam epitaxy (MBE), pulsed laser deposition (PLD), chemical vapor deposition (CVD) and sputtering methods. In this work, the deposition of AlN thin films on Si(100) were performed by radio-frequency reactive magnetron sputtering. Different aspects of using reactive magnetron sputtering for growth of AlN films are discussed in detail in the following section.

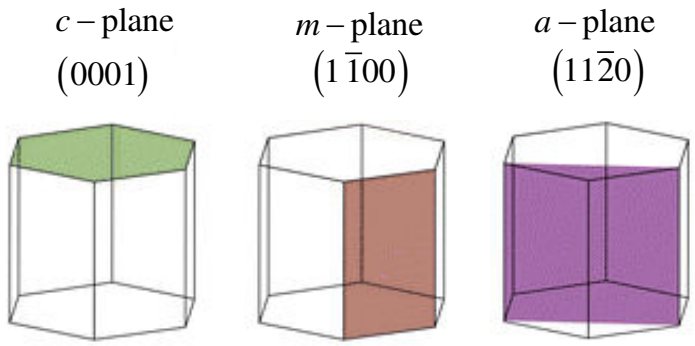

Figure 2.4: *Schematic diagram of common growth planes of AlN crystal. Adapted from Quinn and Yi (2009).*

2.2 Deposition of films by magnetron sputtering

Physical vapor deposition processes (PVD) comprise a group of techniques used for synthesizing metallic or ceramic films. They are used in a diverse range of research and technological fields, such as optics, electronics, chemistry, mechanics or still in the automotive and aerospace industry, because they allow the fabrication of a wide variety of materials.

In general, thin films are produced in a rarefied atmosphere (<0.1 mbar), following three fundamental steps:

- Vaporization of a material from a solid source or target, assisted for example by a plasma.
- Transport of the vaporized material throughout the reactor chamber.
- Condensation onto the surface of the substrate, followed by film nucleation and growth.

A plasma-assisted physical deposition apparatus typically consists of a vacuum chamber, a material source or target, a substrate holder, and a power supply to generate the electric discharge (Fig.2.5). An excellent review on sputtering applied to deposition technology has been provided by Thornton (1973).

Sputtering processes can be performed in a neutral atmosphere, using a noble gas such as argon, or in a reactive atmosphere, where the metal is evaporated in the presence of a reactive gas (in addition to argon) to form a compound. This work focuses on RF reactive magnetron sputtering to deposit polycrystalline AlN films.

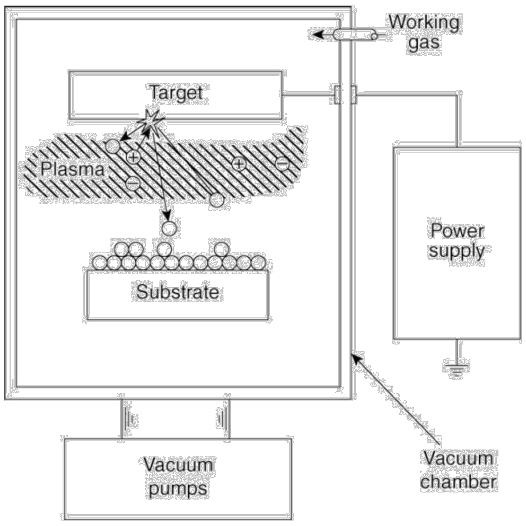

Figure 2.5: *Schematic representation of sputtering process and chamber geometry, along with its main components. Reprinted from Martin (2009).*

2.2.1 Reactive RF magnetron sputtering

Because of their dielectric nature, direct evaporation of electric insulating materials is difficult and inefficient. This issue can be overcome by sputtering the target with a RF power supply in the reactive mode. This approach is advantageous namely due to its high deposition rate compared to other commonly used techniques (Martin (2009)). By definition, reactive sputtering consists of adding a reactive gas to the main noble plasma gas in the deposition process. In the case of AlN films deposited by reactive sputtering, the plasma consist of a mixture of argon and nitrogen in the presence of an aluminum target. The plasma is initiated by ignition, applying a radio-frequency electrical bias to the target. The negative polarization (0.5-3.5 kV) of an electrode in the presence of a rarefied atmosphere at a pressure of about 10^{-2} to 10^{-1} mbar (depending on the chamber size) triggers a glow discharge (Billard and Perry (2005)). This electrical discharge dissociates the gas atoms into ions and electrons. As the gaseous molecules are dissociated, the ions are accelerated to the cathode (target) and electrons are accelerated to the anode (substrate-holder and chamber walls), while in the process, more gas atoms are ionized, owing to collisions with free electrons. When the ions collide with the target surface, they transfer their kinetic energy per unit area (ionic bombardment), causing the atoms of the target to be ejected (sputtered). The vaporized metallic species are transported throughout the chamber towards the substrate surface and the walls of the deposition chamber. At the same time, secondary electrons are produced, and as a consequence, the gas is increasingly ionized. The presence of nitrogen

has three effects on the sputtering process (Boeshore (2006)):

- Nitridation of the aluminum target, which occurs as a thin layer of the AlN compound forms at the surface of the target, causing the sputtering of a mixture of Al, N, and AlN species rather than simply pure aluminum. The amount of these sputtered species strongly depends on the nitrogen content.
- Reactions of nitrogen ions in the plasma can occur with volatilized Al species, forming a metal-nitride compound.
- Further reactions can occur between Al and N, if pure Al atoms are deposited onto the surface of the substrate.

In practical applications, the dominant mechanism is the first one.

2.2.2 Energy of the sputtered species

The atoms ejected from the target surface have an average energy of the order of 5 to 10 eV. On the trajectory between the target and the substrate, the sputtered atoms undergo collisions with the argon and nitrogen ions, in which they can transfer a portion of their kinetic energy. The number of collisions is proportional to the distance traveled by the sputtered atom and to the working pressure. For a discharge at a working pressure of 10^{-2} mbar, the mean free path of the sputtered atoms, i.e the average distance before experiencing a collision with another atom, is of about 1 cm. Since the distance between the target and the substrate is usually of the order of ten centimeters, a large number of the sputtered atoms lose their kinetic energy to a large extent in the various collisions that occur before they reach the substrate. When the atoms arrive at the substrate surface, their kinetic energy reaches values in the range of 0 1 eV, which affects the quality of the films (Billard and Perry (2005)).

2.2.3 The magnetron effect

The magnetron technology is basically used to overcome the low ionization rate of the glow discharge that causes a decrease of the deposition rate (< 0.1 µm/h). In this case, the target is usually equipped with a magnetron configuration, which consists of two concentric magnets of opposite polarities, and a polar piece that closes the magnetic circuit. This configuration confines the electric and magnetic fields within the gas phase in front of the target, trapping the secondary electrons and therefore intensifying the bombardment of ions to the target. In this way, a dense plasma is generated, which leads, in spite of a heterogeneous erosion of the target, to greatly increase the discharge current, and subsequently the deposition rate up to 10 µm/h. The use of a magnetron also leads to a significant decrease of the ignition pressure of the glow discharge to about 10^{-3} mbar, which promotes the synthesis of denser films (Billard and Perry (2005)).

2.2.4 AlN growth process

The microstructure of polycrystalline AlN films, comprising the size, morphology and orientation of crystallites, is highly dependent of the deposition conditions during film growth. An important guideline to explain these dependencies are the structure zone models, developed by the compilation of experimental observations. Among various structure zone models, the most commonly used is the one published by Thornton (1977), depicted in Fig.2.6. This diagram establishes the relationship between morphology, normalized growth temperature (T/T_m , where T is the substrate temperature and T_m is the melting point of the film material), and chamber pressure.

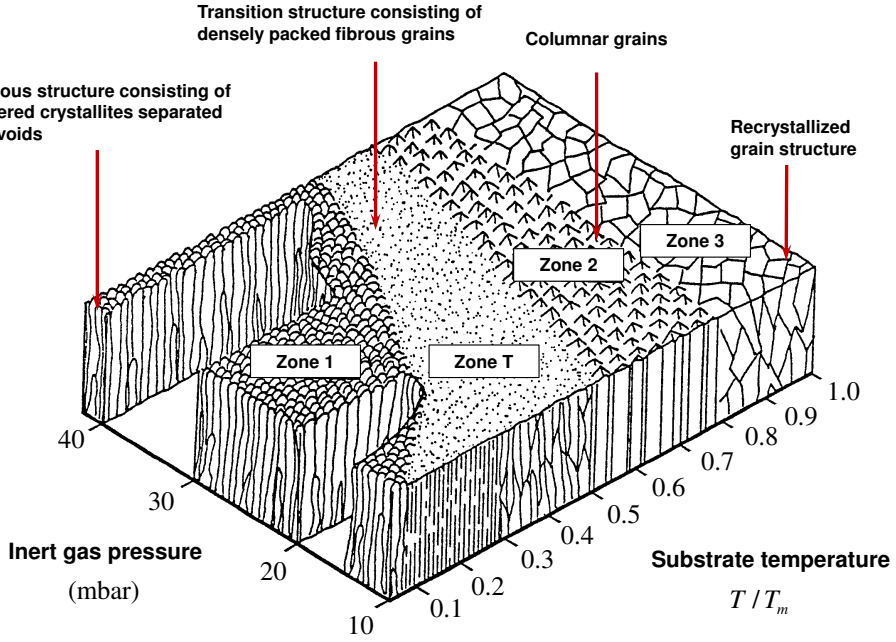

Figure 2.6: *Thornton structure zone model. Adapted from Thornton (1977).*

Four main zones are can be identified (Barna and Adamik (1998), Thornton (1977), Boeshore (2006)):

- Zone 1: The film is composed of fibers of small diameter and the grain boundaries are porous. Neither the bulk diffusion nor the self surface diffusion are dominant, and the growth mechanisms are rather driven by shadowing processes.
- Transition zone: The deposited material is inhomogeneous along the film thickness, being fine crystalline at the zone near the substrate (V-shaped grains), and columnar near the outer surface. Although surface diffusion is very important, grain boundary migration is limited.

- Zone 2: The sputtered layers exhibit a rather homogeneous structure along the film thickness. Surface diffusion is the dominant mechanism and grain boundary migration is allowed by the high substrate temperatures.
- Zone 3: The film is composed of equiaxed three-dimensional grains, and the growth is dominated by bulk diffusion.

Room-temperature RF reactive deposition occurs at normalized growth temperatures of about $T/T_m = 0.1 - 0.2$, and working pressures well below 1 mbar, resulting in films that belong to the transition region and therefore exhibit an structural inhomogeneity along the growth direction (Boeshore (2006)). The forming phenomena of this structural heterogeneity are driven by competitive growth (Van der Drift (1967)), which occurs in three main stages: 1) the nucleation, where atoms of the plasma condense onto the substrate surface, forming small single-crystals with various orientations. 2) The grain growth, in which the nucleation sites continue growing until they encounter neighboring islands. At this point they form grain boundaries and then coalesce. 3) Texture development, where the formed crystallites have different orientations and are composed of various families of crystallographic planes. The further development of the microstructure is determined by the faster growth rate direction, which yields to a columnar structure with a preferred orientation. These growth forming phenomena are directly related to the plasma conditions during deposition and the energy of the arriving adatoms (i.e atoms that lie on a crystal surface and can migrate to nucleation and growth sites). Thus, deposition parameters such as working pressure, applied power and nitrogen content, can be used to control the microstructure of the deposited film (Signore et al. (2013)).

2.2.4.1 Influence of the deposition parameters

The properties of AlN films depend on the kinetics of the sputtered species, which can be altered by varying the growth parameters (Kar et al. (2009)).

- **Working pressure**

Sputtering pressure can have a strong effect on the crystalline quality of sputtered films. Depositing at high pressures reduce considerably the amount of energy imparted to both the plasma species and sputtered material, due to the reduction of the chamber voltage. Additionally, high pressure makes ions species to experiment more collisions, decreasing their mean free path and therefore reducing their kinetic energy. However, ions species with no sufficiently high kinetic energy will not be able to form a highly aligned film with the suitable arrangement of atoms. On the other hand, low pressure increases the mean free path of species yielding to high ion energy and deposition rate, but also significantly increases internal stresses.

- **Applied power**

Generally, the mobility of the reactive species is increased with increasing sputtering power. Thus, the nucleation and growth rate are increased accordingly (Zhang et al. (2005)). Although a high nucleation and deposition rate are favorable, at very higher power the film can be damaged. This is because impacting species can resputter the growing film and cause an increase in the residual stress through high ion impact energies that create interstitials and vacancies (Artieda et al. (2010)).

- **Nitrogen flow rate**

The nitrogen flow is one the most influential parameters in the deposition process, because the chemical reactions that occur at the target surface strongly depend on the reactive gas flow rate. In the absence of N_2, pure Al is sputtered from the metallic target, but as N_2 flow rate is increased, chemical reactions between Al and N_2 take place at the target surface, forming an AlN layer. This process is called target poisoning. If the N_2 content is not high enough, the nitride layer is sputtered at a rate that is higher than nitrification, and the sputtered film is a mix of metal, solid solution of nitrogen in metal, and nitride phases (Felmetsger et al. (2008)). As the flow rate is further increased, the N_2 flow begins to exceed the pumping capability, rapidly nitriding the remaining free Al on the target surface. At a critical value of N_2 content, the target becomes completely poisoned and further increasing the flow does not change neither the chemistry of the target nor the discharge parameters. At this point, if nitrogen flow is reduced, the target returns to the metallic mode, but the transition takes place at lower gas flow values. The hysteretic behavior can be characterized by measuring the bias voltage as a function of nitrogen flow, as the discharge voltage is directly related to the chemical composition of the target surface. The reason is that the insulating layer affects the electrical response of the system. Data of the voltage dependence on the nitrogen flow, obtained in our RF sputtering apparatus, at an applied power of 400 W, working pressure of 2.1 $\times 10^{-3}$ mbar and argon flow rate of 200 sccm are shown in Fig.2.7.

The three aforementioned regimes of the reactive sputtering discharge can be identified in Fig.2.7. When a relatively small amount of nitrogen is added to the argon gas (≈ 3 sccm), the discharge voltage is gradually reduced, while the target remains in the metallic state. This region is called the metallic mode (region M). Further increasing the N_2 content results in a drastic decrease of the discharge voltage, which is known as the metal-dielectric transition (region T), and at a N_2 flow of about 7 sccm, the bias voltage reaches the equilibrium, indicating that the target is completely covered with the nitride layer (region P). This regime is the so-called poisoned mode. During the decrease in N_2 flow, the crossover back to the metal mode occurs al lower values (between 7 and 6 sccm), revealing that the discharge parameters are the most stable and

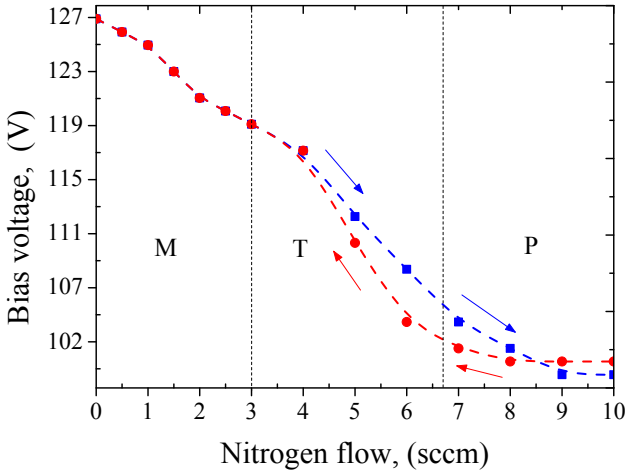

Figure 2.7: *Voltage dependence on the nitrogen flow during RF reactive sputter deposition from an Al target in mixed $Ar + N_2$ atmosphere. The data was obtained at applied power = 400W, working pressure = 2.1 $\times 10^{-3}$ mbar and argon flow rate = 200 sccm discharges. The capital letters M, T and P refer to the metallic, transition and poisoned mode.*

reproducible (Felmetsger et al. (2008)). Therefore, the optimal working point to deposit AlN films should be located in this region of the back branch of the hysteresis loop. This discharge behavior is characteristic of reactive sputtering, and was crucial for obtaining highly-textured AlN films on silicon substrates in this work, as will be discussed below.

2.2.5 Aluminum Nitride thin film preparation

Obtaining highly textured AlN films in the [0001] direction is crucial for two main reasons. The first one is related to the cross-plane thermal properties of the films, which strongly depend on the grained structure. If the films crystallize in a columnar structure, thermal conduction will be favored along the $c-$axis direction, which is of great interest to better study the cross-plane thermal conductivity of polycrystalline AlN films (as is our case). The second reason is that the piezoelectric response of the film is directly related to the $c-$axis alignment of individual grains. Thus, highly (0002)$-$textured films are desirable to look towards an application that electrically induces strain, and potentially modulates thermal transport in a solid-state device.

In this work, AlN films were deposited using the RF magnetron sputtering system shown in Fig.2.8. Images in Fig.2.8(b) and (c) are closer-up views of the substrate holder and the target disposition. Prior to the insertion into the deposition chamber, the substrates were ultrasonically cleaned in acetone, ethanol and then dried with N_2 gas. The sputtering process was conducted

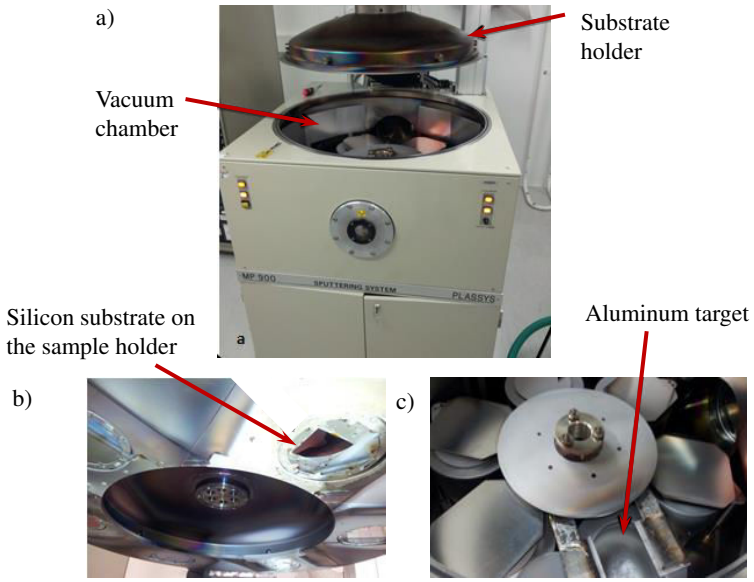

Figure 2.8: *(a) Image of the RF magnetron sputtering system used for AlN films preparation. Closer-up view of the (b) substrate holder and (c) the aluminum target*

in the reactor. Samples with thickness varying from 270 nm up to 1460 nm were prepared on single-crystal Si(100) substrates in the high vacuum chamber with a base pressure of 4×10^{-8} mbar. Samples were sputtered without any external heating from a pure metallic aluminum target of 8-inch diameter in a high purity mixture (99.99%) of nitrogen and argon. To allow cleaning of the target surface and plasma stabilization, the target was pre-sputtered for 30 minutes in pure Ar, prior to film deposition. To obtain high quality AlN films, the deposition parameters, such as N_2/Ar gas pressure, RF power and flow rate, were adjusted based on the poisoning curve depicted in Fig.2.7. Then, the optimum conditions were chosen for the preparation of AlN films.

2.2.5.1 Monolayers

First, in an attempt to obtain high quality AlN films, the working point was chosen at a nitrogen flow of 6 sccm on the back branch of the hysteresis loop. This choice was based on a stability criterion. Indeed, at this point any possible fluctuations of cathode power and nitrogen flow do not lead to a sudden switch of the target condition from the poison to metallic state, which can yield to the degradation of film quality (Felmetsger et al. (2008)). These deposition conditions showed to improve the crystalline alignment of the films in comparison to films obtained at higher nitrogen flow i.e poisoned regime (8-10 sccm).

However, it was found that these improvements still yielded relatively poor crystalline quality and limited out-of-plane texture (See Chapter 5 and 6, where crystalline features and thermal properties of a 850 nm-thick poorly-textured film were characterized).

Because these refinements could not produce sufficient columnar alignment, a better sputtering method was required to deposit highly crystalline AlN films. Following the direction of reported results addressing deposition of high AlN quality films (Signore et al. (2013), Tang et al. (2012), Deng et al. (2012), Tajima et al. (2011), Boeshore (2006)), we operated a two-step deposition process. This technique promotes better conditions for AlN nucleation on the surface of silicon substrates (Felmetsger (2011), Piazza et al. (2012)). In the first stage, high energy was supplied to the adatoms by increasing the RF target power and by decreasing the deposition pressure, in order to increase the surface energy of the substrate and enhance the mobility of impinging species. This additional energy supply was carried out at the expense of uncontrolled residual stress. Moreover, the first step was performed with a higher nitrogen content in order to operate in a deeper poisoned mode and promote the nucleation of small $c-$axis oriented grains (Piazza et al. (2012)). This base layer, which acts as a seed layer, promotes the orientation of the subsequent film growth. During the second stage, deposition was performed at higher pressure and moderate RF target power, to reduce the residual stress and favor well aligned columnar growth.

Deposition parameters for preparing the AlN films are summarized in Table 2.1. The deposition time varied from 30 to 164.5 minutes, depending on the film thickness.

Table 2.1: *Deposition parameters of AlN thin films fixed after process optimization*

Substrate		Si(100)
Substrate temperature (K)		≈ 300
Target		Al (99.99% purity)
Gas		Ar, N_2
Base pressure (10^{-8} mbar)		4
	Step 1	Step 2
Sputtering pressure (10^{-3} mbar)	1.5	2
Ar flow rate (sccm)	192	194
N_2 flow rate (sccm)	8	6
RF power (W)	500	400
Deposition time (min)	2	30 164.5

2.2.5.2 Multilayers

AlN/AlN multilayer samples were prepared to understand the effect of nanoscale defects induced by oxygen impurities on thermal transport properties of polycrystalline thin films. Multilayer preparation aimed at introducing random oxygen impurities at the interface between two AlN layers, deposited one on the top of the other. The experimental process consisted of two iterative steps: first, an AlN layer of 270 nm thick was deposited under the sputtering conditions presented previously (Table 2.1). After film deposition, the process was interrupted by stopping the pumping system and venting the deposition chamber to atmospheric pressure. The iterative interruption of the sputtering process enabled the preparation of multilayer samples, which consisted of two, three, and four AlN layers of 270 nm thick, deposited one on the top of the other. It is worth noting that each layer composing the AlN/AlN multilayers where deposited under the conditions listed in Table 2.1.

2.2.5.3 Brief description of the samples studied in this work

To gain an overall understanding of thermal transport across polycrystalline AlN films deposited onto silicon substrates, the effects of structural evolution along the cross plane and oxygen related defects were studied on three types of samples: poorly-textured monolayers and highly textured mono- and multilayers. A schematic comparison of the three types of samples studied in this work is presented in Fig.2.9.

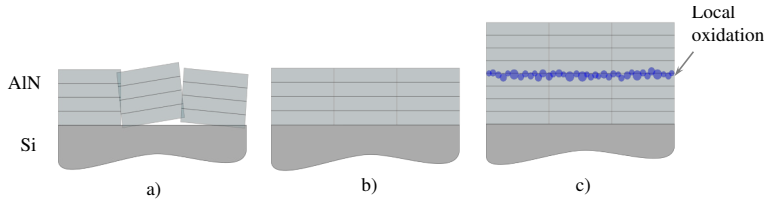

Figure 2.9: *Schematic representation of the three types of samples studied in this work. (a) Poorly-textured monolayers obtained by one-step deposition process, (b) highly textured monolayers deposited by two-step sputtering, and (c) highly-textured multilayers, where a periodical interruption of deposition process (breaking the vacuum), was performed to create interfaces with oxygen-related defects and/or inclusions.*

The first type of samples, [Fig.2.9(a)] was obtained by operating a one-step deposition process and both highly-textured monolayers and multilayers, were deposited by two-step sputtering [Fig.2.9(b)(c)]. The only difference in the preparation method was that, for highly-textured multilayers [Fig.2.9(c)], a periodical interruption of the process was performed to favor local oxidation between AlN/AlN interfaces.

First, a comparison between poorly and highly-textured configurations was carried out to identify the factors governing texture development. Then, the

highly-textured monolayer specimens were used to understand the role of microstructure evolution on thermal transport. The effect of oxygen-related defects was subsequently explored on multilayered specimens. Moreover, to analyze the influence of film thickness and the grain morphology evolution on thermal conduction processes, the thickness was varied from about 270 nm to 1460 nm for monolayers, and from 545 nm to 1107 nm for multilayers. Furthermore, strain-mediated thermal characterization on the three types of samples allowed to explore the influence of lattice deformation caused by externally induced elastic strain on the thermal conductivity. The results of the aforementioned investigations will be presented in Chapter 6.

2.3 Structural analysis

2.3.1 X-ray diffraction

In this work, AlN films were investigated with various X-ray techniques to analyze their crystallographic features. The Bragg-Bretano ($\theta - 2\theta$) configuration was used to identify crystallographic phases and preferred orientations, and rocking curves served to quantitatively determine the out-of-plane crystal misalignment. All the specimens were examined with CuKα radiation ($\lambda = 1.54$Å) using a D8 Bruker diffractometer.

Diffraction techniques use the coherent and incoherent scattering of small-wavelength electromagnetic radiation caused by the atomic arrangement of a material. In a crystalline solid, for example, X-rays (electromagnetic waves of wavelength of the order of the interatomic distance in crystals) interact with atoms that are periodically spaced. These atoms act as scattering centers, and the constructive interference of the radiation leaving the sample (in certain angles) is diffracted in such a way that a pattern is formed. The scattering of an incident X-ray wave by the atomic planes parallel to the specimen surface is sketched in Fig.2.10.

The condition which must be met for diffraction to occur was first stated by Bragg and Bragg (1913), and became to be known as the Braggs' law:

$$n\lambda = 2d\sin(\theta) \tag{2.1}$$

being n an integer referring to the order of the diffraction, λ the X-ray wavelength, d the interatomic spacing and θ the angle of incidence and reflection. This equation states that the scattered rays will be completely in phase if the path difference, $AB+BC$, is equal to a whole number n of wavelengths (Cullity (1978)).

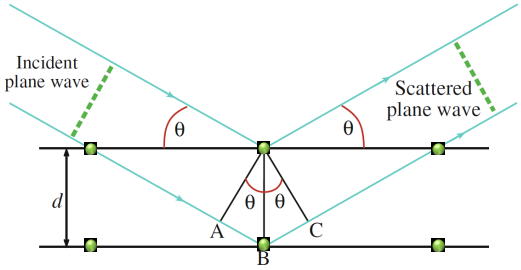

Figure 2.10: *The Bragg description of diffraction in terms of the reflection of a plane wave of wavelength λ. X-rays are incident at an angle θ to the atomic planes of spacing d. The path difference between reflected waves is AB + BC. Reprinted and adapted from Williams and Carter (2009).*

2.3.1.1 Bragg-Bretano configuration: $\theta - 2\theta$ scans

The Bragg-Bretano geometry is certainly the most widespread technique used for symmetrical-powder diffraction. In this particular configuration, the angles of the incident and diffracted electromagnetic radiation are equal (Fig.2.11). Typically, the sample and the detector rotate with a coupled $\theta - 2\theta$ angular movement to ensure a proper focusing condition. Thus, the specimen moves at an angular velocity ω, while the detector scans the sample at an angular velocity of 2ω. Both angles are therefore simultaneously varied in the angular range of interest to collect diffracted intensities from the crystal planes parallel to the film surface. This is not a particular issue in the case of a powder, which shows randomly oriented grains with respect to the surface. Contrarily, when thin films are characterized, this diffraction geometry does not allow to distinguish a uniaxial texture from a biaxially textured.

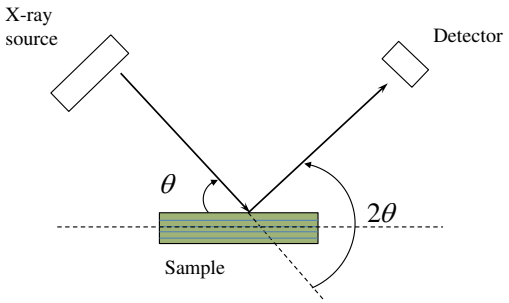

Figure 2.11: *Schematic representation of a symmetric $\theta - 2\theta$ scan using the Bragg-Bretano geometry.*

2.3.1.2 Rocking curves: ω-scans

The preferred orientation direction and the degree of orientation are two main factors that can strongly affect the physical properties of a thin film. In par-

ticular, if the thin film exhibits a columnar structure, with grains oriented perpendicular to the sample surface, heat transfer will be favored in the out-of-plane direction, whereas the in-plane thermal conductivity will be reduced due to higher in-plane grain boundary density. Thereby, thermal conduction processes are strongly anisotropic in thin films. The degree (or distribution) of preferred orientation can be measured by an ω-scan or rocking curve. The first step is to select a family of planes parallel to the sample surface exhibiting significant diffracted intensity. In our case, we use the (0002) Bragg reflection. Then, the detector is fixed at that characteristic 2θ angle (36.041 ° for the (0002) family of planes of AlN) to record the diffraction intensities from the preferentially oriented planes. Simultaneously, the ω angle of sample position is changed in the range of interest. The process of varying the ω angle of the thin film sample is called "rocking". A schematic representation of a rocking curve measurement is shown in Fig.2.12

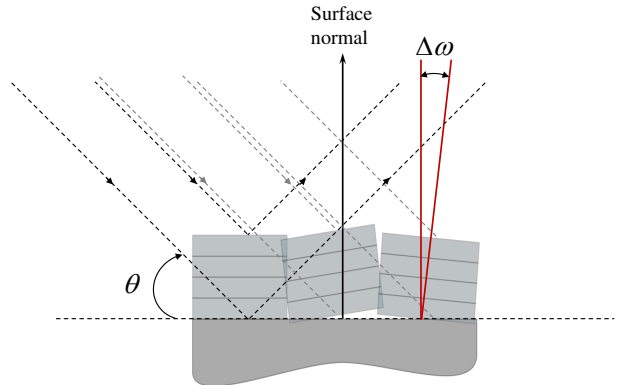

Figure 2.12: *Schematic representation of an ω scan or rocking curve measurement.*

2.3.2 Electron microscopy

2.3.2.1 Scanning electron microscopy

In this work, scanning electron microscopy (SEM) was used to characterize the morphology of fractured film cross-section samples and the columnar grain size. This method is primarily based on the detection of secondary electrons that are backscattered as a consequence of the interaction between a very narrow electron beam and the atoms near or at the sample surface. The electron beam scans the surface of the specimen in a raster pattern, providing information about the morphology (and topography), typically with a resolution of about 5 nm, with a large depth of field. Other signals produced by the interaction of the primary electrons with the sample are used as well: secondary electrons, absorption of the primary electrons, the emission of X-ray photons, and in some

cases, photons with wavelengths near those of the visible light. These interactions are indicative of the topography and/or surface composition (Paqueton and Ruste (2006)).

To analyze their cross-section, the AlN samples were cleaved and cleaned with acetone and ethanol, followed by high-purity nitrogen drying. Columnar grain size distributions were systematically studied by digital SEM processing of the obtained images. A simple thresholding, based on the unprocessed image intensity histogram, allowed to define the edges of columnar grains and measure their dimensions.

2.3.2.2 Transmission electron microscopy

Transmission electron microscopy was used to study the grain structure evolution along the cross-plane and the mechanisms involved in collective crystal growth. In addition, digital processing of TEM micrographs allowed measurement of nanoscale crystallite size distributions near the interface with the substrate.

The principle of operation of TEM relays on the detection of forward scattered electrons that are transmitted through a very thin “electron-transparent" specimen. A nanoscale (<5 nm) beam is focused to impinge the “transparent” sample, and a portion of the further scattered electrons, emerging from an area of the specimen, are focused and projected onto a screen. As in the case of scanning electron microscopy, other scattered electrons can be used to obtain other information, such as chemical composition. By modifying the configuration of apertures and adjusting the electrostatic and electromagnetic lenses, TEM microscopes can switch between a variety of operating modes, namely the bright field (BF), dark field (DF), high-resolution (HRTEM), selected area diffraction (SAED) and scanning (STEM) mode.

In BF mode, an aperture allows to select only the direct transmitted beam of electrons, which is weakened due to the interactions with the sample. The contrast of the obtained image therefore results from mass-thickness and diffraction effects. Thus, darker zones can represent thick areas, regions constituted of atoms with higher atomic number, and/or domains of high crystallinity. This mode is particularly useful to reveal grain and defect structures, as well as second phases i.e precipitates and inclusions. However, contrast interpretation is not straightforward owing to the simultaneous occurrence of other contrast-forming phenomena (Williams and Carter (2009)).

DF imaging is obtained by placing an aperture that blocks the central beam and allows to select electrons that are off-axis scattered by the sample. This means that the image results from the Bragg diffracted beams, and therefore bright contrast arises from crystals which strongly diffract into the objective aperture. This mode enables crystallographic characterization of selected regions and gives useful information about planar defects, stacking faults or particle size.

HRTEM micrographs are obtained by placing an aperture such that both, the primary and the diffracted beams, can pass through the sample. Their interference yields to phase contrast at high magnifications, resolving the crystal lattice. High resolution imaging serves to characterize crystal structure and defects i.e interfaces, grain boundaries and stacking faults.

In SAED, a selected area diffraction aperture is inserted allowing to obtain diffraction patterns from small areas of the studied specimen. This mode is used for local determination of crystallographic structure, symmetry, and orientation of the analyzed area, as well as local measurement of lattice spacing.

STEM differs from other modes as it uses a fine probe that scans the sample point by point, and therefore the image is formed over several seconds or minutes (Williams and Carter (2009)). This mode is often used with a high angle annular dark field detector (HAADF), which collects electrons that are elastically scattered at high-angles in the zone near the primary beam. The contrast of the obtained image strongly depends on the average atomic number of the scattering centers encountered by the incident probe. As a consequence, when it is used with energy-dispersive X-ray spectroscopy (EDX), it is possible to map the chemical element distributions of the studied specimen.

In this work, AlN films were characterized in BF, HRTEM and STEM-HAADF-EDX modes, using a FEI Tecnai Osiris (Scanning) Transmission Electron Microscope at operating voltage of 200 kV. First, to prepare "electron transparent" cross-section slabs, string sawing was used to form thin slices from the bulk AlN sample. After, two slabs were epoxy-bonded together in such a manner that the AlN surfaces were placed face-to-face (Fig.2.13). Mechanical polishing was performed on two parallel faces to gradually decrease the thickness until obtaining a 40 µm-thick specimen, which was then glued onto a cooper support. The final thinning was done by ion milling (FIB), which continued until a small hole perforated both pieces of the sample in the center. This process yielded four observable "electron transparent" areas on each side of the ion-milled hole. An optical micrograph of the bonded together face-to-face slabs with the ion-milled hole is shown in Fig.2.13.

- **Grain size distribution determination by digitally processed SEM and TEM micrographs**

Grain size distributions of AlN samples were measured by electron microscopy techniques. The region near the substrate interface was characterized by TEM, while SEM was used for the columnar region. In the literature, crystallite sizes are often obtained either by XRD (Scherrer equation) or electron microscopy techniques. In this work, the latter was chosen because the Scherrer equation is not applicable to thin films with an heterogeneous microstructure that evolve with film thickness. The reason is that this XRD method was derived based on the assumption that the material is composed of spherical or cubic crystallites, with homogeneous spacial distributions (Langford and Wilson (1978)).

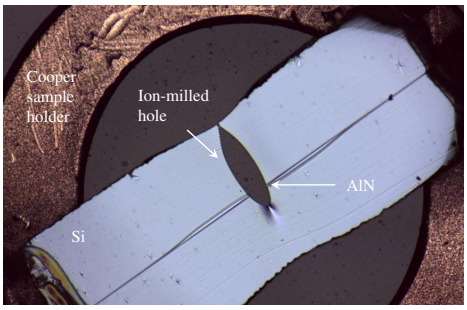

Figure 2.13: *Optical micrograph of the bonded together face-to-face AlN/Si slabs with the ion-milled hole*

Furthermore, it does not take into consideration additional contributions of the peak broadening arising from strain and common crystallographic defects i.e dislocations, stacking faults, etc (Klug and Alexander (1974)).

2.4 Summary

In this chapter, the sputtering technique used to successfully obtain highly-textured AlN samples was described. In addition, the standard experimental techniques employed to characterize the film crystalline structures and morphologies were briefly explained. The experimental strategy adopted to determine crystallite sizes distributions along various regions of the films was also given. The results of the XRD, TEM and SEM characterizations here described have been employed for analyzing thermal properties considering multiscale structural features and crystallographic defects present in AlN films (Chapter 6). The following chapter focuses on the experimental techniques used to measure the thermal conductivity of the studied samples.

Chapter 3

Thin film thermal conductivity measurements

This chapter thoroughly describes the experimental methodology used to characterize the cross-plane thermal conductivity of AlN films and its associated challenges. First, a complete theoretical background of the 3ω technique is provided, including the data reduction and the uncertainty analysis, which is often overlooked in the literature. Uncertainties arising from the assumptions involved in the heat conduction model and from the accuracy level of the apparatus used to measure the experimental variables, are studied in detail. The classic 3ω experimental setup as well as the sample preparation method are detailed. Then, the thickness-dependent thermal conductivity measurements, performed by the 3ω method on AlN monolayer and multilayer systems, are described. To conclude, the design, development and implementation of the experimental setup used to perform strain-dependent thermal conductivity measurements are discussed.

3.1 Challenges and practical considerations

Accurate experimental determination of the thermal conductivity of thin films is essential for ensuring performance of nano-scale devices. Since the late 1980s, the scientific community, motivated by its great technological interest, has devoted tremendous efforts into the development of experimental techniques that provide precise thermal conductivity measurements of two-dimensional structures.

Despite the important advances achieved in the past thirty years, thermal conductivity measurements on these structures remain a highly challenging task, due to the small heat fluxes that have to be detected and the reduced characteristic dimensions of the structures under analysis (Tong (2011)).

Thin films are usually deposited onto a thicker bulk substrate, which serves as the mechanical support structure. Since releasing them from the substrate surface is often difficult and costly, thermal measurements are frequently performed on film-on-substrate systems. The substrate contribution has to be therefore subtracted from the measured properties of the film-on-substrate configuration, which can increase experimental uncertainties. Figure 3.1 represents the typical experimental setup used in cross plane thermal conductivity measurements, along with the associated experimental challenges for film-on substrate configurations.

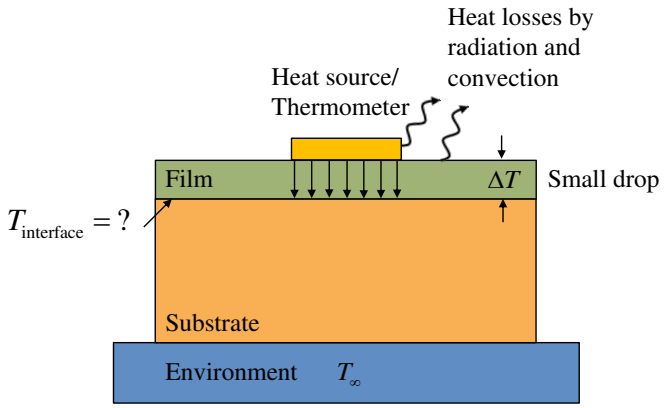

Figure 3.1: *Typical experimental setup for thermal measurement on thin films and associated experimental challenges. Adapted from Borca-Tasciuc and Chen (2004).*

To extract the thermal conductivity of the studied film, experimental techniques typically require the determination of heat flux and/or temperature difference between two points of the specimen under analysis. For low-dimensional systems, the principal challenge is to create a heat flux through the film which is sufficiently high to be detected, without inducing a large temperature rise in the substrate. The second issue is to experimentally measure the small temperature drop across the sample thickness, which can vary from a few nanometers to several microns (Borca-Tasciuc and Chen (2004)).

Thermal conductivity characterization methods can be performed either by steady-state or transient techniques. Steady state experiments, which are performed when the studied system reaches the thermal equilibrium, encounter significant problems related to the parasitic substrate heat flow (large temperature rise in the substrate), and radiation and convection losses that introduce errors in the measurement. If the thermal resistance of the substrate is dominant in the total thermal resistance of the experiment, the temperature difference through the substrate will be considerably higher than the one across the film. Subtracting the substrate contribution to the overall temperature rise will therefore increase the experimental uncertainty. Moreover, since the thermal excitation in DC experiments is continuous, the thermal response is also

sensitive to the boundary conditions between the substrate and the environment. Because such contact resistances are generally not negligible and poorly controlled, they complicate the thermal analysis (Dames (2013)). On the other hand, at room temperature or above, radiation and convection losses from the sample surface will be dominant in the heat transfer if the thermal resistance of the substrate is higher than the one of the measured film, increasing the experimental uncertainties.

Conversely, in transient techniques, the thermal response is studied as a function of time. Transient methods overcome the above-mentioned problems by using alternative heating, which combined with the reduced characteristic length of the experimental geometry, allows us to analyze a very small volume of the sample, confining the heat wave inside the film-on-substrate system.

Known examples of time dependent techniques are the 3ω method and time domain thermoreflectance (TDTR), which have been introduced by Cahill and coworkers in 1987 and 2002 respectively (Cahill and Pohl (1987), Cahill et al. (2002)). These techniques are in continuous evolution, constantly undergoing multiple improvements. They are advantageous compared to the steady-state techniques mainly because they do not require long equilibration times, leading to much faster measurements, and are weakly sensitive to errors induced by radiation and convection losses. In this work, cross plane thermal conductivity measurements were performed by the 3ω method. This frequency domain method was first introduced to measure the thermal conductivity of bulk amorphous solids of low thermal conductivity at high temperatures, and then extended to low dimensional 2D structures, such as thin films and superlattices (Cahill (1990), Lee and Cahill (1997)).

3.2 Fundamentals of the 3ω method

The 3ω method is an electrothermal technique that allows for the experimental determination of the thermal conductivity of a specimen.

The experiments are performed by inducing harmonic Joule heating in a electrical conductive strip, deposited onto the surface of the studied sample. The narrow metal wire is patterned by typical microfabrication techniques, such as photolithography and etching, or metal evaporation through a shadow mask. The metallic strip acts simultaneously as a heater and a measuring probe due to its temperature dependent electrical resistance.

An alternating electric current (AC) with an angular modulation frequency $\omega = 2\pi f$, is applied through the metal strip, inducing a temperature oscillation at a doubled frequency 2ω, which amplitude and phase depends on the thermal properties of the underlying matter. The temperature rise caused by the diffusion of the thermal wave within the system affects the electrical resistance of

the heater, producing a resistance oscillation at a frequency 2ω that is proportional to the AC temperature rise. This resistance oscillation, multiplied by the heating current $I(\omega)$, results in a voltage drop along the strip, which contains a third harmonic component that can then be measured by a signal processing lock-in amplifier.

The measured 3ω voltage is directly related to the thermal wave amplitude, that is then compared to a thermal model depending on the excitation frequency to obtain the effective thermal conductivity of the underlying material. Thus, the 3ω method requires the measured value of the thermal wave amplitude expressed in terms of the first and the third harmonic of the measured voltage. Then, to relate the measured quantities with the thermal properties of the specimen, an analytical solution of the thermal wave amplitude as a function of the thermal conductivity of the specimen under analysis has to be found.

The following subsections describe this process in details, giving the basis for the thermal measurements performed in this work. First, an expression for thermal wave amplitude as a function of the experimental variables is obtained in subsection 3.2.1. Then, data reduction is performed by finding an analytical solution to the temperature oscillation, in the case of an infinitively narrow heater deposited onto a semi-infinite isotropic substrate. The analysis is extended by considering a heater of finite width, as is the case in 3ω experiments (subsection 3.2.2.1). To finish with, in subsection 3.2.2.2, an analytical expression of the thermal wave amplitude induced by a thin film deposited onto a substrate is given, and the classical and differential approaches are described. This part of the dissertation is a detailed review of the data reduction proposed by Cahill and coworkers for the 3ω method, compiling the whole derivation of the experimental thermal conductivity for bulk materials and thin films, which is scattered into several papers in the literature (Cahill and Pohl (1987), Cahill (1989), Cahill (1990), Cahill et al. (1994), Cahill (2002),Borca-Tasciuc and Chen (2004)).

3.2.1 Experimental determination of the temperature wave amplitude

Figure 3.2 shows the typical electrical conductive wire used in 3ω experiments. In general, a metallic layer is directly deposited onto the surface of the specimen, usually by sputtering or evaporation. To improve adhesion of the metallic layer to the sample, an additional film may be required.

The choice of the thermometer material relies on the temperature coefficient of resistivity α, that describes the characteristic change of electrical resistance R_e as a function of temperature T. The coefficient α is defined by:

$$\alpha = \frac{1}{R_{e_0}} \frac{dR_e(T)}{dT} \tag{3.1}$$

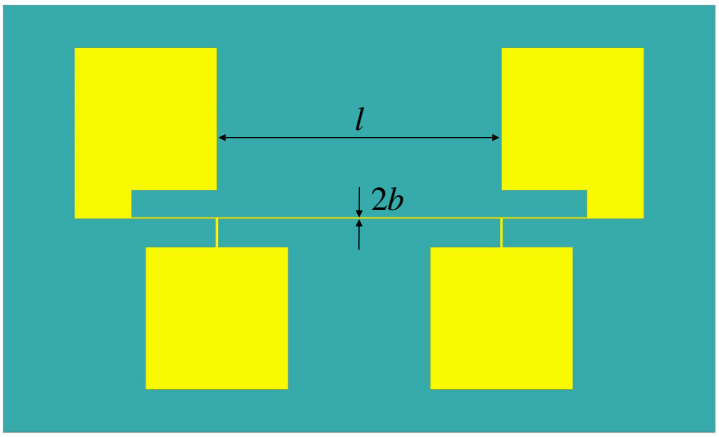

Figure 3.2: *Typical geometry of the electrical conductive strip used in the 3 ω experiments.*

where R_{e_0} is the value of the electrical resistance at a reference temperature T_0. Materials such as gold (Au), platinum (Pt), Aluminum (Al) and silver (Ag) are the most commonly used due to their values of α, which are large enough to produce a measurable 3ω signal (Jacquot (2003)). The deposited metallic layer is then microfrabricated to obtain the four rectangular pads connected by pins to the narrow heating wire. The outer two pads serve to apply the AC electrical current that generates the joule heating. The inner two pads allow for measuring the voltage oscillation across the metal strip, which contains the third harmonic component. The width of the heating line is defined as $2b$ and the length as l, the latter being determined by the distance between the outer pads. In the experiments, a sinusoidal electrical current is applied through the resistive strip:

$$I(t) = I_0 \sin(\omega t) \tag{3.2}$$

where I_0 is the amplitude of the signal. By Joule effect, the dissipated power in the wire is:

$$P = I^2 R_e = \frac{I_0^2 R_e}{2} \left[1 - \cos\left(2\omega t\right)\right] \tag{3.3}$$

Then, the dissipated power in the wire is a sum of a DC component and the heat generated at a frequency 2ω. Equation 3.3 can thus be expressed as a sum of a steady-state term and a sinusoidal component as follows:

$$P = P_{DC} + P_{2\omega} \cos(2wt) \tag{3.4}$$

The power loss generates a temperature fluctuation of amplitude ΔT_{2w} that diffuses through the specimen at the same frequency. Since the electrical resistance of the wire is proportional to the temperature, the heater temperature

rise caused by the underlying material imparts a second harmonic fluctuation in R_e, generally shifted by an angle φ. Equation 3.1, can then be rewritten as:

$$R_e = R_{e_0}\left[1 + \alpha \Delta T_{2w} \cos(2wt + \varphi)\right] \tag{3.5}$$

By applying the Ohm's law, the heater resistance fluctuation at $2w$ results in a voltage oscillation of the form:

$$\begin{aligned} V &= R_e I \\ &= V_0 \sin(\omega t) + \frac{1}{2} V_0 \alpha \Delta T_{2w} \left[\sin(3\omega t + \varphi) - \sin(\omega t - \varphi)\right] \\ &= V_0 \sin(\omega t + \Gamma) + \frac{1}{2} V_0 \alpha \Delta T_{2\omega} \sin(3\omega t + \varphi) \end{aligned} \tag{3.6}$$

where $V_0 = I_0 R_{e_0}$. The ω and the 3ω components of the heater voltage response can be identified in the last line of Eq.3.6. The fist term is typically three orders of magnitude greater than the 3ω component, and is somewhat more difficult to exploit in thermal measurements because it only contains information about the imaginary part of the thermal fluctuation. On the other hand, the second term is proportional to the real and the imaginary part of the temperature oscillation (Dames and Chen (2005),Cahill (1990)), providing a good alternative to directly measure the thermal transfer function of the studied sample in the frequency domain. Since the third harmonic response of the voltage is a very small quantity, the lock-in technique is required to extract the signal. The thermal fluctuation can therefore be obtained from the 3ω component (Eq.3.6) in terms of root mean square quantities (RMS), as usually measured by lock-in amplifiers.

$$\Delta T_{2\omega} = \frac{2}{\alpha} \frac{V_{3\omega,RMS}}{V_{0,RMS}} \tag{3.7}$$

Since in a typical 3ω experiment, $V_{1\omega}$ is at least one thousand times greater than $V_{3\omega}$, the input voltage signal V_0 can be approximated as the first harmonic voltage response $V_{1\omega}$ ($V_0 \approx V_{1\omega}$) and Eq.3.7 becomes:

$$\Delta T_{2\omega} = \frac{2}{\alpha} \frac{V_{3\omega,RMS}}{V_{1\omega,RMS}} \tag{3.8}$$

This relation provides a direct experimental measurement of the thermal wave amplitude. The thermal properties of the specimen under analysis can then be obtained by fitting the measured amplitude of the thermal oscillation to an appropriate analytical model of heat conduction.

The next subsections discuss in details the derivation of the solution to the transient heat conduction equation for a finite width line heater, deposited onto the surface of a film-on substrate system. The heat conduction equation will be solved to determine the temperature rise of the heater $\Delta T_{2\omega}$, which will then be used to find an interrelation with the thermal conductivity of the

analyzed sample. For this purpose, we consider first a simplified geometry, i.e., a one-dimensional line source of heat. Then, the effect of the finite width of the heater will be integrated in the model, allowing for the thermal analysis for bulk materials and thin films.

3.2.2 Analytical solution of the thermal wave amplitude

3.2.2.1 Substrate thermal conductivity measurements

Cahill and Pohl (1987) derived an approximate solution for the AC temperature rise of a heater deposited on an isotropic semi-infinite substrate. To do this, a heater of width much smaller than the wavelength of the diffusive thermal wave was used. This particular geometry leads to a cylindrical heat flow pattern through the studied volume, with the temperature gradients in the radial direction. The theoretical background used to determine the temperature rise of the heater, which allows for the direct determination of the thermal conductivity, will be described in this subsection.

- **Case of an infinitively narrow heater on a semi-infinite isotropic substrate.**

It is convenient to begin the analysis with a simplified geometry, consisting of a one-dimensional line source of heat (Fig.3.3).

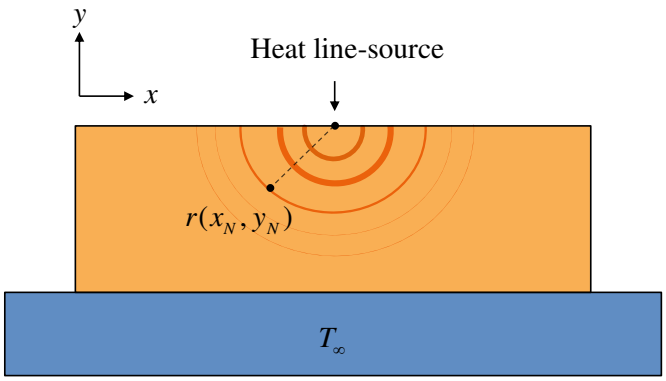

Figure 3.3: *Cylindrical heat pattern generated by a infinitely narrow heater.*

An analytical solution of the heat conduction equation, considering an infinitely narrow line source of heat at the surface of a semi-infinite volume, was first obtained by Carslaw and Jaeger (1959). The expression for the real part of the thermal wave amplitude at a distance $r = (x^2+y^2)^{1/2}$ from the line heat source is:

$$\Delta T_{2\omega} = \mathbb{R}\left[\frac{P_l}{\pi k} K_0(qr)\, \mathrm{e}^{i2\omega t}\right] \tag{3.9}$$

being P_l the power per unit of length generated by the current applied through the strip, k the thermal conductivity of the specimen, K_0 the zeroth order modified Bessel function of the second kind, with argument qr, and $q = (1+i)(2\omega\rho c_p/k)$. The quantity $\lambda = |1/q|$ refers to the penetration depth at which the thermal fluctuation propagates into the sample during one cycle of the AC power heating. Therefore, the penetration depth of the thermal oscillation is given by:

$$\lambda = \left|\frac{1}{q}\right| = \sqrt{\frac{D}{2\omega}} = \sqrt{\frac{k}{2\rho c_p \omega}} \tag{3.10}$$

where D is the thermal diffusivity, ρ is the density and c_p the specific heat capacity.

The exact solution of the thermal wave amplitude (Eq.3.9) is derived considering that the substrate is a semi-infinite isotropic medium, and assuming zero heat flux through the sample surface. Equation 3.9 is also based on the assumptions that the strip thermal mass can be neglected i.e, the heater behaves as an infinitely good thermal conductor with negligible thickness and heat capacity. Additionally, it is considered that the strip is a uniform line source of heat of infinite length in intimate contact with the underneath studied sample, assuming negligible thermal boundary resistance between the heater and the underlaying material.

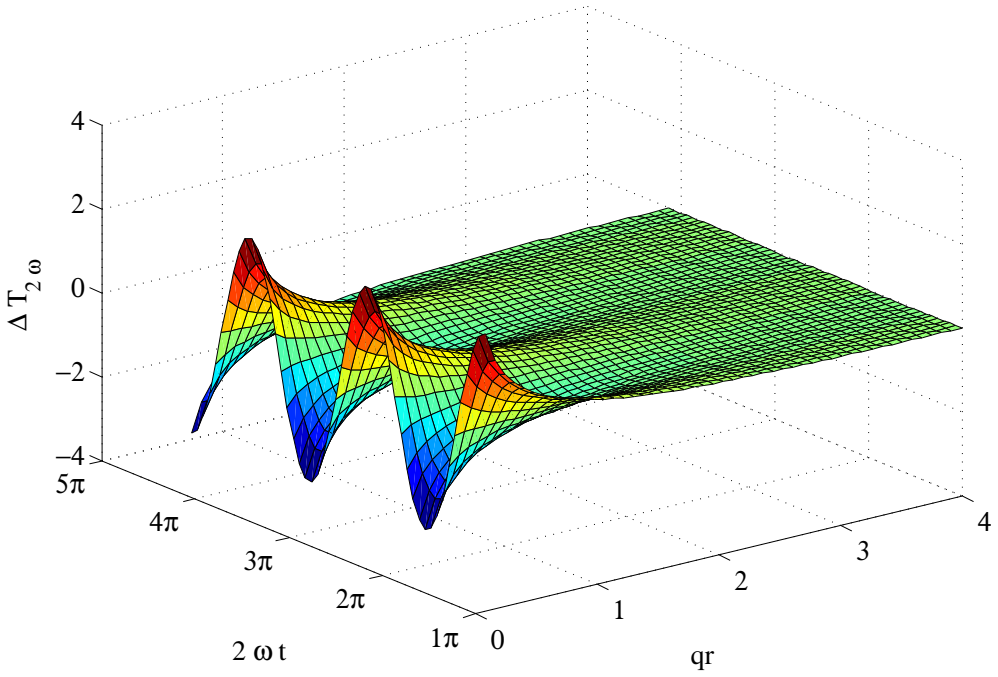

Figure 3.4: *Time evolution of the real part of the thermal wave amplitude at a distance r from an infinitely narrow heater.*

Figure 3.4 shows the time evolution of the real part of the temperature fluctuation as a function of r. Following the zeroth order Bessel function of the second kind, the thermal wave decays rapidly as a function of the distance r away from the heater. By this means, the use of an alternating current allows us to analyze a very small volume of the sample and to be weakly sensitive to heat loss by convection and radiation due to the confinement of the heat wave inside the sample, and to the rapid decay of the temperature oscillations compared to the characteristic radiative times.

To avoid parasitic edge effects in the measurements, the length l of the metallic strip used in the experiments must be very long, such that $l \gg 2b$, and the width $2b$ must be constant all along the heating line. Taking into consideration the semi-infinite medium assumption, equation 3.7 is valid if the distance traveled by the heat wave is smaller than the thickness of the studied sample, such that $d_s \gg \lambda_s$, where the subscript s refers to substrate. Quantitative analysis carried out by Borca-Tasciuc et al. (2001) suggested $d_s/\lambda_s > 5$ to keep errors under 1%, as the amplitude of the thermal fluctuation decays to 1% of its value after 5 thermal wavelengths. However, numerical simulations performed by Jacquot et al. (2002) showed that even a ratio of $d_s/\lambda_s > 2$ appears to be a good approximation (Dames (2013)). Further discussion on the validity range of the above described assumptions, and the methods developed to minimize the effect of these approximations in the uncertainty of the measurements is provided in detail in section 3.3.

- **Case of a heater of finite width**

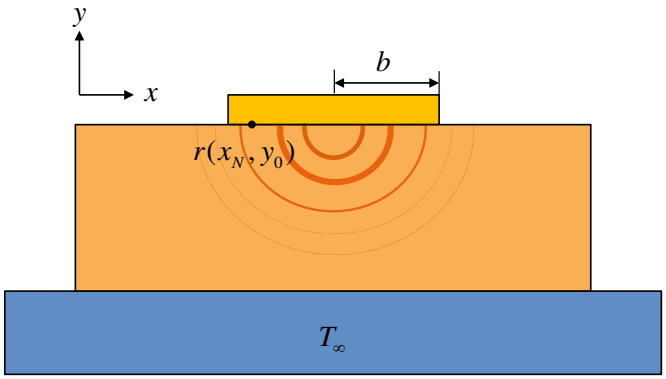

Figure 3.5: *Cylindrical heat pattern from a metallic strip of finite width* $2b$.

The effect of the heater finite width can be included in the model by adding a infinite number of 1D line heaters sources over the whole width $2b$ (Cahill (1990)), which involves a convolution integral. As observed in Fig.3.4, the temperature fluctuation is an *even* function in the time-domain. It is then

convenient to use the cosine Fourier transform with respect to the x coordinate. Considering only the thermal fluctuation at the surface of the sample ($y = 0$) (Cahill (1990)), the Fourier transform in the wavenumber domain η of a zeroth order Bessel function of the second kind K_0, is given by (Bateman et al. (1954)):

$$\Delta T_{2\omega}(\eta) = \frac{P_l}{2k}\frac{1}{\sqrt{\eta^2 + q^2}} \tag{3.11}$$

Since the heat in the metal strip follows as well an *even* behavior over the width, the thermal wave amplitude for a finite width heater can be obtained by the product of Eq.3.11 with the Fourier transform of the heat source in the $x-$space, which in this case can be expressed as a rectangular pulse $rect(x)$ (Koninck and Vengallatore (2008)):

$$\Delta T_{2\omega}(\eta) = \frac{P_l}{2k}\frac{1}{\sqrt{\eta^2 + q^2}}\int_0^\infty rect(x)\cos(\eta x)dx = \frac{P_l}{2k}\frac{\sin(\eta b)}{\eta b\sqrt{\eta^2 + q^2}} \tag{3.12}$$

Taking the inverse transform of Eq.3.12 to switch $\Delta T_{2\omega}$ back to the space domain gives:

$$\Delta T_{2\omega}(x) = \frac{P_l}{\pi k}\int_0^\infty \frac{\sin(\eta b)\cos(\eta x)}{\eta b\sqrt{\eta^2 + q^2}}d\eta \tag{3.13}$$

Since the temperature measurements are performed over the width of the strip, the magnitude of the thermal wave $\Delta T_{2\omega}$ is an averaging across the metal line. Thus, the average temperature rise in the heater can be obtained by integrating Eq.3.13 in the space domain from 0 to b and dividing by $2b$:

$$\Delta T_{2\omega}|_{avg} = \frac{1}{2b}\int_{-b}^{b} T_{2\omega}(x)dx = \frac{P_l}{\pi k}\int_0^\infty \frac{\sin^2(\eta b)}{(\eta b)^2\sqrt{\eta^2 + q^2}}d\eta \tag{3.14}$$

The integral in Eq.3.14 has no direct analytical closed form. To obtain an approximate solution, Cahill (1990) proposed to analyze its limit when the thermal penetration depth is much larger than the strip half width ($\lambda \gg b$). In this case, the wavenumber of the thermal fluctuation is defined over a domain such that $1/\lambda < \eta < 1/b$. Then, the upper limit of the integral in Eq.3.14 can be replaced by $1/b$. Additionally, $\sin(\eta b)/\eta b$ can be evaluated at the limit where b tends towards 0:

$$\lim_{b\to 0}\frac{\sin(\eta b)}{\eta b} = 1 \tag{3.15}$$

The approximated solution to Eq.3.14 is then:

$$\begin{aligned}\Delta T_{2\omega}|_{avg} &\approx \frac{P_l}{\pi k}\left[\ln\left(\frac{1}{bq}+\sqrt{\frac{1}{(bq)^2}+1}\right)\right] \\ &\approx \frac{P_l}{\pi k}\left[-\ln(bq)+\gamma\right] \end{aligned} \tag{3.16}$$

where γ is a constant close to 0.923, often adjusted to fit the experimental data. As $q=(1+i)(2\omega\rho c_p/k)^{1/2}$, in terms of frequency, Eq.3.16 reads :

$$\Delta T_{2\omega}|_{avg} \approx \frac{P_l}{\pi k}\left[-\frac{1}{2}\ln(2\omega)+\frac{1}{2}\ln\left(\frac{k}{\rho c_p b^2}\right)+\gamma\right]-i\frac{P_l}{4k} \tag{3.17}$$

Equation 3.17 indicates that the thermal conductivity of an isotropic substrate can be determined from the slope of the in-phase magnitude of the measured $\Delta T_{2\omega}|_{avg}$ (real part of the thermal oscillation) as a function of the logarithm of frequency:

$$k \approx \frac{P_l}{2\pi}\left[\frac{d}{d\ln(2\omega)}\left(\Delta T_{2\omega}|_{avg}\right)\right]^{-1} \tag{3.18}$$

Direct derivation of k is also possible from the imaginary part of the heat wave (out-of-phase oscillation). However Cahill (1990) has found experimentally that Eq.3.18 is more reliable. This approach is known as the slope method. It is advantageous compared to other transient techniques, because it does not require independent measurements of the thermal diffusivity or the volumetric heat capacity (Koninck and Vengallatore (2008)).

3.2.2.2 Film-on-substrate measurements

Probably one of the most interesting aspects of the 3ω technique is its capability of measuring the thermal conductivity of thin films deposited onto a substrate. Today, this approach is widely used and is considered as one of the most effective experimental methods for thermal characterization of low dimensional 2D structures. Two different methods can be used to achieve thin film thermal conductivity measurements: The classical and the differential 3ω. Both will be described in the following paragraphs.

- **Classical method**

Since nanocrystalline thin films generally exhibit an anisotropic and heterogeneous structure, their thermal properties are direction-dependent. The experimental technique proposed by Cahill et al. (1994), which is an extension of the "slope method", provides an approach to perform cross-plane and in-plane thermal conductivity measurements on thin films. It is based on the fact that using a metal strip which is larger compared to the film thickness L ($2b \gg L$), will lead to a one dimensional heat flux in the direction normal to the film

surface (Fig.3.6a). This behavior can be approximated as a one-dimensional heat conduction model. On the other hand, working with a very narrow heater will result in a divergent heat pattern that spreads along the in-plane direction (Fig.3.6b). In this case, the strip is sensitive to both the cross-plane and the in-plane thermal conductivity components, and the behavior can be approximated as a two-dimensional heat conduction model. It is noteworthy that the discussion rather focuses on cross-plane thermal conductivity measurements, as no in-plane measurements were performed in this work.

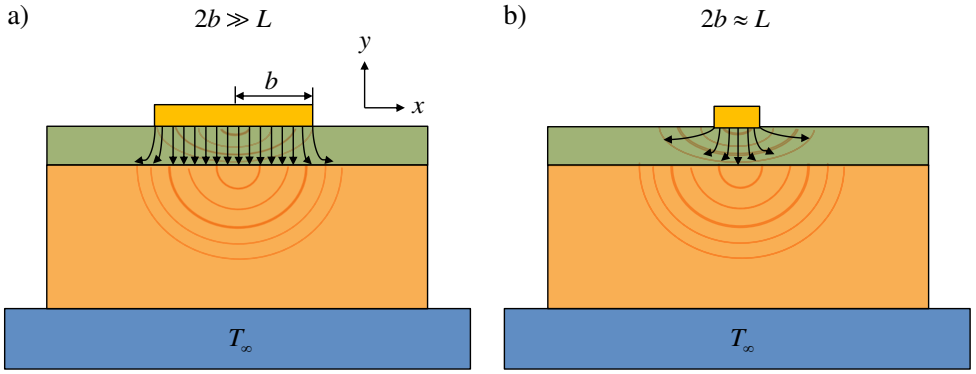

Figure 3.6: *Heat flux produced by (a) a heater much larger than the film thickness $2b \gg L$ (one-dimensional heat conduction) and (b) a narrower heater of width comparable to the film thickness $2b \approx L$ (two dimensional heat conduction).*

In the case of a film with a thermal conductivity k_{eff} much smaller than the one of the substrate k_s, the film-on-substrate system behaves as a series of thermal resistances. Therefore, the studied film contributes to the temperature rise measured along the heater by adding a frequency-independent temperature oscillation. Considering that the power per unit area transfered from the heater is constant in the y direction ($Q = P_l/2b$), the temperature drop across the film can be simply obtained by the Fourier's law:

$$\Delta T_f = \int_0^L \frac{Q}{k_f} dy = \frac{P_l L}{2bk_{eff}} \tag{3.19}$$

where k_{eff} is the effective cross plane thermal conductivity of the studied film. k_{eff} is called "effective" because it does not only comprise the thermal resistance due to the film but also contains the contribution of the thermal boundary resistance between the layer and the substrate.

The increase in the amplitude of the thermal fluctuation due to the thin film can be therefore written as follows:

$$\Delta T_{2\omega}|_{avg} = \Delta T_f + \Delta T_s \tag{3.20}$$

Where the subscripts f and s correspond to the film and the substrate, respectively. In consequence, the thermal conductivity of the film can be obtained by subtracting the calculated temperature rise of the bare substrate from the experimentally measured temperature rise of the strip, caused by the film-on-substrate system (Borca-Tasciuc et al. (2001)).

$$k_{eff} = \frac{P_l L}{2b(\Delta T_{2\omega}|_{avg} - \Delta T_s)} \tag{3.21}$$

Equation 3.21 allows for the direct measurement of the thermal conductivity of the studied film. It is relevant to mention that if the film of interest is electrically conductive, the heater has to be necessarily isolated by a dielectric layer. In this case, a thin silicon oxide film is usually deposited onto the sample surface before deposition of the heater material.

- **Differential method**

The differential 3ω technique is a further extension of the above discussed methods. It is particularly useful for analyzing complex systems composed of several films (involving nucleation or buffer layers), because it allows for the determination of the thermal conductivity of a specific film in the ensemble. In such systems, the voltage drop across the metal strip depends on the temperature rise caused by the whole ensemble of films deposited one on the top of the other. The measured thermal transfer function is therefore the sum of the contributions of the thermal oscillations coming from the different components of the system.

To isolate the signal drop exclusively caused by the film of interest, the differential approach uses the average temperature rise difference measured between two similar sets of experiments, one involving the specimen and another performed on a system without the studied film, which serves as the reference sample.

By removing the signal of the reference sample from that of the specimen with the studied layer, it is possible to subtract the common background contribution of the parasitic interfacial thermal resistances, such as the one between the heater and the underlaying film, and the one between the substrate and the first deposited layer (Dames (2013)). In the same way, the contribution of additional elements, such as buffer or nucleation layers, can also be subtracted from the total experiment temperature rise, which is obtained at comparable power inputs by similar heaters deposited on the specimen and the reference structure. Under this condition, the effective thermal conductivity of the film is given by (Borca-Tasciuc, Kumar, and Chen (2001)):

$$k_{eff} = \frac{L}{2}\left[\left(\frac{2V_{3\omega}b}{P_l \alpha V_{1\omega}}\right)_{R+F} - \left(\frac{2V_{3\omega}b}{P_l \alpha V_{1\omega}}\right)_{R}\right]^{-1}_{avg} \tag{3.22}$$

The subscripts $R+F$ and R correspond to the specimen with the studied film and the reference structure, respectively.
Although the differential 3ω method requires two sets of measurements, a detailed study performed by Borca-Tasciuc et al. (2001), showed that it is advantageous compared to the slope-method because it can reduce the uncertainty in the determination of the thermal conductivity of the film of interest. The value of k_{eff} obtained from Eq.3.22 is insensitive to the substrate thermal conductivity, and the contributions from any additional layers is nearly eliminated by the measurement on the reference sample. Because of the mentioned advantages, the differential techniques was used to perform the thickness-dependent experiments in this work.

3.3 Experimental uncertainty analysis

The main sources of experimental uncertainty in the 3ω measurements arise either from the fundamental assumptions used in the heat conduction model that are incorporated in the measurement procedure, or from the limited accuracy of the apparatus used to measure the variables which are then employed to calculate the thermal conductivity k_{eff}.

3.3.1 Contribution from the assumptions involved in the heat conduction model

Table 3.1 summarizes the main approximations described in the above sections which are involved in the one-dimensional conduction model used to obtain the thermal conductivity of thin films in this work. The experimental design criteria employed to keep measurement errors under 1% and to perform experiments well within the validity range of the assumptions are also discussed.

3.3.1.1 The heater

- **The line-source assumption**

Equation 3.14 is obtained under the assumption that the metal strip is a uniform line source of heat ($\lambda_s \gg b$). Borca-Tasciuc et al. (2001) showed that the line source hypothesis is appropriate when the ratio between the distance traveled by the heat wave inside the substrate and the half width of the strip is $\lambda_s/b > 5$. Experiments in this work were performed using silicon as the bare substrate. Thus, considering the typical values (Hull (1999)) of the specific heat capacity ($c_p = 711$ J/kg$\cdot$K), the density ($\rho = 2330$ kg/ m^3) and the thermal conductivity of Si (147 W/m$\cdot$K), the thermal oscillation propagates at a distance λ_s from 266 to 84 µm inside the prepared samples, at a frequency range varying from 100 to 1000 Hz, respectively. In our experiments, the ratio between the wave penetration depth and the half width of the heater ($b \approx 5$ µm) therefore extends from 16.8 to 53.1. Since these values are greater than 5, it is convenient to use the line source approximation.

Table 3.1: *Fundamental assumptions used in the heat conduction model of the 3ω experiments, experimental design criteria to achieve measurement errors of 1% (from Dames (2013)), and ranges of the measurements performed in this work to obtain reasonable accuracy in thermal measurements.*

	Assumption	**Design criteria** [a] (For 1% Error)	**In this work**
Heater	Line source ($b \to 0$)	$\lambda_s/b > 5$	$b = 5$ µm, $k_s = 147$ W/m·K For $\omega = 100 \quad 1000$ Hz, $\lambda_s \approx 266 \quad 84$ µm $\to \lambda_s/b = 53.1 \quad 16.8$
	Uniform heat source	$2b \approx 10$µm	Edge effects are negligible
	Infinitely long negligible edge effects ($l \to \infty$)	$l/\lambda_s > 4.7$	$l = 4000$ µm For $\omega = 100 \quad 1000$ Hz, $\to l/\lambda_s = 15.05 \quad 47.6$
	Negligible thermal mass infinite thermal conductivity ($k_h = \infty$) negligible heat capacity ($c_{p_h} = 0$) negligible thickness ($d_h = 0$)	High k_h $\lambda_f > L \gg d_h$	$k_h \approx 200$ W/m·K $L \approx 270 \quad 1500$ nm $d_h \approx 250$ nm Errors are small for thicker films but greater for thinner films
	Negligible thermal boundary resistance between the heater and the sample ($R_h = 0$)	Small R_h	$R_h \approx 10^{-8}$m^{2}K/W, Clean interface
Substrate	Isothermal ($k_s \to \infty$)	$(k_{eff}/k_s)^2 < 0.01$	$(k_{eff}/k_s)^2 = 0.0005 \quad 0.002$
	Semi infinite ($d_s \gg \lambda_s$)	($d_s/\lambda_s > 2$)	$d_s = 550$µm For $\omega = 100 \quad 1000$Hz, $\to d_s/\lambda_s = 2.07 \quad 6.5$ [b] Smaller d_s/λ_s for differential 3ω
Heat flow	Quasi static through the film	$\lambda_f/L > 5.7$	$\lambda_f/L = 132.1 \quad 12.5$ For $\omega = 100 \quad 1000$ Hz
	One dimensional across the film neglect edge effects ($2b \gg L$)	$(L/b)(k_{eff_{yx}})^{1/2} > 5.5$ [c]	Assuming a normalized k_{eff_x} $(L/b)(k_{eff})^{1/2} = 32 \quad 9.8$
	zero through the sample surface negligible radiation negligible convection	Small characteristic length of the experimental geometry	Rapid decay of the heat wave and confinement inside the sample

[a] Dames (2013)

[b] For frequencies smaller than 100Hz, the distance traveled by the thermal wave become comparable to the substrate thickness, introducing errors due to the poorly controlled thermal resistance between the specimen and the environment (T_∞). However, smaller d_s/λ_s are tolerable for the differential 3ω method (Dames (2013))

[c] For 5 % error.

- **The uniform heat source assumption (Heater length to neglect end-effects)**

Uniform heat generation within the metal strip is also considered in the analytical model. This assumption clearly breaks down near the edges of the heater. At $x = \pm b$, the heat flux approaches infinity because of the sharp edge between the heater line and the underlying specimen. However, the total heat flow, which is an integral of the heat flux along the heater width, is bounded. Since this is a well known mathematical singularity that does not cause significant errors in temperature predictions, the use of the uniform heat flux approximation is tolerable (Gurrum et al. (2008), Hui and Tan (1997)).

- **The negligible thermal mass consideration**

In the derivation of the sample thermal conductivity, the thermal mass of the heater is also neglected. This approximation requires a heater line with very high thermal conductivity compared to that of the film and the substrate. Langer et al. (1997) reported that a 250 nm thick film of gold has a thermal conductivity of about 200 $W/m \cdot K$. Compared to the thermal conductivity of silicon (147 $W/m \cdot K$) and aluminum nitride thin films (1 50 $W/m \cdot K$), the assumption of the heater as an infinitely good thermal conductor is fairly acceptable. To neglect the specific heat capacity and the thickness of the heater line, Borca-Tasciuc et al. (2001) and Dames (2013) reported that the film thickness L must be smaller than the wave penetration depth inside the film λ_f and much greater than the metal strip thickness d_h. In this work, the thickness of the studied films varies from about 270 to 1500 nm and the penetration depth inside the film from 57.8 to 11.2 µm in a frequency range which extends from 100 to 1000 Hz. Here, λ_f is obtained considering the typical values of the specific heat capacity ($c_p = 600$ J/kgK) and the density ($\rho = 3280$ kg/ m^3) of AlN (Morkoc (2009)). Errors should therefore be negligible for films that are much thicker than the heater ($L = 640$ 1460 nm) but significantly higher for the thinner films.

- **The negligible thermal boundary resistance R_h between the heater and the underlying film**

In the 3ω formulation, the thermal resistance between the heater and the specimen was assumed to be negligible. The validity of this consideration relies in the ability to fabricate metallic strips that are in intimate thermal contact with the specimen surface. The process described in section 3.5 ensures a clean heater-sample interface. Additionally, since the differential 3ω method was predominantly used for the experiments, the effect of the negligible thermal resistance R_h is nearly eliminated.

3.3.1.2 The substrate

Regarding the substrate, the main assumptions involved in the heat conduction models are that it is isothermal ($k_s \to \infty$) and semi-infinite ($d_s \gg \lambda_s$).

- **The substrate is an isothermal medium**

The sensitivity of the 3ω method relies in the ability to create a temperature drop across the studied film that is sufficiently high to be detected, without inducing a significant temperature rise in the substrate. This requires the film's thermal conductivity to be much smaller than the one of the substrate. The effect of the thermal conductivity contrast between the film and the substrate was considered analytically by Borca-Tasciuc et al. (2001), who reported that the squared ratio between the thermal conductivity of the film k_{eff} and the substrate k_s should be smaller than 0.001 in order to keep errors below 1%. In our experiments, the thermal conductivity of the films are well below 15 W/m·K. Thus, the ratio $(k_{eff}/k_s)^2$ varies from 0.0005 to 0.002, ensuring the appropriate conditions for highly sensitive 3ω measurements.

- **The substrate is a semi-infinite medium**

The hypothesis of the semi-infinite size of the sample was studied numerically by Jacquot et al. (2002). Their results suggest that the ratio between the substrate thickness d_s and the wave penetration depth inside the substrate λ_s should be greater than 2. The samples studied in this work were deposited onto 550 µm thick silicon substrates. Considering a frequency range between 100 and 1000 Hz, the corresponding d_s/λ_s varies from 2.07 to 6.54. The ratio $d_s/\lambda_s > 2$ for frequencies higher than 100 Hz, suggesting that experiments must begin from this critical value of frequency in order to perform the measurements well within the linear regime. For smaller frequencies, the distance traveled by the thermal oscillation becomes comparable to the substrate thickness, inducing errors due to the poorly controlled thermal resistance between the specimen and the environment.

3.3.1.3 The heat flow

- **The quasi-static heat flow assumption**

Standard analysis considers that the heat capacity of the studied film is negligible, which is valid for a ratio between the penetration depth inside the film λ_f and the film thickness L greater than 5.7, as suggested by Jacquot et al. (2002). In this work, λ_f/L extends from 12.5 to 132.1, being well within the validity range of the quasi-static heat conduction approximation.

- **One-dimensional heat flow across the film**

Another important condition required to use the one dimensional heat conduction model is that heater width must be much larger than the film thickness in order to minimize the heat flow edge effects. However, the heat spreading along the in-plane direction is not only due to the aspect ratio between heater width and film thickness, but also to the film anisotropy. Borca-Tasciuc et al. (2001) have considered analytically the effect of the heat spreading inside the film for a uniform heat source. The results show that the heat flow can be considered one-dimensional in the direction normal to the film surface, if $(L/b)(k_{eff_{yx}})^{1/2} > 5.5$, which involves errors below 5%. Here, $k_{eff_{yx}}$ is the ratio between the film thermal conductivity in the cross-plane k_{eff_y} and in the in-plane k_{eff_x}. Since k_{eff_x} is typically much smaller than k_{eff_y} for columnar films, and considering that no reported values on the in-plane thermal conductivity of AlN films deposited onto a silicon substrate are available in the literature yet, a normalized value of k_{eff_x} was assumed. Hence, $(L/b)(k_{eff_{yx}})^{1/2}$ varies from 9.8 to 32.8, which is in the validity range of the one-dimensional heat flow assumption.

- **Negligible heat losses by radiation and convection through the sample surface**

Regarding the zero heat flow through the sample surface, the use of an alternating current and the reduced characteristic length of the experimental geometry allow for analyzing a very small volume of the sample and being weakly sensitive to heat lost by convection and radiation due to the confinement of the heat wave inside the sample and to the rapid decay of the temperature oscillations compared to the characteristic radiative times (Cahill (1990)).

3.3.2 Contribution from the accuracy level of the measurement apparatus

To estimate the thermal conductivity, the 3ω method makes use of several experimental variables that are individually measured by various apparatus, which in turn posses a limited accuracy. When mathematical operations are performed on these measured quantities to extract the thermal conductivity of the studied specimen, the uncertainties due to the accuracy limitations of the measurement equipment propagates, affecting the final result.

Kline and McClintock (1953), who laid the very foundations of uncertainty analysis, stated that for a given function F, defined in terms of the uncorrelated variables $\{x, y, z, ...\}$ by a general expression $f(x, y, z, ...)$, the contribution of the uncertainties related to $\{x, y, z, ...\}$ to the combined standard uncertainty, can be determined by means of partial derivatives (i.e rate of variation) of each of these primary variables.

The quantity of interest, defined by F can then be expanded in Taylor series. If the rates of variation in the measured quantities $\{x, y, z, ...\}$ are small, a first order approximation of the Taylor expansion can be used to obtain a reasonable estimation of the propagation of uncertainty from the experimental data into the quantity of interest. Thus, we can represent the uncertainty in our measurement $\pm\Delta f$ associated with F as:

$$\Delta f = \sqrt{\left(\frac{\partial f}{\partial x}\Delta x\right)^2 + \left(\frac{\partial f}{\partial y}\Delta y\right)^2 + \left(\frac{\partial f}{\partial z}\Delta z\right)^2 + \ ...} \tag{3.23}$$

Equation 3.23 states that the squared combined standard uncertainty Δf of the variable of interest F, is a weighted sum of the squared standard uncertainties of the input experimental variables $\{x, y, z, ...\}$. The partial derivatives are called sensitivity coefficients. They describe the dependence of the output estimate in F on the individual uncertainties in the input variables by determining the sensitivity of Δf to the uncertainty in each of the experimental variables (Farrance and Frenkel (2012)). In this work, as stated in subsection 3.2.2.2, the effective thermal conductivity of the studied film is obtained from Eq.3.22

$$k_{eff} = \frac{L}{2}\left[\left(\frac{2V_{3\omega}b}{P_l\alpha V_{1\omega}}\right)_{R+F} - \left(\frac{2V_{3\omega}b}{P_l\alpha V_{1\omega}}\right)_{R}\right]^{-1}_{avg}$$

Since the experimental variable V_{1w} is three orders of magnitude greater than V_{3w} and given that the high purity wave generator and the digital lock-in amplifier used in the experiments are highly accurate, uncertainties in the voltage V_{1w}, the power per unit of length P_l, and the frequency w, are typically negligible (Feser (2010)).

Therefore, in the 3ω experiments, the uncertainty on the measured k_{eff} essentially arises from the uncertainties on the measurements of the film thickness L, the strip width b, the temperature coefficient of electrical resistivity α and the measured voltage V_{3w}, which is a very small quantity. Then considering uncertainties in the calibration of the specimen and the reference sample, and assuming that the variables L, $V_{3\omega}$, b and α are uncorrelated, the uncertainty Δk_{eff} in our measurements can be estimated as:

$$\begin{aligned}\Delta k_{eff} = \Bigg[&\left(\frac{\partial k_{eff}}{\partial L}\Delta L\right)^2 + \left(\frac{\partial k_{eff}}{\partial V_{3\omega}}\Delta V_{3\omega}\right)^2_{R+F} \\ &+ \left(\frac{\partial k_{eff}}{\partial V_{3\omega}}\Delta V_{3\omega}\right)^2_{R} + \left(\frac{\partial k_{eff}}{\partial b}\Delta b\right)^2_{R+F} \\ &+ \left(\frac{\partial k_{eff}}{\partial b}\Delta b\right)^2_{R} + \left(\frac{\partial k_{eff}}{\partial \alpha}\Delta \alpha\right)^2_{R+F} + \left(\frac{\partial k_{eff}}{\partial \alpha}\Delta \alpha\right)^2_{R}\Bigg]^{1/2}\end{aligned} \tag{3.24}$$

Table A.1 in Appendix A, summaries the input variables of the 3ω measurements considered for the uncertainty analysis, and their correspondent sensitivity coefficients. Although the sample preparation process leads to repeatable and uniform heater lines, small differences in the strip width and the temperature coefficient of electrical resistivity are always present from one specimen to another. Thus, the parameters b and α are measured separately for every sample. It is therefore clear that the uncertainty in thermal conductivity highly depends on the system under measurement, and thus varies in each experiment. However, for the sake of clarity, only one example of uncertainty analysis in a 640 nm thick AlN monolayer system is given in table 3.2.

Table 3.2: *Uncertainty analysis in an 640 nm thick AlN monolayer film.*

Measured Variable	Nominal Value	Sensitivity Coefficient		Standard deviation		Weighted Squared Standard uncertainty
L	640 nm	$\frac{\partial k_{eff}}{\partial L}$	4 6×10^{6}	ΔL	1.4 × 10^{-8} m	4 1×10^{-3}
$V_{3\omega_{(R+F)}}$	2 4 mV	$\frac{\partial k_{eff}}{\partial V_{3\omega_{(R+F)}}}$	-2 7×10^{3}	$\Delta V_{3\omega_{(R+F)}}$	8 8×10^{-5} V	5 5×10^{-2}
$V_{3\omega_{(R)}}$	2 3 mV	$\frac{\partial k_{eff}}{\partial V_{3\omega_{(R)}}}$	1 5×10^{3}	$\Delta V_{3\omega_{(R)}}$	1 7×10^{-4} V	6 3×10^{-2}
$b_{(R+F)}$	10µm	$\frac{\partial k_{eff}}{\partial b_{(R+F)}}$	-6 4×10^{5}	$\Delta b_{(R+F)}$	6 5×10^{-8} m	1 8×10^{-3}
b_R	9 3µm	$\frac{\partial k_{eff}}{\partial b_R}$	3 7×10^{5}	Δb_R	6 5×10^{-8}	5 9×10^{-4}
$\alpha_{(R+F)}$	2 37×10^{-3}	$\frac{\partial k_{eff}}{\partial \alpha_{(R+F)}}$	2 7×10^{-3}	$\Delta\alpha_{(R+F)}$	4 7×10^{-5}	1 6×10^{-2}
$\alpha_{(R)}$	2 32×10^{-3}	$\frac{\partial k_{eff}}{\partial \alpha_R}$	-1 5×10^{-3}	$\Delta\alpha_{(R)}$	4 9×10^{-5}	5 3×10^{-3}
k_{eff}	**5.86 W/ m K**			**Δk_{eff}**		3 8×10^{-1}

The last column of table 3.2, states the contribution of the weighted uncertainty in each experimental variable to the standard overall uncertainty in k_{eff}. It is noteworthy that the major uncertainty contributions arise from the parameters $V_{3\omega_{(R+F)}}$, $V_{3\omega_{(R)}}$ and $\alpha_{(R+F)}$. This behavior was observed in all AlN samples. For this particular example, the propagation of uncertainty from the input experimental variables results in an overall uncertainty of $\Delta k_{eff} = 3.83 \times 10^{-1}$, which represents 6.54%. For the other experimental data, the combined standard uncertainty was always below 10%, which is fairly tolerable for 3ω measurements.

3.4 3ω experimental setup

The experimental setup used for the 3ω measurements is shown in Fig.3.7. It consists of a low frequency analog sine wave generator KROHN-HITE 4402B

with a frequency range from 1 Hz to 110 kHz and an harmonic distortion of 0.0005%, a signal conditioning stage used to filter and amplify the signal, a processing stage controlled by a PowerDAQ data acquisition card (UEI PD2-MFS-4-2M/14DG), a computer, and a LABVIEW® software employed to extract the amplitude and phase of the 3ω signal.

The sine wave generator is used to drive a high purity sinusoidal current signal of frequency 1ω across the metal line, producing a 2ω dissipated power per unit length varying between 4.4 and 5.1 W/m, that being equivalent to a current intensity of 40 to 60 mA (RMS) for a typical heater of 10 µm width.

The reference resistance R_{ref}, being also in the closed circuit, oscillates at a frequency 1ω as well. The voltage signal measured between the inner pads of the metal strip is a sum of the 1ω and 3ω components, and the amplitude of the third harmonic voltage is three orders of magnitude smaller than the fundamental one. Therefore, a signal conditioning stage composed of an operational amplifier-based subtraction circuit is used to remove the 1ω component of the measured signal.

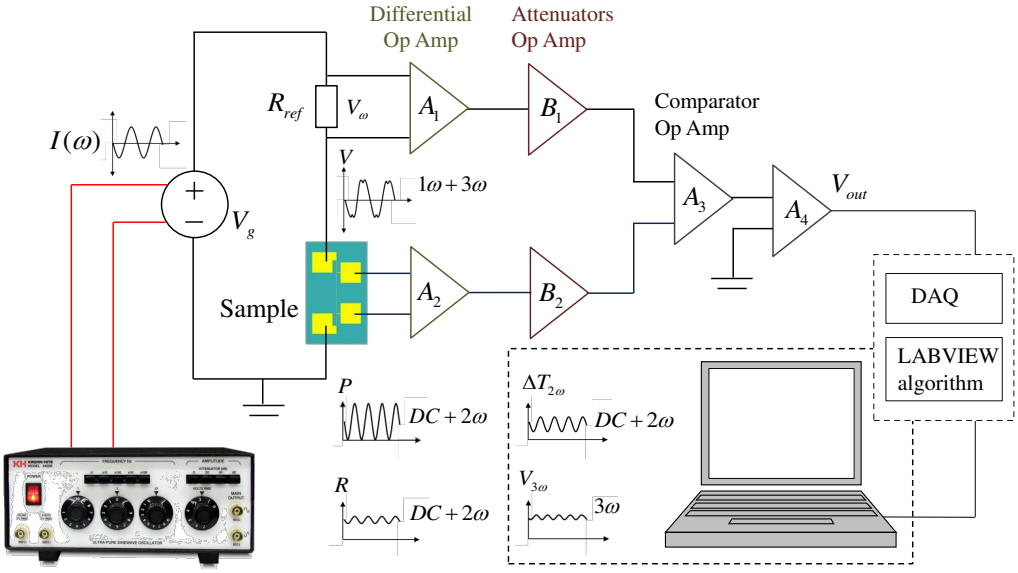

Figure 3.7: *Scheme of the experimental setup used for the 3ω measurements and description of the operational amplifier-based electronic conditioning stage employed to perform the signal treatment.*

First, to remove the fundamental component, the voltage amplitude V between the inner pads of the heater is balanced with the amplitude of the voltage reference signal (V_ω). This operation can be accomplished by the differential

operational amplifiers (Op-amp) A_1 and A_2 and the differential attenuators B_1 and B_2. Then, the signal V_ω is subtracted from V by the comparator A_3.

Since the signal V_{out} obtained after A_4 is still quite noisy and contains parasitic ω and 2ω elements, a numerical treatment is performed by the processing stage, which acts as a digital lock-in amplifier, to extract a proper 3ω signal. The signal difference $V - V_\omega$ is digitalized by the data acquisition card (DAQ) and treated numerically to extract the real component of $V_{3\omega}$ with a LABVIEW® algorithm.

Extracting the real part of the 3ω amplitude is equivalent to determine the third Fourier component of a periodic signal. As the voltage signal V_{out} obtained from the output of the Op-amp A_4 is a periodic signal with period of $T = 2\pi/\omega$, it can be developed as a Fourier series as follows:

$$V_{out}(t) = \sum_{j=0}^{\infty} [a_j \cos(j\omega t) + b_j \sin(j\omega t)] \tag{3.25}$$

where j is an integer. The coefficients a_j and b_j are respectively:

$$a_j = \frac{2}{T} \int_0^{jT} V_{out} \cos(j\omega t) dt \tag{3.26}$$

$$b_j = \frac{2}{T} \int_0^{jT} V_{out} \sin(j\omega t) dt \tag{3.27}$$

Thus, to obtain the real part of the third harmonic voltage signal $\mathbb{R}(V_{3\omega})$, the term a_3 is calculated for each value of frequency w:

$$a_3 = \frac{\omega}{\pi} \int_0^{6\pi/\omega} V_{out} \cos(3\omega t) dt \tag{3.28}$$

Generally, $\mathbb{R}(V_{3\omega})$ is averaged from 100 oscillations at a given frequency w, and the obtained value is used in Eq.3.8 to obtain $\Delta T_{2\omega}$. Then the amplitude of the temperature oscillation is plotted as a function of the logarithm of the angular frequency and the thermal conductivity of the specimen is extracted either from Eq.3.21 or Eq.3.22 depending if the film-on-substrate or the differential approach is used.

In this work, the thermal measurements were performed at the electrical characterization facilities of the Laboratoire des Caractérisations Électriques, CEA-Leti, using the 3ω setup developed by Alexandre Jacquot (Jacquot (2003)).

3.5 Sample preparation

The sample preparation process consists of 3 main steps: surface cleaning, deposition of titanium and gold and microfabrication of the heater.

- **Surface cleaning:**

Since the above described methods assume negligible interfacial thermal resistance between the heater and the sample, it is crucial to obtain a proper interface, where the heater is in intimate contact with the specimen surface. To eliminate possible particulate impurities, the samples used in the experiments were first cleaned with acetone in an ultrasound bath for 5 minutes. The residual solvent was removed with ethanol, followed by drying with high-purity nitrogen.

- **Deposition of Titanium & Gold**

To fabricate the heater, a 20 nm thick titanium (Ti) layer was first deposited by pulsed DC sputtering onto the specimen surface, followed by a 250 nm thick layer of gold. The Ti layer is used for adhesion improvement of the Au thin film.

- **Microfabrication of the heater**

The deposited Au/Ti layers were then patterned by typical micro-fabrication techniques (Fig.3.8).

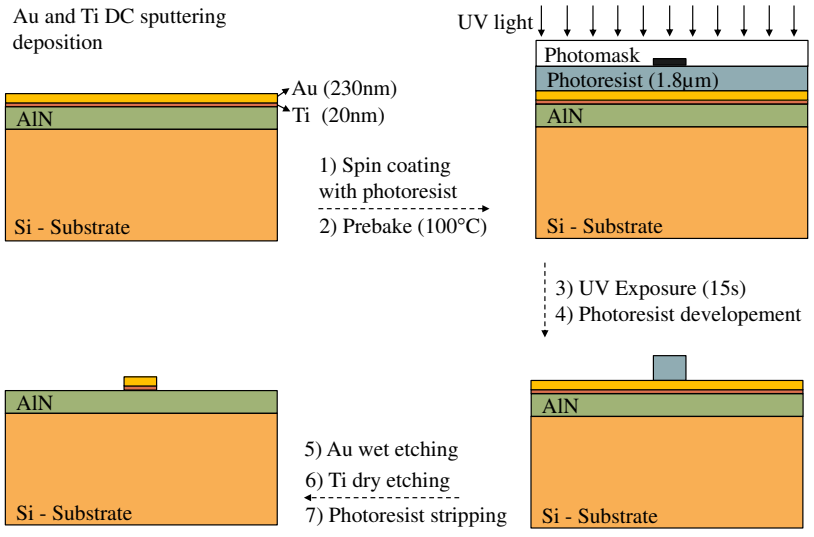

Figure 3.8: *Microfabrication process steps for the 3ω lines patterning.*

First, the samples were covered with a commercial positive photoresist (S1818) by conventional spin coating at 2000 rpm for 15 s, resulting in an homogeneous

resist layer of 1.8 μm , which was prebaked at 100 °C for 2 minutes on a hotplate to eliminate the remaining solvent concentration. The resist-coated samples were covered with a photomask containing the 3ω line patterns and then exposed to ultraviolet light for 15 s. After exposure, the samples were submerged in a developer bath of MF319 for 40 s followed by deionized water cleaning Then, the gold layer was wet chemical etched in a potassium iodide solution ($KI:I_2:H_2O$=100 gr:40 gr:250 ml) for 2 min, and the Ti layer was dry etched by reactive ion etching (RIE) at 10 W using high purity (99.99%) sulfur hexafluoride and oxygen ($SF_6:O_2$=25 sccm:5sccm) at a pressure of 25 mTorr. Finally, the residual photoresist was removed from the sample surfaces using acetone and ethanol, followed by high-purity nitrogen drying.

Figure 3.9(a) is a SEM micrograph of the Ti (20 nm) and the Au (230 nm) layers deposited by DC magnetron sputtering onto the surface of an AlN film. Both, the Ti and the Au layer are continuous and homogeneous. Figure 3.9(b) is a SEM top view of a microfabricated 3ω line strip of $\approx$ 10 μm width. The trapezoidal heater profile observed in Fig.3.9(b) is principally due to the anisotropic nature of the wet etching process. As the potassium iodide solution begins to etch down the Au toward the Ti layer, it simultaneously begins to etch the underneath matter in the lateral direction. Since the regions closest to the photoresist are exposed for a longer period of time to the $KI:I_2:H_2O$ solution, these areas exhibit an increased lateral etch, resulting in a trapezoidal profile of the 3ω pattern.

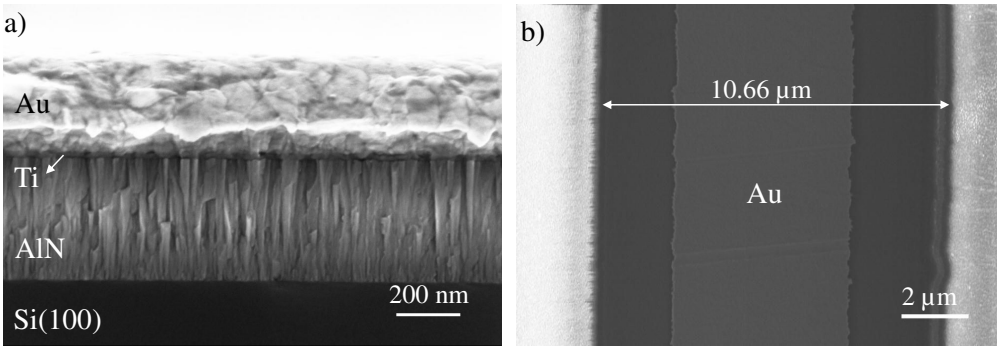

Figure 3.9: *(a) SEM micrograph of 20 nm and 230 nm thick Ti and Au layers deposited onto an AlN film. (b) SEM top view of a microfrabricated* 3ω *strip of* $\approx 10\mu m$ *width.*

The described method of microfabrication led to repeatable heater patterns with uniform width all along the length of the heating lines [Fig.3.9(b)]. The nominal length, width, and thickness of the Au strips used in the experiments were 4000 μm, 10 μm, and 250 nm respectively, including the 20 nm thick Ti layer that improved adhesion.

Photolithography and etching processes of sputtered layers with characteristic anisotropy often lead to width variations from one microfrabricated pattern to another. In our case, the resulting width of the 3ω patterns varied from 9.3 to 10.7 nm [Fig.3.9(b)] from one sample to another, being uniform along the length though. Thus, to be as rigorous as possible when performing the 3ω measurements, the width of the heater lines were measured separately for each sample.

3.6 Thickness dependent thermal conductivity measurements on AlN films

Prior to the 3ω measurements, 3 experimental variables have to be measured for each sample: the thickness of the film, the heater width and the temperature coefficient of the electrical resistance (Eq.3.22).

- **Thickness of the film**

The thicknesses of the monolayer and multilayer samples were measured with a Bruker Dektak 6M contact profilometer. During AlN deposition, a step was patterned by placing a shadowing mask onto the plane Si substrate. Then, profilometer measurements were performed by sensing the deflections of a stylus riding over the patterned step. The measured step-heigh gave the thickness of the AlN film. The reported values of the film thicknesses were obtained by averaging over 5 measurements.

- **Width of the resistive heater**

The width of the heater was measured for each sample with a LEICA optical microscope, calibrated for high precision measurements. The heater width values used for 3ω experiments were obtained by averaging over 5 readings.

- **Temperature coefficient of electrical resistance**

To determinate the temperature coefficient of resistivity of each sample, variations of the electrical resistance as a function of the temperature were measured by the four points probe method. The samples were placed in a vacuum chamber, and a step-wise temperature program was used, holding the samples at constant temperature until thermal equilibrium was reached. The coefficient α was then determined from the slope of the electrical resistance versus temperature curve.

- **Differential 3ω measurements**

Thickness-dependent thermal conductivity measurements were performed by the differential 3ω method on samples with thickness varying from about 270 to 1461 nm and 545 to 1107 nm for monolayers and multilayers, respectively.

The specimens were placed onto a chuck at room temperature, and 4 microprobes were carefully positioned onto the electrical pads to ensure good electrical contact. After probes positioning, the AC signal was turned on, at a frequency of 1kHz. To remove the fundamental component, the voltage amplitude between the inner pads was balanced with the one of the voltage reference signal. The 3ω voltage was then recorded for different modulation frequencies, ranging from 100 Hz to 1 kHz. Within this frequency range, the penetration depth of the thermal wave varied from 266 to 84 µm. Since these penetration depths are larger than the film thicknesses in all the evaluated frequency range, the contribution of the native oxide layer formed at the surface of the silicon substrate, which was evidenced by energy-dispersive X-ray spectroscopy (section 5.5 of Chapter 5), had to be necessarily taken into consideration. This oxide layer usually appears in experiments conducted in ambient air (Saga et al. (1999), Choi et al. (2001)), as is our case.

The thermal conductivity was therefore obtained by measuring two similar structures, one with the AlN film, and another without the studied film, serving as the reference sample. The average temperature rise difference was obtained by removing the signal of the reference sample from that of the specimen with the deposited AlN layer, to isolate the thermal properties of the film. The native oxide contribution was therefore subtracted from the total experiment temperature rise (Eq.3.22), which was obtained at comparable power inputs with similar heaters deposited on the AlN film and the reference Si/SiO_2 structure (without the studied film). For the measurements, the dissipated power per unit length was in the range of 4.4 to 5.1 W/m, that corresponding to a current intensity of 40 to 60 mA (RMS), depending on the sample electrical resistance.

The experimental variables of the 3ω measurements corresponding to the monolayer and multilayer sets of samples, and the reference Si/SiO_2 specimen are summarized in Table B.1 and B.2, respectively (Appendix B). Given that in the experiments, the thermal conductivity of the silicon substrate is at least 18 times higher than the one of the AlN films, and the heater width is 7 times larger than the film thickness, a one-dimensional heat conduction model was used to fit the real part of the temperature oscillation amplitude as a function of heating frequency.

To obtain the thermal boundary resistance R_s between the AlN layer and the substrate, the whole system was considered as a thermal resistance network, such that:

$$\frac{L}{k_{eff}} = \frac{L}{k_{AlN}} + R_s \tag{3.29}$$

where L/k_{eff} is the effective thermal resistance, which contains the contribution of thermal resistance due to the film (L/k_{AlN}) and the one associated to the thermal boundary resistance between the layer and the substrate (R_s). Assuming that R_s is equivalent for all samples, R_s was determined by fitting Eq.3.29 to the experimental data of the thermal resistance L/k_{eff} against the layer thickness L , and extrapolating the linear model to $L = 0$.

For the multilayer AlN films, an additional thermal boundary resistance at interfaces between two AlN layers has to be considered and Eq.3.29 is replaced by:

$$R = \frac{R_{eff} - R_s - NR_{AlN}}{N - 1} \tag{3.30}$$

N being the number of AlN layers and R_{AlN} the intrinsic thermal resistance of each AlN layer.

The next section focuses on the method designed and implemented in this work to measure thermal conductivity of AlN films under strain.

3.7 Strain dependent thermal conductivity measurements

Heat transport processes in nanoscale polycrystalline materials are governed by the rates at which the heat carriers interact with elements that disturb the crystalline lattice. Besides crystallographic defects (dislocations, vacancies, interstitial voids, mass differences, and substitutional impurities), strain is another means of altering the crystal symmetry. Recently, an increased interest on the effect of strain on the thermal properties of low dimensional structures has surged. The main reason is that strain potentially provides a mechanism to dynamically tune thermal conductivity of materials. A reasonable number of theoretical studies had dealt with the influence of elastic strain on the thermal conductivity of thin films in the literature (Wang and Shen (2014), Li et al. (2010), Xu and Li (2009), Samvedi and Tomar (2010), Zhu and Zheng (2009), Picu et al. (2003)). However, there are limited experimental results (Takashiri et al. (2014), Kumar et al. (2013), Alam and Manoharan (2012), Lee et al. (2010)) that show stress/strain effects on the thermal conductivity of thin films. The evident lack of experimental measurements on strain-mediated thermal conductivity is due to the intrinsic complexity associated to simultaneously induce and measure strain in a low-dimensional structure, while performing thermal conductivity measurements. Motivated by the need to characterize the thermal conductivity of thin films as a function of the applied strain, a new measurement technique that couples the 3ω method to a four points bending system was developed in this work.

3.7.1 The 3-omega method coupled to a four points bending system

The method developed here makes use of a classical four-points bending system specially adapted to be used with film-on-substrate samples. It allows for the application of a well-controlled mechanical load to the sample, while simultaneously measuring the stress distribution within the sample and the thermal conductivity of the film.

In order to obtain reliable measurements, it is crucial to have well-established boundary conditions of the independent variables involved in the experiment, i.e. strain and thermal conductivity. For the latter, well-known boundary conditions are ensured by following the thermal design criteria described in section 3.3. However, accurate determination of the intrinsic stresses in the film introduced by the deposition process, growth mechanism and thermal expansion mismatch between the substrate and the studied film, is much more difficult. The four-points bending method is a well-established technique extensively used in materials science and engineering to test the flexural strength (ASTM International (2013)). The strain-mediated thermal conductivity measurement proposed here, couples this classical four-points bending setup to the differential 3-omega technique, providing a simple approach for applying a precise stress distribution during thermal measurements.

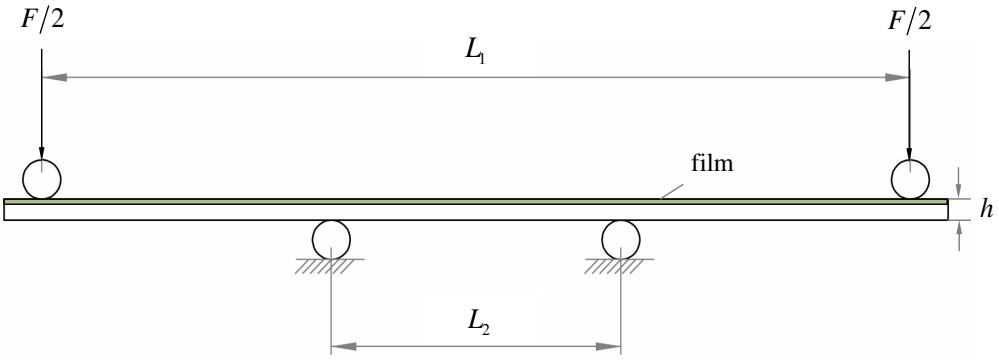

Figure 3.10: *Four-points bending principle.*

In a typical flexure-based four-points bending experiment, a rectangular specimen is centered between 4 cylindrical supports, as illustrated in Fig.3.10. This beam is supported by the inner rods, which are anchored points, separated by a distance L_2. Then, the sample is subjected to deformation by applying two driving loads through the outer two supports, which are separated by a distance L_1. Loading the outer rods by a mechanical force $F/2$, induces a constant bending moment M in the region of the sample located between the inner rods. The sample is therefore bent with a constant radius of curvature

resulting in uniform (uniaxial) stress and strain distributions in this region. Advantageously, unlike other methods to apply stress, such as cantilevers and three-point bending, in the four-points bending method the variation of the sample position does not affect the accuracy of the measurements (Ueda and Pearton (2013)).

The magnitude of uniaxial stress σ (in the longitudinal direction) on the top surface of a rectangular beam between the center and the two inner supports can be calculated by (Prume and Muralt (2007)):

$$\sigma = \frac{Mh}{2I_{xy}} \tag{3.31}$$

being $M = FL_1/4$ the bending moment applied to the load span and $I_{xy} = wh^3/12$ the geometrical moment of inertia, where the parameters w and h are associated to the width and the thickness of the beam, respectively. Therefore, the homogeneous stress distribution at the surface of the studied sample can be written as:

$$\sigma = \frac{3F(L_1 - L_2)}{2wh^2} \tag{3.32}$$

By using the Hook's Law, the strain ε in the longitudinal direction of the thin film can be calculated as:

$$\varepsilon = \frac{\sigma}{E_s} \tag{3.33}$$

being E_s the Young's modulus of the substrate serving as a mechanical support. By accurately knowing the mechanical force used to load the outer rods, equations 3.32 and 3.33 provide a direct approach to experimentally measure the applied stress and strain distributions in the studied film.

3.7.2 Design, development and implementation of the experimental setup

3.7.2.1 Apparatus

A computer-aided design layout of the four point bending system and the experimental setup are shown in Fig.3.11 and Fig.3.12 respectively. The four-points bending mechanism is mounted on two linear rails, which are perpendicular to each other. The first rail guarantees alignment of the four bending bars with respect to the $x-$axis and the second one enables rough positioning of the loading system on the y-axis.

The loading system is composed of two coupled single-axis translation stages, used to precisely position the upper bending bars along the $y-$axis and induce deflection of the rectangular beam by subjecting it to four-point loading through the displacement of the upper rods. The linear $y-$stages consist of a moving platform and a stationary base joined by a bearing system. The position of each

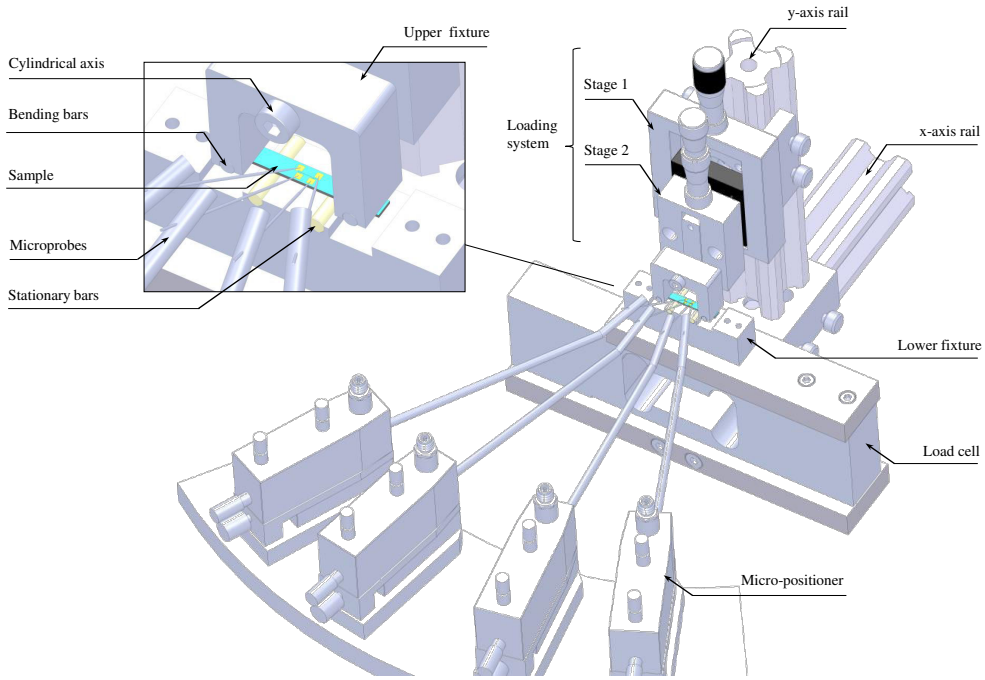

Figure 3.11: *Computer aided design layout of the four-points bending setup. A closer-up view of the sample holder is shown in the inset.*

translation stage is individually controlled by a micrometer screw that acts as a precision linear actuator. The first stage is mounted on a carriage that slides on the $y-$axis rail and the second stage is anchored to the moving platform of the first stage. The displacement resolutions of the micrometric screws of stage 1 and 2 are 20 µm and 0.4 µm, respectively. The assembled $y-$axis translation system enables a high precision and well-controlled application of the mechanical load.

The upper fixture is joined to the stage 2 by a cylindrical bearing axis, which effectively minimize misalignment along the x-axis between the sample and the 4 bending bars, leading to uniform loading on the specimen. Additionally, the upper fixture is U-shaped, leaving enough space to allow for positioning of the microprobes that measure the 3ω voltage (closer-up view of the sample holder in Fig.3.11). The outer bending bars are anchored to the upper fixture and are spaced 20 mm apart ($L_1 = 20$ mm). Hence, the loading system, which includes the joined translation stages and the upper fixture that supports the outer bending bars, is designed to provide highly controlled transverse vertical loads to induce deflection of the studied beam.

On the other hand, the stationary lower fixture is designed to provide reactions to the applied tensile loads at points spaced towards the beam center by 5

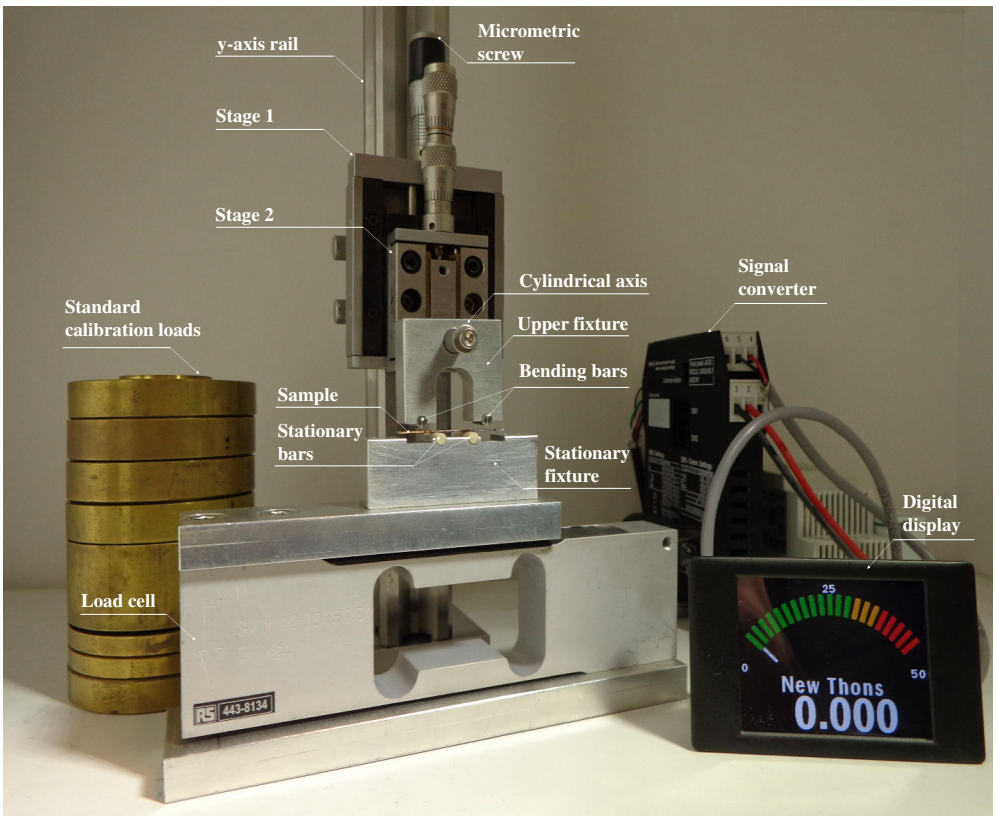

Figure 3.12: *Four-points bending setup and its components.*

mm ($L_2 = 10$ mm). This stationary fixture is mechanically coupled to a high precision strain gauge-based load cell (RS 1042), that senses the force applied to the beam of rectangular cross section. The load cell is composed of a spring element made of an aluminum alloy, four strain gauges that are bonded to the spring element at the regions of smallest cross section, and a bridge circuit (Fig.3.13).

The resistance of the strain gauges varies as a result of elastic deformation of the spring element, caused by the applied load. The strain gauge-based system is connected to a Wheatstone bridge, which translates the variation of the electrical resistance into an analog output that is then displayed on a digital screen.

The load cell was calibrated following the procedure recommended by the supplier (Seneca Uk (2015)). Standard weights from 0.23 to 2.72 kg were placed on the top of the stationary fixture that supports the inner rods, while reading the force signal output of the load cell in the digital screen. The calibration curve is showed in Fig.3.14. The maximum combined uncertainty for the measured force was found to be 0.6%, demonstrating that the applied load can be experimentally determinate with a high level of accuracy.

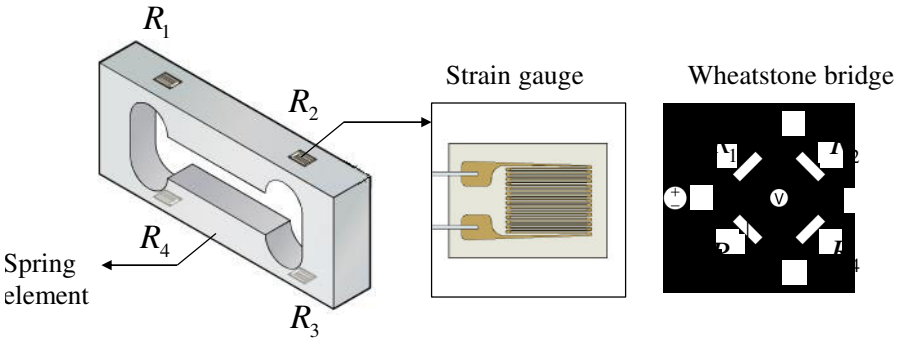

Figure 3.13: *Scheme of load cell components. The load cell consists of an aluminum alloy spring element, four strain gauges bonded to the spring element at the regions of smallest cross section, and a bridge circuit.*

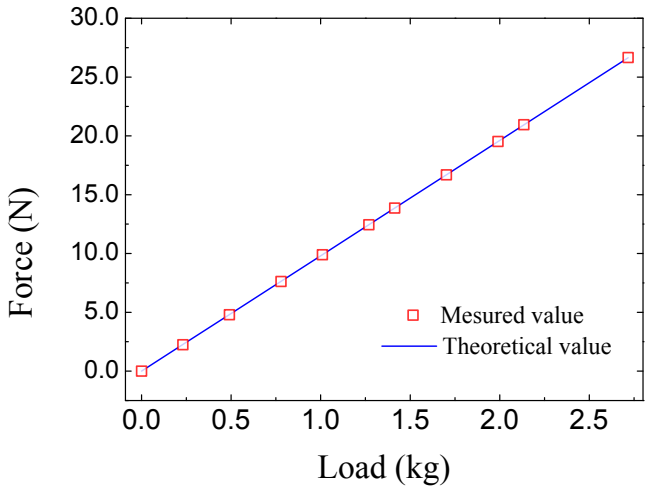

Figure 3.14: *Load cell calibration curve.*

3.7.2.2 Numerical simulations

In order to obtain reliable strain-mediated thermal conductivity measurements, it is crucial to accurately determine the stress distribution in the film. Thus, a three-dimensional four-point bending model was developed by the finite element method, and the numerical results were compared with those obtained analytically.

A beam of nominal length, width and height of 25 mm, 3 mm and 0.51 mm respectively, is subjected to a mechanical load of 10 N in the z-direction, equally distributed on the two outer bending bars. The geometry of the beam was chosen following the direction reported by Prume and Muralt (2007), who developed a four points bending system to measure the transverse piezo-coefficient

of thin films. The dimensions and the mechanical properties of the specimen used in the numerical simulations are summarized in table 3.3.

Table 3.3: *Geometrical parameters and physical properties of the materials used for the numerical simulation.*

Distance between the outer bars L_1	20 mm
Distance between the inner bars L_2	10 mm
Beam length L_b	25 mm
Beam width w	3 mm
Beam thickness h	0.51 mm
Young's modulus of silicon, E_{Si}	130 GPa

Since the film thickness ($\approx$ 1 µm) is much smaller than that of the substrate ($\approx$ 550 µm), it can be assumed that the film is subjected to a uniform strain in the longitudinal direction that is equal to the strain of the surface layer of the silicon beam. The studied beam of rectangular cross section was discretized into 1522 nodal elements. The meshed volume used in the calculations is shown in Fig.3.15. Due to the symmetry of the problem, the analysis can be reduced to a half cross section of the beam in 2D. However, since the physics of the problem does not require high computational power, the simulation was performed for a 3D geometry.

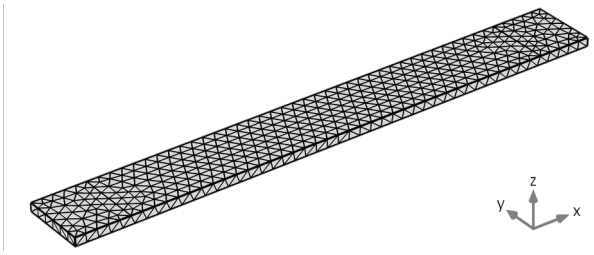

Figure 3.15: *Geometry of the sample used in the numerical simulations to solve the four points bending problem in 3D. To accurately calculate the stress distribution in the sample, the resolution of the meshing elements is higher for narrower regions.*

To perform the numerical simulations, the structure stress resultants are first separately solved using tetrahedral elements under a given loading. Then, each element provides a set of equations to form the general equation set and solve the problem. By using the superposition principle, the combined state of stresses at any point of the beam cross-section can be obtained from the sum of stress values due to each stress resultant (Ziemian (2010)).

In the finite element simulation, the action of the stationary bars is represented by constraining to zero the vertical displacement of the two inner linear nodes, spaced towards the beam center by 5 mm. On the other hand, the action of the outer bending bars is represented by enforcing a prescribed vertical load of 5 N on the two outer linear nodes, spaced 20 mm apart.

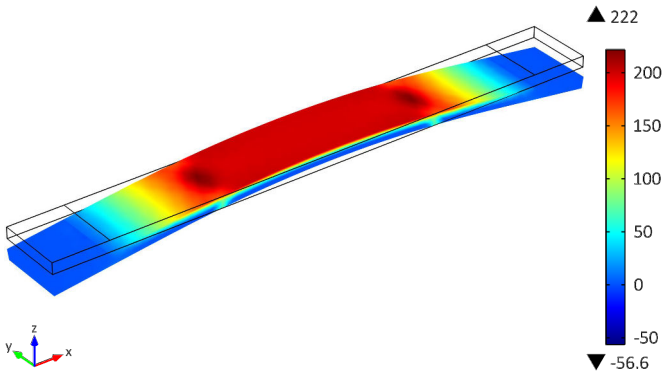

Figure 3.16: *First principal stress distribution of the bending sample under an applied load of 10 N, equally distributed on the two outer linear nodes.*

The first principal stress distribution (σ_1) at the surface of the bending sample is shown in Fig.3.16. The quantity σ_1 is defined in the principal direction, which in this case corresponds to the $x-$axis. A homogeneous stress distribution due to the uniform bending moment induced in the region located between the inner stationary bars can be observed.

A mean value of 199.19 MPa with a standard error of 0.03 MPa was obtained by sampling 50 values of first principal stress at different points in the region of the specimen surface, located between the inner bars.

The corresponding first principal strain ε_1 within the beam is shown in Fig.3.17. Analogously to the first principal stress, a mean value of 1.52×10^{-3} with a standard error of 2.8×10^{-6} was obtained by randomly sampling the specimen surface at different points of the uniform strain region.

Under the assumption that the film thickness is much smaller than the beam height, the obtained numerical results can be compared to the values of the first principal stress and strain obtained analytically with equations 3.31 and 3.33, which are stated in subsection 3.7.1. In this case, the film is subjected to a uniform first principal strain equivalent to that experienced by the surface of the bended silicon beam (Prume and Muralt (2007)). The analytical values of σ_1 and ε_1 experienced by a rectangular beam subjected to an applied load of 10 N, symmetrically distributed between the outer bending bars, are 199.20 MPa and 1.53×10^{-3}, respectively.

The numerical predictions obtained by the finite element method match remarkably well with the analytical results for the first principal stress and strain

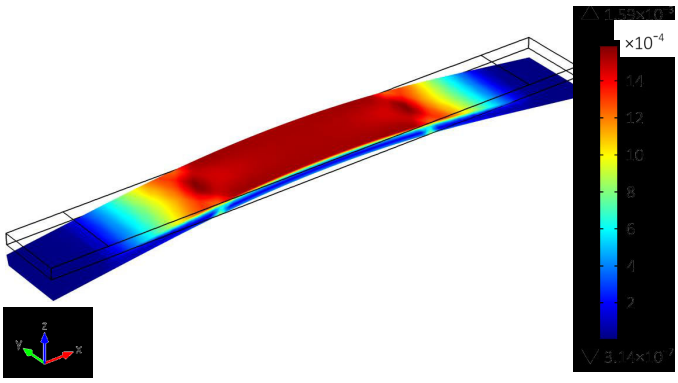

Figure 3.17: *First principal strain distribution of the bending sample under an applied load of 10 N, equally distributed on the two outer linear nodes.*

of the bending structure, with an error below 0.2%. Both, the first principal stress and strain distributions within the bent beam can therefore be accurately determined, either numerically or analytically, by experimentally measuring the value of the applied load.

3.7.2.3 Sample geometry and specimen preparation

Numerical simulations performed by Prume et al. (2010) demonstrated that the sample aspect ratio between the beam length and width should be larger than 8 ($L_b/w > 8$) to obtain a uniform stress distribution along the region of the sample surface located between the two stationary loading bars. Therefore, to fulfill the geometry requirements, the nominal length, width, and thickness of the beams used in the four point bending experiments were 25 mm, 3 mm, and 0.5 mm respectively, leading to an aspect ratio L_b/w of 8.33 (Fig.3.18).

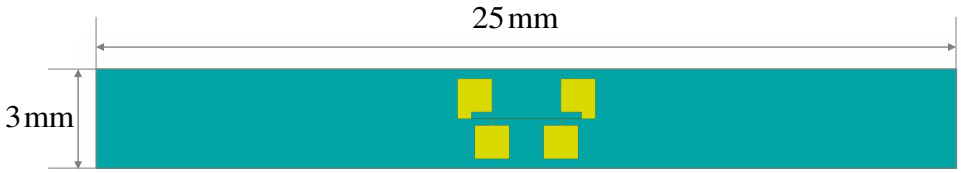

Figure 3.18: *Geometry of the rectangular beam ($L_b/w = 8.33$).*

To obtain the rectangular shape of the bending beams, typical dicing techniques such as mechanical sawing and scribing-cleaving processes were explored. Fracture stresses for sawed and cleaved beams were around 100 MPa and 150 MPa, respectively. Since cleaved samples allowed for the application of higher values of stress before fracture (showing that cleaving led to less induced internal stresses), the latter method was chosen to fabricate the bending beams. Dicing

of the rectangular beams was therefore achieved by indenting the surface of the sample with a sharp tungsten tip coupled to a precision automated head. Cutting lines of 25 mm spaced from each other by 3 mm were indented on the sample surface to form the suited rectangular shape. It is noteworthy to signal that the samples were aligned in relation to the (100)Si cleaving planes prior to indenting, to ensure that scribing was well performed following the Si[100] crystallographic direction to facilitate posterior cleaving.

Additionally, to measure the thermal conductivity of the sample while deflecting the rectangular beam, a 3ω pattern was microfrabricated at the beam center, in the region of uniform stress distribution, as shown in Fig.3.18. Alignment of the 3ω pattern at the beam center was achieved by using the cutting lines as a reference for the photolithography process. Then, the heater patterning was obtained by following the microfabrication process described in section 3.5.

3.7.2.4 Thermal measurements under external applied strain

Thermal conductivity measurements under external induced strain were performed by coupling the 3ω method to a 4 points bending system, as described in previous sections. To investigate how microstructure and crystal orientation distributions influence strain-thermal transport coupling, thermal conductivity of highly and poorly textured AlN monolayers were measured as a function of strain. These measurements were also performed on a AlN/AlN multilayer to determine the influence of oxygen related defects on strain-mediated thermal transport.

As in the case of thickness-dependent measurements, L, $2b$ and α were measured for each sample. In addition, prior to strain-dependent measurements, the effective thermal conductivities of the studied specimens were measured by placing the samples onto a chuck at room temperature, following the classical 3ω methodology (Eq.3.21). The main objective of these prior measurements was to test the feasibility of the experiment by comparing the results to those obtained on the newly developed experimental set-up. After measuring the effective thermal conductivities of the studied samples by the classical 3ω technique, strain-mediated measurements were carried out by an analogous experimental procedure to the one described in section 3.6.

At room temperature, the specimens were placed onto the stationary lower rods and 4 micro-probes were carefully positioned onto the electrical pads. A slight load was exerted to the sample when electrical contact was achieved. The forces applied by the microprobes were controlled by reading the load-cell output. Each microprobe was then positioned in the $y-$axis to exert a force of 0.047 N, and these forces were kept constant all along the strain-mediated measurements.

First, a 3ω measurement was performed without external applied load, except for the microprobe forces, which represent an overall load of ≈ 0.2 N, in the $-y$-direction. R_{e_0}, $V_{1\omega}$ and P_l were then registered, and the 3ω voltage signal was recorded for different modulation frequencies, ranging from 100 Hz to 1 kHz. After measurement, the probes were released and the y-translation system was positioned to allow for a uniform mechanical loading on the specimen. The applied force was controlled by adjusting the micrometric screw displacement to settle the desired load value, which was read from the digital display. When the desired load value was reached, the microprobes were repositioned onto the electrical pads (with an overall force of ≈ 0.2 N). Then, the 3ω voltage signal was measured for the same frequency range, and R_{e_0}, $V_{1\omega}$ and P_l were recorded as well. This process was reproduced for various values of mechanical load by monotonically increasing the applied force, until specimen fracture. Contrarily to thickness-dependent measurements, the contribution of the native silicon oxide layer was not subtracted from the total experiment temperature rise and the effective thermal conductivities were determined by Eq.3.21. The reason is that the differential technique requires a larger number of prior measurements, and in particular, the strain-coefficient of the electrical resistance (see next section) has to be characterized for two sets of samples: the reference specimen and the films-on-substrate system. Thus, the classical method was preferred to avoid introduction of additional experimental uncertainties.

It is worth noting that indenting the sample surface with a sharp tungsten tip generates microfractures and internal stresses which, in turn, induce and expand a zone of inelastic deformation below the contact area, from which cracks ultimately initiate (Lawn and Wilshaw (1975)). This inelastic deformation, (typically localized at the edges of the cleaved surface) depends on the surface mechanical properties, which may vary from one sample to another due, for example, to differences in grain sizes (Wasmer et al. (2005)). As a consequence, the prepared beams showed different fracture stress values. Thus, the load and the mechanical strain range achieved in the experiments varied from sample to sample, because of the specimen-dependent fracture stress value.

3.7.2.5 Metal strip calibration: Measurement of the strain-coefficient of the electrical resistance

Electrical resistance of metallic wires changes as a function of elastic strain. This phenomenon was first investigated by Lord Kelvin in 1856 (Thomson (1856)), and is today the working principle of the strain gauges.

In our experiments, when applying a mechanical load to the AlN sample, the 3ω pattern is as well subjected to strain.

As described above, the 3ω measurement principle relies on the ability of the heater electrical resistance to vary with temperature. It is therefore necessary to accurately characterize the electrical resistance changes that can be induced

within the resistive strip due to external elastic strain. Thus, electrical resistance measurements as a function of strain were performed on a heater of 10 µm width. Strain-mediated electrical resistance measurements were achieved by coupling the 4-points bending system to a probe station, which allow for measuring the electrical resistance by the four-points probe method. The ex-

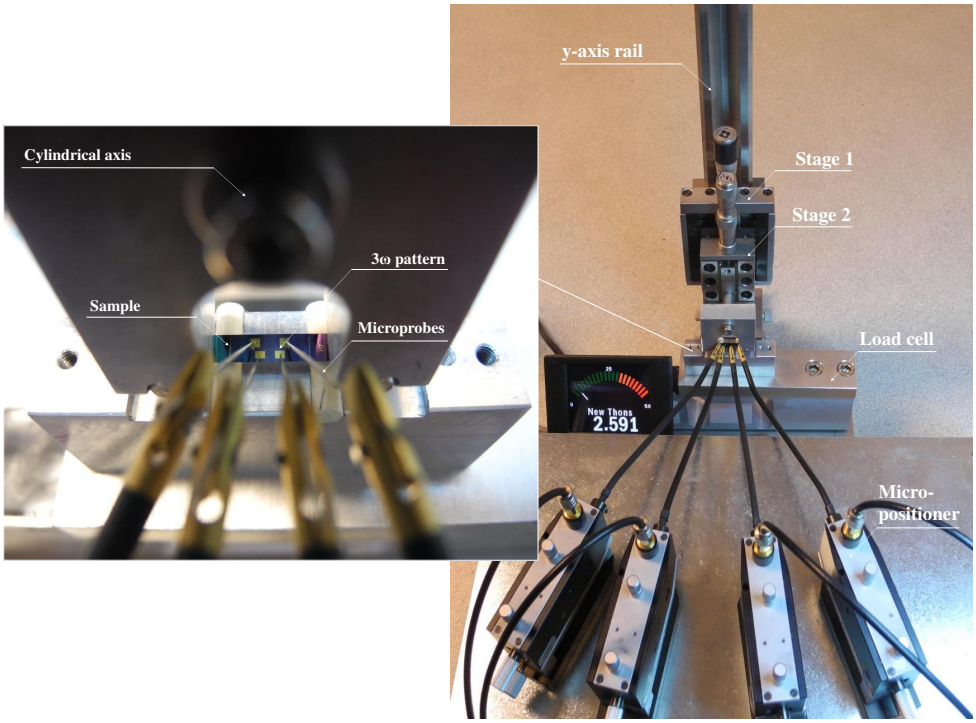

Figure 3.19: *Four points bending setup, mounted to perform strain-mediated V(I) measurements. The inset is a closer-up view of the experiment performed on a 3ω strip onto the surface of an AlN/Si beam.*

perimental set-up is shown in Fig.3.19. A closer-up view of the experiment performed on a 3ω strip onto the surface of an AlN/Si beam is depicted in the inset.

Strain-mediated electrical resistance measurements were carried out at room temperature by using an analogous methodology to the one described previously for thermal characterization (subsection 3.7.2.4). The specimen was placed on the stationary inner bars and the microprobes were positioned onto the electrical pads by adjusting their contact force to 0.47 N for each microprobe. Without external applied load, a first measurement was performed by driving a current between the outer pads that varied from -1 mA to 1 mA, while measuring the voltage signal between the inner pads. This process was

reiterated through a series of 5 pre-programmed voltage *versus* current [V(I)] measurements, while the lock-in amplifier recorded the voltage signal.
After measurement, the probes were released and the $y-$translation stage was positioned to achieve the desired load. After loading, the probes were repositioned and the experiments were reiterated by gradually increasing the applied load. For each value of force, 5 series of V(I) measurements were recorded. Then, the electrical resistance was determined from the slope of the voltage *versus* current curve.
To serve as example, Fig.3.20 depicts the typical raw data obtained from a V(I) measurement for a load of 11 N (fixed constant value of strain $= 1,69 \times 10^{-3}$ m/m). It is noteworthy that the resistance decays abruptly near current values that approach zero, because dV/dI tends toward infinity when $I = 0$.

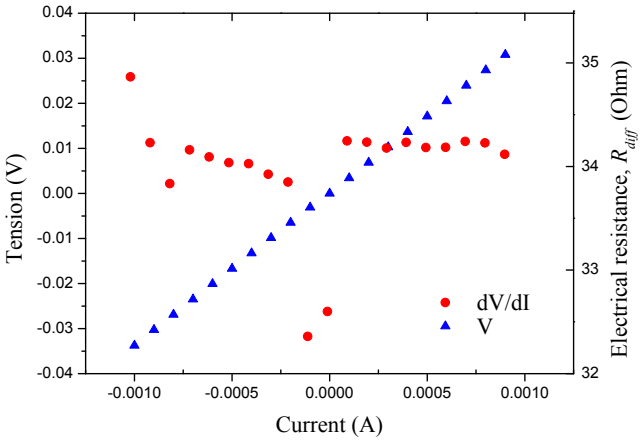

Figure 3.20: *Typical raw data of a V(I) measurement for a load of 11 N (obtained for a fixed constant value of strain* $= 1,69 \times 10^{-3}$ m/m*). A current varying from -1 mA to 1 mA is driven between the outer pads, while the voltage is measured between the two inner probes. The electrical resistance as a function of strain is obtained by determining the slopes of the various V (I) curves measured for different strain values.*

3.8 Summary

The experimental methodology used to measure the thermal conductivity of AlN films was thoroughly described in this chapter. The procedures followed to perform thickness and strain-dependent 3ω measurements were also detailed. In addition, the method used to implement a novel experimental approach, specially developed in this work to study the thermal response of films-on-substrate systems subjected to strain was reported. To explain the experimental results obtained for the thermal conductivity of AlN films using the differential 3ω method, a theoretical model was developed. The following chapter describes this theoretical framework, which is then used in Chapter 6 to correlate the measured thermal properties of AlN samples with their structural features.

Chapter 4

Thermal conductivity model for polycrystalline materials with a non-homogeneous microstructure

The theoretical model presented in this chapter was developed in collaboration with the Thermal Nanoscience Group (EM2C) at École Centrale Paris, by Dr. Ordonez-Miranda, CNRS Researcher.

In this chapter, a theoretical analysis of thermal conductivity for nanograined polycrystalline AlN films is conducted by considering the films as a serial assembly of three layers, composed of parallelepiped grains. Such analysis is crucial to gain understanding of thermal transport in AlN films and analyze the thickness-dependent thermal conductivity measurements presented in Chapter 6. In addition, the thermal conductivity model presented here provide useful guidance to describe and control the thermal properties of materials of great interest in new technological applications such as GaN, diamond, or ZnO, which usually exhibit non-homogeneous structures.

Accurate theoretical description of the thermal properties of nanocrystalline materials is a challenging task, due to their anisotropic and heterogeneous structures which consists of grains with irregular geometry and size. The scattering events of the energy carriers inside the material increase as a result of the reduced dimensions of these grains, which adds to the effect of phonon interactions with grain boundaries and other crystallographic defects, such as oxygen impurities. Thus, the difficulty in predicting their thermal conductivity is intensified by the large number of scattering mechanisms involved. Because of this, the theoretical description of the thermal properties of polycrystalline thin films has been little explored.

To develop a model for the thermal conductivity of nanograined polycrystalline materials, the distribution of the grain shape and size along the growth direction of the film has to be taken into account. In Fig.4.1, a schematic representation of the distribution of the grain structure along the axis normal to the film plane is depicted. According to Song et al. (2011) and Belkerk et al. (2012), AlN film microstructure evolves from randomly oriented nanograins, which align into small size grains, and then coalesce to form a $c-$axis oriented columnar structure [Fig.4.1(a)].

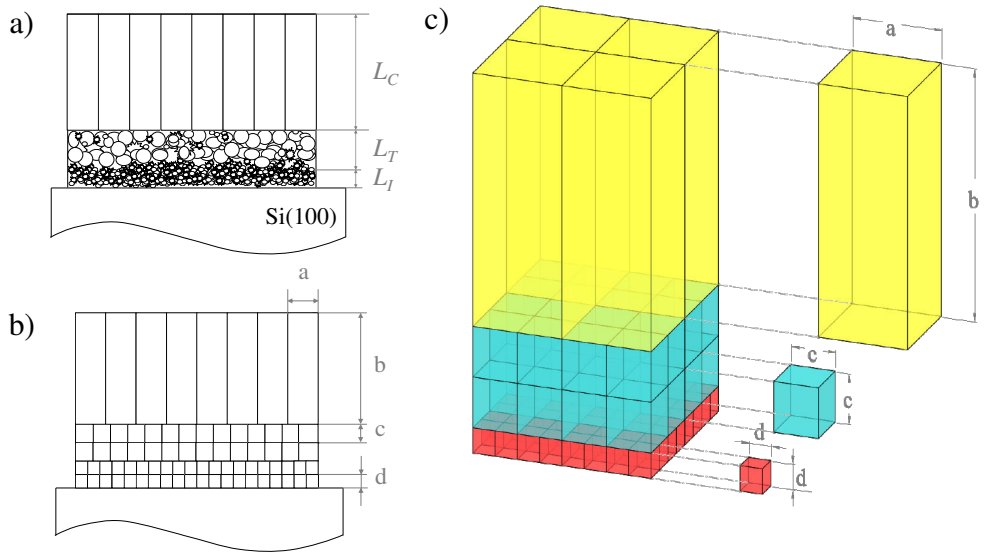

Figure 4.1: *(a) Scheme of the grain structure of AlN films on Si(100) along the cross-plane, according to Song et al. (2011) and Belkerk et al. (2012). Modeled grain structure in 2d (b) and in 3d (c), consisting of cubic grain shapes for the near-interface and transition regions, and right parallelepiped grain shapes for the columnar region.*

Based on these prior studies and the results established from a transmission electron microscopy analysis, presented in chapter 5, it was found that AlN thin films can be modeled as a serial assembly of grains, which evolve along the cross-plane. Each AlN layer can be divided into three sub-layers, namely the near-interface, transition, and columnar regions. Different grain size distributions and shapes therefore need to be considered for each region of the film.

The modeled grain structure, consists of cubic grain shapes with average lengths d and c for the near-interface and transition regions, respectively. For the columnar region, the grains were considered as right parallelepipeds with an average length a for each side of the base and an average height b. The spatial distribution of grains inside the film samples is presented in 2d and 3d in Fig.4.1(b) and (c), respectively. As shown in Fig.4.1(a), L_I, L_T and $L_C = b$ are

the thickness of the near-interface, transition, and columnar regions, respectively.

The effective thermal conductivity k_{eff} of the multilayered films given in Eq.3.30 (Section 3.6), can be written in terms of the thermal conductivity k_{AlN} of each layer of thickness L, such that:

$$\frac{NL}{k_{eff}} = \frac{NL}{k_{AlN}} + (N-1)R + R_s \tag{4.1}$$

Under the three sub-regions consideration, an AlN film behaves as a system composed of three stacked layers. Therefore its cross-plane thermal resistance L/k_{AlN} can be calculated as a sum of resistances in series arising from each structural domain:

$$\frac{L}{k_{AlN}} = \frac{L_I}{k_I} + \frac{L_T}{k_T} + \frac{L_C}{k_C} \tag{4.2}$$

where k_n represent the thermal conductivity of the interface ($n = I$), transition ($n = T$), and columnar ($n = C$) regions and L_n are the values of their corresponding thicknesses, such that $L = L_I + L_T + L_C$.

The thermal conductivity of each domain (k_n) can be calculated with an expression obtained by Majumdar (1993), who derived it from the kinetic theory (Ziman (1960)):

$$k_n = \frac{k_{0n}}{1 + 4l_n/3L_n} \tag{4.3}$$

Here k_{0n} is the bulk thermal conductivity when $L_n \to \infty$ and l_n is the mean free path (MFP) of phonons in the region n. Equation 4.3 is derived under the assumption of pure diffusive reflection of phonons at the boundaries of each region. Given the grained structure of the prepared specimens, this type of scattering is expected to be dominant. Thus, the use of this equation to model the thermal conductivity is well justified.

Because of the irregular geometry associated to the spatial distribution of grains inside the films and the increasing interfacial scattering of phonons as the characteristic size of the crystallites is scaled down, the determination of k_{0n} and l_n is quite difficult. This problem can be solved by considering the grains as right parallelepipeds to a first approximation [Fig.4.1(c)]. Under the regular grain geometry assumption, AlN films behave as a serial assembly of grains and therefore its bulk thermal resistance d_n/k_{0n} can be expressed as:

$$\frac{d_n}{k_{0n}} = \frac{d_n}{k_{gn}} + R_g \tag{4.4}$$

where k_{gn} is the thermal conductivity of a single grain with average size d_n in the direction of heat conduction in region n, and R_g is the average interface thermal resistance between grains.

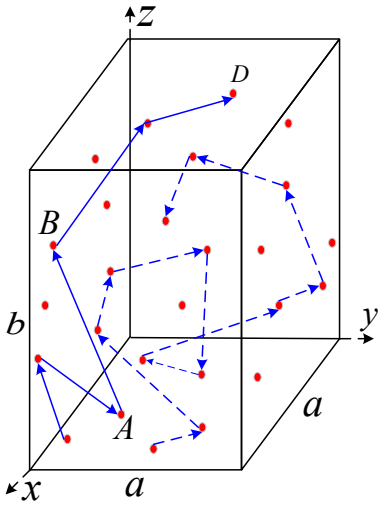

Figure 4.2: *Phonon-phonon (dashed arrows) and phonon-boundary (solid arrows) scattering processes inside a parallelepiped grain.*

Considering that the intrinsic MFP (l_0) of phonons inside the grains can be of the order of d_n, the dynamics of the carriers is not only driven by the interactions among them, but also their collisions with the inner surface of the grains, as depicted in Fig.4.2.

The influence of both scattering processes can be independently combined according to the Matthiessen's rule (Chen (2005)). Hence the effective MFP (l_n) of phonons in each grain, and therefore in each region, is given by:

$$\frac{1}{l_n} = \frac{1}{l_0} + \frac{1}{D_n} \tag{4.5}$$

with l_0 and D_n being the MFP due to the phonon-phonon and phonon-boundary scattering processes, respectively. Since these two scattering mechanisms are considered to be independent of each other, D_n can be associated to the average distance traveled by phonons inside a grain.

Furthermore, the grain thermal conductivity, k_{gn}, can be estimated using the kinetic theory (Ziman (1960)), such that:

$$k_{gn} = \frac{\rho_n c_{p_n} \nu_n l_n}{3} \tag{4.6}$$

where ρ_n and c_{p_n} are the density and the specific heat capacity of AlN, respectively, and ν_n is the phonon group velocity in bulk aluminum nitride. Assuming that the variation of the parameters ρ_n , c_{p_n} and ν_n with the presence of grains is negligible, the combination of Eq.4.5 with Eq.4.6 yields:

$$k_{gn} = \frac{k_0}{1 + l_0/D_n} \tag{4.7}$$

where $k_0 = (\rho_n c_{p_n} \nu_n l_0)/3$ is the bulk thermal conductivity of single-crystalline AlN. Using equations 4.4 and 4.7, the following expression for the bulk thermal conductivity k_{0n} is obtained:

$$k_{0n} = \frac{k_0}{1 + l_0/D_n + a_{Kg}/d_n} \tag{4.8}$$

where $a_{Kg} = R_g k_0$. This quantity is the so-called Kapitza radius of the grain boundary. Equation 4.8 implies that the effect of the interface appears for grain sizes comparable or smaller than the Kapitza radius ($d_n < a_{Kg}$), and it becomes stronger for smaller grains.

In order to find an expression for k_n, it is convenient to replace k_{0n} from Eq.4.8 in 4.3, as follows:

$$k_n = k_0 \left[\left(1 + \frac{4l_n}{3L_n} \right) \left(1 + \frac{l_0}{D_n} + \frac{a_{Kg}}{d_n} \right) \right]^{-1} \tag{4.9}$$

Using the Matthiessen's rule (Eq.4.5), k_n can be finally written as:

$$k_n = k_0 \left[\left(1 + \frac{4l_0}{3L_n} \left(\frac{1}{1 + l_0/D_n} \right) \right) \left(1 + \frac{l_0}{D_n} + \frac{a_{Kg}}{d_n} \right) \right]^{-1} \tag{4.10}$$

On the other hand, to obtain an expression for k_{AlN}, it is convenient to rewrite Eq.4.2 as:

$$\frac{k_0}{k_{AlN}} = \sum_n \left(\frac{L_n}{L} \frac{k_0}{k_n} \right) \tag{4.11}$$

where the sum is evaluated for the three regions inside the layer ($n = I, T, C$). Therefore, the combination of equations 4.10 and 4.11, yields:

$$\begin{aligned} k_{AlN} = k_0 \Bigg[1 + \frac{l_0}{L} \left(4 + \sum_n \frac{L_n}{D_n} \right) \\ + \frac{a_{Kg}}{L} \sum_n \left(\frac{L_n}{d_n} + \frac{4l_0/d_n}{3(1 + l_0/D_n)} \right) \Bigg]^{-1} \end{aligned} \tag{4.12}$$

Equation 4.12 indicates that the reduction of the bulk thermal conductivity in a polycrystalline film mainly arises from the reduced dimensions of the system and the diffusive scattering due to phonon-boundary interactions within the grained structure. It is noteworthy that the contribution of a_{Kg} is weighted by the total number of grain rows, which is given by $\sum_n L_n/d_n$.

Moreover, assuming pure diffusive reflection of the energy carriers at the grain boundaries, Chen (1998) has shown that the interfacial thermal resistance among grains R_g, is given by:

$$R_g = \frac{2}{\rho_n c_{p_n} \nu_n} \tag{4.13}$$

Considering the typical values for the density ($\rho_{AlN} = 3260$ kg m^{-3}), specific heat capacity ($c_{p_{AlN}} = 600$ J kg^{-1} K^{-1}) and phonon speed ($\nu_{AlN} = 4210$ m s^{-1}) in AlN at room temperature, the grain interfacial thermal resistance is estimated as $R_g = 2.4 \times 10^{-10}$m^2 K W^{-1}. This value is at least two orders of magnitude smaller than the one of the AlN film-Si substrate and AlN layer-AlN layer interfaces, as shown in chapter 6. Therefore, this suggests that the grain-grain resistance has a relatively small contribution to the reduction of the effective thermal conductivity (k_{eff}), as indicated by equations 4.1 and 4.12.

To determine the MFP of phonons in the columnar region (D_c), diffusive scattering at the grain interfaces is assumed. By this means, the energy carriers are reflected from the grain boundaries with equal probability to any direction, as is the case for rough interfaces. From Fig.4.2, it can be seen that the symmetry of the problem establishes that the mean free distance traveled by a phonon from an arbitrary point $A = (x, y, 0)$ on the plane $z = 0$ to any other point on the four adjacent planes is the same. In terms of the points $B = (\zeta, 0, z)$ and $D = (\xi, s, b)$, where ζ, ξ, s and b are arbitrary coordinates on the adjacent and parallel planes to $z = 0$, this condition yields $5D_c = 4I_1 + I_2$ where :

$$I_1 = \frac{1}{a^3 b} \int_0^b \int_0^a \int_0^a \int_0^a \sqrt{(x-\zeta)^2 + y^2 + z^2}\; dx\; d\zeta\; dy\; dz \tag{4.14}$$

$$I_2 = \frac{1}{a^4} \int_0^a \int_0^a \int_0^a \int_0^a \sqrt{(x-\xi)^2 + (y-s)^2 + b^2}\; dx\; d\xi\; dy\; ds \tag{4.15}$$

The integrals stated in Eq.4.14 and Eq.4.15 can be evaluated using a convenient computer algebra system (CAS), such as Mathematica, Matlab or Maple. The obtained results for the MFP D_C due to phonon-grain interface collisions are shown in Fig.4.3.

For large parallelepiped grains where $b \gg a$, D_C exhibits a linear behavior as a function of a mean distance equal to the sum of a fraction of the length of its sides. On the other hand, for cubic grain shapes $b = a$, $D_C = 0.926a$. This indicates that the mean distance traveled by a phonon between two random points before experiencing a collision is 7.3 % smaller than the length of the cubic grain sizes. The geometric MFPs inside the grains of the near-interface and the transition regions are therefore $D_I = 0.926d$ and $D_T = 0.926c$, respectively.

Finally, the effective thermal conductivity of a multilayer structure can be derived from equations 4.1, 4.7 and 4.12:

$$k_{eff} = k_0 \left[\frac{k_0}{k_{AlN}} + \frac{a_{Ks}}{NL} + (N-1)\frac{a_K}{NL} \right]^{-1} \tag{4.16}$$

being $a_{Ks} = R_s k_0$ and $a_K = R k_0$, which represent the Kapitza radii of the Si-substrate/AlN-film and AlN-layer/AlN-layer interfaces, respectively. The

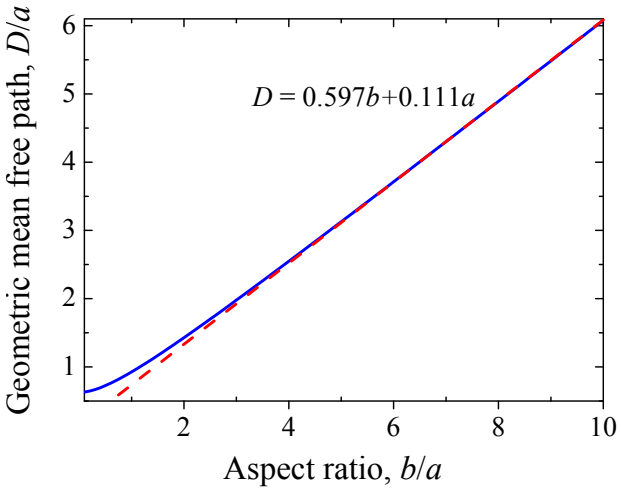

Figure 4.3: *Mean free path of phonons due to their collisions with the inner surface of a parallelepiped grain.*

denominator in equation 4.16 indicates the reduction of the bulk thermal conductivity k_0 due to the effects of the grain size, layer thickness, and interface thermal resistance.

The contribution of each of these parameters to the reduction of the thermal conductivity of nanoscale polycrystalline AlN films in comparison with their bulk single-crystalline counterparts, is determined by their relative values with respect to the total film thickness. It is worth noting that for monolayer systems with $N = 1$, the effect of the Kapitza radius a_K disappears, as expected.

Equation 4.16 was used to obtain the theoretical values of k_{eff} for both monolayer and multilayer sets of samples, which are presented in chapter 6 below. The bulk thermal conductivity $k_0 = 250$ W m^{-1} K^{-1} and phonon MFP $l_0 = 110$ nm of AlN were taken from Morkoc (2009) and Slack et al. (1987) to perform the calculations. All other variables involved in equations 4.12 and 4.16, such as thicknesses and grain size distributions of each structural domain, and thermal boundary resistances were measured experimentally by statistical analysis of electron micrographs and the differential 3ω method. The experimental results obtained from the crystallographic and structural studies, used to describe phonon transport in AlN films through this analytical model, are presented in the chapter that follows.

Part III

Results and discussion

Chapter 5

Microstructure and crystallographic analysis of Aluminum Nitride films

Phonon transport in nanocrystalline films has proven to be directly related to the structural features present within the films. To explore this relationship, the accurate characterization of grain morphology and size is necessary. Understanding the growth mechanisms and evolution of texture along the cross-plane of polycrystalline AlN films is crucial to describe their thermal conductivity. This chapter reports on the structural and chemical characterizations performed to explain phonon transport phenomena in the studied samples. First, the preferred orientation, crystalline structure, and out-of-plane disorientation were studied by $\theta - 2\theta$ and ω X-ray diffraction (XRD) scans. Then, the microstructure and the distribution of crystallographic orientations along the cross-plane were investigated by transmission electron microscopy. Furthermore, atomic structure, grain boundaries, and crystallite sizes were analyzed. The grain structure and size evolution were investigated by statistical analysis of digitally processed micrographs, obtained with both transmission and scanning electron microscopy. Finally, chemical composition was studied by EDX analysis. The results here obtained are later used to correlate, through an analytical model, the structural features and multiscale defects with the cross-plane thermal conductivities measured for polycrystalline AlN films in Chapter 6.

5.1 Texture evolution and out-of-plane accommodation through film thickness

As explained in Chapter 1, it has been observed that the crystalline structure of AlN films exhibit striking differences between the region near the substrate

interface and the outer surface of the film (Belkerk et al. (2012), Duquenne et al. (2012)), which can strongly affect thermal conduction processes. In this work, this structural evolution was first investigated using XRD techniques, and the results are presented below.

5.1.1 Preferred orientation : $\theta - 2\theta$ scans

Figure 5.1 shows XRD $\theta - 2\theta$ spectra of monolayer and multilayer AlN samples of different thicknesses. The AlN $\theta - 2\theta$ spectra can be indexed to the hexagonal structure with space grouping $P6_3mc$ (Hermann-Mauguin notation), corresponding to the wurtzite phase with lattice parameters a and c of 3.11 Å and 4.98 Å, respectively (Fig.2.1).

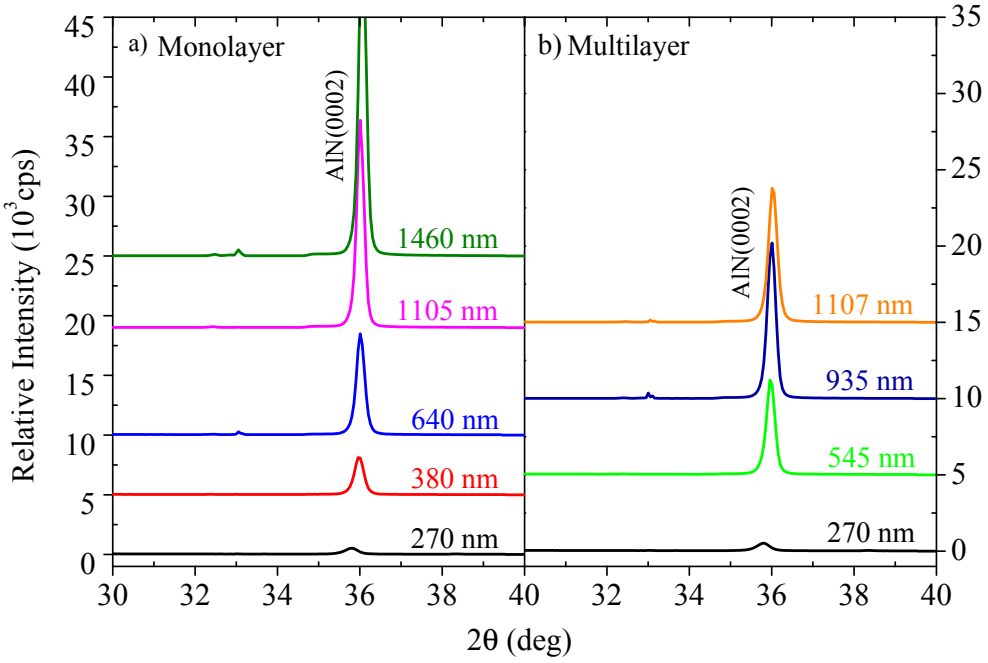

Figure 5.1: *XRD $\theta-2\theta$ scan patterns of the AlN a) monolayer and b) multilayer films of different thicknesses. Black, green, blue and orange solid lines refer to multilayers $L_1 = 1 \times (\approx 270$ nm), $L_2 = 2 \times (\approx 270$ nm), $L_3 = 3 \times (\approx 270$ nm) and $L_4 = 4 \times (\approx 270$ nm) respectively.*

According to the standard diffraction powder pattern of w-AlN (JCPDS-ICDD file No. PDF 00-025-1133 from the diffraction database), a film composed of randomly oriented crystallites, examined with Cu K_α radiation in a Bragg-Bretano configuration, would produce diffraction peaks of significant intensity at 2θ angles of 33.216°, 36.041° and 37.917°. The diffracted intensities related to the above-mentioned angles correspond to the $(10\bar{1}0)$, (0002) and $(10\bar{1}1)$

families of planes. However, in Fig.5.1 only the Bragg peaks corresponding to the diffraction planes (0002) are observed near $2\theta = 36.04°$ for all samples. Thus, both configurations exhibit strong out-of-plane fiber texture along the [0001] direction. The absence of other additional AlN peaks in the XRD patterns suggest that precipitation or formation of a secondary phase does not occur, as expected. AlN is a line compound (*i.e* it does not have variable composition neither intermediate phases) and wurtzite is the thermodynamically stable structure under ambient conditions. It is noteworthy to mention that the $\theta - 2\theta$ geometry (Bragg-Brentano) used to obtain the patterns showed in Fig.5.1, only allows to collect diffracted X-rays from crystal lattice planes that are parallel to the film surface. The presence or absence of an in-plane-texture of the film is therefore not characterized by these spectra.

From Fig.5.1, it can be seen that the intensity of the (0002) AlN diffraction peak gradually increases with the film thickness, for both the monolayer and multilayer systems, as a result of a mixed contribution to coherent scattering of additional atomic planes and better out-of-plane crystallite alignment (Fig.5.6). The increase of the peak intensity as a function of the film thickness measured in multilayers is lower compared to the one in monolayers. The reduced intensity of the diffracted beam can be attributed to larger crystallite disorientation and to the presence of oxygen-related defects at AlN/AlN interfaces in multilayers, which do not diffract X-rays (this interfacial local oxidation was evidenced by EDX analysis and will be discussed in section 5.5).

Furthermore, as the film thickness increases (for AlN monolayers and multilayers), the observed (0002) peak shifts towards higher angles. As explained by Darakchieva et al. (2004), this peak shift probably arises from strain lattice relaxation mechanisms occurring through the cross-plane. The slight (0002) peak shift towards higher angles can be clearly observed by plotting the logarithm of the relative intensity as a function of the 2θ angle, from 32.7° to 38°, as shown in Fig.5.2. The thickness dependent 2θ angle varies from 35.8° to 36.04° for monolayer films, with thicknesses varying from 270 nm to 1460 nm. The same 2θ angle shift is observed for multilayer films of thicknesses varying from 270 nm to 1107 nm.

The effect of uniform strain on the direction of the X-ray reflection (parallel to the sample surface) is illustrated in Fig.5.3. When a thin film is subjected to out-of-plane uniform tensile strain, the spacing of the reflecting planes parallel to the sample surface become larger than the one of an unstrained film. The corresponding diffraction peak therefore shifts toward lower angles (Cullity (1978)).

Strain within a thin film can be either extrinsic or intrinsic. The former is imposed by unintended external factors such as temperature gradients, and the latter is associated to changes in the internal structure of the material, due to substitutional impurities during growth, grain structure or fabrication process

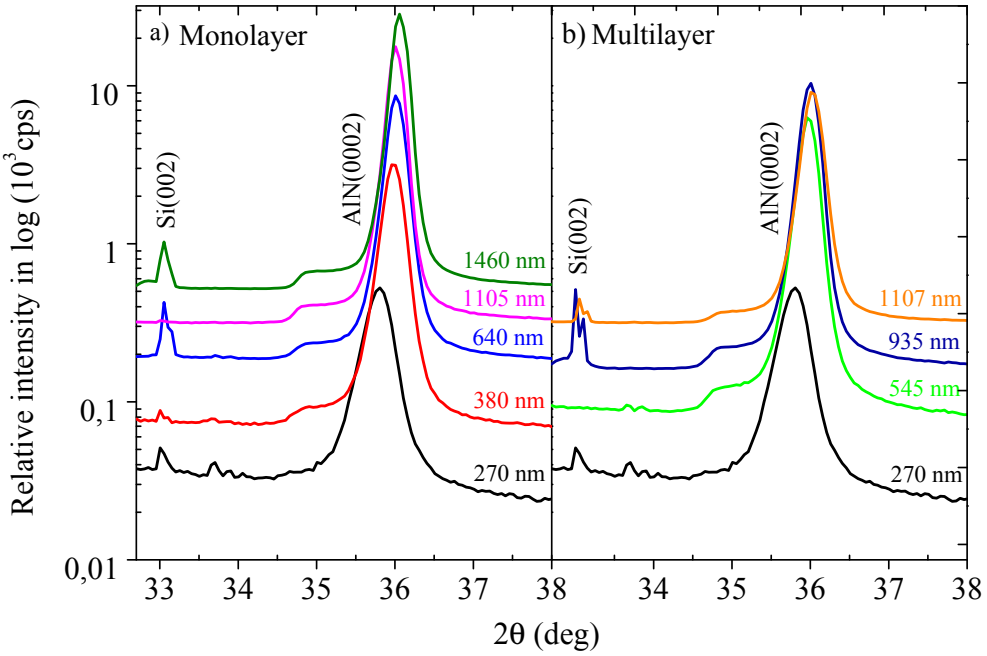

Figure 5.2: *XRD $\theta - 2\theta$ scan patterns of the AlN a) monolayer and b) multilayer films of different thicknesses.*

defects. Extrinsic strain is commonly uniform through the thickness and is evidenced by XRD techniques when the corresponding diffraction peak shifts to lower angles (in the case of out-of-plane tensile strain) but does not otherwise change its shape, as shown in Fig.5.3. On the other hand, intrinsic strain is generally non-uniform and in XRD $\theta - 2\theta$ can be identified as a broadened diffraction peak. The overall peak shift observed in Fig.5.2 can therefore be attributed to extrinsic strain within the film. Extrinsic strain occurs mainly from adhesion to the substrate. Thus, there are two major phenomena that can explain the (0002) peak shift in AlN films: induced strain due to differential thermal expansion and/or lattice mismatch between the film and the substrate.

Under room temperature conditions, the coefficient of thermal expansion of monocrystalline diamond silicon is 2.62 $\times 10^{-6}$ K^{-1} (Hull (1999)), while that of wurtzite aluminum nitride (for the a lattice parameter) is 4.2 $\times 10^{-6}$ K^{-1} (Morkoc (2009)). In the deposition process, AlN species impinge on the Si substrate with high kinetic energy, increasing the temperature of the system to about 100°C. When the deposition is completed, the film-on-substrate samples experience a temperature drop until thermal equilibrium is reached at room temperature. This cooling process causes the lattice of AlN films to shrink, but this contraction is restricted due to its adhesion to the substrate, which experiences a lower deformation. This effect causes the AlN unit cell to remain subjected to tensile strain in the direction parallel to the surface, therefore exhibiting larger interatomic spacing compared to an unstrained AlN film.

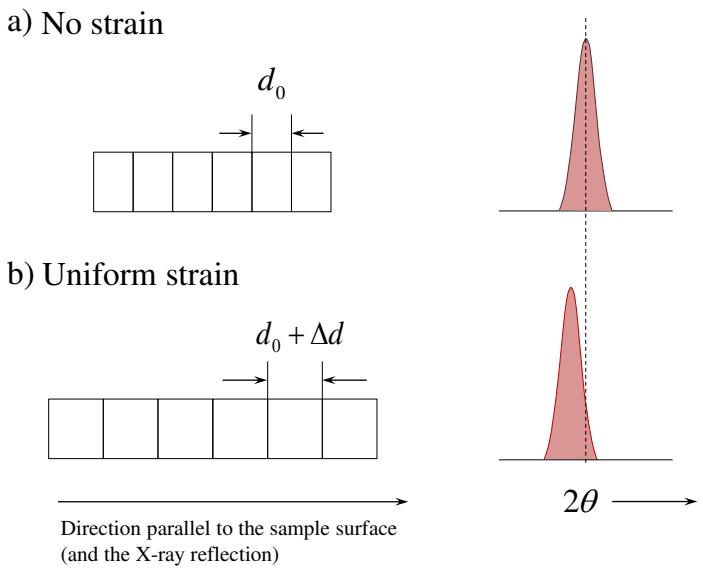

Figure 5.3: *Effect of lattice strain on diffraction peak position. Position of a diffraction peak for a) a non-strained thin film with lattice spacing d_0 and b) a strained film with increased lattice spacing $d_0 + \Delta d$ in the direction parallel to the sample surface (and therefore the X-ray reflection).*

On the other hand, the a lattice parameter for Si and AlN are 5.43 Å and 3.11 Å, respectively. Therefore, a lattice spacing change can occur within the AlN films, because of the growth mechanisms settled up to accommodate the large lattice mismatch at the region near the interface with the silicon substrate.

Larger interatomic spacing generated by both mentioned phenomena can be detected by the diffraction of XRD peaks that shifts towards lower angles. However, the differential thermal expansion mechanism is more likely to be at the origin of the (0002) AlN peak shift. The reason is that lattice mismatch should not play an important role because, in our experiments, AlN does not grow directly onto the bare Si surface, but onto the native oxide layer formed at the surface of the silicon substrate. The presence of this SiO_x layer was evidenced by EDX analysis, which will be detailed in section 5.5. This oxide layer usually appears when the silicon native oxide is not removed in-situ before deposition (Saga et al. (1999), Choi et al. (2001)), as is our case.

From Fig.5.2, it is possible to observe that thinner films exhibit higher strain, evidenced by the diffraction of the (0002)AlN peak at lower angles. This can be therefore explained by the growth mechanisms causing a lattice spacing increase, due to the induced strain generated by different thermal expansion coefficients. The growth mechanism causing an increase of the lattice spacing

should take place in all studied samples, nonetheless the peak shift is observed exclusively for thinner films. Since thinner films have less diffracting planes compared to thicker films, the contribution of the strained planes to coherent scattering is significantly higher than the one of their thicker counterparts, in which the crystal planes that accommodate the lattice spacing as the film grows have a more significant contribution.

It is noteworthy that an additional peak located at $2\theta = 32.91°$ is observed for several monolayer and multilayer samples in Fig.5.2. The diffraction angle of this Bragg peak coincides exactly with the (002) reflection of silicon, although it should be typically absent by symmetry. That is because, for some crystals, there are particular atomic arrangements which reduce the intensities of some diffracted beams to zero. The allowed or missing reflections are described by the selection rules, which are derived from the structure factor, a mathematical description of the resultant wave scattered by all the atoms of a unit cell.

For example, the expected reflections in a diamond cubic structure, such as silicon, are given by the selection rule $h + k + l = 4n$, where n is any positive integer and h, k, and l are unmixed Miller indices i.e. h, k, l are all odd or all even. Conversely, the forbidden reflections are given by the selection relation $h + k + l \neq 4n$, where h, k, l are mixed or all even (Cullity (1978)). Hence, for single crystalline (001)Si, the only diffraction peak expected is the (004) reflection, because other (00l) reflections are necessary absent due to their vanishing structure factors. However, the peak located at $2\theta = 32.91°$ has been usually observed in $\theta - 2\theta$ XRD scans (Burnette et al. (2008), Lim et al. (2005), Reynolds et al. (2012), Carvalho and Menezes (2013), Lee and Schlesinger (1988)). In fact, the significant intensity of the peak originates from multiple diffraction effects, as reported by Hwang (2001). In other words, the beam is diffracted from consecutive scattering caused by different planes in the silicon substrate. Hence, the final diffracted beam may appear to correspond to a forbidden reflection.

From the $\theta - 2\theta$ scans it was observed that all AlN samples exhibited a textured structure oriented in the [0001]-direction. In addition, the increase of the (0002) peak with film thickness suggested that thicker films are better aligned than thinner ones. However, from $\theta - 2\theta$ scans is not possible to determine the degree of orientation of the crystallites within the film. To quantitatively characterize the quality of the film texture, ω-scans were performed and the results will be discussed in the following section.

5.1.2 Out-of-plane disorientation : ω scans

The quality of the texture of the polycrystalline samples was analyzed by performing ω-scans of the (0002)AlN reflection. The average out-of-plane disorientation of monolayer samples, represented by the full width half maximum (FWHM) of the X-ray rocking curve measurements is presented in Fig.5.4.

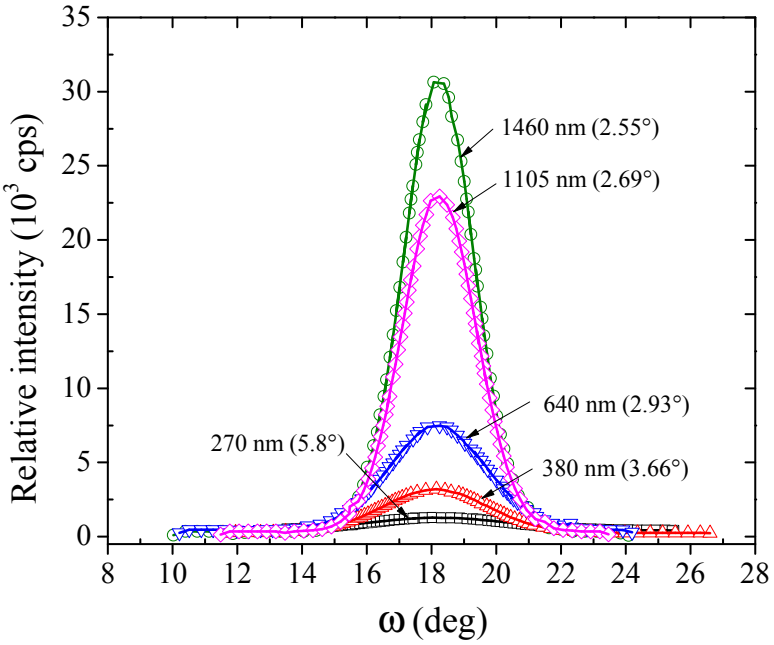

Figure 5.4: *XRD rocking curves (ω-scans) of the* (0002) *reflection of monolayer films of different film thicknesses.*

From 5.4, it is possible to observe that while the intensity of the peaks essentially increases for thicker films, the base shape of the curves remains identical, indicating similar nucleation mechanisms and growth conditions in monolayered samples of different thicknesses (Felmetsger (2011)). Furthermore, the degree of crystallographic orientation remains reasonably high even for thin samples, as observed for the ≈ 270 nm thick monolayer specimen, which exhibits a FWHM of 5.8°.

The (0002) rocking curves measured for a monolayer and a multilayer of approximately equivalent thickness are shown in Fig.5.5 for comparison. The ω-scan associated to the ≈ 1107 nm thick multilayer exhibits lower intensity when compared to its monolayer counterpart of ≈ 1105 nm, suggesting that the interfacial oxidation (section 5.5) slightly increases the average out-of-plane disorientation. Yet, both configurations present the same base shape, in a way similar to that of the monolayer set of samples. This result indicates that whereas interfacial oxidation limits to some extent the growth of well-oriented crystallites, it does not have significant influence in nucleation and growth mechanisms.

Figure 5.6 depicts the rocking curve FWHM values associated to both monolayer and multilayer samples, as a function of film thickness. For both sets of samples, it can be observed that the FWHM value of the rocking curve decreases with the increase of the film thickness.

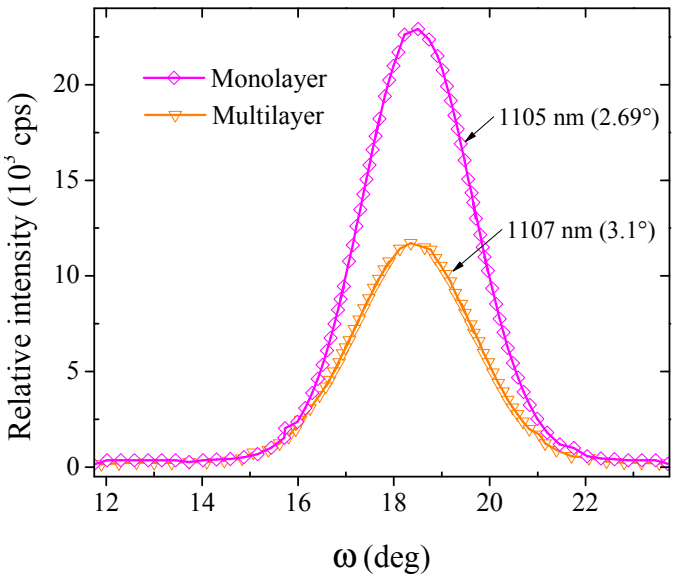

Figure 5.5: *Comparison between* (0002) *rocking curve measurements for a monolayer and a multilayer of equivalent thickness.*

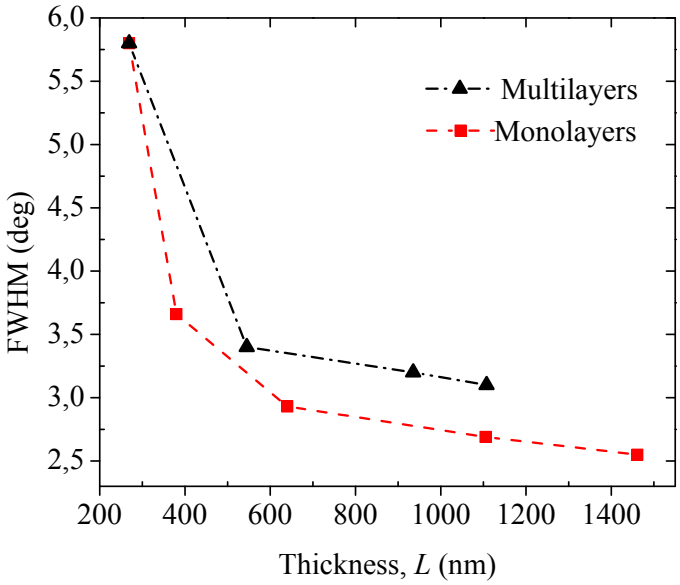

Figure 5.6: *FWHM values of the* (0002) *XRD rocking curves of monolayer and multilayer films as a function of the film thickness.*

The sharpening of the angular distribution of the crystalline orientation with increasing film thickness, observed for monolayers in Fig.5.4, and for both configurations in Fig.5.6, can be associated to the competitive growth mechanisms occurring as the film grows. It has been shown by Knuyt et al. (1995) that

the dependence of the textural evolution on the energy dissipation per volume is related to the increase of the effective temperature of the surface atoms, which cause a sharpening of the angular distribution of the crystalline orientation. During the AlN deposition, the temperature increases with deposition time due to the high impact energy of the species impinging the substrate. At higher temperatures, an increased number of grain boundaries become mobile, resulting in the lateral growth of grains. As a result of this process, a preferred orientation develops and strengths gradually with thickness.

The orientation selection is determined by the family of crystallographic planes with the direction of fastest growth. Thus, the faster growing crystallites will dominate over the slower growing ones, leading to a texture controlled by minimization of the surface energy (Barna and Adamik (1998)). Particularly, the development of a preferred out-of-plane orientation of AlN films in the $c-$axis direction has been identified as the result of competitive growth of (0001) planes over $(10\bar{1}0)$ planes. Additionally, it has been shown that a relationship exists between the energy supplied to the adatoms during the growth and the different growth rates on both families of planes. Higher energies promote overgrowth and coalescence of grains oriented along the [0001] direction (Clement et al. (2003)). In other words, the (0002) oriented small-grains formed at the interface with the silicon substrate, further connect and transfer to bigger grains with the same growth direction, favored by the energy supplied in the deposition process. Since deposition conditions promote higher growth rate in the [0001] direction, more and more $(10\bar{1}0)$ oriented grains are buried by adjacent (0002) oriented crystallites. This "competition" finishes when crystallites exhibiting the (0002) crystal faces proceed to the free surface (Barna and Adamik (1998)). The described competitive growth and coalescence processes are governed by the tendency to reduce the surface energy, which has been identified as the driving force for the evolution in crystal growth (Knuyt et al. (1996)).

On the other hand, the lower out-of-plane texture observed in multilayers compared to the one in monolayered structues, can be explained by the presence of oxygen atoms at interstitials and lattice sites. This localized oxidation possibly induces crystal defects that limit the subsequent well-oriented crystallite growth, therefore increasing the FWHM of the multilayer rocking curves.

Although XRD techniques give useful insights into texture development mechanisms, electron transmission microscopy allows to precisely characterize the various crystallographic features present in different regions along the film thickness. Furthermore, electron microscopy techniques open up the possibility of accurately measure the grain structure and size evolution, whereas XRD methods have proven to be less adapted to quantitatively determine crystallite sizes in heterogeneous structures (see section 2.3.2 in Chapter 2). The results of the electron microscopy investigation for AlN samples are discussed below.

5.2 Microstructure and crystallite orientation : TEM

In this section, the evolution of the microstructure, as well as the morphology and size of grains along the cross-plane, are investigated by a transmission electron microscopy study. Three different AlN samples were analyzed for comparison. First, to gain an overall understanding of mechanisms involved in the growth of highly textured films, monolayer and multilayer samples of about 640 nm and 935 nm [$L = 3 \times (\approx 270$ nm)] were studied. Then, to identify the factors governing texture development, a poorly textured (FWHM = 8.5°) monolayer of 850 nm was investigated. These 3 samples were also studied by strain-mediated thermal conductivity measurements (section 6.2 of Chapter 6).

For this study, all micrographs were captured along the [011] zone axis of silicon, which was parallel to the electron beam. A cross sectional bright field TEM image of the ≈640 nm thick monolayer is shown in Fig.5.7.

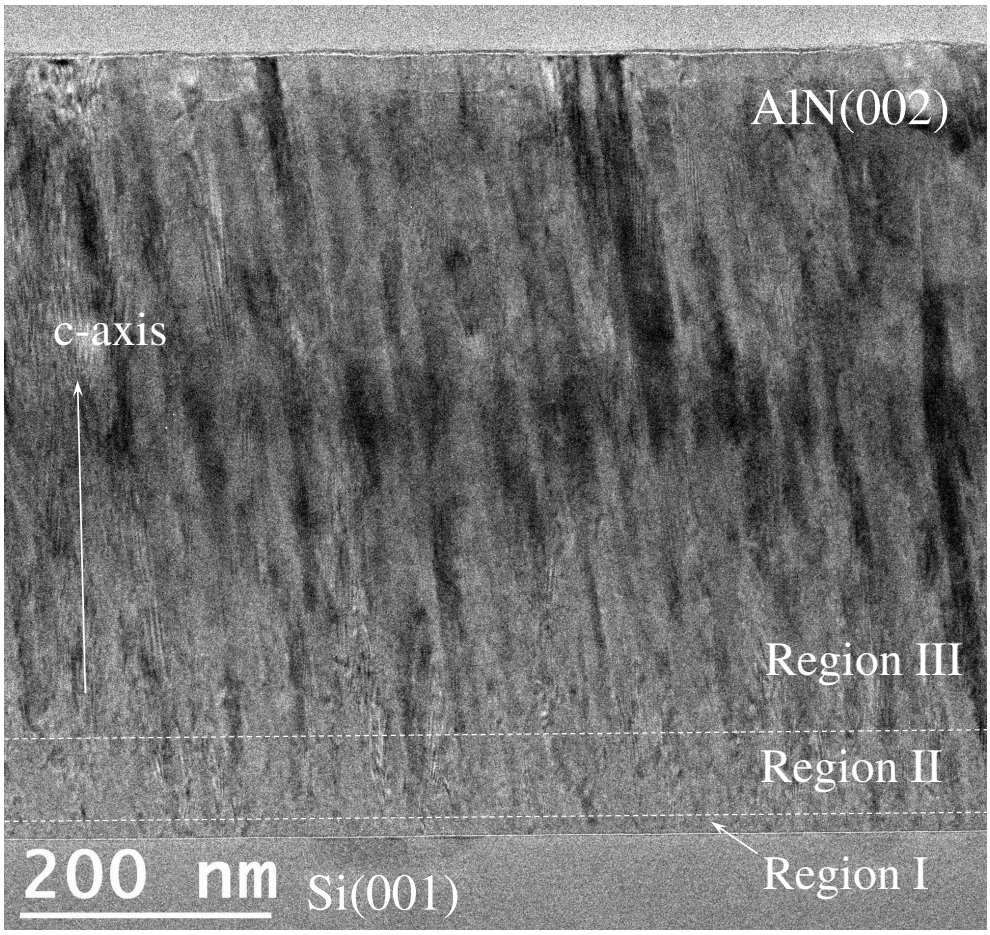

Figure 5.7: *Cross sectional bright field TEM image of a highly c-axis oriented 640nm thick AlN monolayer film, obtained along the zone axis [0 1 1] of silicon.*

Equivalent microstrucutural features were found for the 3 analyzed samples, as can be seen in Fig.C.1 (Appendix C). Therefore, it can be said that Fig.5.7 represents the global microstructure of AlN films deposited in this study.

It is possible to observe that AlN films feature a columnar structure, which is characteristic of the zone T or transition zone of the Thornton zone model (Thornton (1977)), described in section 2.2.4 of Chapter 2. This V-shaped columnar structure is typically found in AlN films sputtered without any external heating, occurring at normalized substrate temperatures between 0.1 and 0.3, and pressures well below 1 mbar (Boeshore (2006)), as is our case. The individual columns are dense, indicating sufficient adatom surface mobility to sustain local crystal growth. Columns also exhibit slightly faceted tops, which is due to atomic shadowing (Petrov and Barna (2003)). Furthermore, a clear structural non-homogeneity along the $c-$axis can be observed.

Three different structural domains can be identified from Fig.5.7: the region I near the interface with the silicon substrate, where the column boundaries can not be observed, the region II between the columnar and near-interface region, where column boundaries become recognizable, and the region III or columnar region, where the grains are large, exhibiting defined column boundaries and diameters that increase with layer thickness. Each of these domains was analyzed in detail by high resolution transmission electron imaging (HRTEM) and by its corresponding fast Fourier transform (FFT) pattern, which gives information about the reciprocal lattice. The results are analyzed in next sections. In order to identify planes, orientations and zone axes in AlN samples, FFT patterns were indexed by the JCPDS-ICDD file used for XRD analysis (No.00-025-1133). On the other hand, the FFT pattern associated to the silicon substrate was indexed to the cubic structure with space grouping $Fd3m$ (Hermann-Mauguin notation), corresponding to the diamond phase with lattice parameter a of 5.43 Å (JCPDS-ICDD file No.00-027-1402). The TEM Fast Fourier transform pattern of Si(100) can be found in Fig.D.1 of Appendix D. Indexation was performed by measuring the distance between the center and the diffraction spots in the array, which corresponds to the reciprocal lattice.

5.2.1 Domain I: The region near the interface with the silicon substrate

An atomic resolution micrograph (HRTEM) of the near-interface region for a $\approx$ 640 nm monolayer is shown in Fig.5.8(a), along with its corresponding fast Fourier transform pattern (b). At the interface with the silicon substrate, a continuous interlayer with a disordered atomic structure is observed within a limited thickness of a few nanometers ($\approx$ 3 nm). Previous works (Song et al. (2011), Hwang (2001) have reported that such amorphous interfacial layer is composed of SiO_x, and arises either from the native oxide formed at the surface

of silicon substrate, or from the reaction of residual oxygen in the vacuum chamber. Other studies attributed the composition of this disordered structure to Si-N bounds creation at the early stage of AlN growth, when N_2 first interacts with the Si substrate (Darakchieva et al. (2004)). The associated FFT shown in inset of 5.8(a) exhibit a random pattern with a large nearly-homogenous white spot, typical of an amorphous phase, confirming the highly disordered atomic structure of this interfacial layer. To reveal de chemical nature of this layer, EDX analyses were performed and the results are further discussed in section 5.5 of this chapter.

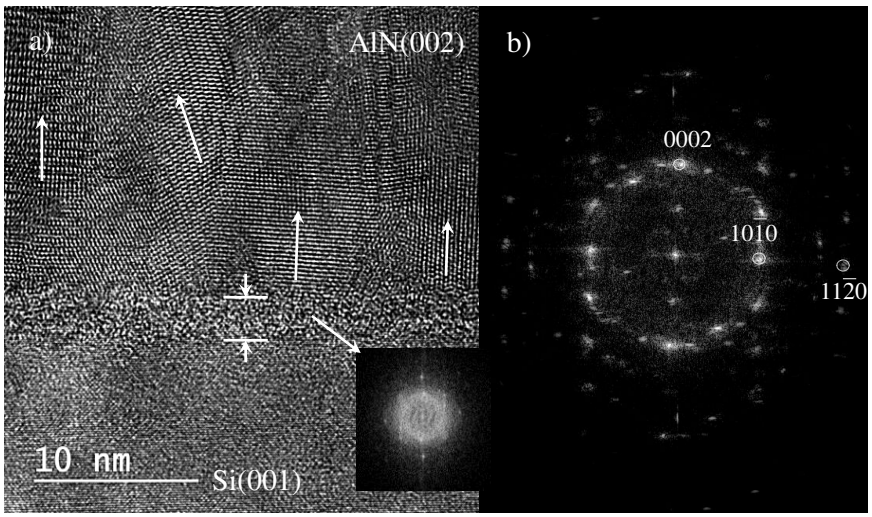

Figure 5.8: *a) HRTEM close-up view of the near-interface region (domain I), revealing an amorphous-like layer of about 3 nm at the Si/AlN interface and b) its corresponding indexed FFT pattern.*

Immediately after the disordered layer, at the near-interface region, a polycrystalline region, evidenced by periodical bright and dark contrasts, can be identified. The growth of this polycrystalline domain begins directly from the limit of the amorphous interlayer, and is composed of small crystallites of about 4 nm. The corresponding FFT pattern shown in Fig.5.8(b), reveals that (0002), (10$\bar{1}$0) and (11$\bar{2}$0) atomic planes form at an early growth stage. The heterogeneous spot arrangement forming diffraction rings evidences the near random orientation of these families of planes. From HRTEM micrographs, thicknesses of 3.9, 3.7 and 2.9 nm were measured for the near-interface region of monolayer, multilayer and poorly textured samples, respectively.

5.2.2 Domain II: The micro-crystalline transition region

A HRTEM close-up view of the first 40 nm of the transition region, captured from the 640 nm monolayer sample, is presented in Fig.5.9.

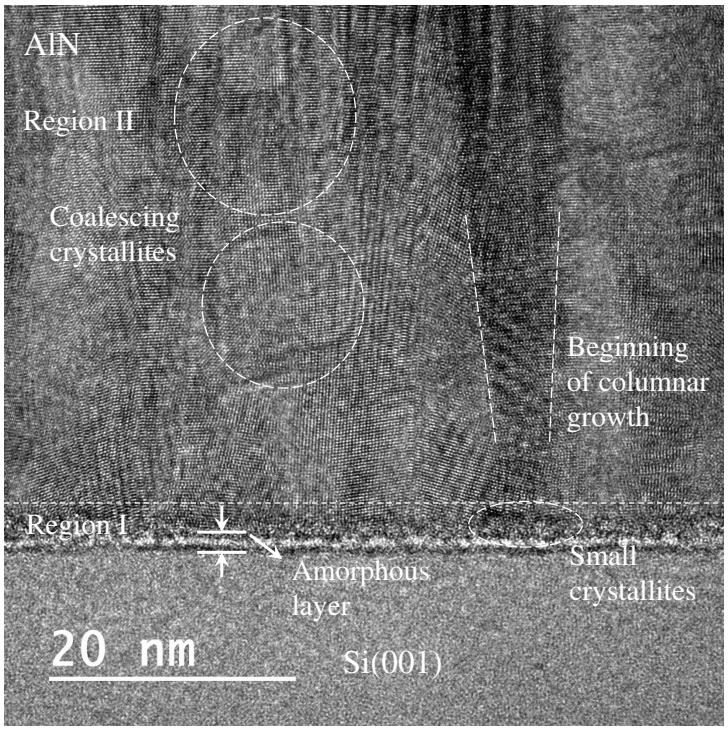

Figure 5.9: *HRTEM close-up view of the beginning (first 40 nm) of the micro-crystalline transition region (domain II), revealing the amorphous-like layer of about 3 nm at the Si/AlN interface, the coalescence of small crystallites, and the initial growth stage of a columnar grain.*

Both region I and region II can be identified in the micrograph. They are separated by a white dashed line. At the near-interface zone (domain I), Fig.5.9 reveals the amorphous layer reported above, and immediately after, very small crystallites of about 2 nm of diameter. Within the first 30 nm of the micro-crystalline transition region (domain II), the presence of larger crystallites ($\approx$ 6 nm of diameter), which coalesce to form the base of a columnar grain can be observed, as indicated by the dashed circles. Furthermore, Fig.5.9 evidences the initial growth stage of a V-shaped columnar grain with a diameter that increases with film thickness, as pointed out by the non-parallel dashed lines.

Figure 5.10(a) is a cross-plane HRTEM micrograph of the transition region, captured at a distance from the silicon substrate of about 160 nm, at the limit of the transition domain with the columnar region. At this thickness value, a columnar grain with (0002) orientation can be identified. The lattice planes

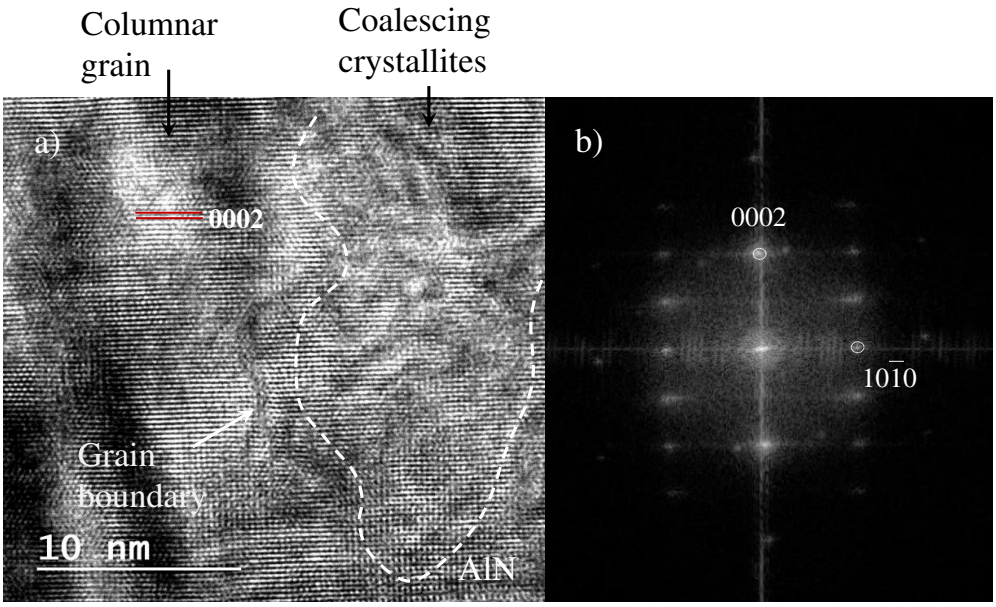

Figure 5.10: *a) HRTEM close-up view of the micro-crystalline transition region (domain II) at the limit with the columnar domain, revealing a (0002) oriented columnar grain (red parallel lines) and its grain boundary. Coalescing crystallites of different shapes and grain sizes can also be identified (dashed white line). b) shows the corresponding indexed FFT pattern.*

of $d-$spacing of 0.249 nm, corresponding to the (0002) family of AlN planes, are clearly observed through the columnar grain, as indicated by the parallel red lines. The weaker contrast at the grain boundary indicates the presence of local disorder. Also, coalescing crystallites with irregular shapes and sizes can be identified in the region next to the grain boundary, as marked by the dashed white line. The FFT pattern shown in Fig.5.10(b) reveals a dominant c-axis preferred orientation, which is due to the overgrowth of (0002) oriented grains with higher perpendicular growth rate, with respect to other detected orientations (Shetty (2012)).

5.2.3 Domain III: The columnar region

Figure 5.11(a) is a HRTEM micrograph of two neighbor columns in the columnar region. The observed contrast difference between columns is very likely due to the different in-plane orientations of the columnar grains. A highly ordered structure along the $c-$axis can be inferred from Fig.5.11, where only (0002) lattice planes of $d-$spacing of 0.249 nm are observed. The grain boundary between both columns appears with a weaker contrast, indicating the presence of

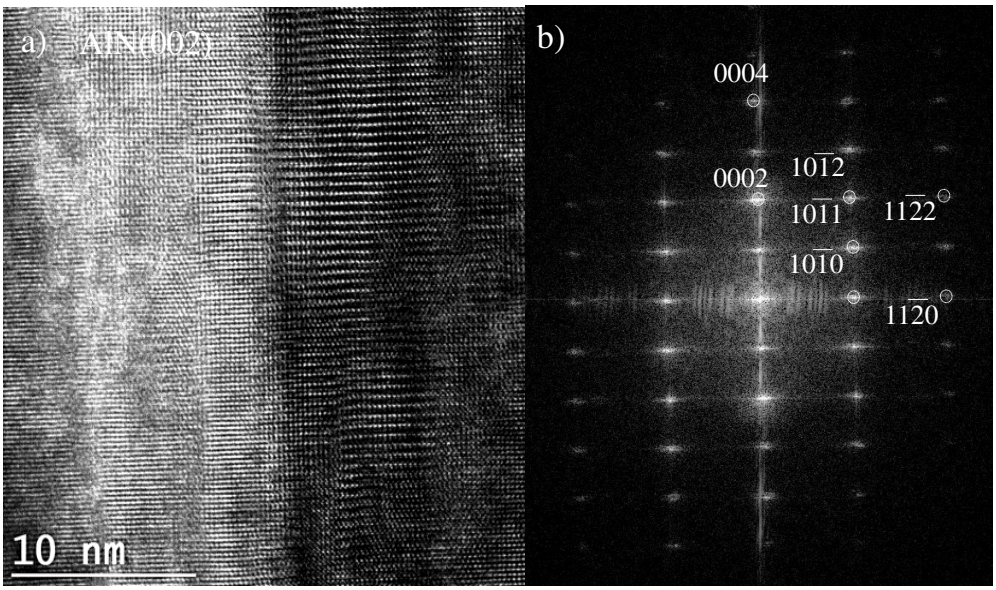

Figure 5.11: *a) HRTEM micrograph of two adjacent columnar grains in the columnar region (domain III), and b) its corresponding indexed FFT pattern.*

local disorder. The corresponding FFT pattern (Fig.5.11(b)) scatters the characteristic spots of (0002) atomic planes and their (0004) reflection, indicating the exclusive presence of the (0002) preferred orientation, and thus confirming the high periodicity array of the AlN crystal lattice in the columnar region. The scattered spots corresponding to the (0002) and (0004) have zone axes along the $[11\bar{2}0]$ and $[10\bar{1}0]$ directions, and the characteristic spots associated to the $(10\bar{1}0)$ and $(11\bar{2}0)$ families of planes have a zone axis along the [0001] direction.

5.2.4 Multilayers

Multilayer films exhibit very similar structural features compared to monolayer samples. A HRTEM micrograph of the near-interface region from a $L = 3 \times (\approx 270$ nm) multilayer and its corresponding indexed FFT pattern, shown in Fig.5.12, evidence the similarities in growth mechanisms for both sets of samples. Again, an amorphous layer of about 3 nm can be identified at the surface of the silicon substrate. Directly onto the amorphous layer, small crystallites of different shapes and sizes (< 7 nm) with different orientations are observed, as indicated by the dashed lines. The interplanar spacing of 0.249 nm, measured on the crystallites is characteristic of the (0002) family of planes, which exhibits near-random orientation at this early growth stage. Furthermore, on the left side of Fig.5.12(a), the very beginning of a columnar grain can be seen. In the FFT pattern, an elongated arc along the characteristic spot corresponding to the (0002) planes indicates that these crystallites

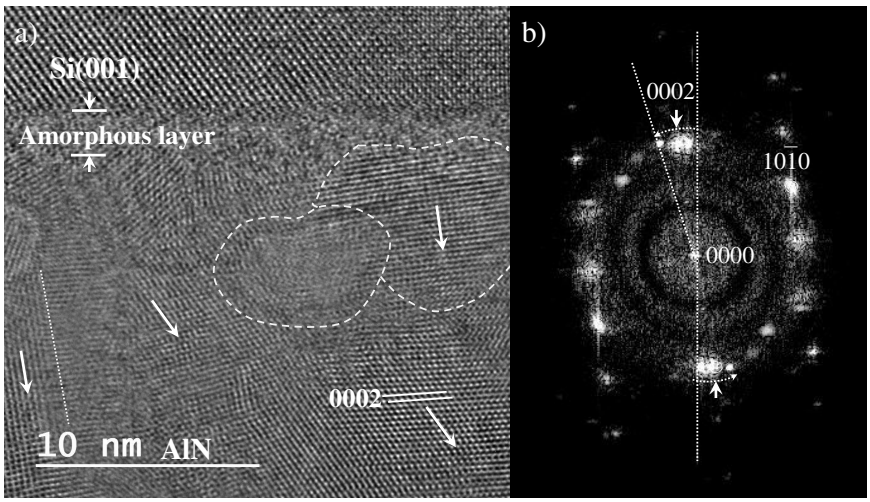

Figure 5.12: *a) HRTEM close-up view of the near-interface region (domain I) for a 935 nm [$L = 3 \times (\approx 270$ nm)] multilayer and b) its corresponding indexed FFT pattern. Note that in the HRTEM micrograph, the Si substrate is displayed on top and the AlN film on the bottom.*

are misoriented with respect to the [0001] direction. The (0002) diffraction arc has a deviation angle with respect to the axis passing across the center of the (0000) spot of 10° and 17° for the inner and outer (0002) reflections, respectively. This means that out-of-plane disorientation of the crystallites captured in the micrograph, with respect to the $c-$axis, varies from 10° to 17° approximately. These results indicate that both monolayer and multilayer samples undergo similar growth mechanisms at the early stage, which is expected since interfacial oxidation is induced at thicknesses of ≈ 270 nm and 540 nm for the $L = 3 \times (\approx 270$ nm) multilayer.

To gain overall understanding of the structural modifications due to interfacial oxidation (which was evidenced by the EDX study presented in section 5.5), TEM analysis was performed within the zones at which AlN films were subjected to oxidation. Two bright field TEM images of the oxidized interface between two successive AlN layers are displayed in Fig.5.13.

Interfacial oxidation between two AlN layers, deposited one on the top of the other, is clearly evidenced by the marked horizontal contrast, as designated by the horizontal white arrows. The darkened region interrupting columnar growth indicates the presence of planar defects, induced by substitutional oxygen impurities. Indeed, it has been verified by Slack (1973) and Slack et al. (1987) that oxygen enters the AlN structure as Al_2O_3. Each three oxygen atoms thus generate one aluminum vacancy. The dark spots at the interface, signalized by red arrows, originate from these oxygen inclusions in the AlN lattice, which scatter electrons differently, resulting in a higher contrast (Valdre (1971)). The growth of columnar grains appears to restart directly from

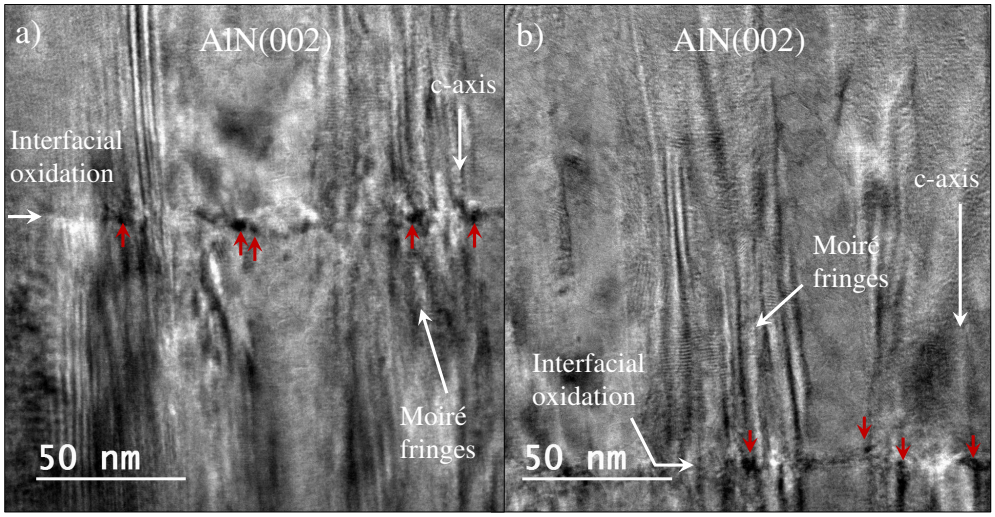

Figure 5.13: *Bright field TEM images of the oxidized interface between two successive AlN layers of a $L = 3 \times (\approx 270$ nm$)$ multilayer, captured in the columnar region (Domain III). Dark spots showing oxygen inclusions are indicated by the red arrows.*

the region of localized oxidation, forming equiaxed columnar grains of similar diameters throughout the adjacent thickness. The pronounced contrast variations are known under the name of Moiré fringes, and their presence is due to the high density of defects in this zone. Indeed, the observed Moiré fringes appear as a result of lattice distortion induced by oxygen-related defects, such as Al vacancies, mass differences and the impurity inclusions. Since oxygen replace nitrogen, vacancies in the aluminum sublattice are produced (Slack et al. (2002)), which causes a deformation of the crystal lattice in order to adjust the interplanar distances. Two overlapping crystallites with different $d-$spacings give rise to different Bragg reflections that interfere, therefore generating the observed Moiré patterns (Williams and Carter (2009)).

Figure 5.14(a) is a HRTEM micrograph of the columnar domain, captured from the $L = 3 \times (\approx 270$ nm$)$ multilayer. Despite the presence of Moiré fringes indicating lattice distortion, in the columnar region, grains are formed of highly periodic arrays of (0002) planes oriented in the [0001] direction. This is evidenced by the FFT pattern, which scatters the same characteristic diffraction spots as for the one of the monolayer sample shown in Fig.5.11(b). A slight deviation from the axis passing across the (0000) reflection can be observed in Fig.5.14, as illustrated by the red arrow. The measured deviation angle is 3.3°, indicating the average out-of-plane disorientation of the columnar grains in this region with respect to the c-axis. This result matches remarkably well the FWHM value of the rocking curve measured for the same multilayer, that was 3.2° (see subsection 5.1.2).

Figure 5.14 reveals that growth mechanism after localized oxidation are very similar for multilayers. However, oxygen inclusions at interstitials and lattice

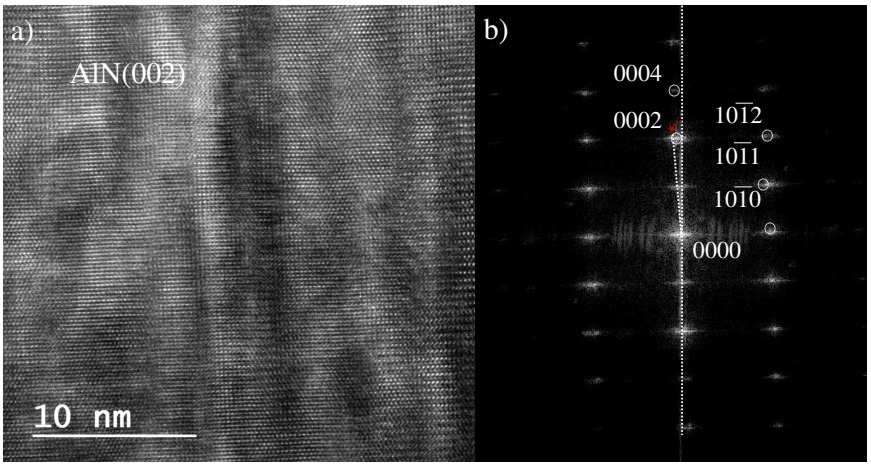

Figure 5.14: *a) HRTEM micrograph of columnar grains from a $L = 3\times$ (≈ 270 nm) multilayer (domain III), and b) its corresponding indexed FFT pattern.*

sites limit to some extent the subsequent well-oriented crystallite growth, therefore increasing the out-of-plane disorientation.

5.3 Evolution of the grains size distributions

5.3.1 Near-interface and transition regions

Figure 5.15 is a HRTEM image of the microstructure of the interface and transition zones, captured at low magnification from a 850 nm monolayer (88K). From Fig.5.15 and the systematic TEM analysis presented above, it can be inferred that both monolayer and multilayer AlN films are made of small grains of different sizes and shapes in the region near the silicon substrate. These grains then coalesce to form the columnar structure in the transition region. To accurately determine the thermal conductivity of such complex-grained systems, it is necessary to experimentally characterize the evolution of grains, considering the different crystallite size distributions and shapes along the cross plane.

The measurement of the mean crystallite size in nanoscale polycrystalline materials is generally accomplished by manual, software-assisted, or fully automated analysis of TEM micrographs. Manual analyses can be achieved by direct measurements on a calibrated micrograph. Yet, this "by eye and by hand" method can be tremendously tedious and typically results in no more than a few tens of grains being counted, yielding to a sample that is not statistically meaningful. Grain size distribution measurement can also be software-assisted, using image

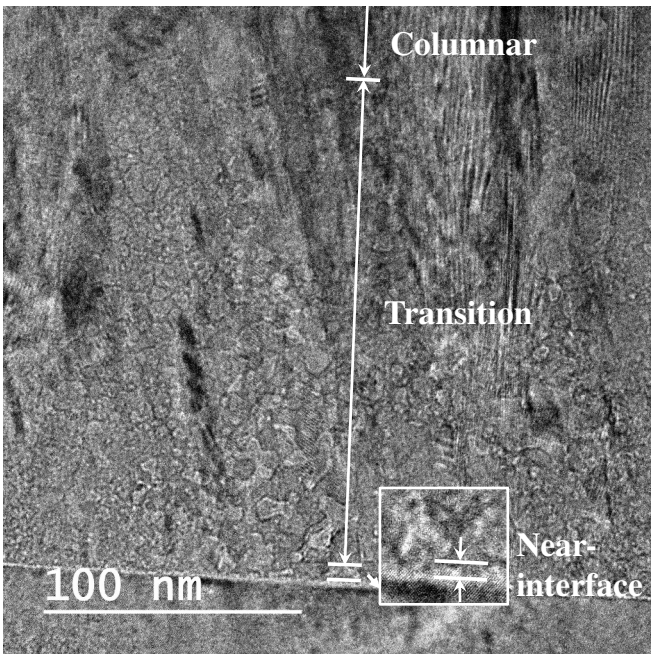

Figure 5.15: *Evolution of the grained structure through the c-axis from small grains at the near-interface region to aligned grains in the columnar region. The inset shows a close-up view of the near-interface region.*

analysis packages involving thresholding algorithms, such as imagej®. However, software-assisted image processing of TEM micrographs is not straightforward. The reason behind the difficulty of processing TEM images is that two beams are used to generate a HRTEM micrograph: a direct beam and a Bragg-diffracted beam. When these beams are in phase with one another, strong variations in contrast are observed (Pyrz and Buttrey (2008)). This problem is exacerbated by the fact that ordered arrays detected by the transmission electron microscope generate a noisy uneven background with frequency components that are different from the grain frequencies. Because of this, conventional image processing involving thresholding algorithms designed to locate and measure particles is prone to failure.

In this work, this problem was solved by applying a digital filter to enhance crystallite edge detection. It was demonstrated by Sierra-Sosa (2014) that a spiral phase digital filter, which changes the HRTEM image from discrete spatial coordinates m and n to frequency coordinates f_x and f_y with the Laguerre-Gauss transform, can define crystallite edges. Spiral phase filtering was hence applied to enhance grains edge detection from TEM images of each sample, taken at three different magnifications (88, 360, and 710 K) to have statistically meaningful populations. The applied filter assigns a phase or field discontinuity to each structure and then convolves the obtained pattern to a function of the form $e^{i \tan(f_x/f_y)}$, resulting in defined outlines of the grain edges.

To serve as an example, the results obtained by the implementation of the spiral phase filter on HRTEM images acquired at 88K and 710K from a monolayer and a multilayer sample are shown in Fig.5.16(a) and (d) respectively.

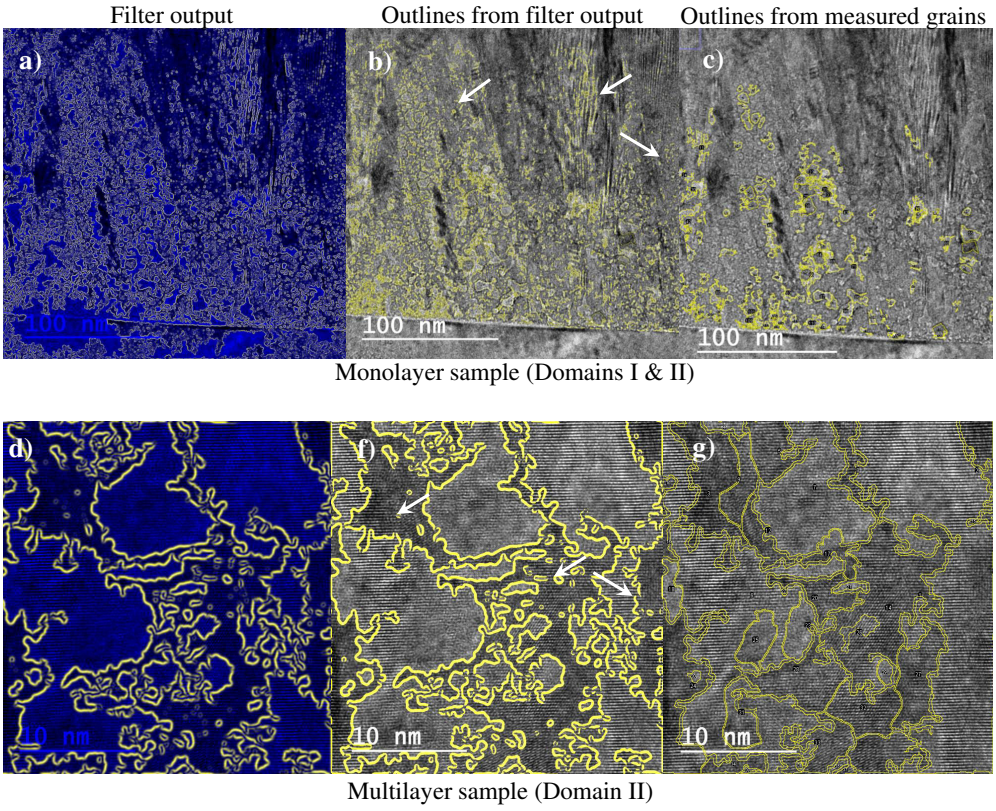

Figure 5.16: *a), d) Crystallite edge detection by a spiral phase digital filter for a monolayer and a multilayer, respectively. b), f) Original micrographs with overlayed 8-bit binary image (in yellow) containing simple outlines of the filter output for identified grains. c), g) Original micrographs with overlayed 8-bit binary images containing outlines of the measured grains, which were traced by edge identification. The analyze particles module of the software imagej® was used to identify edges from the processed output image of the phase digital filter (b), (f) and measure the total area of each crystallite (c), (g).*

Figures 5.16 (a) and (b) are pseudo-color representations from edges synthesized by the spiral phase filter, which are merged with the original image of the monolayer and multilayer samples, respectively. Figures 5.16 (b) and (f) are 8-bit binary images containing outlines of the filter output for the identified grains, overlayed to the original HRTEM micrographs. From these outlines, it can be seen that some contrast features in the micrographs (indicated by the white arrows) are identified by the filter as grains. These elements, identified by the filter as crystallite edges, are in fact strong contrast variations in

the HRTEM micrographs. Hence, after filter application, human intervention was still needed to refine crystallite identification by manually eliminating the spurious filter outcomes. Figures 5.16 (c) and (g) are 8-bit binary images containing the final outlines used to measure grain sizes, which were traced by edge identification. As it can be observed from these figures, the spurious outcomes are excluded and only the well defined crystallites are used to perform the measurements.

After this treatment, the "analyze particles" module of the software imagej® was used to identify edges from the final output image and measure the total area of each crystallite. The yellow outlines in figures 5.16 (c) and (g) are examples of the measured grains used to estimate the crystallite size distributions. For the near-interface and transition regions, populations of around 200 grains for each sample were analyzed. The crystallite size distribution for these regions were determined considering the grains like cubes with average lengths d and c for the near-interface and transition regions, respectively [Fig.4.1(b) and (c)]. The mean size was calculated by using the distribution function $y(x)$, as follows:

$$\bar{x} = \left[\int_{x_{min}}^{x_{max}} xy(x)dx\right]\left[\int_{x_{min}}^{x_{max}} y(x)dx\right]^{-1} \tag{5.1}$$

were $\bar{x}$ is the average grain size, x is the grain size, and x_{min} and x_{max} are the smallest and the biggest grain size, respectively.

Figure 5.17 shows the grain size distributions in both the interface and transition regions of 640 nm and 850 nm thick samples obtained by digital image processing. Mean sizes of 4.41 and 4.11 nm were obtained in the near-interface region of 640 nm and 850 nm AlN films, respectively. Analogously, the corresponding mean size values for the transition region were 11.09 nm and 9.04 nm. The similar shapes of the grain size distributions and the proximity of the mean size values (Fig.5.17) suggest that the grain size in the near-interface and the transition regions are thickness and sample independent. These results imply that both monolayer and multilayer AlN configurations undergo similar lattice strain relaxation and (0002) grain overgrowth mechanisms.

Furthermore, from statistical measurements on HRTEM micrographs, thicknesses of 185, 193 and 186 nm were measured for the transition region of monolayer, multilayer and poorly textured samples, respectively. The proximity of these values suggest that, at this critical thickness, small crystallites have coalesced to form V-shaped columnar grains, and for larger film thickness the aligned columnar structure develops.

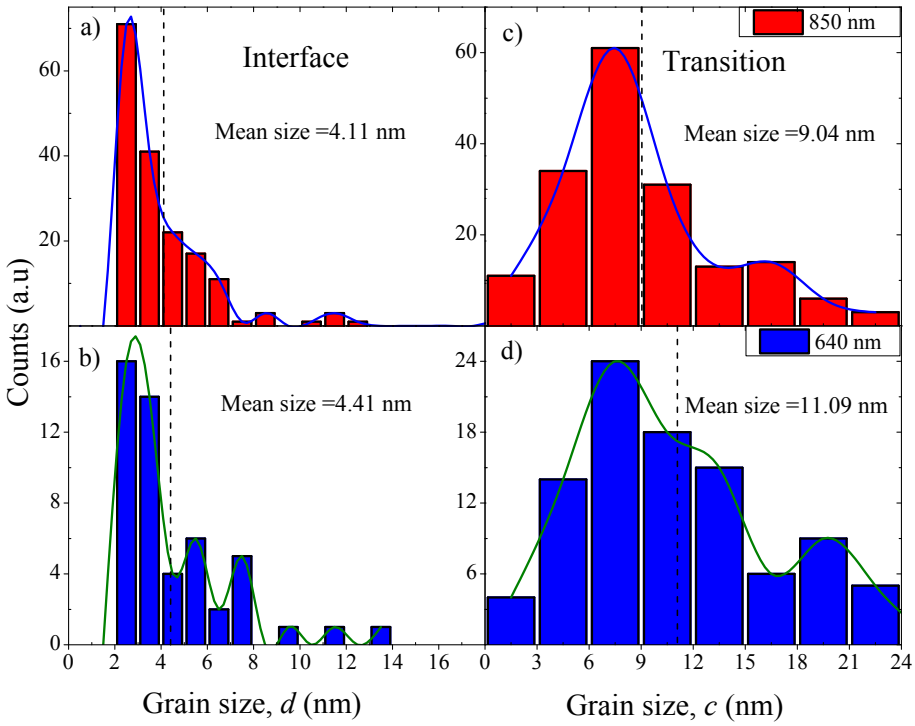

Figure 5.17: *Grain size distribution associated to the a), b) near interface and c), d) transition regions for 640 nm and 850 nm thick samples, respectively. The filled rectangles in the legends refer to the film thickness.*

5.3.2 Columnar region

The grain size distributions in the columnar region of all AlN samples were systematically studied in a similar way based on digital SEM image processing and considering a right parallelepiped grain shape with an average length a for each side of the base and an average height b [Fig.4.1(b) and (c)]. Image processing of SEM micrographs is quite more straightforward than TEM analysis, because there are no ordered arrays that generate frequency noise, although speckle and uneven background can still be present. By setting a threshold based on the unprocessed image intensity histogram, defined edges of columnar grains can be obtained.

To serve as an example, an original micrograph (a) and a 8-bit binary image, containing outlines of the threshold filter outcome for edge detection (b) of columnar grains from a 380 nm monolayer, are presented in Fig.5.18.

After filtering, a measurement axis is drawn on the edge outline image at the top region of the columnar array, as indicated by the white arrow. Then, a two-dimensional graph of the intensities of pixels along the measurement axis is generated by the profile-plot command of imagej®, as shown in Fig.5.19.

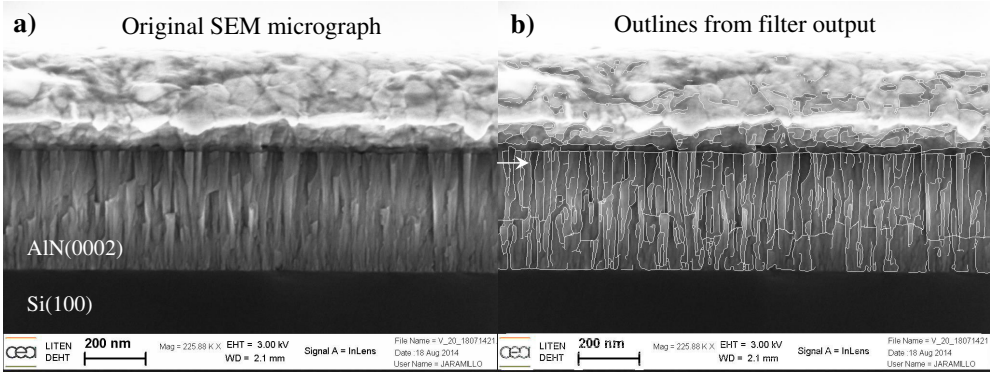

Figure 5.18: *a) Original SEM micrograph of a 380 nm thick monolayer, b) overlayed 8-bit binary image containing outlines of the threshold filter output for edge detection of columnar grains. The arrow shows the area of column diameter measurement.*

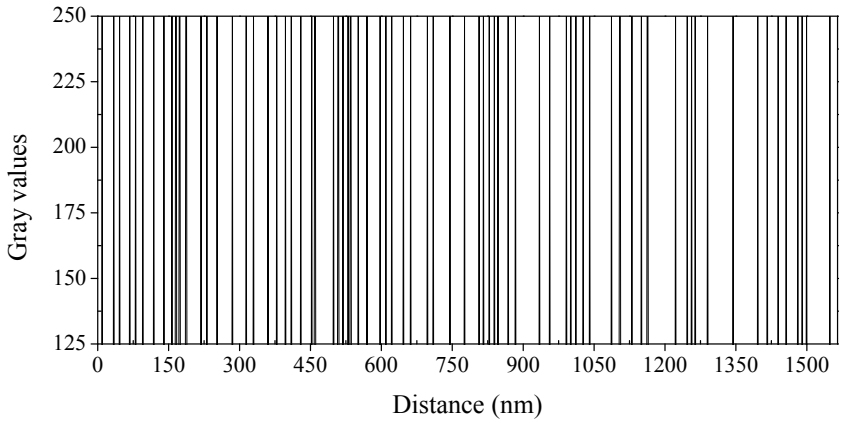

Figure 5.19: *Profile plot of the edge detection output for columnar grains at the top region of the columnar array (380 nm thick monolayer). The $x-$axis represents the distance along the measurement line and the $y-$axis is the pixel intensity.*

The $x-$axis represents the distance along the measurement line and the $y-$axis is the pixel intensity. Column diameter can therefore be easily obtained by subtracting the distance between two black lines in the upper zone of the profile plot. Measurements on both monolayer and multilayer sets of samples were performed using this method. The populations used to obtain the columnar diameter distributions were of about 220 grains for each sample. Furthermore, since it was found that the length of the columnar grains is about forty times the average columnar diameter, both were measured separately.

The evolution of columnar diameter as a function of thickness for the AlN monolayers and multilayers is given in Fig.5.20. The columnar grain diameter appears to increase with thickness for both sets of samples. A broadening of the

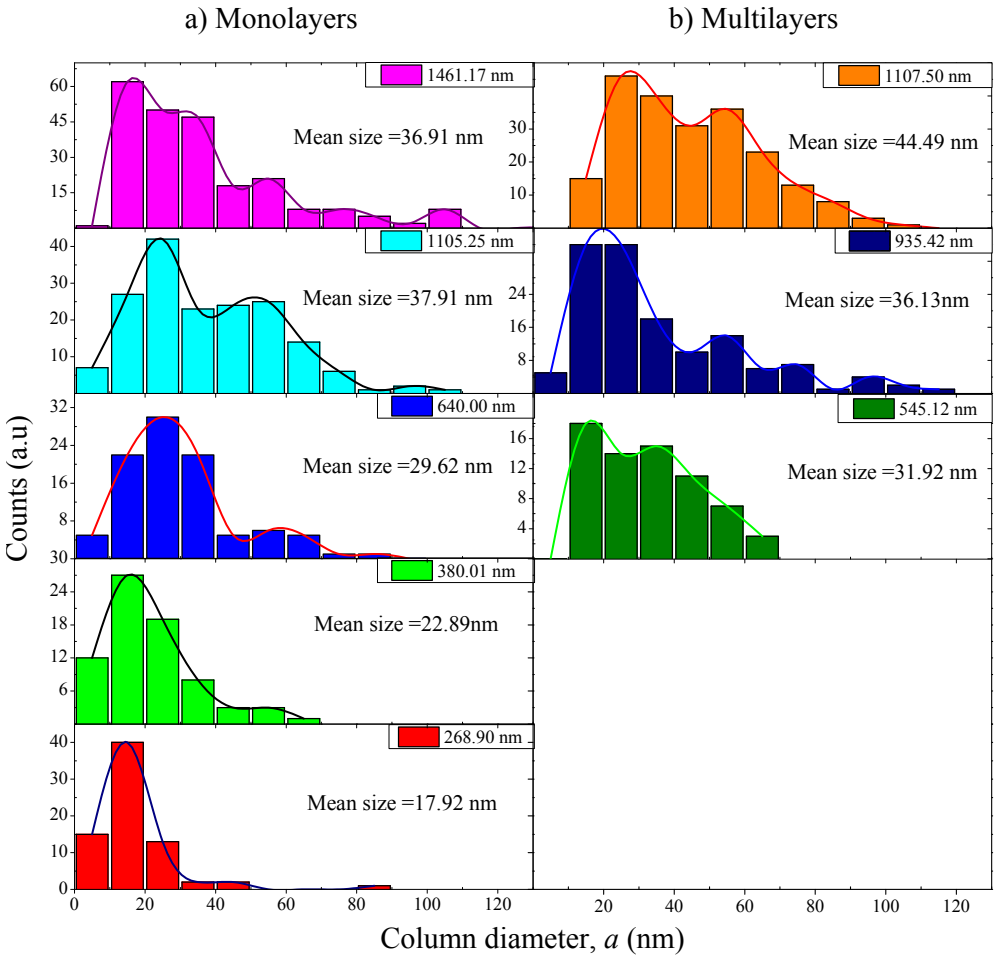

Figure 5.20: *Evolution of column diameter through the cross-plane of AlN a) monolayer and b) multilayer samples as a function of film thickness. The filled rectangles in the legends refer to the film thickness.*

distribution is also observed, indicating a wider range of columnar diameters for thicker films. This fact can be explained by the competition between the nucleation rate and adatom mobility, which inhibits the coalescence of all nucleation sites. Hence, some islands do not coalesce with their neighbors, promoting the subsistence and growth of small grains.

5.4 Competitive growth in AlN films

In sections 5.1, 5.2 and 5.3, experimental evidence of AlN films evolution from small crystallites with near-random orientation (at the interface with the substrate) towards a columnar structure with a strong out-of-plane fiber texture

along the [0001] direction (near the outer surface), was presented. These experimental observations, involving the evolution of size and morphology of grains as well as that of the orientation of crystals, can be described by a fundamental structure forming phenomenon: the competitive growth.

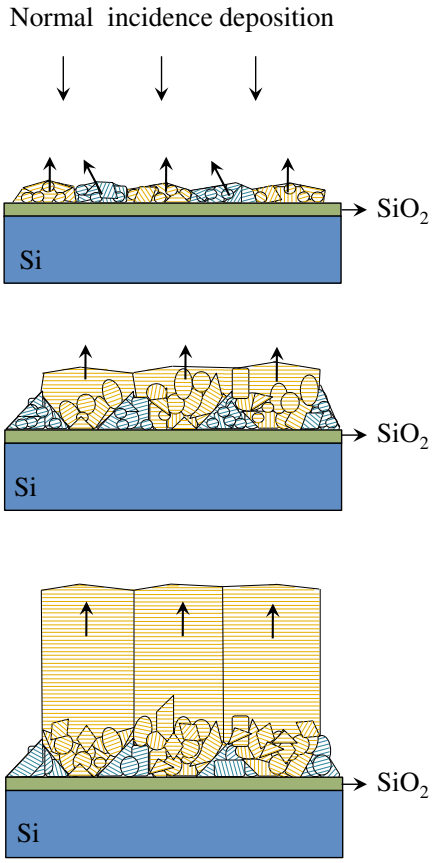

Figure 5.21: *Structure evolution AlN films grown by normal incidence deposition. The (0002) family of planes with* [0001] *growing direction are represented by the orange parallel lines. The blue lines refer to other possible families of planes with a different growth direction, such as* $(10\bar{1}0)$ *and* $(11\bar{2}0)$.

In Fig.5.21, the observed structure evolution of polycrystalline AlN films sputtered by normal incidence deposition is sketched. From the results presented above, it can be inferred that the growth of AlN films by reactive sputter deposition occurs in three stages: nucleation, crystal growth and texture development. These fundamental structure forming phenomena have been described in detail by Knuyt et al. (1995), Barna and Adamik (1998), Petrov and Barna (2003) and Deng et al. (2012).

(1) Nucleation:
At the very first stage of growth, adatoms from the plasma condense onto the bare substrate surface, forming individual nucleation sites and then developing by liquid-like coalescence. Since primary nucleation occurs directly onto the amorphous interlayer, the forming nuclei exhibit near random orientations.

(2) Crystal growth:
As more and more adatoms condense, discretized (0002), $(10\bar{1}0)$ and $(11\bar{2}0)$ single-crystal islands with different shapes and sizes grow from the nuclei in a randomly oriented fashion. Since enough energy is supplied during the deposition process, the adatom mobility is sufficiently high to promote a net mass transport by surface diffusion between planes and grains, yielding to coalescence and grain coarsening. This process is mainly controlled by the minimisation of the substrate-crystal interface energy. Thus, since deposition is performed at substrate temperatures where grain boundary migration is low (Zone T of the Thornton zone model), a small grained structure is formed at the early random growth stage.

(3) Texture development:
A growth competition among the neighboring crystals with (0002), $(10\bar{1}0)$ and $(11\bar{2}0)$ growing faces occurs. The high energy supplied during deposition process promotes (0002) crystallites to grow over the $(10\bar{1}0)$ and $(11\bar{2}0)$ growing ones, because of their fastest growth direction perpendicular to the substrate surface. This competition favors the development of V-shaped grains which is accompanied by an increase of the volume of $c-$axis preferentially oriented crystallites. This process concludes in the development of a columnar structure when only grains exhibiting (0002) oriented crystal faces proceed to the free surface.

5.5 Chemical characterization by energy-dispersive X-ray spectroscopy

Qualitative chemical analysis was performed by high-angle annular dark-field scanning transmision microscopy (HAADF-STEM) in parallel with energy-dispersive X-ray spectroscopy (EDX). This characterization aimed at obtaining information mainly about the chemical nature of the amorphous interlayer observed in the HRTEM micrographs and to characterize the AlN/AlN interfaces on multilayered samples. It was found that monolayer and multilayer samples exhibit equivalent chemical element compositions, except for localized oxidation, which is only present in multilayer configuration. For the sake of clarity, the discussion is therefore focused on the results obtained for the multilayer specimen. However, the HAAD-STEM and EDX analysis for a 850 nm monolayer can be found in Fig.E.1 (Appendix E).

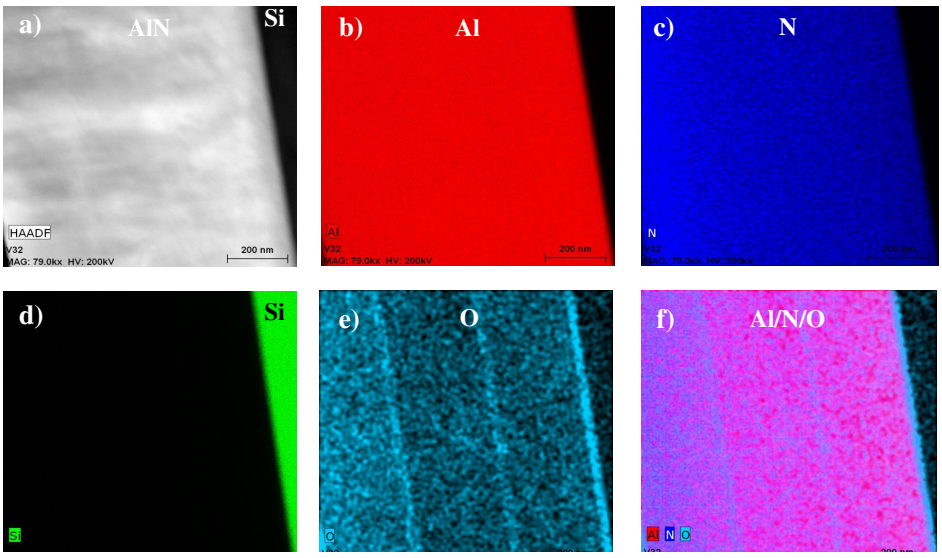

Figure 5.22: *a) HAADF-STEM image of a $L = 3 \times (\approx 270$ nm) nm multilayer and its corresponding individual element distribution maps of b) Aluminum in red c) Nitrogen in blue, d) Silicon in green, e) oxygen in cyan and f) Al/N/O composite, performed by energy-dispersive X-ray spectroscopy (EDX).*

The EDX spectra were acquired for acquisition times of about 300 s, and an operating voltage of 200 KV. Figure 5.22 is a high-angle annular dark-field image and its corresponding chemical distribution maps obtained by energy-dispersive X-ray spectroscopy on a $L = 3 \times (\approx 270$ nm) nm multilayer sample. The color maps of Al K_α (red) and N K_α (blue) depicted in Fig.5.22(b) and (c) respectively, show that both elements are uniformly distributed within the film. The individual (O in cyan) and composite (Al/N/O in red, blue and cyan) element mappings presented in Fig.5.22(e) and (f) respectively, show the presence of localized oxidation between two successive AlN layers and at the interface with the silicon substrate.

Figure 5.23 is a Si-O composite element distribution map with a close-up view of the interface with the silicon substrate, clearly evidencing the presence of random oxygen impurities between two successive AlN layers. Additionally, an overlap of Si and O elements at the substrate interface can be observed. The continuous amorphous interlayer observed in Fig. 5.8(a) and 5.12(a) of the TEM study is a 3 nm native oxide formed at the surface of the silicon substrate.

It is noteworthy to mention that besides the interfacial oxidation and the SiO_2 layer, evidenced by the increase of oxygen concentration in the element map, an homogeneous oxygen background can be detected. This background is associated to the fact that the analyzed specimen was mounted on a copper sample holder. A copper element mapping, depicted in Fig.5.24, confirms that the

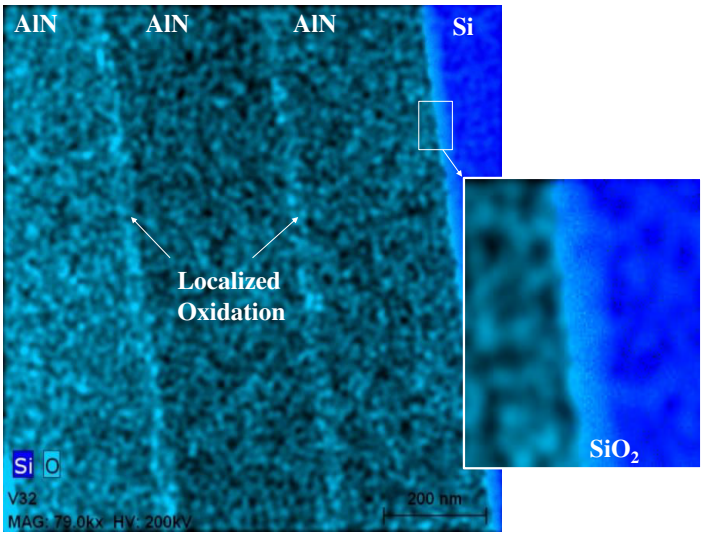

Figure 5.23: *Composite element distribution map performed by energy-dispersive X-ray spectroscopy (EDX) on a* $L = 3 \times (\approx 270$ nm$)$ *multilayer sample. The relative distribution of silicon is presented in blue and the one of oxygen is showed in cyan. The presence of random oxygen impurities at the interface between two successive AlN layers is evidenced by the increase of oxygen concentration in the oxygen element map. The inset shows the interface between AlN and the silicon substrate. It reveals the overlap of silicon and oxygen distributions at the Si/AlN interface, which confirms the presence of a silicon dioxide interlayer formed at the silicon surface.*

observed oxygen uniform background arises from the oxidized surface of the copper sample holder.

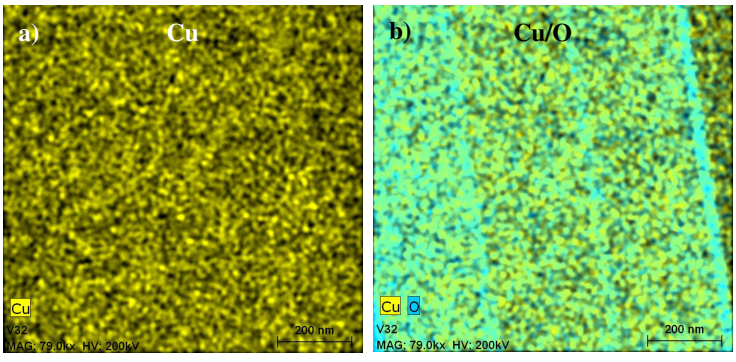

Figure 5.24: *a) Cu and b) Cu/O element distribution maps performed by energy-dispersive X-ray spectroscopy (EDX), indicating that the detected homogeneous oxygen background is associated to the oxidized surface of the copper sample holder.*

5.6 Summary

The growth mechanisms and evolution of texture along the cross plane of polycrystalline AlN films were studied using X-ray diffraction techniques. Microstructure and distribution of crystallographic orientations were analyzed by transmission electron microscopy, and grain structure and size evolution were investigated by statistical analysis of digitally processed micrographs obtained with transmission and scanning electron microscopy. Also, chemical analysis was performed by energy-dispersive X-ray spectroscopy.

The XRD $\theta - 2\theta$ spectra of the AlN samples exhibited a single AlN peak near $\theta = 36.04°$, characteristic of the (0002) AlN orientation. The FWHM of the rocking curves of the (0002) peak (at 36.04°), performed at $\omega = (\theta/2) = 18.02°$ for monolayers and multilayers, showed a high degree of crystallographic orientation. The average out-of-plane disorientation of the crystallites within the samples decreased from 5.8° to 2.55° with film thicknesses varying from 268.9 nm to 1461.2 nm, indicating that the average misalignment with respect to the [0001] direction was inferior to 5.8°. Thus, from XRD analysis, it was found that highly (0002) oriented monolayer and multilayer films were successfully obtained.

Microstructure and crystallographic orientation analyses showed that AlN films evolve from a near-random crystallite orientation towards a strong out-of-plane fiber texture along the [0001] direction near the outer surface. This trend was sample-independent, indicating that monolayer and multilayer systems undergo similar growth mechanisms.

In multilayer films, local interfacial oxidation was found to induce lattice distortion and planar defects, due to oxygen substitutional impurities in the AlN lattice. Oxygen-related defects limited the subsequent well-oriented crystallite growth, yielding to lower out-of plane alignment. Yet, no significant influence on growth mechanisms was evidenced. Columnar growth appeared to restart directly from the locally oxidized region, forming equiaxed columnar grains of similar diameters throughout the adjacent thickness.

Grain size distributions in the interface and transition regions were found to be thickness and sample independent, suggesting that monolayer and multilayer films are subjected to similar lattice strain relaxation and grain overgrowth mechanisms. Also it was evidenced that with film thickness, the column diameters increase and the distributions become broader, indicating wider range of column diameters for thicker films. These results showed that the competition between nucleation rate and adatom mobility inhibits the coalescence of all nucleation sites, promoting the subsistence and growth of small grains.

The EDX chemical study showed that aluminum and nitrogen are uniformly distributed within the films, and evidenced that the amorphous interlayer observed in all samples at the surface of the silicon substrate is in fact a 3 nm native oxide layer. EDX analysis evidenced as well the presence of localized oxidation between two successive AlN layers in multilayered systems.

Chapter 6

Tuning the thermal conductivity of polycrystalline films via multiscale structural defects and strain

Every solid of finite dimension contains a finite number of atoms, and therefore, a sonic spectral distribution of free vibrations of lattice atoms. These quantized, elastic waves are similar to photons and may be called phonons.

P. Debye

This chapter reports on the effects of structural heterogeneity, oxygen related defects and strain-induced lattice distortion on the cross-plane thermal conductivity of polycrystalline AlN films, deposited on silicon substrates. First, 3ω measurements as a function of film thickness were performed to correlate the cross-plane thermal conductivity of films with structural features, such as microstructure, texture, crystallite size and interfacial atomic structure. The influence of local oxidation at the interface of AlN layers on phonon transport was investigated by thickness-dependent thermal conductivity measurements on multilayered samples. Then, a physical description of scattering phenomena at the interface, grain boundaries, and oxygen related defects, as a function of the characteristic structural heterogeneity in polycrystalline thin films was achieved by comparing the experimental results to the theoretical predictions. After the thickness-dependent thermal conductivity study, the influence of lattice deformation caused by externally induced elastic strain on the thermal conductivity of monolayer and multilayer AlN films was investigated experimentally. To perform thermal measurements as a function of strain, a novel

experimental approach consisting of a 4-points bending system coupled to the 3ω method was used.

The theoretical and experimental results on thermal conduction mediated by multiscale structural defects are expected to contribute to the understanding and to control thermal transport in nano and microscale polycrystalline thin films. With strain-dependent thermal conductivity measurements, a new means of exploring dynamic modulation of heat transfer across thin films is provided.

6.1 Thickness-dependent thermal conductivity measurements on monolayers and multilayers

The effective thermal conductivities of monolayer and multilayer samples were measured as a function of film thickness using the differential 3ω technique. The studied monolayer and multilayer samples were deposited following the RF sputtering process described in sections 2.2.5.1 and 2.2.5.2 (Chapter 2), respectively. These deposition processes resulted in polycrystalline AlN films of various thicknesses, ranging from 270 nm to 1460 nm for monolayers, and from 545 nm to 1107 nm for multilayers. The latter set of samples consisted of two, three, and four AlN layers of 270 nm thick, deposited one on the top of the other. The apparatus, sample preparation and experimental methodology used to perform 3ω measurements have been described in detail in sections 3.4, 3.5 and 3.6 of Chapter 3. The experimental results provided in this section are useful to understand the relation between multiscale structural defects and thermal conduction processes within polycrystalline films.

Cross thermal conductivity values at room temperature were obtained assuming a one-dimensional heat conduction model to fit the real part of the experimental thermal wave amplitude as a function of the modulation frequency. Given that in the experiments, the thermal conductivity of the silicon substrate is at least 18 times higher than the one of the AlN films, and the heater width is 7 times larger than the thicker film, using a one-dimensional heat conduction model was well justified. Moreover, since the penetration depths of the thermal oscillation were larger than the film thicknesses over the entire frequency range (Section 3.6 of Chapter 3), the contribution of the native oxide layer, which was evidenced by the TEM study (Section 5.5 of Chapter 5), had to be considered. Because our main interest was to study the thermal properties of polycrystalline AlN films, their thermal response had to be isolated by removing that of the SiO_2 amorphous layer. Thus, the experiments were carried out by the differential method, measuring two similar structures. The first one was a native-SiO_2/Si structure (without the studied film), which served as a reference sample and the second one consisted on the above mentioned AlN film-on-substrate systems. The results of thermal measurements on the SiO_2/Si reference sample, which give information about the thermal conductivity of the native oxide, are discussed in the next section.

6.1.1 The native silicon oxide layer

As evidenced in section 5.2, the native SiO_2 layer that forms at the surface of the silicon substrate is very thin (about 3 nm), and uniform along the entire surface. In the 3ω method, the only constrain on the sample size is the dimensions of the metal strip (Cahill and Pohl (1987)). In other words, there is no limit for film thickness of the measured sample. The only experimental concern involved in measuring such a thin layer may be the electrical isolation of the metallic paths, which must be ensured. To confirm that no electrical leakage occurred and to test repeatability, three measurements $M1, M2$ and $M3$ of the in-phase component of the temperature wave amplitude *versus* $\ln(\omega)$ were performed for the SiO_2/Si reference structure. Because of the finite thickness of the Si substrate and the nanoscale thickness of the native silicon oxide layer, the frequency range was limited to $30-300$ Hz. Within this frequency domain, the thermal penetration depths varied from 485.1 to 153.4 μm, respectively (Eq.3.10). The limited frequency range used in experiments allowed for analyzing a very small volume of the sample, confining the heat wave inside the SiO_2/Si system. The thermal response as a function of the Au/Ti heater frequency is shown in Fig.6.1. The pentagons, filled circles and triangles refer to measurements $M1, M2$ and $M3$, respectively. The reference temperature oscillation of the bare silicon substrate (solid lines) was obtained using Eq.3.18. The slope of $\Delta T_{2\omega}$ as a function of the logarithm of frequency yields the thermal conductivity of the Si substrate, which is $k_{Si} \approx 147$ W/m·K.

The presence of the 3 nm silicon oxide layer produces a frequency independent increase in the real part of the thermal wave amplitude, as it can be observed in Fig.6.1. Thermal conductivity data calculated using Eq.3.21 for the three experiments on the native silicon oxide layer are summarized in table 6.1.

Table 6.1: *Room temperature thermal conductivity values for* 3ω *experiments* $M1, M2$ *and* $M3$ *performed on the native silicon oxide layer. The thermal conductivity data were calculated using Eq.3.21.*

3ω experiment	Thermal conductivity (W/m·K)	Effective thermal resistance ($\times 10^{-8}$ K·m^2/W)
M1	0.129	2.33
M2	0.113	2.65
M3	0.107	2.80

The proximity of the experimental data (standard deviation of = 0.011 and 0.24×10^{-8} for thermal conductivity and resistance, respectively) demonstrates the repeatability of the measurement. In addition, the obtained values fall

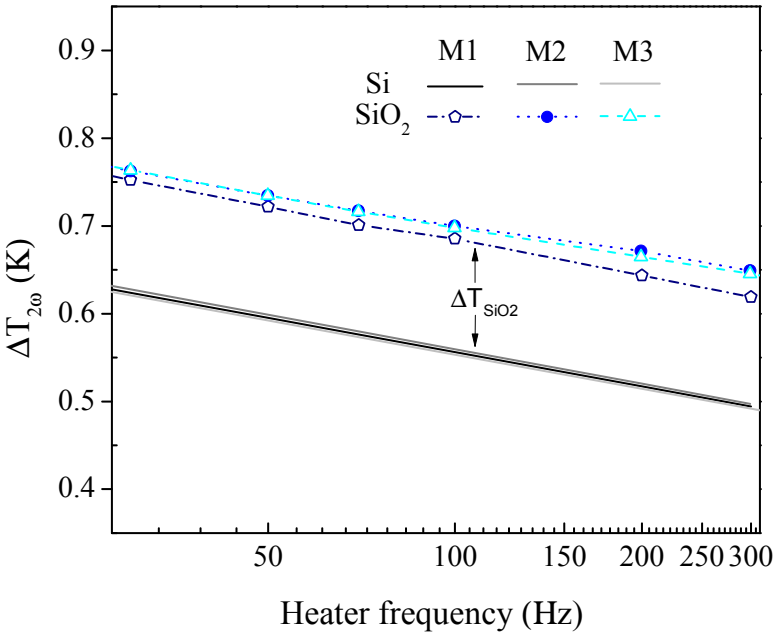

Figure 6.1: *In-phase component of the amplitude of the temperature fluctuation ($\Delta T_{2\omega}$) at a frequency 2ω , as a function of the logarithm of the modulation frequency (ω). Three different $\Delta T_{2\omega}$ measurements (M1, M2, M3) of the Au/Ti heater were acquired for the SiO_2/Si reference sample. Pentagons, filled circles and triangles correspond to M1, M2 and M3 respectively. The solid lines refer to the silicon substrate and are calculated with the slope method (Eq.3.18).*

within a reasonable range, considering the reduced thickness of the measured film, and are in good agreement with experimental data reported by Yamane et al. (2002) and Lee and Cahill (1997) for very thin SiO_2 layers at room temperature. These investigations have experimentally demonstrated that a systematic decrease in the thermal conductivity of amorphous solids occurs as the film thickness decreases, which can explain the low value measured in this work. Process and thickness dependence of the effective thermal conductivity of silicone dioxide, measured by Yamane et al. (2002), are depicted in Fig.6.2. The values obtained in this study are plotted as well for comparison. The dashed lines represent the calculated thermal conductivity, which was obtained by considering an intrinsic thermal conductivity for the a-SiO_2 layer which is constant and independent of film thickness, and assuming a thermal resistance between the SiO_2 layer and the silicon substrate. Our results match remarkably well with the thermal conductivity calculations for a thickness of about 3 nm.

Several hypothesis can explain the above mentioned thickness-dependent behavior of the thermal conductivity of the a-SiO_2 layer. The first possible explanation is that diffusive reflection of phonons at the layer boundaries increases as the film thickness decreases. Phonon-boundary interactions are particularly important when the film thickness becomes comparable to or smaller than the

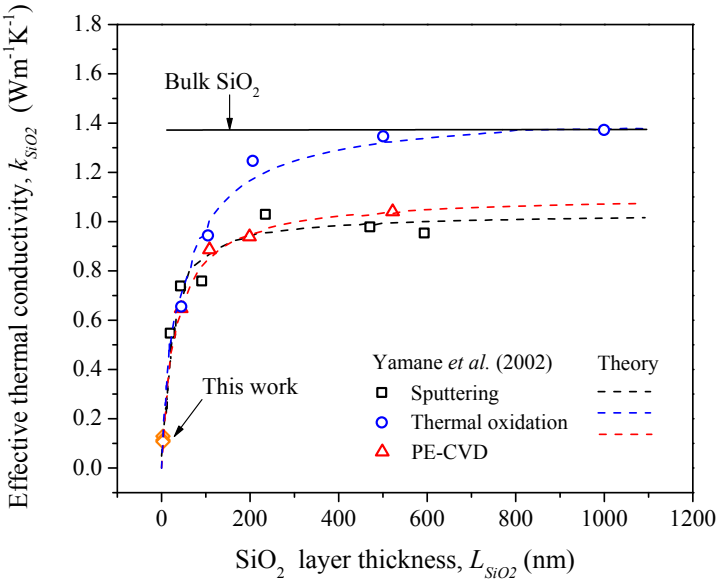

Figure 6.2: *Process and thickness dependence of thermal conductivity of silicon dioxide measured by Yamane et al. (2002) and this study. Open diamonds are the data obtained in this work.*

carriers mean free path. In the case of amorphous silicon oxide, the average phonon mean free path, $l_0 = 0.6$ nm, is nearly equal to the average intermolecular spacing, $d_{SiO2} = 0.491$ nm (Kaviany (2011)), and therefore, the lattice vibrations are rather localized. This is owing to the local distortions of the lattice structure which are comparable to interatomic spacings (the smallest length scale of the system). Thus, phonons of wavelengths comparable to the smallest system length scale are dominant in thermal conduction. Because, at room temperature, long wavelength phonons constitute a small fraction of the energy in the material, one can therefore argue that carriers with mean-free-paths comparable to the thickness of the native a-SiO_2 layer do not contribute significantly to the thermal conductivity. Yet, Goodson (1993), who studied in detail size effects on amorphous solids, demonstrated theoretically that phonon-boundary scattering in very thin films can contribute significantly to the reduction of the bulk thermal conductivity if the film thickness approaches the smallest length scale in the system. Extrapolating his results at room temperature to a 3 nm thick a-SiO_2, it can be estimated that the reduction of the bulk thermal conductivity due to phonon-boundary effects yields to a final value of 0.4 W/m$\cdot$K. Therefore, the reduced dimensions of the studied SiO_2 layer may play a role in degrading thermal conduction, but phonon-boundary scattering is not entirely sufficient to account for the low thermal conductivity obtained in this study.

On the other hand, the second possibility is that a thermal boundary resistance between the a-SiO_2 layer and the Si substrate affect the effective thermal

conductivity, causing it to decrease as the layer thickness is reduced. This thermal boundary resistance can be obtained using Eq.3.29 by extrapolating the effective thermal resistances as a function of the inverse of the film thickness to a linear model. Since the data of this work is limited to a unique thickness (3 nm), corresponding to the native oxide silicon layer, determination of the thermal boundary resistance between the a-SiO_2 layer and the Si substrate is not feasible. However, the results presented here can be compared to the experimental data reported by Lee and Cahill (1997) and Yamane et al. (2002), who both found a thermal boundary resistance of about $\approx 2.0 \times 10^{-8}$ m^2K/W. In this work, the average effective thermal resistance of the a-SiO_2 native layer was estimated as $\approx 2.6 \times 10^{-8}$ m^2K/W, which is in very good agreement. The slight difference of 0.6×10^{-8} m^2K/W can be attributed to the 3 nm thick SiO_2 layer, which contributes to the overall thermal resistance. Therefore, the low a-SiO_2 thermal conductivity obtained here can be explained by two main mechanisms: phonon-boundary and interfacial scattering, the latter being dominant. As a result of both contributions, the thermal conductivity of the native oxide layer is dramatically reduced in comparison with that of bulk a-SiO_2 (1.4 $W/m \cdot K$ Goodson (1993)).

To the best of our knowledge, measurements of the effective thermal conductivity and resistance of the native amorphous silicon oxide, often present in microelectronic devices, have not been reported so far. Thus, the results presented here may be helpful to understand cross-plane thermal transport in these structures.

6.1.2 Aluminum Nitride monolayers and multilayers

After the analysis of the reference sample given in the previous section, the discussion focuses on the thermal measurements carried out for the film-on-substrate structures, which allow for the determination of the thermal conductivity of the AlN films exclusively. This is achieved by removing the a-SiO_2 contribution from the overall thermal response of the AlN-on-Si systems. The results are discussed below.

6.1.2.1 The effect of thickness and interfacial oxidation in the amplitude of the temperature fluctuation

The real part of the amplitude of the temperature fluctuation measured within the heater, as a function of the logarithm of frequency for the monolayer set of samples, is depicted in Fig.6.3. The dashed lines represent the analytical fits performed for the experimental data. The reference amplitude of the temperature oscillation, associated to the bare silicon substrate (solid line), and to the SiO_2 native layer (open circles), are included as well for comparison. For the thickness dependent measurements, the frequency was limited to a range

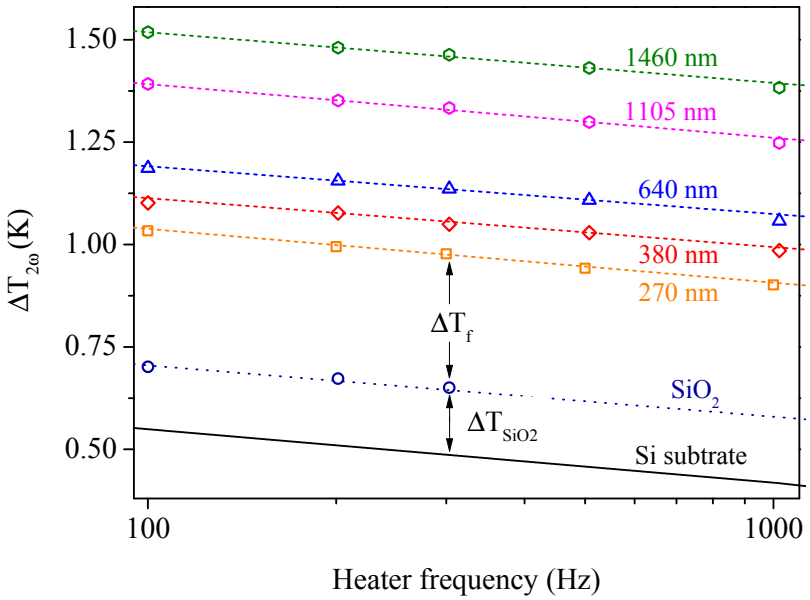

Figure 6.3: *Thickness dependence of the thermal wave amplitude* ($\Delta T_{2\omega}$) *generated within the heater by AlN monolayers of different thicknesses, as a function of the logarithm of the modulation frequency.*

varying from 100 to 1000 Hz, confining the heat fluctuation well within the AlN/Si structure.

As can be observed in Fig.6.3, the diffusion of the thermal fluctuation into the AlN films of different thicknesses produces a frequency independent temperature rise through the metal strip, which gradually increases with layer thickness. The offset between the calculated Si temperature (solid line) and the blue open-circle data represents the temperature change caused by the a-SiO_2 layer. The offsets between the temperature corresponding to the native silicon oxide and the experimental data are the temperature rise (ΔT_f) generated by the monolayer AlN films of different thicknesses. The gradual increment of this offset directly indicates that the AlN thermal resistance increases as the film thickness increases.

An equivalent trend of the thermal response can be observed for multilayered systems. The amplitude of the temperature fluctuation measured for the multilayer set of samples *versus* $\ln(\omega)$ is shown in Fig.6.4. As in Fig.6.3, Si and a-SiO_2 temperature amplitudes are plotted as well. While the thermal response essentially increases for thicker films, the rate of increase of the absolute value of $\Delta T_{2\omega}$ is higher compared to the one measured for their monolayer counterparts of equivalent thickness. For example, the heat wave amplitude measured for a 1107.5 nm thick multilayer sample at 100 Hz is 1.57 K, which represents an increase of 14% of the thermal wave amplitude obtained for an AlN monolayer

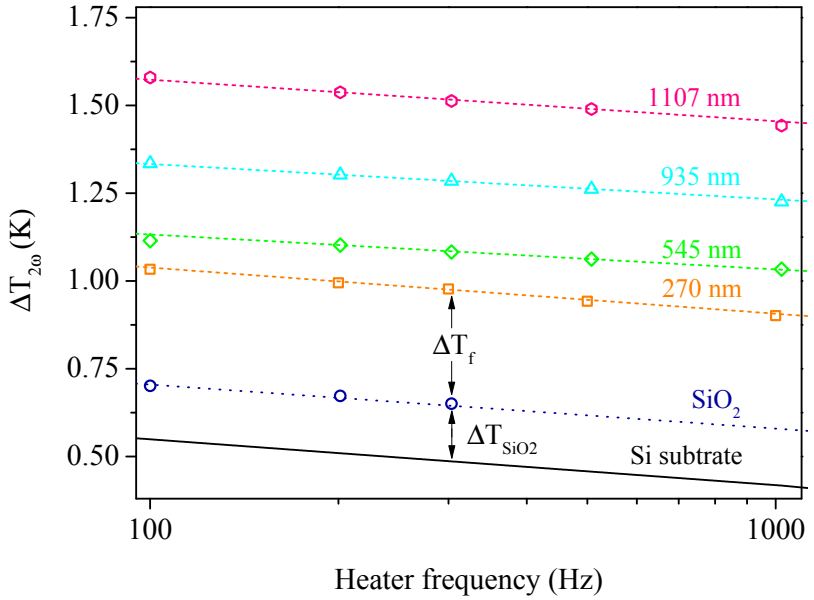

Figure 6.4: *Thickness dependence of the thermal wave amplitude ($\Delta T_{2\omega}$) generated within the heater by AlN multilayers of different thicknesses, as a function of the logarithm of the modulation frequency.*

with approximately the same thickness at the same frequency. This effect corresponds to the additional thermal resistance induced by interfacial oxidation. Oxygen impurities at the interface between AlN/AlN layers act as a thermal barrier, increasing the diffusive scattering of lattice vibrations and thus yielding a further increase in the temperature within the film.

To obtain the effective thermal conductivity, the measured heat wave amplitudes were compared to an analytical model of the differential 3ω technique, and the results will be discussed below.

6.1.2.2 Dependence of the thermal conductivity on the film structural inhomogeneity and interfacial oxidation

The obtained overall temperature rise of the heater, presented in Fig.6.3 and Fig.6.4, was generated by the whole underlying structure, i.e the AlN film and the native silicon oxide layer. Thus, to obtain the effective thermal conductivity of AlN films, their thermal properties had to be isolated. This was achieved by subtracting the signal of the reference sample from that of the specimen with the deposited AlN layer, using Eq.3.22. In this way, the heat wave amplitudes measured for both sets of samples, which are directly related to the 3ω signal, were compared to an analytical model as a function of the excitation frequency. The experimental variables corresponding to the monolayer and the multilayer specimens, used to obtain the effective thermal conductivities, are listed in Table B.1 and B.2, respectively (Appendix B).

Using the differential 3ω technique is advantageous for several reasons. Particularly, by subtracting the signal of the a-SiO_2/Si reference structure from the total temperature rise, the common background contribution of the parasitic interfacial thermal resistances, such as the one between the heater and the underlying film, are removed. Furthermore, the obtained values of k_{eff} are insensitive to the substrate thermal conductivity, and the contribution from the a-SiO_2 native layer, which represents an important thermal resistance in the analyzed systems, is eliminated by the measurement on the reference sample. The obtained experimental results are summarized in Table 6.2.

Table 6.2: *Room temperature thermal properties measured experimentally for monolayer and multilayer AlN films.*

		L (nm)	k_{eff} (W/m·K)	R_{eff}[a] ($\times 10^{-9}$ K·m^2/W)	R[b] ($\times 10^{-9}$ K·m^2/W)
Monolayers		268.9	3.12 ± 0.28	86.16 ± 8.40	
		380.1	4.27 ± 0.22	89.01 ± 4.52	
		640.0	5.86 ± 0.38	109.29 ± 7.53	
		1105.2	7.41 ± 0.23	149.13 ± 5.24	
		1461.2	8.21 ± 0.39	178.06 ± 8.40	
Multilayers	2 × (≈ 270 nm)	545.1	5.07 ± 0.22	107.43 ± 8.41	12.45
	3 × (≈ 270 nm)	935.4	5.84 ± 0.38	160.21 ± 8.26	12.38
	4 × (≈ 270 nm)	1107.5	5.93 ± 0.23	189.90 ± 8.80	12.52

The obtained thermal boundary resistance between the substrate and AlN films was estimated to be $R_s = 62.74 \times 10^{-9}$ K·m^2/W.

[a]The effective thermal resistance was calculated with Eq.3.29, by considering the whole system as a serial network of thermal resistances.

[b]The thermal boundary resistance R at interfaces between two AlN layers was determined with Eq.3.30

The measured effective thermal conductivity k_{eff} as a function of the film thickness, and in comparison with its theoretical predictions determined with Eq.4.16, is shown in Fig.6.5, for both the monolayer and multilayer configurations. The predictions of the developed model for thermal conductivity of polycrystalline films match quite well the experimental data, with an error below 10%. The slight theoretical overestimation of k_{eff} for both monolayer and multilayer configurations can be attributed to the regular grain geometry approximation. As shown in Fig.5.15 (Chapter 5), the near-interface and the transition regions are composed of grains with irregular shapes and different sizes, yet the modeled structure was approximated as a serial assembly of cubic grains. However, the theoretical model developed in Chapter 4 yields remarkably satisfactory predictions of the thermal conductivity of the polycrystalline AlN films, demonstrating that the newly developed model for effective thermal

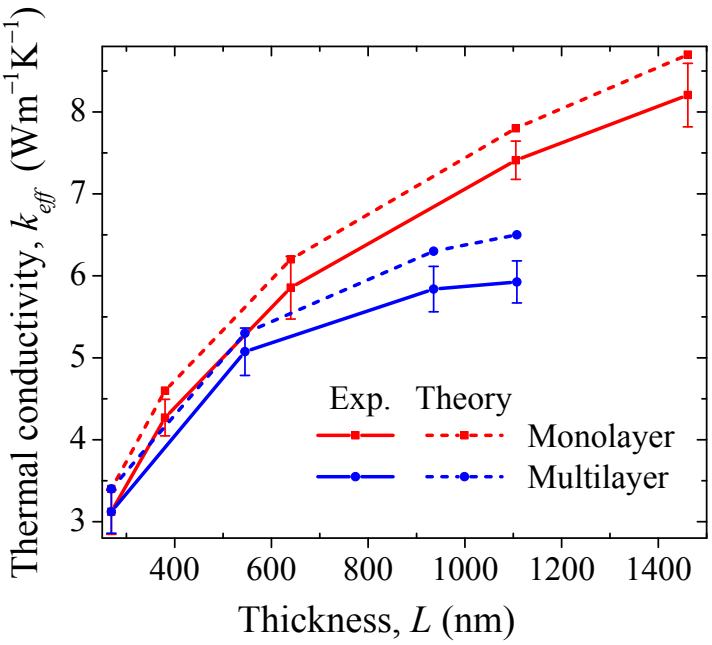

Figure 6.5: *Comparison between the experimental and theoretical values of the effective thermal conductivity of grained monolayers and multilayers, as a function of the film thickness.*

conductivity is valid for polycrystalline materials exhibiting a non-homogeneous grained structure.

Figure 6.5 shows a systematic decrease in the measured thermal conductivity as the film thickness decreases for both sets of samples. Variations from 1460 to 270 nm for monolayers and from 1107 to 545 nm for multilayer, result in a reduction of the effective thermal conductivity from 8.21 to 3.12 W/m·K and from 5.93 to 5.07 W/m·K, respectively. These results suggest that the effect of film thickness on k_{eff} is stronger for monolayered samples. Furthermore, for relatively thick films, the increase of the effective thermal conductivity appears to be gradually attenuated. In order to explain in details the above-mentioned experimental findings, the discussion focuses, in first instance, on a comparison with the state-of-the-art thermal measurements on AlN polycrystalline thin films.

- **Monolayers**

The results obtained in this work are in good agreement with other experimental data reported by Zhao et al. (2004), Choi et al. (2006) and Pan et al. (2012) for effective thermal conductivities at room temperature of polycrystalline AlN films deposited by RF sputtering on Si substrates. These investigations have reported values that vary from 0.5 to 50 W/m·K (See section 1.2 of Chapter 1), and have observed a strong dependence on film thickness (as is our case), as well

as on deposition conditions and techniques. More recently, an equivalent trend has been observed by Belkerk et al. (2012) and Duquenne et al. (2012), who studied thermal transport properties of AlN films deposited by balanced and unbalanced magnetron sputtering. Both studies found that the balanced magnetron process yielded to effective thermal conductivities of 2.5 - 50 $W/m \cdot K$ for 800 - 3500 nm thick AlN films. On the other hand, unbalanced magnetron sputtering led to $k_{eff} = 20 - 130$ $W/m \cdot K$ for film thicknesses varying from 150 to 3500 nm. These investigations somehow addressed the thickness-dependence problem qualitatively, by attributing the decrease of k_{eff} with film thickness to synthesis conditions, microstructure and average grain size, according to the Scherrer equation (XRD analysis). Though, it has been shown that XRD techniques are inaccurate to quantitatively describe crystallite sizes for thin films with heterogeneous structure, and therefore TEM analysis is required in this case (refer to section 2.3.2 of Chapter 2 and Klug and Alexander (1974)). Crystalline quality, structural features and thickness of the different regions of the films were identified as major factors degrading thermal properties of AlN films. Also, the disordered atomic structures and grains of different shapes and sizes observed in the near interface and transitions regions were interpreted as thermal resistances. Yet, a physical description of thermal conductivity as a function of both morphology and grain structure evolution along the cross plane direction of AlN thin films has not been achieved so far.

We propose such a description based on the electron microscope analysis presented in Chapter 5. It was found that the grained structure of AlN films evolves through the $c-$axis from small grains at the near interface region to larger aligned grains in the columnar region (see section 5.3). Statistical analysis indeed revealed that the mean grain size is about 4 and 10 nm in the near-interface and transition regions respectively, while the mean diameter of columnar grains varies with film thickness from 18 to 37 nm in the columnar region. It is noteworthy that, besides the evolution of the mean diameter, an increment of the columnar height from 80 to 1270 nm was observed as the film thickness increased. Since phonon mean free path in single-crystalline AlN is about 110 nm at room temperature (Slack et al. (1987)), one can argue that size effects in the near-interface and transition regions lead to the drastic reduction of the thermal conductivity as the film thickness decreases. Conversely, in the columnar region, where grain boundaries extend along the direction of thermal transport studied in this work, phonon-boundary scattering is reduced as a result of the increased mean grain size. This effect may shadow to some extent the impact of the thermal resistances associated to the high density of grain boundaries and the size effects in the interface and transition domains. That is because the relative contribution of each domain is determined by its corresponding thickness with respect to the total film thickness. Higher mean free paths and lower scattering rates in the columnar region can therefore explain, conceptually, the trend observed in Fig.6.5 for thicker films.

- **Multilayers**

Concerning the thermal conductivity of multilayered films with local oxidized interfaces, measurements similar to the ones presented here have not been reported so far to our knowledge. However, several studies have investigated the effect of oxygen related defects in k_{eff} of aluminum nitride. Slack (1973) has found that thermal conductivity of AlN is affected by oxygen content, because oxygen impurities are incorporated into the crystal lattice by replacing nitrogen atoms in substitutional sites. Increased scattering of phonons is therefore caused by these mass-related defects. Furthermore, Yagi et al. (2011) have reported that k_{eff} decreases from 28 to 3.5 $\mathrm{W/m \cdot K}$ for AlN films with oxygen concentrations varying from 1.1 to 13.6 at.% (atomic percent) respectively.

From the microstructural and crystallographic analysis presented in Chapter 5 (see Fig.5.13 in subsection 5.2.4), we have found that local oxidation yields to grain-boundary-like planar defects. These 2D-defects are induced by substitutional oxygen impurities in the direction perpendicular to the thermal transport here studied i.e grain-boundary-like defects are parallel to the film surface. Also, TEM analysis revealed that oxygen inclusions produce lattice distortion, evidenced by Moiré patterns, which in turn lead to high density of strain-mediated crystal defects in the oxidized regions. Since these oxygen-related defects are localized transversely with respect to the out-of-plane direction, in which thermal properties are measured, they strongly impede thermal conduction. The increased scattering due to phonon-defect interactions therefore yields to the significant overall reduction observed in effective thermal conductivities of multilayer films.

As for the a-SiO_2 layer (See section 6.1.1), the thermal boundary resistance between AlN films and the substrate should be considered as well, given that it is directly related to the thickness-dependent behavior of the effective thermal conductivity. In the following section, the impact on thermal conduction of the thermal boundary resistance between AlN and the native oxide layer, on which AlN films are directly grown, will be discussed.

6.1.2.3 Impact of the thermal boundary resistance on the effective thermal conductivity

Thickness dependent thermal resistances for monolayer and multilayer configurations were obtained by considering the specimens as a serial network of thermal resistances. The effective thermal resistances R_{eff} for both sets of samples are shown in Fig.6.6, as a function of the film thickness, and are summarized in the fifth column of Table 6.2. Here, R_{eff} includes the interfacial thermal resistances R and R_s. Assuming that R_s is equivalent for all samples, the experimental data of R_{eff} were extrapolated to $L = 0$ by using the linear model in Eq.3.29. As can be seen from Fig.6.6, there is a linear dependence of the thermal resistance on the film thickness according to Eq.3.29. The use

of this series-circuit relationship implies that the columnar region extends to the total film thickness, and therefore R_s includes the overall resistive contributions associated to the near-interface and transition regions. Yet, as exposed in section 5.3, the TEM study revealed that the thickness of the microscrystalline transition domain is not negligible, $L_T \approx 190$ nm for all the studied samples, and this assumption is therefore inaccurate. However, this linear model can be used, as a first approximation, to provide insight into the effect of the resistance associated to the structural features present in the region near the interface with the substrate. A more accurate treatment would take into consideration the relative thicknesses of each domain with respect to the total film thickness. This can be achieved by using Eq.4.1 and Eq.4.2 from the theoretical model developed in Chapter 4. Since Eq.3.29 has been widely used to study the thermal boundary resistance (Lee and Cahill (1997), Yamane et al. (2002), Belkerk et al. (2012), Duquenne et al. (2012)), the analysis focuses, initially, in this approach to allow for a comparison with the literature. Then in section 6.1.3, the discussion will be extended through the theoretical model, by considering the corresponding thickness and structural features of each domain.

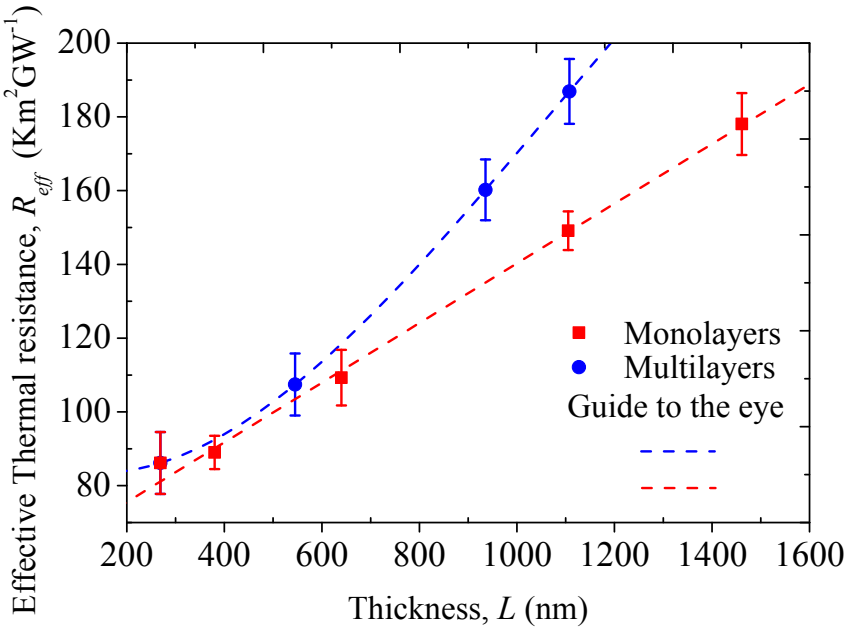

Figure 6.6: *Effective thermal resistance as a function of the film thickness, for the monolayer and multilayer configurations.*

By using Eq.3.29, the thermal boundary resistance between the substrate and the AlN films near room temperature was estimated as $R_s = 62.74 \times 10^{-9}$ m^2K/W, for both the monolayer and multilayer configurations. The obtained value falls within a reasonable range and is in good agreement with other experimental data reported for polycrystalline AlN films, deposited on silicon

substrates. For example, our result is comparable to the thermal boundary resistance estimated by Belkerk et al. (2012) and Duquenne et al. (2012), who both found that R_s varied from about 40×10^{-9} to 10×10^{-9} m^2K/W for AlN films prepared by unbalanced and balanced magnetron DC sputtering, respectively. The difference between the reported values and the one obtained in this work can be attributed to the strong dependence of thermal properties on the deposition processes. From the few studies reported on the thermal properties of polycrystalline AlN films, it clearly appears that unbalanced and balanced DC magnetron sputtering lead to higher thermal conductivities, and therefore lower thermal boundary resistances, compared to RF processes. The above-mentioned technique yields films which are more dense and have larger grain sizes, thereby resulting into lower values of R_s. Furthermore, it is worth noting that Belkerk and Duquenne (and their coworkers), have reported the presence of an intermediate amorphous region between the Si substrate and the AlN films, which was rather associated to the growing mechanisms of polycrystalline AlN (a-AlN in the early growth stage) than to the native silicon oxide (a-SiO_2). Yet, a cleaning process to eliminate the a-SiO_2 native layer performed prior to film deposition was not mentioned. It is therefore unclear if the obtained R_s contains the thermal resistance of an amorphous AlN structure near the interface, or involves the contribution of the a-SiO_2/AlN interface. In this study, it was found that polycrystalline AlN grows directly onto the native a-SiO_2 layer of about 3 nm, which formed at the surface of the bare silicon substrate. In addition, the TEM analysis presented in Chapter 5, did not reveal any evidence of an a-AlN structure at the early growth stage. Results obtained for AlN films sputtered on SiO_2 may therefore be better suited for comparison purposes.

Kato et al. (2001) reported thermal conductivities from 5.6 to 8.4 $W/m \cdot K$ for AlN films of thicknesses ranging from 1 to 3 μm, deposited by RF magnetron sputtering on silica-glass substrates. Their results are similar to the ones obtained in this study. Kato and coworkers did not reported the thermal boundary resistance, but it can be easily determined with Eq.3.29, as $R_s = 100 \times 10^{-9}$ m^2K/W. Yet, the resulting value is calculated based only on the 3 data points reported in their study, and therefore, the determination of R_s may have a large uncertainty. Nevertheless, it can be seen that films directly grown onto a-SiO_2, exhibit higher values for the thermal resistance of the interface. This substrate-dependent behavior has also been observed recently by Belkerk et al. (2014), who obtained a R_s value for films grown on a-Si_3N_4 that is 3 times higher than the one measured for films deposited on bare Si substrates. Given the highly disordered nature of the native oxide layer, the significant value of the thermal boundary resistance obtained in this work can be attributed to the fact that AlN films do not grow directly onto the bare Si substrate but on an amorphous structure of about 3 nm.

From Fig.6.6, an asymptotic behavior for the multilayer effective thermal resistance near small thickness values ($L \to 0$) can be identified. This result suggests

that the thermal boundary resistance R_s between the AlN film layer and the a-SiO_2 layer on the Si substrate does not depend on the synthesis conditions or film thickness, but on the structures and defects of the near-interface and transition regions. This indicates that these nanoscale features, along with the solid-solid interface, represent the major contribution to the overall thermal resistance, causing the largest number of diffusive scattering events of the energy carriers. Therefore, the dominant role of the thermal resistance of the interface and transition region in the thermal transport across polycrystalline films can be attributed to the carrier-boundary scattering mechanisms. The obtained values of the interface thermal resistance R at the interface between two AlN layers are reported in the last column of Table 6.2. Despite the fact that the major contribution to the overall thermal resistance is given by R_s, the considerable values of R measured in multilayers suggest that phonons also undergo significant diffusive scattering by oxygen related defects localized between two AlN layers.

The discussions developed in sections 6.1.2.2 and 6.1.2.2 were addressed rather from a phenomenological and conceptual basis than from a physical description which quantitatively explains the experimental results obtained in this work. By correlating structural features with thermal transport properties, and investigating the role of grain boundaries and size effects, a physical interpretation describing quantitatively the effect observed in Fig.6.5 and Fig.6.6 will be formulated in the section immediately to follow.

6.1.3 Correlation between structural features and thermal conductivity

It might be useful to evoke and consider the mechanisms governing thermal transport in polycrystalline films before drawing a plausible quantitative explanation for the findings presented in section 6.1.2. In a grained structure, besides phonon-phonon and phonon-boundary interactions, two additional scattering processes affect thermal conduction. In nanograined materials, lattice vibrations mean free paths are reduced due to increased grain boundary scattering and scattering within the grains, owing to the reduced grain size. The former mechanism refers to the intergranular transport, while the latter is associated to the intragranular transport. The model developed in Chapter 4 provides a useful tool to understand the influence on thermal properties of grain boundaries and size effects in polycrystalline films with a structure that evolves along the cross plane direction, as is our case. Understanding the role of the abovementioned processes is a crucial issue in thermal analysis of nanocrystalline materials, due to their impact on thermal performance. In this section, the relative importance of these parameters is studied in detail by correlating the structural features of polycrystalline AlN films with their thermal transport properties. The results presented here are therefore expected to be helpful

to improve thermal performance of electronic devices involving nanocrystalline layers with non-homogeneous structures.

6.1.3.1 The impact of grain size on phonon mean free paths

In section 5.3 of Chapter 5, it was evidenced that the near-interface and transition regions are composed of very small grains of mean sizes of about 4 and 10 nm, respectively. At a critical thickness ($\approx$ 190 nm), these nanograins have coalesced to form V-shaped columnar grains, and for larger film thickness, the aligned columnar structure develops. The size evolution of grains as a function of film thickness is shown in Fig.6.7.

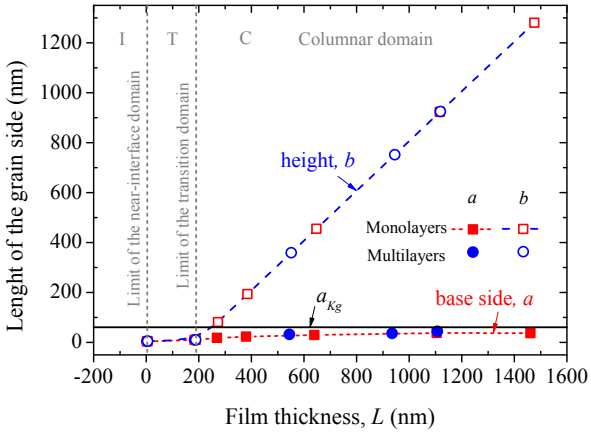

Figure 6.7: *Size evolution of grains as a function of film thickness. The increase of column diameter, or the base side of the parallelepiped structure, is represented by the short-dashed red line while grain height by the dashed blue line. The solid black line refers to the calculated Kapitza radius of grains. The capital letters I, T and C refer to the near-interface, transition and columnar regions, and the dotted gray lines represent the limit of each domain.*

Grains within the columnar region exhibit diameters that gradually increase with film thickness. This trend is represented in Fig.6.7 by the short-dashed red line, showing that the average length of the base size (column diameter) increases from approximately 18 nm to 40 nm for 270 to 1460 nm-thick AlN films. On the other hand, the height of the columnar grains (dashed-blue line) increases linearly from about 80 to 1200 nm with film thickness. By means of equation 4.8 in Chapter 4, it was stated that the effect of the interface between grains appears for grain sizes comparable or smaller than the Kapitza radius ($d_n < a_{Kg}$), which was estimated as $a_{Kg} = 60$ nm for AlN. The Kapitza radius is represented in Fig.6.7 by the black-solid line. As can be observed, the mean grain sizes in the near-interface and transition regions are well below this value, and the diameter of columnar grains throughout the entire thickness range is, as well, smaller than a_{Kg}. It is therefore expected that the effect of grain

size will be predominant in the near-interface and transition regions whereas in the columnar region it will principally affect thermal transport in the in-plane direction. Note that the column diameters and the Kapitza radius of grains are of the same order of magnitude. This result provides insight into the transport mechanism reducing the in-plane thermal conductivity, which is generally lower than the cross plane k for polycrystalline films with anisotropic structure (Graebner et al. (1994), Spina (2007), Aubain (2013)).

As described in the theoretical model, mean size of grains limits the distance traveled by the energy carriers before experiencing a collision, due to diffusive scattering at the grain boundaries. By evaluating the integrals in Eq.4.14 and Eq.4.15 it was found that, in the columnar region, the phonon MFPs due to phonon-grain interface collisions exhibit a linear behavior, with a mean distance $D_C = 0.597b + 0.111a$. In the near-interface and transition region, $b = a$ because of the considered cubic grain geometry, and numerical integration yields to $D_I = 0.926c$ and $D_T = 0.926d$. By considering the different values of mean grain size measured for each region, the MFPs D_n of phonons due to their collisions with the inner grain surfaces can be determined. The obtained results are depicted in Fig.6.8(a), which represents the evolution of D_n as a function of film thickness.

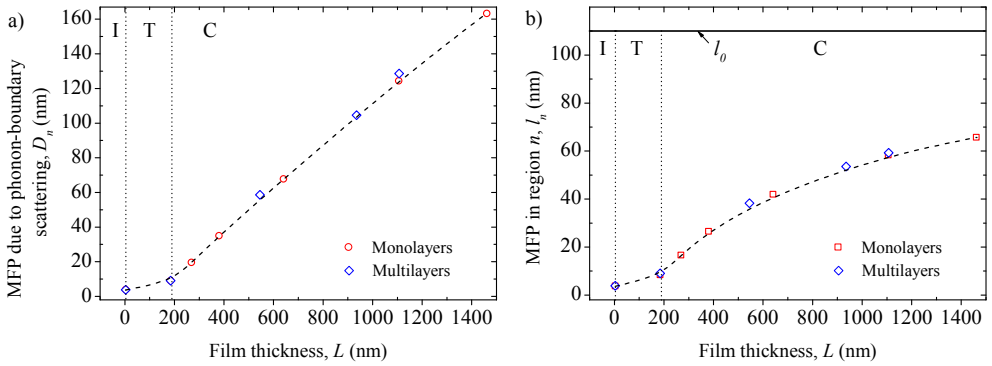

Figure 6.8: *(a) Mean free paths of phonons due to their collisions with the inner surface of grains, as a function of film thickness. (b) Effective mean free path inside grains, l_n, involving phonon-phonon and phonon-boundary scattering mechanisms. The results are evaluated using the mean grain sizes measured in each region.*

As expected, the MFPs D_n are considerably low for the near-interface and transition regions (3.8 and 9.3 nm respectively), while in the columnar region D_C increases linearly with film thickness. Yet, the dynamics of the energy carried is not only driven by their interactions with the inner grain surfaces, but also by the collisions among them. Therefore, the MFP inside grains, l_n is affected by both processes (Eq.4.5). Results for l_n are shown in Fig.6.8(b). Since the effect of both scattering processes are considered in the model, the MFPs l_n of nanocrystalline AlN films are much smaller than the single crystal

mean free path l_0, particularly for the near-interface and transition regions. In the columnar domain, it can be observed that l_n increases with film thickness, gradually approaching the monocrystalline value, $l_0 = 110$ nm (Slack et al. (1987)). This trend indicates that if the grain is large enough ($L \to \infty$), l_n becomes l_0, as expected. Thus, it is clear that the increase of the thermal conductivity for both monolayer and multilayer samples observed in Fig.6.5 is a consequence of the increment of effective phonon MFPs with grain size.

To better understand the role of phonons MFPs due the collisions among carriers and their interactions with the grain boundaries on the increase of AlN thermal conductivity with film thickness, the ratios of the reciprocals of the MFPs l_0 and D_n to the effective MFP of phonons in each grain l_n (l_0^{-1}/l_n^{-1} and D_n^{-1}/l_n^{-1}), have been calculated. Figure 6.9 represents the ratios determined with the experimental values of mean grain sizes in each structural domain of the AlN films (Fig.6.7).

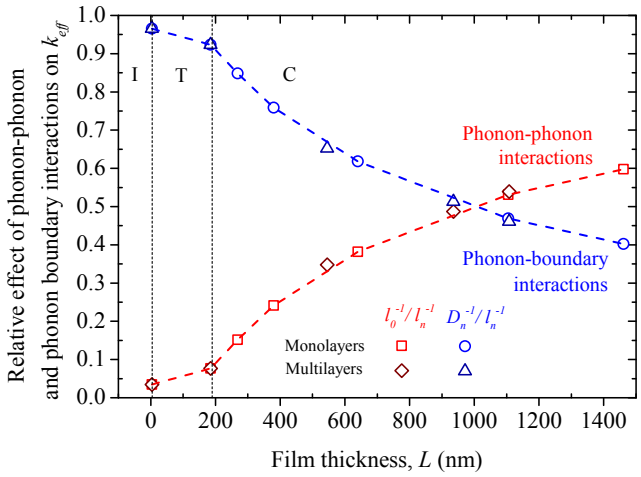

Figure 6.9: *Relative effect of phonon-phonon (red-dashed line) and phonon boundary (blue-dashed line) interactions on the thermal conductivity of polycrystalline AlN layers, as a function of the film thickness.*

From Fig.6.9 it can be clearly observed that, in the near-interface and transition regions, the reduction of MFP arises primarily from the collision of phonons with the inner surface of grains, due to the reduced length scale of the structure. While the effect of MFP due to grain boundary scattering is 0.97 and 0.92 at the interface and transition domains respectively, the impact of phonon-phonon interactions on the reduced effective MFP is 0.035 and 0.077. This trend clearly indicates that, in the small-grained domains of AlN films, the reduction of the effective phonon MFP is governed by the collisions of the energy carriers with the structure boundaries. On the other hand, at the columnar region, it can be seen that MFPs owing to phonon-boundary scattering rapidly decreases with film thickness (and therefore with grain size). At the same time, the effect

of MFPs due to phonon-phonon interactions exhibits the opposite behavior, increasing as the film thickness increases. These results reveal that, as the grains become larger and wider, the effect of D_n attenuates and the one associated to phonon-phonon collisions becomes stronger. Near 1000 nm, a crossover is observed, indicating that MFPs reduction due to phonon-phonon interactions becomes more important than the effect related to phonon-boundary scattering. The observed behavior is thereby consistent because, as film thickness increases, thermal conduction within grains which are large enough will be rather driven by phonon-phonon interactions, as in a perfect single-crystal. Accordingly, we show that the reduction of the thermal conductivity of both monolayer and multilayer systems observed as the film thickness decreases, is the result of the effective MFPs reduction due to the increase of collisions with the boundaries of grains. The mean dimension of these grains is indeed reducing when the film thickness decreases.

6.1.3.2 The effect of grain boundaries and size effects on the effective bulk thermal resistance

To understand the linear increase of the effective thermal resistance with layer thickness, observed in Fig.6.6, it is convenient to first consider the AlN layers as an effective medium composed of grains, as described in our model. In Eq.4.4, the effective bulk thermal resistance (d_n/k_{n0}) of polycrystalline materials can be divided in two components: one arising from the interface among grains (R_g) and the other from the intrinsic thermal resistance associated to the grain itself (intragranular resistance). Here, the term "bulk" refers to the fact that the layer is assumed to be an infinite medium, i.e the effect of the thickness is not considered at this point. Using Eq.4.4, the effective bulk thermal resistance was determined, and the results are shown in Fig.6.10.

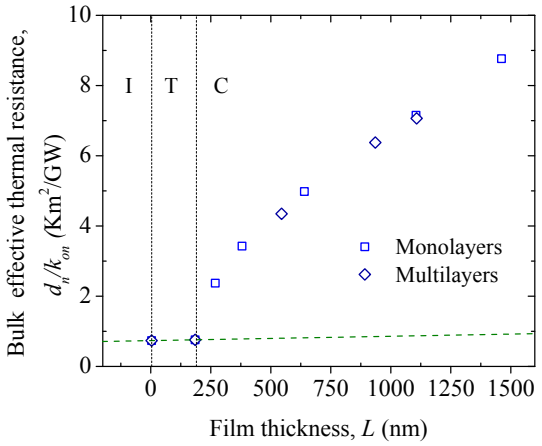

Figure 6.10: *Bulk effective thermal resistance as a function of the film thickness, for the monolayer and multilayer configurations.*

As can be seen in Fig.6.10, the effective bulk thermal resistance of polycrystalline AlN in the near-interface and transitions regions is very low, of about 7.5 $\times 10^{-10}$ K $\cdot$ m^2/W (green-dashed line), evidently due to the reduced length scale of the grains in those domains. In the columnar region, conversely, $d_n/k_0 n$ increases with film thickness with a linear-like behavior. To explain this result, the effects of the intrinsic intragranular (R_{gn}) resistance, and the one associated to the interface among grains R_g, can be determined performing an analysis similar to the one used for the MFPs in the previous section. By this means, the ratios between R_{gn}, R_g and the effective bulk thermal resistance R_{n0} were calculated as a function of the grain size which evolves with film thickness, and are presented in Fig.6.11.

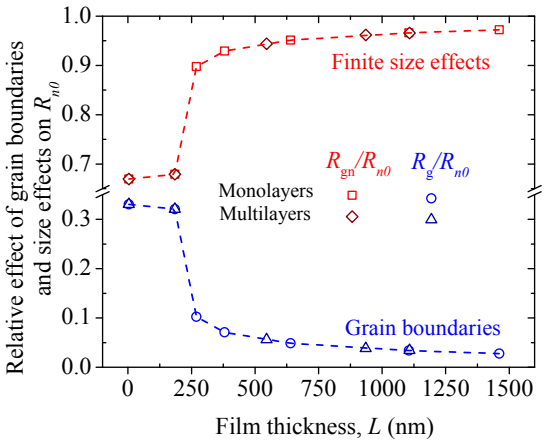

Figure 6.11: *Effects of grain boundaries and finite size on bulk thermal resistance ($R_{n0} = d_n/k_{n0}$), as a function of the film thickness.*

As can be seen from Fig.6.11, the impact of R_{gn} is higher throughout the thickness range, and with film thickness, the effect of the intragranular resistance becomes stronger, while the one related to interface among grains drops and becomes weaker. This result indicates that, as film thickness increases and therefore the grain size, the finite size effects get stronger than the one of the grain boundaries, because the intrinsic thermal resistance of the grains increases as the grains become larger. Yet, at the near-interface and transition regions, both effects are substantially present. In those domains, the impact of R_{gn} and R_g are respectively 0.67 and 0.32, indicating that both effects play a significant role. At about 190 nm, in the limit of the transition domain, R_g rapidly drops and the intragranular resistance becomes the most significant parameter, causing the increase of the effective thermal resistance with film thickness. These results are in agreement with the value obtained for R_g in Chapter 4, which was estimated as 2.4 $\times 10^{-10}$ K $\cdot$ m^2/W. It was experimentally demonstrated that the film-substrate and layer-layer interfacial thermal resistances were at least two orders of magnitude higher that R_g (see Table 6.2), suggesting that grain-

grain resistance had a relatively small contribution to the overall reduction on the effective thermal conductivity. This is equivalent to the behavior observed in Fig.6.11. Finally, as L tends towards large thicknesses, the intragranular resistance effect approaches 1, indicating that the intrinsic resistance of the grain is the only factor limiting thermal transport, as is the case for a perfect bulk single crystal, which can be viewed as an infinitely large grain. Furthermore, our results are in good agreement with an analysis recently performed, using a similar method, by Dong et al. (2014). They studied the relative importance between grain boundaries and size effects on thermal conductivity of nanocrystalline diamond, by considering an effective grain size, but the grain size evolution along the cross-plane was not taken into consideration. In their study, Dong and coworkers observed an equivalent trend to the one obtained in this work, in which the strongest influence arise from the finite size effects at large grain sizes.

6.1.3.3 Effect of the resistances of different structural domains on the effective thermal resistance of AlN

After studying the small-scale phenomena playing an important role on the effective thermal conductivity and resistance of AlN films, such as the effect of phonon MFPs, grain boundaries and limited size of grains, we can appeal to a "more macroscopic" examination. By means of Eq.4.2, we saw that, under the "three sub-regions" consideration, the effective resistance of AlN films can be divided into three components arising from the different structural domains, namely the near-interface, transition, and columnar regions. It is noteworthy that here, the effective resistance refers exclusively to the AlN films, and do not include the interfacial resistance between the films and the substrate. To obtain the AlN effective thermal resistance (L/k_{AlN}), k_n was calculated for $n = I,\ T,\ C$ with Eq.4.10 and k_{AlN} with Eq.4.11. Note that the expression for AlN effective thermal resistance, $L/k_{AlN} = \sum_n L_n/k_n$, takes into consideration the relative thicknesses of each domain with respect to the total film thickness, contrarily to the bulk effective thermal resistance, d_n/k_{n0}, discussed in the previous section.

The obtained results for L/k_{AlN} as a function of the film thickness for the monolayer and multilayer configurations are plotted in Fig.6.12. The contributions of the near-interlace and transition region to the effective thermal resistance are represented by the short-dashed red line and the dashed green line respectively.

As expected, $R_I = L_I/k_I$ and $R_T = L_T/k_T$ remain constant over the entire thickness range and $R_{AlN} = L/k_{AlN}$ gradually increases with film thickness as a result of increased mean grain sizes. Determining the ratios R_I/R_{AlN}, R_T/R_{AlN} and R_C/R_{AlN} was required to evaluate the role of each structural domain in the effective thermal resistance of AlN layers. The results for the

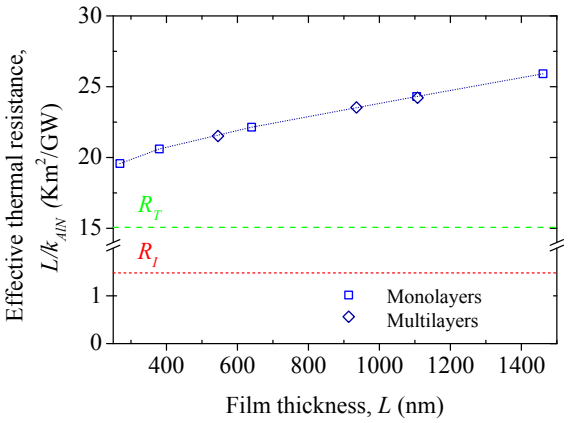

Figure 6.12: *AlN effective thermal resistance (L/k_{AlN}) as a function of the film thickness for the monolayer and multilayer configurations. The short-dashed red line refers to the resistance of the near-interface and the dashed-green line to the one of transition region.*

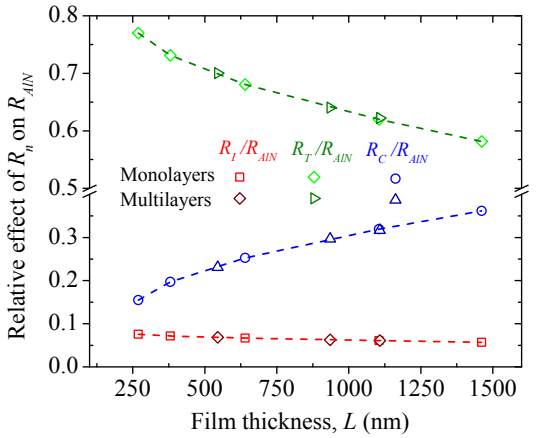

Figure 6.13: *Relative influence of the three different structural domains ($R_n = L_n/k_n$) on the AlN effective thermal resistance, as a function of the film thickness. The red, green and blue dashed lines represent the near-interface, transition, and columnar regions, respectively.*

effect of the contributions resulting from each structural domain (R_n) on the AlN effective resistance are depicted in Fig.6.13.

From Fig.6.13, it can be observed that both the relative influences of the near-interface and transition regions decrease as the films become thicker. Yet, the values for the transition region are higher throughout the thickness range, over R_I/R_{AlN} and R_C/R_{AlN}. This indicates that the influence of the transition region is stronger, certainly because the aspect ratio of grain size to region thickness is largely weaker for this domain. As a consequence, this zone which is composed of very small grains ($\approx$ 10 nm), extends over a thickness of about 190

nm, representing a high thermal resistance. Regarding the interface domain, it can be seen, as expected, that its effect is stronger for thinner films and gradually decreases with thickness. The results in Fig.6.13 suggest that this domain has a weaker influence on the effective thermal resistance of AlN films. This is owing to the small thickness of the near-interface region that approaches 4 nm. Conversely, the effect associated to the columnar domain strengthens gradually with film thickness. The columnar region has an aspect ratio of grain size to region thickness which is higher than the one of the transition region but lower than that of the interface region, and it increases with film thickness (because grain size increases as well). It is therefore expected that the influence of this region becomes more and more important for thicker films, but its value do not reach the one of the transition region, which represent a higher thermal resistance for the overall film thickness. In the previous section, it was showed that for thiner films, the most significant contribution comes from the effect of grain boundaries while for thicker films the intrinsic resistance of the grains has higher influence. This is in agreement with the trend observed here for the three regions.

6.1.3.4 Influence of the intrinsic and interfacial thermal resistances on the effective thermal conductivity of AlN films

After understanding the influence of each structural domain on the effective thermal resistance of AlN films, it is then possible to continue towards the comprehension of the effect of the resistance associated to AlN and the one related to the interface between the films and the substrate. First, monolayer systems will be considered, and the study will extend to the multilayer configuration by analyzing the impact of local oxidation. In this way, the description might provide, to conclude, a global perspective of the parameters influencing AlN film thermal conductivity.

- **Monolayers**

To better understand the effective thermal resistance of monolayered AlN films deposited onto Si substrates, the effects of the thermal boundary resistance between AlN and its substrate and the one of AlN (Eq.4.11) were calculated on the basis of Eq.4.16. The principle used for the analysis remains the same. The ratios of R_{AlN} and R_s to R_{eff} were calculated for monolayers. The obtained results are shown in Fig.6.14.

For thinner films, the most significant contribution comes from the interface between the film and the substrate, whereas the effect of R_{AlN} shows a much smaller value (0.73 for R_s/R_{eff} compared to 0.27 for R_{AlN}/R_{eff}). As the film thickness increases, the effect of R_s weakens while that of AlN strengthens. The thickness-dependent behavior of the effective thermal conductivity, observed in Fig.6.5, can therefore be explained as the resulting mixed contribution of the weakening influence of the interfacial thermal resistance and the increase on

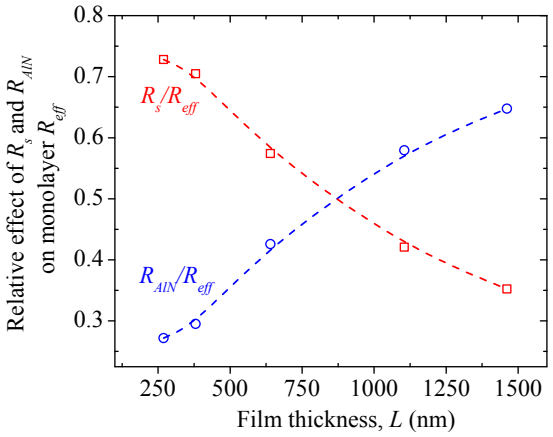

Figure 6.14: *Relative influence of the intrinsic AlN and interfacial thermal resistances (R_{AlN} and R_s respectively) on the effective thermal resistance of monolayered films deposited on Si substrates. The red and blue dashed lines represent R_s/R_{eff} and R_{AlN}/R_{eff}, respectively.*

phonon MFPs for thicker films. At about 850 nm a crossover of the effects is observed, and for thicker films, the influence of the AlN thermal resistance becomes stronger. At 1460 nm, the effect of R_{AlN} reaches a maximum value of 0.65 and that of R_s drops to 0.35. This result is consistent with the experimental observations, because the mean grain sizes increase as the films become thicker. Therefore, the intrinsic AlN resistance begins to be predominant in the thermal transport. Thus, the trend observed for R_{AlN} is useful to explain the increase of the effective thermal resistance, which becomes more important at larger thicknesses.

- **Multilayers**

An analogous exploration can be performed to understand what happens in multilayer specimens. Thermal transport on multilayered samples is not only driven by the effects related to the intrinsic AlN and interfacial resistances, but also by local oxidation, which acts as an additional thermal resistance. The latter quantity was measured experimentally and the obtained values are summarized in Table 6.2, for samples consisting of two ($N = 2$), three ($N = 3$), and four ($N = 4$) AlN layers ≈ 270 nm thick, deposited one on the top of the other. The influence of these groups of parameters was investigated by calculating the ratios of R_s, R_{AlN} and R, the latter referring to the interfacial thermal resistance between two successive AlN layers owing to localized oxidation, to the effective thermal resistance, R_{eff}. The obtained results are plotted in Fig.6.15.

An equivalent trend to the one observed for monolayered specimens can be identified in Fig.6.15. At small values of film thickness ($L \to 0$), R_s appears as the parameter governing thermal transport, and the effect of the intrinsic AlN

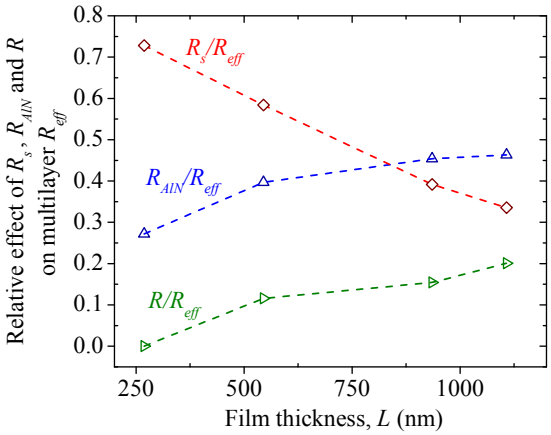

Figure 6.15: *Relative effect of the intrinsic AlN resistance (R_{AlN}), as well as AlN-Si (R_s) and AlN/AlN (R) interfacial thermal resistances on the effective resistance (R_{eff}) of multilayered films deposited on Si substrates. The red, blue and green dashed lines represent R_s/R_{eff}, R_{AlN}/R_{eff} and R/R_{eff} respectively.*

resistance exhibits low values. Then, as the film thickness increases, the impact of the AlN-Si interface drops down and the one associated to R_{AlN} raises. As for monolayers, a crossover can be identified at about 850 nm, and for thicker films the effect of the AlN resistance becomes stronger than that of the AlN-Si boundary resistance. However, the increase of the influence of R_{AlN} appears to be gradually attenuated. On the other hand, it can be seen that the effect of AlN/AlN oxidized interfaces, which is weaker compared to the ones corresponding to R_{AlN}/R_{eff} and R_s/R_{eff} over the entire thickness range, increases with film thickness. Therefore for thicker films, both resistance components R_{AlN} and R contribute to reducing k_{eff} (Fig.6.5) and increasing R_{eff} (Fig.6.6). For example, for a $L = 4 \times 270$ nm multilayer, the impact of $R/R_{eff} = 0.2$ adds to the influence of $R_{AlN}/R_{eff} = 0.46$, whilst for a monolayer of approximately the same thickness (1105 nm) $R_{AlN}/R_{eff} = 0.57$. This result provides a clear explanation to the fact that the effect of film thickness on k_{eff} is strongest for monolayered samples. This is because, in monolayers, R_s and R_{AlN} are the exclusive parameters impeding the increase of k_{eff}, while, in multilayers, the effect of R adds. Consequently, the observed attenuation of the k_{eff} increase, which appeared to be more pronounced for multilayers, can be explained as a result of adding contributions of R_{AlN} and R, which increase as the films become thicker.

6.1.4 Statically tailoring thermal conductivity by structural inhomogeneity and interfacial oxidation

The experimental and theoretical results presented in section 6.1 demonstrate that the structural inhomogeneity and oxygen defects of polycrystalline AlN

films can be efficiently used to statically tune their cross-plane thermal conductivity.

Differential 3ω measurements showed a systematic decrease of the effective thermal conductivity when decreasing film thickness. For multilayers with thickness varying from 1107 to 270 nm, a reduction of $\approx 47\%$ on the effective thermal conductivity was observed. On the other hand, for their corresponding monolayer counterparts of approximately the same thickness, the effective thermal conductivity decreased by $\approx 58\%$. The analytical model developed for nanocrystalline materials with non-homogeneous structure (Chapter 4) was used to thoroughly describe the mechanisms influencing the thermal conductivity. It was found that the thickness-dependent behavior appears as a result of the interface thermal resistance, as well as the grain boundaries and finite size effects associated to the structural inhomogeneity. Particularly, small grains in the near-interface and transition regions cause a drastic decrease in the phonon MFPs due to collisions with grain boundaries. It was demonstrated that both the effects of the interfacial thermal resistance and the resistance resulting from the small-grained domains, weaken with film thickness. At the same time, the increase of phonon MFP and the resistance of the columnar region, which is lower than that of the near interface and transition regions, strengthen because of the grain evolution towards greater mean sizes. Therefore, the resistances due to the interface and the small-grained regions dominates thermal conduction for thinner films, whilst for thicker films, the increased MFPs and intrinsic resistance resulting from the columnar region predominate. Thus, as the film thickness increases, the effects of the interface and the small-grained domains are shadowed by the effect of the columnar region. The reason is that the relative contribution of each domain to thermal transport is determined by its corresponding thickness with respect to the total film thickness.

Furthermore, it was evidenced experimentally that local oxidation in multilayer systems yields to an overall reduction in thermal conductivity. For example, an effective thermal conductivity of 5.93 $\mathrm{W/m \cdot K}$ was measured for a 1107 nm-thick multilayer structure, which represents a reduction of 20% of the thermal conductivity of an AlN monolayer with approximately the same thickness. It was shown that the low values of k_{eff} obtained for multilayered structures result from phonon scattering at grain-boundary-like planar defects induced by substitutional oxygen impurities. These 2D defects are localized transversely with respect to the out-of-plane axis, strongly limiting thermal conduction in the direction here studied. The 3ω experiments evidenced as well that the increase of k_{eff} attenuates with film thickness, and this trend appears to be more pronounced for multilayer samples. It was found that this behavior is a consequence of adding contributions coming from the intrinsic resistance of AlN and AlN-AlN interfaces. In monolayers, R_s and R_{AlN} are the exclusive parameters limiting the increase of k_{eff} while in multilayers, the contribution of R adds, further weakening to the increase of the effective thermal conductivity.

By means of a simple yet accurate theoretical model, we have therefore explained the experimental observations obtained from differential 3ω measurements. From this results, it is clear that grain mean sizes along the cross-plane direction, and structural features at the interface and transition domains, are key elements to tailor thermal properties of nanocrystalline films with inhomogeneous structures. Depending on the suited application, the grained structure can be controlled to obtain better thermal conductors or improved thermal insulators. This can be achieved by applying the fundamental principles of structure forming phenomena of polycrystalline films, and using zone models (Barna and Adamik (1998), Thornton (1977)).

While an in-depth discussion addressing the application of these principles to control mean grain size falls outside of the scope of this dissertation, a few words must be said about the driving mechanism of grain evolution. Although forming phenomena of polycrystalline films are highly complex and involve all deposition parameters, efforts to control grain size might be focused on the dependence of these phenomena on temperature. Grain structure evolution is driven by the tendency for the smallest possible surface energy and therefore the energy supplied to the system, namely as temperature, has a crucial role in mean grain size (Knuyt et al. (1995)). Thus, to obtain highly conductive materials, a great amount of energy needs to be supplied during deposition process to promote the development of an homogeneous structure along the film thickness. Epitaxial growth at high temperature may be better suited for this purpose. On the other hand, decreasing the supplied energy favors the growth of films composed of fibers with very small diameters (1 - 10 nm), which contain high density of defects and in which the grain boundaries are porous. This structure is well adapted for low conductivity applications. Other means of disturbing phonon transport, such as, dislocations, vacancies, interstitial voids, mass differences, and substitutional impurities can also be used to reduce thermal conductivity. As demonstrated in this work, local oxidation at interfaces can be effectively employed to impede thermal transport in the cross-plane direction.

The experimental results and the analysis of different effects on thermal properties presented in section 6.1 can be used to understand, predict and statically control thermal properties of polycrystalline layers with structural features that evolve along the film thickness. They are expected to be useful in improving thermal performance of electronic devices and thermoelectric materials.

Now that the ability of statically tailoring thermal properties of nanocrystalline thin films by structural inhomogeneity and interfacial oxidation has been demonstrated, the analysis can be extended by examining the possibility to dynamically modulate heat transfer. In the section that follows, the influence of lattice deformation caused by externally induced elastic strain on the thermal conductivity of monolayer and multilayer AlN films is investigated experimentally.

6.2 Strain-dependent thermal conductivity measurements

Thermal measurements as a function of strain were achieved using a novel experimental approach consisting of a 4 points bending system coupled to the 3ω method. The main objective of performing strain dependent experiments was to explore the possibility to dynamically modulate heat transfer across films of polycrystalline aluminum nitride. As discussed in the previous sections, heat transport processes in nanoscale polycrystalline materials are dominated by interactions of phonons with elements that disturb the crystalline lattice. Elastic strain provides the possibility to dynamically alter the crystal symmetry and therefore potentially modulate thermal conduction. Despite of the promising technological applications and the emerging interest on the subject, very few studies have investigated experimentally the effect of strain on thermal transport in small length-scale systems. The main reason relies on the intrinsic complexity of simultaneously inducing and measuring strain in a low-dimensional structure, while performing thermal conductivity measurements. Motivated by the evident lack of experimental results and the need to characterize the thermal conductivity of thin films as a function of strain, the newly measurement technique coupling the 3ω and a four points bending system was used to investigate strain-mediated thermal conduction. The new set-up developed in this work and the experimental methodology used to carry out experiments was thoroughly described in section 3.7 (Chapter 3).

Three different AlN samples were analyzed for comparison. First, to investigate the influence of out-of-plane crystal orientation distributions on strain-mediated thermal conductivity, highly and poorly textured AlN monolayers were investigated. In this case, thermal conductivity of highly-textured (FWHM = 2.93°) and poorly-textured (FWHM = 8.5°) monolayer samples were measured as a function of elastic-induced strain. Then, to study the influence of oxygen-related defects on thermal transport, strain-dependent thermal measurements were also performed on a 935 nm [$L = 3 \times (\approx 270$ nm)] AlN/AlN multilayer. The deposition processes were described in sections 2.2.5.1 and 2.2.5.2 (Chapter 2). In particular, these 3 samples were chosen because their fracture stresses were the highest in the experimental sample set and their effective thermal conductivities were similar. Indeed, several samples fractured while inducing four-point-deflections therefore impeding the recording of sufficient data points. Differences in fracture stresses values from one sample to another arose from the scribing-cleaving processes used to fabricate the rectangular beams, as described in subsection 3.7.2.3 (Chapter 3). The specimens chosen to perform strain-mediated thermal measurements, were therefore those with fracture stresses that allowed collecting a maximum of experimental data points. These 3 samples were also studied by transmission electron microscopy, as described in section 5.3.

Prior to strain-dependent measurements, the effective thermal conductivities of the studied specimens were measured by placing the samples onto a chuck at room temperature, following the classical 3ω methodology. The main objective of these prior measurements was to test the feasibility of the experiment on the newly developed experimental set-up. Contrarily to thickness-dependent measurements, the contribution of the native silicon oxide layer was not subtracted from the total experiment temperature rise, and the effective thermal conductivities were determined by Eq.3.21. The reason is that the differential technique requires a larger number of prior measurements, and therefore can introduce additional experimental errors. As described in subsection 3.7.2.5, when applying a mechanical load to the AlN sample, the 3ω pattern is as well subjected to strain. Thus, the response of the electrical resistance as a function of strain has to be necessarily characterized. The differential technique (used in thickness-dependent experiments) will require two sets of measurements of the strain coefficient of electrical resistance. Because of time limitations and to avoid introduction of any additional experimental uncertainties, Eq.3.21 was therefore used to extract the effective thermal conductivities of the studied samples, following the procedure of thin film-on-substrate measurements. Furthermore, it was recently demonstrated by Wang and Shen (2014), who theoretically studied the effect of stain on thermal properties of Ni/Al laminated structures, that the interfacial thermal resistance varies as a function of tensile strain. By investigating the effect of strain on the AlN/SiO_2 specimens, the impact of the interfacial thermal resistance is involved and can be observed experimentally.

The main properties of the studied specimens are listed in table 6.3 as well as the effective thermal conductivities κ_{eff} obtained with Eq.3.21 by following the typical 3ω procedure for film-on-substrate systems.

Table 6.3: *Physical properties of the samples analyzed under strain in 3ω measurements*

Sample	Crystallinity	Thickness (nm)	Rocking curve FWHM (°)	κ_{eff} [a]
Monolayer	Highly textured	640	2.93	4.90 ± 0.29
Multilayer	Highly textured	935	3.20	4.98 ± 0.25
Monolayer	Poorly textured	850	8.50	5.08 ± 0.23

[a]The reported values, κ_{eff} were obtained with Eq.3.21 by placing the samples onto a chuck at room temperature, following the classic 3ω methodology. They include the contribution of the SiO_2 layer, which is not the case for the k_{eff} values reported in Table 6.2.

It is worth to mention that the values in Table 6.3, referring to the effective thermal conductivity of the AlN/SiO_2 structures, are denoted as κ_{eff} to differentiate them clearly from k_{eff} values. The latter were obtained by removing the thermal response of the SiO_2 layer, and thus make reference to the effective thermal conductivity of AlN films only.

As explained in subsection 3.7.2.5 (Chapter 3), in strain-dependent measurements, the heater is also subjected to deflection. In this case, the total resistance change is the consequence of the temperature rise due to the underlying matter and the induced strain. Then, it is necessary to accurately characterize the variations of the electrical resistance generated in the resistive strip by the deformation due to the applied mechanical load. Next section deals with the results obtained from the strain-dependent measurements of the electrical resistance.

6.2.1 Effect of elastic strain on the heater electrical resistance

The electrical resistance response of a Au/Ti heater deposited on a 850-nm thick AlN monolayer (FWHM=8.5°) was measured as a function of externally induced strain, following the experimental procedure described in subsection 3.7.2.5 (Chapter 3). In the experiments, the applied force varied from 0 to 11 N, which represents a strain ranging from 0 to 1.69×10^{-3} (m/m). For each value of applied mechanical load, 5 series of voltage *versus* current [V(I)] measurements were recorded. Then, the electrical resistance was determined from the slope of the voltage *versus* current curve. The measured variations of electrical resistance, R_e, as a function of strain, ε, are shown in Fig.6.16.

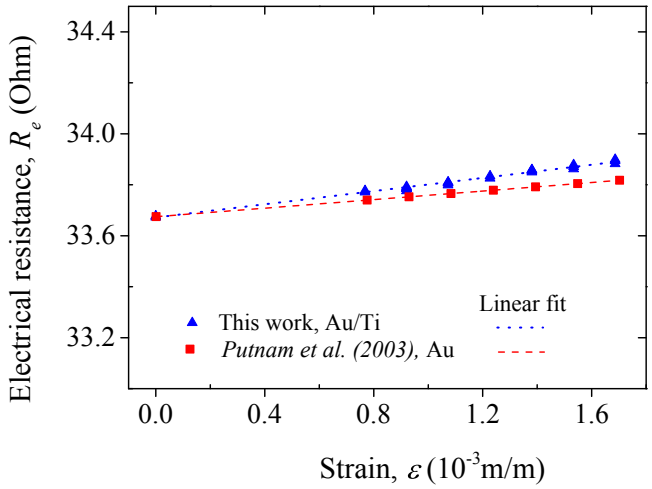

Figure 6.16: *Variation of electrical resistance as a function of strain for a Au/Ti heater (blue-dotted line). Results obtained by Putnam et al. (2003)(red-dashed line)*

It is noteworthy that strain-dependent electrical measurements were performed for this particular heater, assuming that variations of the slopes of the electric resistance *versus* strain curves from one heater to another are small.

From Fig.6.16, it can be seen that the electrical resistance changes from 33.7 to 33.9 Ω in the studied strain-range. The variations in electrical resistance

as a function of strain arise from the geometrical changes taking place in the deformed body and the physical changes within the metal itself (Kuczynski (1954)). From the experimental data, it is possible to extract the coefficient of strain sensitivity of resistance, (or gauge factor):

$$F = \frac{1}{\varepsilon}\frac{dR_e}{R_{e0}} \tag{6.1}$$

Note that the coefficient of strain sensitivity of resistance is a dimensionless quantity. Using Eq.6.1, the gauge factor for the studied Au/Ti strip was estimated as $F = 3.84$. This result is comparable to the coefficient of strain sensitivity of resistance calculated by Putnam et al. (2003), who obtained $F = 2.5$ for an Au heater of 300 nm of thickness and of 30 μm length. Their results are included in Fig.6.16 for comparison (red-dashed line). In the 3ω measurements, the total relative resistance change will therefore be affected by the strain-dependent response. This problem is analogous to the one encountered while using strain gauges to measure the amount of deformation of a body. Since the resistance of the gauge also responds to changes in temperature, thermal-related effects need to be taken into consideration to avoid errors in strain measurements. In this case, the equation describing the total relative resistance change of the gauge due to thermal and the geometrical/physical effects can be expressed as the sum of a temperature and a strain-related term (Sharpe (2008)), such that:

$$\frac{\Delta R_e}{R_{e0}} = \left[\alpha + F(\beta_{AlN} - \beta_h)\right]\Delta T \tag{6.2}$$

where β is the coefficient of thermal expansion and the subscripts AlN and h refer to the AlN film and the Au/Ti heater respectively. The effect of strain on the total temperature rise can be included in the model by combining equation 6.2 and 3.6, which yields:

$$\Delta T_{2\omega|avg} = \left[\frac{2}{\alpha + F(\beta_{AlN} - \beta_h)}\right]\frac{V_{3\omega,RMS}}{V_{1\omega,RMS}} \tag{6.3}$$

By considering typical values of the coefficients of thermal expansion of AlN $\beta_{AlN} = 4.2 \times 10^{-6}$ 1/K (Morkoc (2009)) and gold $\beta_h = 13.6 \times 10^{-6}$ 1/K (Magisa et al. (2014)), and combining Eq.6.3 and Eq.3.21, the effective thermal conductivities of the AlN/SiO_2 samples can be determined as a function of strain. A similar approach has been used by Putnam et al. (2003) to perform high precision 3ω measurements of the thermal conductivity of composites of nanoscale alumina particles in polymethylmethacrylate (PMMA) matrices. In their investigation, the effect of strain in the metal line, due to the high thermal expansion coefficient of the PMMA substrates, was compensated by a strain-related correction of the electrical resistance, which yielded satisfactory results. In the following subsections, the results obtained by strain-mediated thermal measurements are discussed.

6.2.2 Strain-dependent thermal conductivity measurements on AlN samples

Initially, the effective thermal conductivities of AlN samples were measured on the 4-point bending set-up (4PB) without external mechanical loading, except for the contact force exerted by the micro-probes, which represented a negligible contribution of 0.2 N. By placing the samples onto the bending set-up, the boundary condition between the substrate and environment is changed, because the beam is exclusively supported by the stationary lower rods. This is not the case in classic measurements, where the samples are mounted onto a chuck. In general, the 3ω method is insensitive to this boundary condition owing to the confinement of the heat wave inside the sample. As the modulation frequency in experiments varied from 100 Hz to 1 kHz, the thermal fluctuation was well localized within the film and substrate. Thus, neglecting thermal exchange with the environment is supposed to be a good approximation. However, measurements on unstrained samples were performed to check for effects related to the boundary condition between the substrate and the environment, which can be a source of error in the experiment. The effective thermal conductivities of the unstrained AlN samples were extracted using Eq.6.3 and Eq.3.21. The values of κ_{eff} obtained for $\varepsilon > 0$ on the 4PB set-up and, for comparison, the results obtained on a chuck are listed in Table 6.4.

Table 6.4: *Comparison between κ_{eff} measurements of unstrained samples performed onto a chuck at room temperature (classical 3ω method) and on the four points bending set-up.*

Sample	Thickness (nm)	Rocking curve FWHM (°)	κ_{eff} on chuck [a] (W/m·K)	κ_{eff} on 4PB set up [b] (W/m·K)
Monolayer	640	2.93	4.90 ± 0.29	4.74 ± 0.30
Multilayer	935	3.20	4.98 ± 0.25	5.10 ± 0.24
Monolayer	850	8.50	5.08 ± 0.23	5.33 ± 0.28

[a] Effective thermal conductivities of AlN samples measured by placing the samples onto a chuck at room temperature, following the classic 3ω method.
[b] κ_{eff} results obtained by placing the samples on the four points bending set up without external mechanical load.

The results obtained on the 4PB set-up show good agreement with the measurements performed on a chuck at room temperature, and are consistent within the uncertainty of the measurement. Thus, measurements at zero induced-strain suggest that experiments performed on the four-points bending set-up are not affected from the environment boundary condition. After discarding the possibility of background steady heating affecting thermal measurements, the effective thermal conductivities κ_{eff} were measured by gradually increasing the mechanical load (and therefore the strain), until specimen fracture. Fig.6.17

compares the obtained results for the three studied samples. The dashed lines and the equations in the top corners refer to the analytical fits performed for the experimental data, and the type of sample studied is represented schematically fore the sake of clarity.

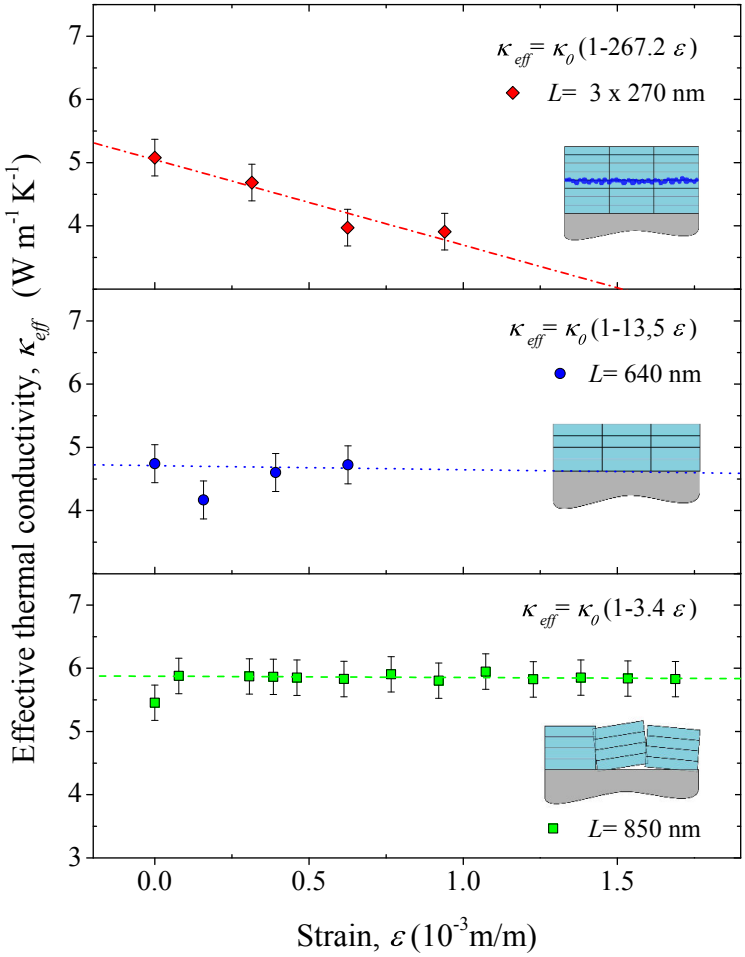

Figure 6.17: *Effective thermal conductivities (κ_{eff}) as a function of strain. Filled rectangles (green) and circles (blue) refer, respectively, to poorly and highly-textured monolayers, and filled diamonds (red) to the multilayered structure. The dashed lines and the equations on the top corners represent the analytical fits performed for the experimental data.*

Analysis of the data in Fig.6.17 is not trivial due to the experimental points that deviate from the values of effective thermal conductivity obtained by the classical 3ω method and at zero-strain. This is particularly striking for the poorly-textured monolayer (green-filled squares), where the measurements performed on a chuck yielded $\kappa_{eff} = 5.08 \pm 0.23$ W/m$\cdot$K and on the 4PB set-up resulted in $\kappa_{eff} = 5.33 \pm 0.23$ W/m$\cdot$K. At strain values superior to 0, the obtained κ_{eff} rises to about 5.9 W/m$\cdot$K and appears to remain constant

throughout the studied strain range. Thus, the analysis is not straightforward due to results obtained at $\varepsilon > 0$, which are no longer within the uncertainty of the measurement performed by the classical method. When monitoring the heating power and the average temperature rise due to the film (Eq.3.21), any particularly significant changes, which could explain the slight increase in the measured effective thermal conductivities at $\varepsilon > 0$, were detected. P_l and ΔT_f were about 56 W/m and 0.84 K, respectively, for all the experiments on the poorly-textured specimen. Additionally, based on the analytical fit and assuming that the observed effect is indeed related to thermal conduction, a uniaxial strain of ε will decrease κ_0 (reference thermal conductivity at zero strain) by a factor of $\approx (1 - 3.4\varepsilon)$. This result is remarkably similar to the correction factor obtained for R_{e0} from the strain-dependent electrical resistance measurements, which was estimated as $\approx (1 + 3.8\varepsilon)$ for the same heater. Although this coincidence can be an isolated fact, the proximity of both factors possibly suggest that the measured effect arises rather from the strain-dependent electrical resistance of the heater than from a real variation of the thermal conductivity. Furthermore, such a small change could not be detected by the 3ω method, because the variation is smaller than the experimental uncertainty.

Measurements concerning the highly-textured monolayer (filled blue-circles) exhibit as well a data point (at $\varepsilon = 1.6 \times 10^{-4}$) lying out of the uncertainty range determined by the classical method ($\kappa_{eff} = 4.98 \pm 0.25 \mathrm{W/m \cdot K}$). This is possibly due to a poor contact between the microprobes and the metallic pads. Although the force of the microprobes was controlled throughout the experiment, the bent geometry of the beam can affect the electrical contact while measuring the $V_{3\omega}$ voltage signal. This can be monitored by the heating power, which for this particular data point was about 39 W/m, contrarily to a value of ≈ 50 W/m, recorded for the other measurements. Any noticeable changes were detected when comparing the temperature rise measured for different strain values throughout the experiment. The average temperature change induced by the film was about $\Delta T_f = 0.65$ K over the studied range of strain for this particular specimen. Furthermore, as in the case of the poorly-textured sample, the variation of the effective thermal conductivity falls within the uncertainty of the measurement, indicating that a detectable change does not occur over the studied strain-range.

On the other hand, the experimental κ_{eff} measured for the multilayer specimen exhibit a significant decrease as a function of uniaxial strain. The measured decrease of the effective thermal conductivity represents a variation of about 23%. Monitoring of the heating power, which was about 55 W/m for all the experimental points did not show striking differences between the four measurements. Yet, a significant increase of the average temperature change due to the film was detected. The results are listed in Table 6.5.

It is unlikely that such a decrease of the effective thermal conductivity, measured for the $L = 3 \times (\approx 270$ nm) multilayered specimen, arises from variations

Table 6.5: *Average temperature rise, ΔT_f, due to a $L = 3 \times 270$ nm multilayer film as a function of strain.*

Uniaxial strain	**Temperature rise due to the film**
ε, ($\times 10^{-4}$ m/m)	ΔT_f, (K)
0.00	0.93
3.15	1.01
6.25	1.19
9.40	1.19

in the thermal transport properties of the material, due to the limited range of uniaxial strain studied in this work.

It may be helpful to put these results into the context of recent studies, both theoretical and experimental, addressing the effect of strain on thermal conductivity. The evident lack of experimental results, reporting strain-mediated thermal conductivity measurements on thin films, makes challenging such comparison. To our knowledge, published works are limited to experiments carried out by Alam and Manoharan (2012) who observed a reduction of the thermal conductivity of about one order of magnitude at about 2.4% strain for 50 nm thick freestanding amorphous silicon nitride. The same group has reported recently that 2.5% tensile strain can increase thermal conductivity of 200 nm thick freestanding amorphous silicon thin films from 1 to 2.4 W/m·K (Alam and Pulavarthy (2015)). In the first work, the thermal conductivity dependence was attributed to increased vibration localization due to strain, and in the second study, the effect was associated to strain-induced changes in microstructure and carrier density. Besides the fact that these results seem to be contradictory, a comparison with our results is not feasible because the underlying mechanisms governing thermal transport in polycrystalline materials differ largely from those involved in amorphous solids.

On the other hand, theoretical studies have reported very weak changes of the thermal conductivity for crystalline materials throughout the range of strain analyzed in this work. For example, Yang et al. (2014) showed that the thermal conductivity of perfect single crystalline 13 nm-thick silicon thin film decrease by 0.5% for $\varepsilon = 0.0016$, and attributed the effect to a strain-induced red shift of the density of states of high frequency phonons. Moreover, Wang and Shen (2014) studied a Ni/Al laminated structure and showed that interfacial thermal resistance increases with tensile strain. However, the mechanisms driving thermal conduction in single crystalline materials can not be compared to those affecting thermal transport in nanoscale polycrystalline materials. Since to the best of our knowledge, any data addressing the effect of strain on polycrystalline films or structures exhibiting oxygen related defects have been reported

so far, all sources of experimental uncertainty should be carefully identified to analyze the relevance of the results obtained in this study. The discussion that follows gives some details about the potential sources of error.

Several concerns related to the experimental technique deserve further scrutiny. In our experiments, Eq.6.2 is used to include the strain-dependent electrical resistance change in the determination of the heater temperature rise (Eq.6.3). Although gauge manufacturers use this approach to control the thermal output and achieve self-temperature compensation in strain-measurements (Sharpe (2008)), unconsidered effects due to strain on electrical and thermal properties of the heater can influence thermal measurements. Additionally, Eq.6.2 is derived by assuming equal coefficients of thermal expansion in both axial and transverse directions for the gauge and specimen. This is not necessarily true, yet this is a required simplification to derive the expression. Moreover, the thermal expansion coefficients, β_{AlN} and β_h, used to extract the total temperature rise, were taken from the literature, because experimental determination is challenging and the facilities to characterize β were not available. This consideration may introduce experimental errors owing to the fact that thermal expansion coefficients of thin film depend on thickness and differences in physical properties (i.e grain size) related to deposition parameters and techniques (Mag-isa et al. (2014)). Also, geometrical changes taking place in the deformed metal strip were assumed to be negligible. Strain-induced width changes estimated for a Au/Ti heater of width $2b = 10$ µm, yielded variations of about 20 nm for the maximum strain value attained in the experiments ($\varepsilon = 0.0017$). The variations associated to the geometrical dimensions of the heater can introduce small but not negligible experimental error of $\approx 2\%$. Several reasons therefore make conclusions from the results obtained by strain-dependent measurements non trivial. The first one relies on the lack of experimental evidence and understanding of the underlying physics that drives the dynamics of energy carriers in polycrystalline films subjected to strain. The second is associated to the considerations involved in the strain-mediated experiments, which may not be always fulfilled, increasing the potential sources of uncertainty.

It is worth noting that the experimental observations yielded different strain-dependent behaviors for the analyzed specimens. Both, poorly and highly-textured monolayers exhibited minute variations, if at all, of the effective thermal conductivity as a function of strain. Interestingly, the multilayered sample showed an opposite trend, with κ_{eff} values that decrease drastically with increasing uniaxial tensile strain. Two possibilities are envisioned. First, assuming that the observed effect is indeed related to thermal conduction, one can argue that phononic transport in monolayer AlN films is weakly dependent on elastic tensile strain. Yet, externally-mediated deformation along with another means of disturbing the crystal lattice, namely planar defects introduced via localized oxidation, can dynamically reduce the thermal conductivity. The second alternative is that either unclear effects of strain on electrical and thermal

properties of the metallic strip, or other unconsidered variables, such as those aforementioned, induce experimental errors. However, if the latter assumption happens to be true, the issue concerning the different trends observed for the studied samples remains unresolved. Thus, beyond the observation of a pronounced strain-related effect on the measured κ_{eff} of an AlN/AlN multilayer, this investigation raises two questions. The first concerns the effect of strain on the thermal conductivity of polycrystalline films and low-dimensional structures in general, which is yet unclear. Further understanding is required to estimate, for example, if strain along with oxygen-related defects, are an effective means to induce significant changes in transport properties. The second issue inquires about the ability of the 3ω technique, coupled to a 4PB system, to characterize the thermal conductivity of thin films as a function of strain. To further understand the effect of strain on thermal properties and validate the preliminary results here observed, other thermal characterization techniques which do not involve the electrical or optical response variations of a metallic layer to derive thermal properties of the studied material, should be used to perform strain-mediated thermal measurements.

6.3 Summary

The impact of local oxidation and morphology evolution of grains along the cross plane direction of polycrystalline films of aluminum nitride on their thermal conductivity has been investigated both experimentally and theoretically. The diffusive scattering of phonons due to oxygen-related defects localized at the interface between two AlN layers has been studied by thermal measurements of the multilayered configuration. The obtained results describe the thickness-dependent behavior of the thermal conductivity of nanoscale polycrystalline AlN films through a simple yet accurate analytical model. The relative influence on thermal conduction of phonon MFPs, grain boundaries, size effects and thermal resistances associated with the different structural domains present in inhomogeneous films was studied by correlating structural features with thermal properties. The theoretical and experimental results presented in sections 6.1 demonstrate that the structural inhomogeneity and oxygen defects of polycrystalline AlN films can be efficiently used to statically tune their cross-plane thermal conductivity. These findings can be extended to other materials of great interest in new technological applications such as GaN, diamond, or ZnO, which usually exhibit the characteristic structural non-homogeneity. Dynamic modulation of thermal transport was explored through strain-dependent thermal conductivity measurements, by coupling a four-points bending system to the classical 3ω set-up. The effective thermal conductivity measured for poorly and highly-textured monolayers did not show variations with increasing uniaxial tensile strain, while for the multilayered specimen, a significant decrease was detected. A reduction of about 23% was observed while increasing tensile strain

to 0.095%. It is unlikely that such a drastic decrease of the effective thermal conductivity arises from real variations in the thermal transport properties of the material, due to the limited range of uniaxial strain studied in this work. Careful scrutiny of possible uncertainty sources should be carried out to further understand and analyze the relevance of the observed strain-mediated effect. Perhaps more importantly, this study raises the question of the impact of strain in thermal conduction and on the applicability of the now available methods to study it (or at least the one here investigated). These questions highlight the need of developing new means of accurately characterize thermal conduction on low-dimensional structures, while simultaneously inducing strain.

Conclusion

This work was dedicated to the investigation of the thermal conductivity of nanoscale polycrystalline AlN films. Its main objective was to understand fundamental phonon transport phenomena in nanocrystalline structures and draw new insights into effective means of modulating heat transfer across them. The approach used to achieve this goal extended from film fabrication and understanding of the growing phenomena, to the characterization of their physical properties and the thermal transport analysis, focusing on the effect of multiscale defects and strain. Understanding the influence of structural features and other multiscale crystallographic defects, is a key element for enhancing the performance and reliability of micro- and optoelectronic devices, and look towards new solutions for controlling phonon transport in solid-state systems.

AlN films were deposited by reactive RF magnetron sputtering and it was found that a two-step deposition process yielded optimum conditions for high crystalline quality and strong fiber texture. In the first process step, high energy was supplied to the growing surface by operating at high RF power applied to the target and low working pressure (500 W and 1.5×10^{-3} mbar respectively, for the sputtering chamber used). These conditions enhanced the surface energy of the substrate and the mobility of impinging species, forming a seed layer that promoted the orientation of the subsequent film growth. In addition, using high nitrogen flow rate (8 sccm) allowed for operating in a deeper poisoned mode to promote the nucleation of small $c-$axis oriented grains. During the second step, deposition was performed at higher pressure, moderate RF target power and lower nitrogen flow to reduce the deposition rate and the energy supplied to the adatoms, favoring well aligned columnar development (2×10^{-3} mbar, 400W and 6 sccm, respectively). In this way, highly (0002) oriented AlN films with a fiber texture were successfully obtained. In addition, highly-textured AlN/AlN multilayer samples were prepared to understand the effect of interfaces between layers and associated nanoscale defects induced by oxygen impurities on thermal transport properties. For this set of samples, a periodical interruption of the deposition process was performed to create interfaces with oxygen-related defects between two AlN layers, deposited one on the top of the other.

Microstructure and crystallographic analyses showed that the angular distribution of the crystalline orientations of the AlN film sharpens with increasing film thickness. It was found that their structure evolves from near-random crystallite orientations towards a strong fiber texture along the $c-$axis near the outer surface of the film. The crystallographic misalignment with respect to the $c-$axis decreased from 5.8 to 2.55° for film thickness varying from about 270 to 1460 nm. This evolving textured structure can be divided in three zones, namely the near-interface, transition and columnar region. On the other hand, it was found for multilayers, that air exposure after deposition of an AlN layer yields to local oxidation of the AlN/AlN interfaces, which induce lattice distortion and planar defects that originate from oxygen inclusions in the AlN lattice. This oxygen-related defects limited to some extent the development of texture, yielding to lower out-of-plane alignment. Grain size distributions, measured by statistical analysis of TEM images, showed nanoscale mean sizes in the interface and transition regions of about 4 nm and 10 nm respectively. These values were found to be sample and thickness-independent, suggesting that monolayer and multilayer films are subjected to similar lattice strain relaxation and grain growth mechanisms. In addition, statistical measurements of SEM images showed that with film thickness, the mean column diameter increased from about 18 to 45 nm, and the distributions became broader. This result suggests that the competition between nucleation rate and adatom mobility inhibits to some extent the coalescence of crystals developed from all nucleation sites, promoting the subsistence and growth of small grains. Moreover, TEM and EDX analyses, evidenced the presence of a native amorphous SiO_2 layer of about 3 nm on the surface of the silicon substrate in all the studied samples. For multilayer specimens, the presence of random oxygen impurities between two successive AlN layers was evidenced. Based on the results of these XRD, TEM and SEM structural characterizations, analysis of the thermal properties considering multiscale structural features and defects present in AlN films was possible.

The impact of local oxidation and morphology evolution of grains along the cross plane direction of polycrystalline AlN films on their thermal conductivity was investigated by the differential 3ω technique on monolayer and multilayer samples. Thermal measurements showed that the effective thermal conductivity decreases systematically as the film thickness decreases. For multilayer samples with thicknesses ranging from about 1107 to 270 nm, a reduction of $\approx 47\%$ on the effective thermal conductivity was measured, whereas for their corresponding monolayer counterparts of approximately the same thickness, the effective thermal conductivity decreased by $\approx 58\%$.

An analytical model for nanocrystalline materials with inhomogeneous structures was used to explain the experimental results. The model takes into account the distribution of the grain geometry and size, considering the films as a system of three stacked layers, composed of parallelepiped grains. The

experimental values of the thermal conductivity of the monolayer and multilayer films were found to be well predicted by the developed model, with a deviation of less than 10%. By correlating the structural features measured by the TEM and SEM studies with the model predictions, it was found that the thickness dependent behavior of the thermal conductivity arises as a consequence of the interfacial thermal resistance between the AlN films and the substrate, as well as from the size effects associated to the structural inhomogeneity, and to a smaller extent, from grain boundaries. It was demonstrated that the effect of the interfacial thermal resistance and the resistance of the small-grained domains weakens with increasing film thickness. Conversely, the increase of phonon MFPs and resistance of the columnar region, which is lower than that of the small-grained regions, strengthen due to the grain evolution towards greater mean sizes. Thus, the resistances due to the interface with the substrate and to the near-interface and transition regions dominate thermal conduction for thinner films, whilst for thicker films, the increased MFPs and intrinsic resistance resulting from the columnar region predominate. These changes in the transport mechanisms were found to arise due to the relative contribution of each domain to thermal transport with respect to the total film thickness.

For multilayer systems, it was evidenced experimentally that local oxidation at AlN/AlN interfaces yields to an overall reduction of the effective thermal conductivity. An effective thermal conductivity of 5.92 $\mathrm{W/m \cdot K}$ was measured for a multilayer structure of ≈1107 nm-thick, which represented a reduction of $\approx 20\%$ of the thermal conductivity of an AlN monolayer with approximately the same thickness, due to increased phonon scattering by oxygen-related defects at the interface of AlN layers. TEM analysis revealed that these defects are localized transversally with respect to the out-of-plane axis, strongly limiting cross-plane thermal conduction. By means of the theoretical model, it was shown that in multilayers, the effective thermal conductivity is reduced as a consequence of adding contributions arising from the intrinsic resistance of AlN and AlN/AlN interfaces. These experimental and theoretical results demonstrate that adding or removing multiscale defects, such as those associated to the structural inhomogeneity and the oxygen-related defects in nanocrystalline AlN films, are an effective means to statically tune their cross-plane thermal conductivity. The results obtained from this investigation are expected to contribute to the understanding and control of thermal transport properties of polycrystalline layers with structural features that evolve along the film thickness.

Finally, thermal measurements as a function of strain were performed using a novel experimental approach consisting of a 4-points bending system coupled to the 3ω method. The new experimental set-up developed in this work was adapted to be used with film-on-substrate samples. It allowed the application of a well-controlled mechanical load to the sample, while simultaneously measuring the strain within the specimen and performing 3ω thermal

conductivity measurements on the film. The main objective of these experiments was to explore the dynamic modulation of heat transfer due to lattice deformation caused by externally induced strain. Experimental observations yielded different strain-dependent behaviors for the analyzed samples, which were namely highly-textured monolayer and multilayer samples, and a poorly-textured monolayer specimen. For both poorly and highly-oriented monolayers, any significant changes were detected over the studied strain-range, while a pronounced decrease of about 23% was measured on the highly-textured multilayer specimen, for an induced uniaxial strain ranging from 0 to 0.09%. Considering the limited range of strain investigated in this work, it is unlikely that such an important decrease arises from variations in thermal conduction processes. Further understanding of the underlying physics that drives the phonon dynamics in nanocrystalline materials subjected to strain is required to estimate if uniaxial strain along with oxygen-related defects, are effective means to induce significant changes in transport properties. In addition, all sources of experimental uncertainty should be carefully identified to analyze the relevance of the results obtained in this study.

To conclude, this work made progress towards the understanding of heat transfer and thermal conductivity modulation in polycrystalline thin films by:

- Accurately describing the role of the structural inhomogeneity along the film thickness in thermal properties using both experimental and analytical means. The obtained results yield an experimental approach to perform structural characterization of polycrystalline films, and describe their thickness-dependent thermal conductivity through an analytical model.
- Identifying new strategies to statically tune thermal conductivity of nanocrystalline films, such as the modification of grain sizes within the different structural domains present in films with non-homogeneous structures, and the introduction of local oxidation at the interface between layers, which provides a simple and inexpensive method to reduce the thermal conductivity of thin films.
- Developing a novel experimental technique that allows for well-controlled mechanical loading and experimental determination of induced strain within the specimen. The apparatus, which is a simple and easily-reproducible set-up, enables to perform 3ω thermal conductivity measurements, while inducing strain.

Future directions

Although this investigation provides useful insights into thermal conduction modulation, there are several extensions that could be pursued:

1. To control mean grain size within the various structural domains present in polycrystalline films, deposition parameters should be adjusted to obtain grain size distributions adapted to a particular targeted objective in terms of thermal conduction. The effect of the substrate temperature and the nitrogen gas flow at the early deposition stage should be carefully investigated, because of their strong effect on nucleation mechanisms.

2. Temperature-dependent thermal measurements should be performed to understand the role of the multiscale defects as a function of temperature.

3. Further efforts should be addressed to understand and decouple the effect of strain on the heater electrical resistance to confirm the results obtained in this work.

4. It could be interesting to analyze materials that change their structural properties under strain. In particular, shape memory alloys or phase transition materials should be considered. To serve as an example, Li et al. (2014) theoretically showed very recently that large reversible changes of thermal conductivity, induced by mechanical stress, can be achieved with multiferroic-twinned films. The study suggested that changes in thermal conduction can be induced by variation of the density of twin boundaries perpendicular to the direction of heat flow.

5. Finally, materials such as ferroelectric thin films should be considered as a potential candidate to strain-mediated thermal conductivity investigations. Indeed, in an edge-cutting study, Ihlefeld et al. (2015) have achieved experimentally the reversible tuning of phonon transport at room temperature by the reconfiguration of the domain wall density of a lead zirconate titanate bilayer, induced by the application of an electric field.

Appendix A

Uncertainty propagation in the differential 3ω method

Table A.1 summarizes the input variables of the 3ω measurements considered for the uncertainty analysis, and their correspondent sensitivity coefficients.

Table A.1: *Uncertainty propagation in the differential* 3ω *method*

Measured variable	**Sensitivity Coefficients**[a]	**Partial Derivative**
L	$\frac{\partial k_{eff}}{\partial L}$	$\frac{1}{4}\left[\left(\frac{V_{3\omega}b}{P_l\alpha V_{1\omega}}\right)_{R+F} - \left(\frac{V_{3\omega}b}{P_l\alpha V_{1\omega}}\right)_{R}\right]^{-1}$
$V_{3\omega_{(R+F)}}$	$\frac{\partial k_{eff}}{\partial V_{3\omega_{(R+F)}}}$	$-\frac{L}{4}\left(\frac{b}{P_l\alpha V_{1\omega}}\right)_{R+F}\left[\left(\frac{V_{3\omega}b}{P_l\alpha V_{1\omega}}\right)_{R+F} - \left(\frac{V_{3\omega}b}{P_l\alpha V_{1\omega}}\right)_{R}\right]^{-2}$
$V_{3\omega_{(R)}}$	$\frac{\partial k_{eff}}{\partial V_{3\omega_{(R)}}}$	$\frac{L}{4}\left(\frac{b}{P_l\alpha V_{1\omega}}\right)_{R}\left[\left(\frac{V_{3\omega}b}{P_l\alpha V_{1\omega}}\right)_{R+F} - \left(\frac{V_{3\omega}b}{P_l\alpha V_{1\omega}}\right)_{R}\right]^{-2}$
$b_{(R+F)}$	$\frac{\partial k_{eff}}{\partial b_{(R+F)}}$	$-\frac{L}{4}\left(\frac{V_{3\omega}}{P_l\alpha V_{1\omega}}\right)_{R+F}\left[\left(\frac{V_{3\omega}b}{P_l\alpha V_{1\omega}}\right)_{R+F} - \left(\frac{V_{3\omega}b}{P_l\alpha V_{1\omega}}\right)_{R}\right]^{-2}$
b_R	$\frac{\partial k_{eff}}{\partial b_R}$	$\frac{L}{4}\left(\frac{V_{3\omega}}{P_l\alpha V_{1\omega}}\right)_{R}\left[\left(\frac{V_{3\omega}b}{P_l\alpha V_{1\omega}}\right)_{R+F} - \left(\frac{V_{3\omega}b}{P_l\alpha V_{1\omega}}\right)_{R}\right]^{-2}$
$\alpha_{(R+F)}$	$\frac{\partial k_{eff}}{\partial \alpha_{(R+F)}}$	$\frac{L}{4}\left(\frac{V_{3\omega}b}{P_l\alpha^2 V_{1\omega}}\right)_{R+F}\left[\left(\frac{V_{3\omega}b}{P_l\alpha V_{1\omega}}\right)_{R+F} - \left(\frac{V_{3\omega}b}{P_l\alpha V_{1\omega}}\right)_{R}\right]^{-2}$
α_R	$\frac{\partial k_{eff}}{\partial \alpha_R}$	$-\frac{L}{4}\left(\frac{V_{3\omega}b}{P_l\alpha^2 V_{1\omega}}\right)_{R}\left[\left(\frac{V_{3\omega}b}{P_l\alpha V_{1\omega}}\right)_{R} - \left(\frac{V_{3\omega}b}{P_l\alpha V_{1\omega}}\right)_{R}\right]^{-2}$

Appendix B

Experimental variables of 3ω measurements

The experimental variables of the 3ω measurements corresponding to the monolayer and multilayer sets of samples, and the reference specimen are summarized in Table B.1 and B.2, respectively.

Table B.1: *Experimental variables of* 3ω *measurements on monolayer .*

Quantity	**Units**	**Monolayer samples**				
		S1	S2	S3	S4	S5
Thickness, L	$(\times 10^{-7})$ m	2.689	3.801	6.400	11.052	14.612
2b	$(\times 10^{-6})$ m	10.651	9.520	10.000	9.890	10.322
α	$(\times 10^{-3})$ 1/K	2.456	2.477	2.365	2.310	2.439
$V_{3\omega}$	$(\times 10^{-3})$ V	2.172	4.891	2.396	4.247	3.355
$V_{1\omega}$	V	1.728	1.771	1.722	1.786	1.794
P_l	W/m	5.005	4.378	4.928	4.863	5.144

Table B.2: *Experimental variables of 3ω measurements on multilayer samples, and the reference specimen.*

Quantity	**Units**	**Multilayer samples**			**Reference**
		S6	S7	S8	S9
L	$(\times 10^{-7})$ m	545.1	935.4	1107.5	3.0
2b	$(\times 10^{-6})$ m	9.651	10.005	10.003	9.316
α	$(\times 10^{-3})$ 1/K	2.425	2.519	2.451	2.315
$V_{3\omega}$	$(\times 10^{-3})$ V	3.285	3.115	3.932	2.306
$V_{1\omega}$	V	1.772	1.864	2.034	2.877
P_l	W/m	4.425	4.602	4.999	4.979

Appendix C

Cross-sectional brigth field TEM micrographs

From Fig.C.1 it can be seen that the 3 analyzed AlN films feature a V-shaped columnar structure, typically observed in AlN films sputtered without any external heating, as is our case. The individual columns are dense, and a clear structural non-homogeneity along the $c-$axis can be identified.

For all analyzed samples, three different structural domains can be recognized (Fig.C.1): the region (1) near the interface with the silicon substrate, where the column boundaries can not be observed, the region (2) between the columnar and near-interface region, where column boundaries become recognizable, and the region (3) or columnar region, where the grains are large, exhibiting defined column boundaries and diameters that increase with layer thickness. Regions are indicated by the circled numbers in the figure.

From this comparative TEM study, it was found that collective crystal growth of highly and poorly textured films is globally driven by the same mechanisms, only differing by the growth rate of a particular orientation, which is determined by the energy supplied during the deposition process.

Microstructure of the poorly textured AlN sample only differs from the highly (0002) oriented films by a slight tilt of the AlN $c-$axis relative to the substrate normal [Fig.C.1(c)]. It has been shown by Deng et al. (2012) that this $c-$axis tilt angle is due to a larger growth rate along the $[10\bar{1}0]$ direction, favored by the deposition conditions (lower energy supplied to the adatoms during the growth).

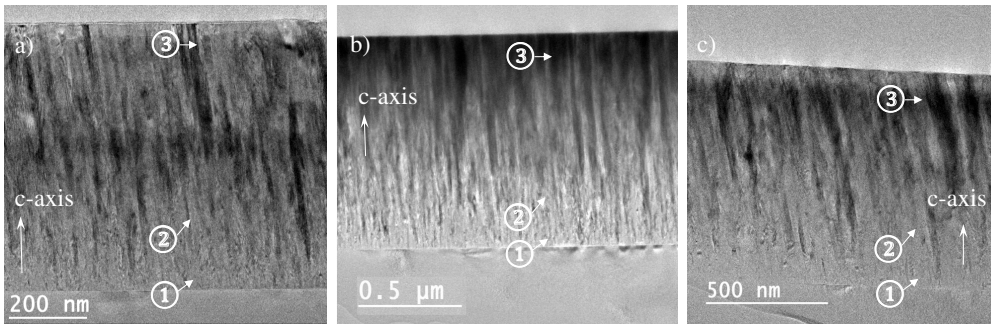

Figure C.1: *Cross sectional bright field TEM images obtained along the* [011] *zone axis of silicon. a) highly c-axis oriented 640nm thick AlN monolayer film, b) highly c-axis oriented 935 nm thick AlN multilayer, and c) poorly textured 850 nm thick monolayer.*

Appendix D

Fast Fourier transform pattern of (100) single crystal silicon

The FFT pattern obtained from a cross sectional HRTEM micrograph of the Si/AlN interface is shown in Fig. D.1. The obtained pattern is in complete agreement with the typical FFT spot array of crystalline (100) silicon reported in the literature (Galca et al. (2012)). The FFT pattern was obtained HRTEM micrograph captured with the electron beam parallel to the [011] Si zone axis.

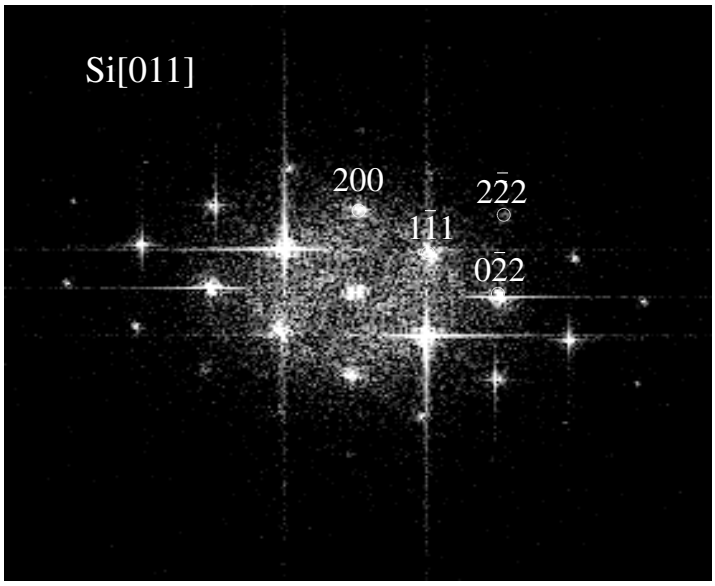

Figure D.1: *Fast Fourier transform pattern of (100) single crystal silicon, obtained from a cross sectional HRTEM micrograph of the Si/AlN interface. The micrograph was captured with the electron beam parallel to the [011] zone axis.*

Appendix E

EDX spectroscopy on a 850 nm monolayer

Figure E.1 is a high-angle annular dark-field image and its corresponding chemical distribution maps obtained by energy-dispersive X-ray spectroscopy on a 850 nm monolayer sample. These EDX spectra were acquired for acquisition times of about 60 s, and an operating energy of 200 KV.

The color maps of Al K_α (red) and N K_α (blue) depicted in Fig.E.1(b) and (c) respectively, show that both elements are uniformly distributed within the film.

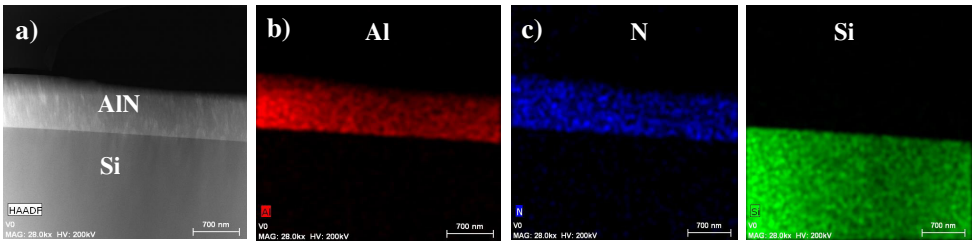

Figure E.1: *a) HAADF-STEM image of a 850 nm monolayer and its corresponding individual element distribution maps of b) aluminum in red c) nitrogen in blue, d) silicon in green, performed by energy-dispersive X-ray spectroscopy (EDX).*

References

Adamik, M., P. Barna, and I. Tomov (1998). Columnar structures in polycrystalline thin films developed by competitive growth. *Thin Solid Films 317*, 64 68. *(p. 12)*

Alam, M. and M. Manoharan (2012, April). Influence of strain on thermal conductivity of silicon nitride thin films. *Journal of Micromechanics and Microengineering 22*(045001), 045001 1 9. *(p. 7, 19, 20, 71, 159)*

Alam, M. and R. Pulavarthy (2015, August). Mechanical Strain Dependence of Thermal Transport in Amorphous Silicon Thin Films. *Nanoscale and and Microscale Thermophysical Engineering 19*(1), 1 16. *(p. 20, 159)*

Artieda, A., C. Sandu, and P. Muralt (2010). Highly piezoelectric AlN thin films grown on amorphous, insulating substrates. *Journal of Vacuum Science & Technology A: Vacuum, Surfaces, and Films 28*(3), 390 393. *(p. 33)*

ASTM International (2013). Standard Test Method for Flexural Strength of Advanced Ceramics at Ambient Temperature. *ASTM International C1161-13*. *(p. 72)*

Aubain, M. (2013). *Determination of the thermal conductivity of dielectric thin films through experimental measurement and crystallographic analysis*. Ph. D. thesis, University of California, San Diego. *(p. 141)*

Barna, P. and M. Adamik (1998, April). Fundamental structure forming phenomena of polycrystalline films and the structure zone models. *Thin Solid Films 317*, 27 33. *(p. 12, 14, 31, 103, 119, 151)*

Bateman, H., A. Erdélyi, H. van Haeringen, and L. Kok (1954). *Tables of integral transforms*. London: McGraw-Hill, New York. *(p. 54)*

Belkerk, B. E., S. Bensalem, A. Soussou, M. Carette, H. Al Brithen, M. Djouadi, and Y. Scudeller (2014). Substrate-dependent thermal conductivity of aluminum nitride thin-films processed at low temperature. *Applied Physics Letters 105*, 2219051 2219054. *(p. 138)*

Belkerk, B. E., A. Soussou, M. Carette, M. a. Djouadi, and Y. Scudeller (2012). Structural-dependent thermal conductivity of aluminium nitride produced by reactive direct current magnetron sputtering. *Applied Physics Letters 101*(15), 1519081 1519081. *(p. 16, 86, 96, 135, 137, 138)*

Billard, A. and F. Perry (2005). Pulvérisation cathodique magnétron. *Techniques de l'ingénieur. Matériaux métalliques 33*, 1 21. *(p. 29, 30)*

Boeshore, S. (2006). *Aluminum Nitride Thin Films on Titanium: Piezoelectric Transduction on a Metal Substrate*. Ph. D. thesis, University of California. *(p. 30, 31, 32, 36, 105)*

Borca-Tasciuc, T. and G. Chen (2004). Experimental Techniques for Thin-Film Thermal Conductivity Characterization. In *Thermal Conductivity Physics of Solids and Liquids*, pp. 205 237. *(p. 46, 48)*

Borca-Tasciuc, T., a. R. Kumar, and G. Chen (2001). Data reduction in 3ω method for thin-film thermal conductivity determination. *Review of Scientific Instruments 72*(4), 2139. *(p. 53, 57, 58, 60, 61, 62)*

Bragg, W. and W. Bragg (1913). The reflection of X-rays by crystals. *Proceedings of the Royal Society of London. Series A 89*, 246 248. *(p. 38)*

Braginsky, L., N. Lukzen, V. Shklover, and H. Hofmann (2002, October). High-temperature phonon thermal conductivity of nanostructures. *Physical Review B 66*(13), 134203. *(p. 13)*

Burnette, J. E., S. Kiesel, D. E. Sayers, and R. J. Nemanich (2008, February). Titanium Interlayer Mediated Epitaxy of CoSi2 on Si1âˆ'xGex. *Thin Solid Films 516*(8), 1809 1817. *(p. 100)*

Cahill, D., M. Katiyar, and J. Abelson (1994). Thermal conductivity of a-Si: H thin films. *Physical Review B*. *(p. 48, 55)*

Cahill, D. and R. Pohl (1987). Thermal conductivity of amorphous solids above the plateau. *Physical Review B*. *(p. 47, 48, 51, 127)*

Cahill, D. G. (1989, May). Thermal conductivity of thin films: Measurements and understanding. *Journal of Vacuum Science & Technology A: Vacuum, Surfaces, and Films 7*(3), 1259. *(p. 48)*

Cahill, D. G. (1990). Thermal conductivity measurement from 30 to 750 K: the 3ω method. *Review of Scientific Instruments 61*(2), 802. *(p. 47, 48, 50, 53, 54, 55, 62)*

Cahill, D. G. (2002). Erratum: Thermal conductivity measurement from 30 to 750 K: The 3ω method [Rev. Sci. Instrum. 61, 802 (1990)]. *Review of Scientific Instruments 73*(10), 3701. *(p. 48)*

Cahill, D. G., K. Goodson, and A. Majumdar (2002). Thermometry and Thermal Transport in Micro/Nanoscale Solid-State Devices and Structures. *Journal of Heat Transfer 124*(2), 223. *(p. 47)*

Carrete, J., N. Mingo, and S. Curtarolo (2014, September). Low thermal conductivity and triaxial phononic anisotropy of SnSe. *Applied Physics Letters 105*(10), 101907. *(p. 17)*

Carslaw, H. and J. Jaeger (1959). *Conduction of heat in solids*. Oxford: Oxford University Press. *(p. 51)*

Carvalho, R. and A. Menezes (2013). Lattice strain distribution resolved by X-ray Braggsurface diffraction in an Si matrix distorted by embedded FeSi2 nanoparticles. *Journal of Applied Crystallography 46*, 1796 1804. *(p. 100)*

Chang, C. W., D. Okawa, A. Majumdar, and A. Zettl (2006). Solid-state thermal rectifier. *Science (New York, N.Y.) 314*, 1121 1124. *(p. 7, 18)*

Chávez-Ángel, E., J. S. Reparaz, J. Gomis-Bresco, M. R. Wagner, J. Cuffe, B. Graczykowski, A. Shchepetov, H. Jiang, M. Prunnila, J. Ahopelto, F. Alzina, and C. M. Sotomayor Torres (2014). Reduction of the thermal conductivity in free-standing silicon nano-membranes investigated by non-invasive Raman thermometry. *APL Materials 2*. *(p. 13)*

Chen, G. (1998). Thermal conductivity and ballistic-phonon transport in the cross-plane direction of superlattices. *Physical Review B 57*(23), 958 973. *(p. 13, 89)*

Chen, G. (2005). *Nanoscale Energy Transport and Conversion: A Parallel Treatment of Electrons, Molecules, Phonons, and Photons*. Oxford, New York: Oxford University Press. *(p. 88)*

Chen, G. and C. Dames (2005, December). Thermal Conductivity of Nanostructured Thermoelectric Materials. In *Thermoelectrics Handbook*, pp. 16 42. CRC Press. *(p. 13)*

Choi, J., J. Lee, and J. Kim (2001). Phase evolution in aluminum nitride thin films on Si (100) prepared by radio frequency magnetron sputtering. *Thin Solid Films 384*, 166 172. *(p. 70, 99)*

Choi, S. R., D. Kim, S.-H. Choa, S.-H. Lee, and J.-K. Kim (2006, May). Thermal Conductivity of AlN and SiC Thin Films. *International Journal of Thermophysics 27*(3), 896 905. *(p. 15, 16, 134)*

Clement, M., E. Iborra, J. Sangrador, A. Sanz-Hervas, L. Vergara, and M. Aguilar (2003). Influence of sputtering mechanisms on the preferred orientation of aluminum nitride thin films. *Journal of Applied Physics 94*(3), 1495 1500. *(p. 103)*

Crommie, M. and A. Zettl (1990). Thermal Conductivity of Single-Crystal Bi-Sr-Ca-Cu-O. *Physical Review B 41*(16), 978 982. *(p. 13)*

Cullity, B. (1978). *Elements of X-ray diffraction* (2nd ed.). Addison-Wesley Series in Metallurgy and Materials. *(p. 38, 97, 100)*

Dames, C. (2013). Measuring the thermal conductivity of thin films : 3 omega and related electrothermal methods. *Annual Review of Heat Transfer 16*(16). *(p. 47, 53, 57, 59, 60)*

Dames, C. and G. Chen (2005). 1ω, 2ω, and 3ω methods for measurements of thermal properties. *Review of Scientific Instruments 76*(12), 124902. *(p. 50)*

Darakchieva, V., J. Birch, M. Schubert, T. Paskova, S. Tungasmita, G. Wagner, A. Kasic, and B. Monemar (2004, July). Strain-related structural and vibrational properties of thin epitaxial AlN layers. *Physical Review B 70*(4), 0454111 04541110. *(p. 97, 106)*

Deng, R., P. Muralt, and D. Gall (2012). Biaxial texture development in aluminum nitride layers during off-axis sputter deposition. *Jornal of Vacuum Science & Technology A 30*(5), 0515011 0515019. *(p. 36, 119, 173)*

Ding, Z., J. Jiang, Q. Pei, and Y. Zhang (2015). In-plane and cross-plane thermal conductivities of molybdenum disulfide. *Nanotechnology 26*, 065703. *(p. 19)*

Dong, H., B. Wen, and R. Melnik (2014, January). Relative importance of grain boundaries and size effects in thermal conductivity of nanocrystalline materials. *Scientific reports 4*(7037), 1 5. *(p. xxvi, 6, 13, 14, 145)*

Duquenne, C., M.-P. Besland, P. Y. Tessier, E. Gautron, Y. Scudeller, and D. Averty (2012, January). Thermal conductivity of aluminium nitride thin films prepared by reactive magnetron sputtering. *Journal of Physics D: Applied Physics 45*(1), 0153011 0153018. *(p. 16, 96, 135, 137, 138)*

Farrance, I. and R. Frenkel (2012). Uncertainty of measurement: A review of the rules for calculating Uncertainty components through functional relationships. *(p. 63)*

Felmetsger, V. (2011). Deposition of ultrathin AlN films for high frequency electroacoustic devices. *Journal of Vacuum Science & Technology A: Vacuum, Surfaces, and Films 29*(2), 0210141 0210147. *(p. 36, 101)*

Felmetsger, V. V., P. N. Laptev, and S. M. Tanner (2008, November). Crystal orientation and stress in AC reactively sputtered AlN films on Mo electrodes for electro-acoustic devices. *2008 IEEE Ultrasonics Symposium* (1), 2146 2149. *(p. 33, 34, 35)*

Feser, J. P. (2010). *Scalable routes to efficient thermoelectric materials*. Ph. D. thesis, UC Berkeley. *(p. 63)*

Ftouni, H. (2013). *Transport thermique dans des membranes très minces de SiN amorphe*. Ph. D. thesis, Universite de Grenoble. *(p. 20)*

Fuchs, K. (1938, January). The conductivity of thin metallic films according to the electron theory of metals. *Mathematical Proceedings of the Cambridge Philosophical Society 34*(01), 100 108. *(p. 13)*

Galca, A., G. Stan, L. Trinca, C. Negrila, and L. Nistor (2012, December). Structural and optical properties of c-axis oriented aluminum nitride thin films prepared at low temperature by reactive radio-frequency magnetron sputtering. *Thin Solid Films 524*, 328 333. *(p. 175)*

Gan, M., V. Samvedi, and V. Tomar (2014, October). Raman Spectroscopy-Based Investigation of Thermal Conductivity of Stressed Silicon Microcantilevers. *Journal of Thermophysics and Heat Transfer*, 1 13. *(p. 19, 20)*

Glassbrenner, C. and G. Slack (1964). Thermal conductivity of silicon and germanium from 3 K to the melting point. *Physical Review 134*(4A), A1058 A1069. *(p. 13)*

Goodson, K. E. (1993). *Thermal conduction in microelectronic circuits*. Ph. D. thesis, Massachusetts Institute of Technology, Dept. of Mechanical Engineering. *(p. 129, 130)*

Graebner, J., M. Reiss, and L. Seibles (1994). Phonon scattering in chemical-vapor-deposited diamond. *Physical Review B 50*(6), 3702 3707. *(p. 141)*

Gunes, M. and M. Ozenbas (2015). Effect of grain size and porosity on phonon scattering enhancement of Ca 3 Co 4 O 9. *Journal of Alloys and Compounds 626*, 360 367. *(p. 17)*

Gurevich, V. (1986). *Transport in phonon systems*. Amsterdam: North-Holland Publishing Company. *(p. 14)*

Gurrum, S. P., W. P. King, and Y. K. Joshi (2008). A semianalytical solution for the 3ω method including the effect of heater thermal conduction. *Journal of Applied Physics 103*(11), 113517. *(p. 60)*

Hanada, T. (2009). Basic Properties of ZnO, GaN, and Related Materials. In *Oxide and Nitride Semiconductors*, Volume 12, pp. 1 19. Springer Berlin Heidelberg. *(p. 27)*

Hao, Q. (2012). Effective medium formulation for phonon transport analysis of nanograined polycrystals. *Journal of Applied Physics 111*(1), 014307. *(p. 6)*

Hao, Q. (2014, July). General effective medium formulation for thermal analysis of a polycrystal - The influence of partially specular phonon transmission across grain boundaries. *Journal of Applied Physics 116*(3), 034305. *(p. 13)*

Hao, Q., G. Chen, and M.-S. Jeng (2009). Frequency-dependent Monte Carlo simulations of phonon transport in two-dimensional porous silicon with aligned pores. *Journal of Applied Physics 106*(11), 114321. *(p. 13)*

Hao, Q., G. Zhu, G. Joshi, X. Wang, A. Minnich, Z. Ren, and G. Chen (2010). Theoretical studies on the thermoelectric figure of merit of nanograined bulk silicon. *Applied Physics Letters 97*(6), 0631091 0631093. *(p. 13)*

Hopkins, P. E. (2013). Thermal Transport across Solid Interfaces with Nanoscale Imperfections: Effects of Roughness, Disorder, Dislocations, and Bonding on Thermal Boundary Conductance. *ISRN Mechanical Engineering 2013*(1), 1 19. *(p. 7, 18)*

Hui, P. and H. S. Tan (1997). On the effect of nonlinear boundary conditions for heat conduction in diamond heat spreaders with temperature-dependent thermal conductivity. *IEEE Transactions on Components Packaging and Manufacturing Technology Part A 20*, 537 540. *(p. 60)*

Hull, R. (Ed.) (1999). *Properties of crystalline silicon*. London, United Kingdom: INSPEC, Institution of Electrical Engineers. *(p. 58, 98)*

Hwang, B. (2001). Calculation and measurement of all (002) multiple diffraction peaks from a (001) silicon wafer. *Journal of Physics D: Applied Physics 34*(16), 2469 2474. *(p. 100, 105)*

Ihlefeld, J., B. Foley, and D. Scrymgeour (2015). Room Temperature Voltage Tunable Phonon Thermal Conductivity via Reconfigurable Interfaces in Ferroelectric Thin Films. *Nano letters 15*, 1791 1795. *(p. 19, 167)*

Iskandar, A., A. Abou-Khalil, M. Kazan, W. Kassem, and S. Volz (2015). On the interplay between phonon-boundary scattering and phonon-point-defect scattering in SiGe thin films. *Journal of Applied Physics 117*(12), 125102. *(p. 18)*

Jacquot, A. (2003). *Ingénierie des matériaux et de microgénérateurs thermoélectriques planaires*. Ph. D. thesis, Institut National Polytechnique de Lorraine. *(p. 49, 66)*

Jacquot, A., B. Lenoir, and A. Dauscher (2002). Numerical simulation of the 3ω method for measuring the thermal conductivity. *Journal of Applied Physics 91*(7), 4733 4738. *(p. 53, 61)*

Jaramillo-Fernandez, J., J. Ordonez-Miranda, E. Ollier, and S. Volz (2015, March). Tunable thermal conductivity of thin films of polycrystalline AlN by structural inhomogeneity and interfacial oxidation. *Physical chemistry chemical physics : PCCP 17*(12), 8125 37. *(p. 14)*

Jeng, M., R. Yang, D. Song, and G. Chen (2008). Modeling the thermal conductivity and phonon transport in nanoparticle composites using Monte Carlo simulation. *Journal of Heat Transfer 130*, 042410. *(p. 13)*

Júnior, A. F. and D. Shanafield (2004). Thermal conductivity of polycrystalline aluminum nitride (AlN) ceramics. *Ceramica 50*, 247 253. *(p. 12)*

Kar, J., G. Bose, and S. Tuli (2009). Growth of AlN films and its process development for the fabrication of acoustic devices and micromachined structures. *Journal of Materials Engineering and Performance 18*(8), 1046 1051. *(p. 32)*

Kato, R., A. Maesono, and R. Tye (2001). Thermal conductivity measurement of submicron-thick films deposited on substrates by modified ac calorimetry (laser-heating Ångstrom method). *International journal of thermophysics 22*(2), 617 629. *(p. 138)*

Kaviany, M. (2011). *Essentials of Heat Transfer: Principles, Materials, and Applications*. Cambridge University Press. *(p. 11, 129)*

Kazan, M., G. Guisbiers, S. Pereira, M. R. Correia, P. Masri, a. Bruyant, S. Volz, and P. Royer (2010). Thermal conductivity of silicon bulk and nanowires: Effects of isotopic composition, phonon confinement, and surface roughness. *Journal of Applied Physics 107*(8), 083503. *(p. 13)*

Kazan, M. and S. Volz (2014, February). Calculation of the lattice thermal conductivity in granular crystals. *Journal of Applied Physics 115*(7), 073509. *(p. 13)*

Kim, I., A. Madan, and M. Guruz (2001). Stabilization of zinc-blende cubic AlN in AlN/W superlattices. *Journal of Vacuum Science & Technology A: Vacuum, Surfaces, and Films 19*(5), 2069 2073. *(p. 27)*

Klemens, P. (2001). Theory of thermal conduction in thin ceramic films. *International journal of thermophysics 22*(1), 265 275. *(p. 12)*

Kline, S. J. and F. A. McClintock (1953). Describing the uncertainties in single sample experiments. *Mechanical Engineering*, 3 8. *(p. 62)*

Klug, H. and L. Alexander (1974). *X-ray diffraction procedures* (2nd ed.). John Wiley & Sons. *(p. 43, 135)*

Knuyt, G., C. Quaeyhaegens, J. D'Haen, and L. Stals (1995, March). A quantitative model for the evolution from random orientation to a unique texture in PVD thin film growth. *Thin Solid Films 258*, 159 169. *(p. 102, 119, 151)*

Knuyt, G., C. Quaeyhaegens, J. DHaen, and L. Stals (1996). A model for thin film texture evolution driven by surface energy effects. *physica status*

solidi (b) 195(1), 179 193. *(p. 103)*

Kobayashi, W., Y. Teraoka, and I. Terasaki (2010, June). A Trial Thermal Rectifier. *Journal of Electronic Materials 39*(9), 1488 1492. *(p. 7, 18)*

Koninck, D. D. and S. Vengallatore (2008). *Thermal Conductivity Measurements Using the 3-Omega Technique : Application to Power Harvesting Microsystems*. Ph. D. thesis, McGill University. *(p. 54, 55)*

Kragh, H. (2000). Max Planck: the reluctant revolutionary. *Physics World 13*, 31 35. *(p. 3)*

Kuczynski, G. (1954). Effect of elastic strain on the electrical resistance of metals. *Physical review 94*(1), 61 64. *(p. 154)*

Kumar, S., T. Alam, and A. Haque (2013). Thermo-mechanical coupling and size effects in micro and nano resonators. *Micro and Nano Systems Letters 1*(2), 1 9. *(p. 7, 19, 20, 71)*

Langer, G., J. Hartmann, and M. Reichling (1997). Thermal conductivity of thin metallic films measured by photothermal profile analysis. *Review of Scientific Instruments 68*(3), 1510 1513. *(p. 60)*

Langford, J. and A. Wilson (1978). Scherrer after sixty years: a survey and some new results in the determination of crystallite size. *Journal of Applied Crystallography 11*, 102 113. *(p. 42)*

Lawn, B. and R. Wilshaw (1975, June). Indentation fracture: principles and applications. *Journal of Materials Science 10*(6), 1049 1081. *(p. 81)*

Lee, H.-F., S. Kumar, and M. Haque (2010, December). Role of mechanical strain on thermal conductivity of nanoscale aluminum films. *Acta Materialia 58*(20), 6619 6627. *(p. 7, 19, 20, 71)*

Lee, J. and T. Schlesinger (1988). Characterization of yttria stabilized zirconium oxide buffer layers for high temperature superconductor thin films. *Journal of Applied Physics 64*(11), 6502 6504. *(p. 100)*

Lee, S.-M. and D. G. Cahill (1997). Heat transport in thin dielectric films. *Journal of Applied Physics 81*(6), 2590 2595. *(p. 47, 128, 130, 137)*

Li, N., J. Ren, L. Wang, G. Zhang, P. Hänggi, and B. Li (2012, July). Colloquium: Phononics: Manipulating heat flow with electronic analogs and beyond. *Reviews of Modern Physics 84*(3), 1045 1066. *(p. 4, 7, 18)*

Li, Q., X. Cui, S. Li, and W. Yang (2015). Synthesis and Phase Stability of Scandia, Gadolinia, and Ytterbia Co-doped Zirconia for Thermal Barrier Coating Application. *Journal of Thermal Spray Technology 24*(1-2), 136 146. *(p. 18)*

Li, S., X. Ding, J. Ren, X. Moya, J. Li, J. Sun, and E. Salje (2014, January). Strain-controlled thermal conductivity in ferroic twinned films. *Scientific reports 4*, 63751 637517. *(p. 18, 167)*

Li, X., K. Maute, M. L. Dunn, and R. Yang (2010, June). Strain effects on the thermal conductivity of nanostructures. *Physical Review B 81*(24), 245318. *(p. 7, 19, 71)*

Lim, C. W., C.-S. Shin, D. Gall, J. M. Zuo, I. Petrov, and J. E. Greene (2005). Growth of CoSi2 on Si(001) by reactive deposition epitaxy. *Journal of*

Applied Physics 97(4), 0449091 0449096. *(p. 100)*

Liu, W. and M. Asheghi (2004). Phonon-boundary scattering in ultrathin single-crystal silicon layers. *Applied Physics Letters 84*(19), 3819 3821. *(p. 13)*

Madan, A., I. Kim, S. Cheng, and P. Yashar (1997). Stabilization of cubic AlN in epitaxial AlN/TiN superlattices. *Physical Review Letters 78*, 1743. *(p. 27)*

Mag-isa, A., B. Jang, J. Kim, H. Lee, and C. Oh (2014). Coefficient of thermal expansion measurements for freestanding nanocrystalline ultrathin gold films. *International journal of of Precision Engineering and Manufacturing 15*(1), 105 110. *(p. 155, 160)*

Maiti, C. K., L. K. Bera, and S. Chattopadhyay (1999). Strained-Si heterostructure field effect transistors. *Semiconductor Science and Technology 13*, 1225 1246. *(p. 7, 19)*

Majumdar, A. (1993). Microscale heat conduction in dielectric thin films. *Journal of Heat Transfer 1*(February), 7 16. *(p. 87)*

Majumdar, C. K. (1969). On Next-Nearest-Neighbor Interaction in Linear Chain. I. *Journal of Mathematical Physics 10*(8), 1388. *(p. 13)*

Maldovan, M. (2013, November). Sound and heat revolutions in phononics. *Nature 503*(7475), 209 17. *(p. 4, 5)*

Martin, P. (2009). *Handbook of deposition technologies for films and coatings: science, applications and technology*. Elsevier Ltd. *(p. 29)*

Mayadas, A. and M. Shatzkes (1970). Electrical-resistivity model for polycrystalline films: the case of arbitrary reflection at external surfaces. *Physical Review B 1*(4), 1382 1389. *(p. 12)*

Miyazaki, K., T. Arashi, D. Makino, and H. Tsukamoto (2006). Heat conduction in microstructured materials. *IEEE Transactions on Components and Packaging Technologies 29*, 247 253. *(p. 13)*

Moram, M. and M. Vickers (2009). X-ray diffraction of III-nitrides. *Reports on Progress in Physics 72*, 036502. *(p. 26)*

Morkoc, H. (2009). General Properties of Nitrides. In *Handbook of Nitride Semiconductors and Devices*, Volume 1, pp. 1 1255. Wiley - VCH Verlag GmbH and Co. KGaA. *(p. 15, 60, 91, 98, 155)*

Murphy, K., B. Piccione, M. Zanjani, J. Lukes, and D. Gianola (2014). Strain- and defect-mediated thermal conductivity in silicon nanowires. *Nano letters 14*, 3785â˜'3792. *(p. 7, 18)*

Nan, C.-W. (1993, January). Physics of inhomogeneous inorganic materials. *Progress in Materials Science 37*(1), 1 116. *(p. 6)*

Ordonez-Miranda, J., L. Tranchant, Y. Chalopin, T. Antoni, and S. Volz (2014, February). Thermal conductivity of nano-layered systems due to surface phonon-polaritons. *Journal of Applied Physics 115*(5), 054311. *(p. 13)*

Pan, T. S., Y. Zhang, J. Huang, B. Zeng, D. H. Hong, S. L. Wang, H. Z. Zeng, M. Gao, W. Huang, and Y. Lin (2012). Enhanced thermal conductivity

of polycrystalline aluminum nitride thin films by optimizing the interface structure. *Journal of Applied Physics 112*(4), 0449051 0449055. *(p. 15, 16, 134)*

Paqueton, H. and J. Ruste (2006). Microscopie électronique à balayage Principe et équipement. *Techniques de l'ingénieur P865v2*. *(p. 41)*

Petrov, I. and P. Barna (2003). Microstructural evolution during film growth. *Journal of Vacuum Science & Technology A: Vacuum, Surfaces, and Films 21*(5), S117 S128. *(p. 105, 119)*

Piazza, G., V. Felmetsger, P. Muralt, R. H. Olsson III, and R. Ruby (2012, November). Piezoelectric aluminum nitride thin films for microelectromechanical systems. *MRS Bulletin 37*(11), 1051 1061. *(p. 36)*

Picu, R. C., T. Borca-Tasciuc, and M. C. Pavel (2003). Strain and size effects on heat transport in nanostructures. *Journal of Applied Physics 93*(6), 3535. *(p. 7, 19, 71)*

Planck, M. (1901). On the law of distribution of energy in the normal spectrum. *Annalen der Physik 4*, 553 ff. *(p. 3)*

Pourbafrani, M. and R. Razavi (2015). Effect of microstructure and phase of nanostructured YSZ thermal barrier coatings on its thermal shock behaviour. *Surface Engineering 31*(1), 64 73. *(p. 17)*

Prume, K. and P. Muralt (2007). Piezoelectric thin films: evaluation of electrical and electromechanical characteristics for MEMS devices. *IEEE Transactions on Ultrasonics, Ferroelectrics, and Frequency Control 54*(1), 8 14. *(p. 73, 76, 78)*

Prume, K., S. Tiedke, and T. Schmitz-Kempen (2010). Double-beam and four-point: Piezoelectric thin film characterization for MEMS applications. *Mikroniek 50*(4), 31 35. *(p. 79)*

Putnam, S. a., D. G. Cahill, B. J. Ash, and L. S. Schadler (2003). High-precision thermal conductivity measurements as a probe of polymer/nanoparticle interfaces. *Journal of Applied Physics 94*(10), 6785 6788. *(p. 155, 156)*

Pyrz, W. D. and D. J. Buttrey (2008). Particle Size Determination Using TEM: A Discussion of Image Acquisition and Analysis for the Novice Microscopist. *Langmuir 24*(20), 11350 11360. *(p. 113)*

Quinn, J. and K. Yi (2009). *Solid State Physics: Principles and Modern Applications*. Springer Science+ Business. *(p. 25, 26, 28)*

Reynolds, G. J., M. Kratzer, M. Dubs, H. Felzer, and R. Mamazza (2012, April). Sputtered Modified Barium Titanate for Thin-Film Capacitor Applications. *Materials 5*(12), 575 589. *(p. 100)*

Saga, K., H. Kuniyasu, and T. Hattori (1999). Influence of Ambient Oxygen and Moisture on the Growth of Native Oxides on Silicon Surfaces. *Test. electrochem. 1*, 1 3. *(p. 70, 99)*

Samvedi, V. and V. Tomar (2010, April). The role of straining and morphology in thermal conductivity of a set of Si-Ge superlattices and biomimetic Si-Ge nanocomposites. *Journal of Physics D: Applied Physics 43*(13),

135401. *(p. 7, 19, 71)*

Schlegel, N., S. Ebert, G. Mauer, and R. Vaß en (2015). Columnar-Structured Mg-Al-Spinel Thermal Barrier Coatings (TBCs) by Suspension Plasma Spraying (SPS). *Journal of Thermal Spray Technology 24*(1-2), 144 151. *(p. 17)*

Seneca Uk (2015). Z-SG Configuration Manual. *(p. 75)*

Sharpe, W. N. (Ed.) (2008). *Handbook of experimental solid mechanics* (1st ed.). New York: Springer Science + Business Media. *(p. 155, 160)*

Shetty, A. (2012). *Off-Axis Texture and Crystallographic Accommodation in Multicomponent Nitride Thin Films Deposited by Pulsed Magnetron Sputtering*. Ph. D. thesis, École Polytechnique Fédérale De Lausanne. *(p. 108)*

Sierra-Sosa, D. (2014). *Estudio de singularidades de fase con aplicaciones a la metrología*. Ph. D. thesis, Universidad Nacional de la Plata. *(p. 113)*

Signore, M., E. Bellini, and A. Taurino (2013). Structural and morphological evolution of aluminum nitride thin films: Influence of additional energy to the sputtering process. *Journal of Physics and Chemistry of Solids 74*(10), 1444 1451. *(p. 32, 36)*

Slack, G. (1973). Nonmetallic crystals with high thermal conductivity. *Journal of Physics and Chemistry of Solids 34*, 321 335. *(p. 15, 110, 136)*

Slack, G., R. Tanzilli, R. Pohl, and J. Vandersande (1987). The intrinsic thermal conductivity of AIN. *Journal of Physics and Chemistry of Solids 48*(7), 641 647. *(p. 91, 110, 135, 142)*

Slack, G. a., L. J. Schowalter, D. Morelli, and J. a. Freitas (2002, December). Some effects of oxygen impurities on AlN and GaN. *Journal of Crystal Growth 246*(3-4), 287 298. *(p. 7, 18, 111)*

Song, J.-H., J.-L. Huang, J. C. Sung, S.-C. Wang, H.-H. Lu, and D.-F. Lii (2011, April). Interfacial Microstructure Evolution of (B, Al)N Films Grown on Diamond Substrates. *Thin Solid Films 519*(13), 4212 4215. *(p. 86, 105)*

Spina, L. L. (2007). Bulk-micromachined test structure for fast and reliable determination of the lateral thermal conductivity of thin films. *Journal of microelectromechanical Systems 16*(3), 675 683. *(p. 141)*

Su, Z., J. P. Freedman, J. H. Leach, E. a. Preble, R. F. Davis, and J. a. Malen (2013). The impact of film thickness and substrate surface roughness on the thermal resistance of aluminum nitride nucleation layers. *Journal of Applied Physics 113*(21), 213502. *(p. 15)*

Suriano, F., M. Ferri, and F. Moscatelli (2015). Influence of Grain Size on the Thermoelectric Properties of Polycrystalline Silicon Nanowires. *Journal of Electronic ... 44*(1), 371 376. *(p. 17)*

Tajima, J., R. Togashi, H. Murakami, Y. Kumagai, K. Takada, and A. Koukitu (2011, July). Control of in-plane epitaxial relationship of c -plane AlN layers grown on a -plane sapphire substrates by hydride vapor phase epitaxy. *Physica Status Solidi (C) 8*(7-8), 2028 2030. *(p. 36)*

Takashiri, M., S. Tanaka, H. Hagino, and K. Miyazaki (2014, September).

Strain and grain size effects on thermal transport in highly-oriented nanocrystalline bismuth antimony telluride thin films. *International Journal of Heat and Mass Transfer 76*, 376 384. *(p. 7, 19, 20, 71)*

Tang, G., J.-q. Liu, B. Yang, J.-b. Luo, H.-s. Liu, Y.-g. Li, C.-s. Yang, D.-n. He, V. D. Dao, K. Tanaka, and S. Sugiyama (2012, June). Fabrication and analysis of high-performance piezoelectric MEMS generators. *Journal of Micromechanics and Microengineering 22*(6), 065017. *(p. 36)*

Thomson, W. (1856). Elements of a mathematical theory of elasticity. *Philosophical Transactions of the Royal Society of London 146*(January), 481 498. *(p. 81)*

Thornton, J. (1973). Sputter Coating-Its Principles and Potential. *SAE Transactions*, 730544. *(p. 28)*

Thornton, J. (1977). High rate thick film growth. *Annual review of materials science 7*, 239 260. *(p. 31, 105, 151)*

Tian, H., D. Xie, Y. Yang, T. Ren, and G. Zhang (2012). A novel solid-state thermal rectifier based on reduced graphene oxide. *Scientific reports 2*(529), 1 7. *(p. 7, 18)*

Tian, Z., S. Lee, and G. Chen (2014). A Comprehensive Review of Heat Transfer in Thermoelectric Materials and Devices. *Annual Review of Heat Transfer 17*, 425 483. *(p. 14)*

Tong, X. C. (2011). *Advanced Materials for Thermal Management of Electronic Packaging*, Volume 30. *(p. 45)*

Turney, J. E., a. J. H. McGaughey, and C. H. Amon (2010). In-plane phonon transport in thin films. *Journal of Applied Physics 107*(2), 024317. *(p. 13)*

Ueda, O. and S. J. Pearton (2013). *Materials and Reliability Handbook for Semiconductor Optical and Electron Devices*. *(p. 19, 73)*

Valdre, U. (Ed.) (1971). *Electron microscopy in material science* (1st ed.). London, United Kingdom: Ettore Majorana International Centre for Scientific Culture. *(p. 110)*

Van der Drift, A. (1967). Evolutionary selection, a principle governing growth orientation in vapour-deposited layers. *Philips research reports 22*, 267 288. *(p. 32)*

van Zwol, P. J., K. Joulain, P. Ben Abdallah, J. J. Greffet, and J. Chevrier (2011, May). Fast nanoscale heat-flux modulation with phase-change materials. *Physical Review B 83*(20), 201404. *(p. 18)*

van Zwol, P. J., L. Ranno, and J. Chevrier (2012, June). Tuning near field radiative heat flux through surface excitations with a metal insulator transition. *Physical review letters 108*(23), 234301. *(p. 18)*

Wang, L. and B. Li (2007, October). Thermal Logic Gates: Computation with Phonons. *Physical Review Letters 99*(17), 177208. *(p. 7, 18)*

Wang, X. and S. Shen (2014, March). Effects of temperature and strain on thermal properties of Ni/Al laminated structure. *Computational Materials Science 84*, 13 17. *(p. 7, 19, 71, 153, 160)*

Wang, Z., J. Alaniz, W. Jang, J. Garay, and C. Dames (2011). Thermal conductivity of nanocrystalline silicon: importance of grain size and frequency-dependent mean free paths. *Nano letters 11*, 2206 2213. *(p. 6)*

Wasmer, K., C. Ballif, R. Gassilloud, C. Pouvreau, R. Rabe, J. Michler, J.-M. Breguet, J.-M. Solletti, a. Karimi, and D. Schulz (2005, May). Cleavage Fracture of Brittle Semiconductors from the Nanometre to the Centimetre Scale. *Advanced Engineering Materials 7*(5), 309 317. *(p. 81)*

Williams, D. B. and C. B. Carter (2009). *Transmission Electron Microscopy: A Textbook for Materials Science* (2nd ed.), Volume V1-V4. Springer Science + Business Media. *(p. 39, 41, 42, 111)*

Wu, H., J. Carrete, Z. Zhang, Y. Qu, and X. Shen (2014). Strong enhancement of phonon scattering through nanoscale grains in lead sulfide thermoelectrics. *NPG Asia Materials 6*(6), 1 11. *(p. 17)*

Xingli, Z. and S. Zhaowei (2011). Effects of vacancy structural defects on the thermal conductivity of silicon thin films. *Journal of Semiconductors 32*, 053002. *(p. 18)*

Xu, Y. and G. Li (2009). Strain effect analysis on phonon thermal conductivity of two-dimensional nanocomposites. *Journal of Applied Physics 106*(11), 114302. *(p. 7, 19, 71)*

Yagi, T., N. Oka, T. Okabe, N. Taketoshi, T. Baba, and Y. Shigesato (2011, November). Effect of Oxygen Impurities on Thermal Diffusivity of AlN Thin Films Deposited by Reactive RF Magnetron Sputtering. *Japanese Journal of Applied Physics 50*(11), 11RB01. *(p. 136)*

Yamane, T., N. Nagai, S.-i. Katayama, and M. Todoki (2002). Measurement of thermal conductivity of silicon dioxide thin films using a 3ω method. *Journal of Applied Physics 91*(12), 9772 9776. *(p. 128, 129, 130, 137)*

Yang, H., G. Bai, L. Thompson, and J. Eastman (2002). Interfacial thermal resistance in nanocrystalline yttria-stabilized zirconia. *Acta Materialia 50*, 2309 2317. *(p. 13)*

Yang, N., X. Xu, G. Zhang, and B. Li (2012). Thermal transport in nanostructures. *AIP Advances 2*(4), 0414101 24. *(p. 7, 18)*

Yang, R., G. Chen, M. Laroche, and Y. Taur (2005). Simulation of Nanoscale Multidimensional Transient Heat Conduction Problems Using Ballistic-Diffusive Equations and Phonon Boltzmann Equation. *(p. 13)*

Yang, Z., R. Feng, F. Su, D. Hu, and X. Ma (2014). Isotope and strain effects on thermal conductivity of silicon thin film. *Physica E: Low-dimensional Systems 64*, 204 210. *(p. 159)*

Yu, R., M. Salamon, J. Lu, and W. Lee (1992). Thermal conductivity of an untwinned YBa 2 Cu 3 O 7-δ single crystal and a new interpretation of the superconducting state thermal transport. *Physical review letters 69*(9), 1431 1434. *(p. 13)*

Zhang, J., H. Cheng, Y. Chen, and A. Uddin (2005). Growth of AlN films on Si (100) and Si (111) substrates by reactive magnetron sputtering. *Surface and Coatings Technology 198*, 68 73. *(p. 33)*

Zhang, T. and T. Luo (2013, September). High-Contrast, Reversible Thermal Conductivity Regulation Utilizing the Phase Transition of Polyethylene Nanofibers. *ACS nano 7*(9), 7592 600. *(p. 18)*

Zhao, W., P. Wei, Q. Zhang, H. Peng, W. Zhu, D. Tang, and J. Yang (2015). Multi-localization transport behaviour in bulk thermoelectric materials. *Nature communications 6*, 1 7. *(p. 18)*

Zhao, Y., C. Zhu, S. Wang, J. Z. Tian, D. J. Yang, C. K. Chen, H. Cheng, and P. Hing (2004). Pulsed photothermal reflectance measurement of the thermal conductivity of sputtered aluminum nitride thin films. *Journal of Applied Physics 96*(8), 4563 4568. *(p. 15, 16, 134)*

Zhu, L. and X. Zheng (2009, November). Modification of the phonon thermal conductivity in spatially confined semiconductor nanofilms under stress fields. *EPL (Europhysics Letters) 88*(3), 36003. *(p. 7, 19, 71)*

Zhu, T. and R. Oliver (2012). Unintentional doping in GaN. *Physical Chemistry Chemical Physics 14*, 9558 9573. *(p. 26)*

Ziemian, R. D. (2010). *Guide to Stability Design Criteria for Metal Structures* (6th ed.). John Wiley & Sons. *(p. 77)*

Ziman, J. M. (1960). *Electrons and phonons: the theory of transport phenomena in solids*, Volume 20. London, United Kingdom: Oxford University Press. *(p. 11, 87, 88)*